Precision Spectroscopy on OH

Dissertation
zur Erlangung des mathematisch-naturwissenschaftlichen Doktorgrades
"Doctor rerum naturalium"
der Georg-August-Universität Göttingen

im Promotionsprogramm Physik
der Georg-August University School of Science (GAUSS)

vorgelegt von
Arthur Fast
aus Alma-Ata, Kasachstan

Göttingen, 2019

Betreungsausschuss

Dr. Samuel A. Meek, Department of Precision Infrared Spectroscopy on Small Molecules, Max-Planck-Institute for Biophysical Chemistry, Georg-August University of Goettingen

Prof. Dr. Ansgar Reiners, Department of Solar and Stellar Astrophysics, Institute for Astrophysics, Georg-August University of Goettingen

Mitglieder der Prüfungskommission

Referent: Dr. Samuel A. Meek, Department of Precision Infrared Spectroscopy on Small Molecules, Max-Planck-Institute for Biophysical Chemistry, Georg-August University of Goettingen

Korreferent: Prof. Dr. Ansgar Reiners, Department of Solar and Stellar Astrophysics, Institute for Astrophysics, Georg-August University of Goettingen

Weitere Mitglieder der Prüfungskommission:

Prof. Dr. Claus Ropers, Department of Ultrafast Dynamics and Nano-Optics, IV. Physical Institute, Georg-August University of Goettingen

Prof. Dr. Stefan Mathias, Department of Ultrafast Dynamics in Condensed Matter, I. Physical Institute, Georg-August University of Goettingen

Prof. Dr. Dirk Schwarzer, Department of Reaction Dynamics, Max-Planck-Institute for Biophysical Chemistry / Institute for Physical Chemistry, Georg-August University of Goettingen

Dr. habil. Holger Nobach, Department of Fluid Dynamics, Pattern Formation and Nanobiocomplexity, Max-Planck-Institute for Dynamics and Self-Organization, Georg-August University of Goettingen

Tag der mündlichen Prüfung: 27. Mai 2019

Abstract

This thesis describes the implementation of a high precision laser system which, as a first demonstration of its capabilities, has been used to measure electronic transitions from the $X^2\Pi_{3/2}$, $v'' = 0$, $J'' = 3/2$ rovibronic ground state to the 12 lowest levels of the $A^2\Sigma^+$, $v' = 0$ vibronic state in the hydroxyl radical (OH) and the 16 lowest levels of the same vibronic state in the deuterated hydroxyl radical (OD). The relative uncertainty of the absolute frequency measurements is within a few parts in 10^{11}. These electronic transition frequencies are determined by comparing the spectroscopy laser with reference frequency standards using an optical frequency comb (OFC). The OFC transfers the high short term stability of a narrow-linewidth I_2 stabilized referenced laser onto the spectroscopy laser around 308 nm. The second reference used with the OFC is an atomic clock, which provides an absolute accuracy of the measured transitions frequencies. The OH and the OD molecules are inside a highly collimated molecular beam, with the ultraviolet (UV) laser beam propagating perpendicular to it. This setup reduces possible pressure shifts and Doppler-broadening. Additionally, the laser beam is retroreflected to reduce Doppler-shifts. Shifts due to Zeeman-, AC-Stark- and saturation-effects are also considered in the analysis, in an effort to determine the zero-field transition frequencies.

Previous studies determined the absolute $A \leftarrow X$ transition frequencies with an accuracy of approximately 100 MHz, based on rich Fourier-transform spectra. In contrast, this thesis supplies absolute electronic transition frequencies with an uncertainty of less than 100 kHz. These new measurements of the optical transition frequencies were combined with existing data for fine and hyperfine splittings in the A state and used to fit the parameters of an effective Hamiltonian model of the $A^2\Sigma^+$, $v' = 0$ state of each isotopologue. Some of these newly-determined spectroscopic constants, are orders of magnitude more precise than the previous values.

Future experiments will benefit from the improved accuracy of the electronic excitation frequencies determined in this experiment. As a next step, a new mid infrared laser will be used to probe the vibrational excitation frequencies of OH. This OFC-stabilized mid-infrared optical parametric oscillator (OPO), which provides a narrow linewidth and wide tuning range, is also described in this thesis.

Contents

Chapter 1

Introduction

The standard model (SM) of particle physics is the essential pillar of modern physics. It has proven reliable in describing various physical phenomena related to three of the fundamental forces of the universe: the electromagnetic, the weak and the strong interaction. By now, all particles predicted by the SM have been found. However, the effort to incorporate gravity into the SM has, thus far, been unsuccessful. This blind spot of the SM is especially inconvenient, considering confirmed astronomical observations of 'dark matter'[1]. The dark matter interacts only by gravitational interaction, and most of it consists not by particles in the SM[2]. Furthermore, the Nobel prize awarded discovery of the acceleration of the universe[3–5] demands 'dark energy', which interacts as repulsive gravity. Considering the composition of the universe of 69 % dark energy, 26 % dark matter and only 5 % matter described in the SM[6], curiosity drives modern physics to get a glimpse beyond the SM. The large hadron collider (LHC) at CERN provides a direct way of measuring new particles based on collision experiments at the TeV energy scale, but there is a second way of observing new physics, with compact setups and at low energies, namely high-precision spectroscopy on atoms and molecules.

One example for the application of high-precision spectroscopy is the search for electric dipole moments (EDMs) of fundamental particles. The matter anti-matter asymmetry in the universe requires a violation of time-reversal symmetry[7], which would also be observable in an EDM. Theories that include physics beyond the SM predict EDM sizes that would be within the measurable reach of precision spectroscopy experiments[8]. A current frontier of measuring the electron EDM is using laser cooling of molecules to further improve the measurement precision[9]. In addition to the violation of the time-reversal symmetry, modern theories also predict a violation of the Lorentz symmetry, parity and charge conjunction[10], as well a variation of the fundamental constants[2,11]. The potential variation of the fundamental constants is a test of the equivalence principle, which is the pillar of the general relativity[12]. Since it's fairly likely that at least some of these symmetry violations will never be found, the capabilities for finding these small effects grows with the improvement of atomic clocks. Modern clocks reach a total uncertainty of 2×10^{-18}[13].

The core of this thesis is an atomic clock referenced laser system. It is designed to stabilize both a mid-infrared and an ultraviolet continuous wave (CW) laser, making it a general purpose system of measuring physics beyond the SM.

1.1 The Hydroxyl Radical

The investigation in this thesis is focused on the hydroxyl radical (OH), although the application of the laser system is not limited to this particular molecule. OH has a long history in various scientific fields, since it is a prototypical open-shell diatomic molecule. For instance, it was the first free radical in microwave spectroscopy[14] and interstellar radio frequency spectroscopy[15]. Furthermore, it is essential in the fields of atmospheric and climate science[16] and combustion[17]. Since the first deceleration of the OH[18], it has been used for low-energy collision studies[19,20], deceleration[21], electrostatic trapping[22] and evaporative cooling[23]. In laboratory studies, the detection of the OH is commonly carried out by laser induced fluorescence (LIF) of the $A^2\Sigma^+$-$X^2\Pi$ transitions. However, a more recent approach is based on the $1 + 1'$ multiphoton ionization (MPI), using $A \leftarrow X$ excitation as the first step[24]. The best previous measurements of the A-X transition frequencies resulted in an absolute frequency uncertainty of approximately $0.005\,\mathrm{cm}^{-1}$ ($150\,\mathrm{MHz}$)[25–27]. Depending on the application, this accuracy is sufficient for measurements with a frequency-doubled pulsed dye laser with a typical bandwidth of $0.1\,\mathrm{cm}^{-1}$. For high-resolution spectroscopy using a narrow linewidth ($< 1\,\mathrm{MHz}$) CW laser however, these uncertainties become inconvenient. Thus, our first step in characterizing OH has been to make precise measurements of the $A^2\Sigma^+$, $v' = 0 \rightarrow X^2\Pi_{3/2}$, $v'' = 0$, $J'' = 3/2$ transitions. Only with these measurements, it is possible to investigate the vibrational transitions or even proceed to experimentally more challenging systems.

1.2 Variation of Fundamental Constants

There are a variety of unitless fundamental constants that can only be determined by precise measurements since their value is not predicted by any theory. In 1937 Dirac built a hypothesis, which connected the expansion of the universe with the change of the fundamental constants[28]. The drift rate estimated by Dirac has since been ruled out, but the general idea of the variation of constants lives on in modern theories beyond the SM[29].

Historically, Thompson first suggested in 1975 using precise measurements of molecular absorption lines as a test of the potential variation of the electron to proton mass ratio μ[30]. Since then, multiple astronomical measurements followed to estimate an upper limit of the variation $\Delta\mu/\mu$[11]. The vibrational transition frequency ν is proportional to the square root of μ (Table 1.1). Therefore, an variation of μ is associated with a change of ν

Table 1.1: Scaling factors for different systems in the non-relativistic approximation, with the electron to proton mass ratio μ, the fine structure constant $\alpha \approx 1/137$ and the Rydberg constant $R_y = \alpha^2 m_e c^2/2$ (adapted from [29,31]).

Sample	Transition	Scaling
^{133}Cs	hyperfine structure	$\mu\alpha^2 R_y$
^{16}OH or ^{16}OD	electronic	R_y
	vibrational	$\mu^{1/2} R_y$

with

$$\frac{\partial \nu}{\partial \mu} \propto \frac{1}{2}\mu^{-1/2} \quad \rightarrow \quad \frac{\Delta\nu}{\nu} \approx \frac{1}{2}\frac{\Delta\mu}{\mu}. \tag{1.1}$$

If there is a potential change of the vibrational frequency $\Delta\nu$, we can deduce a change of the proton to electron mass ratio $\Delta\mu$. A variation of ν is more likely to be observed if the temporal spacing between two measurements is significant. Astronomical observations make it possible to gaze into the past on time scales beyond comparison on earth. For example, Levshakov et al. evaluated the spectra of a quasar, which led to a constraint of $|\Delta\mu/\mu| < 5.7 \times 10^{-5}$ between when the light was absorbed by a distant gas cloud and today [32]. Considering the time of $\Delta t \approx 11\,\mathrm{Gyr}$ between these observations, one obtains an upper limit of $|\Delta\mu/\mu| < 5 \times 10^{-15}\,\frac{1}{\mathrm{yr}}$. However, the universe itself is an uncontrolled environment, and the analysis of the data relies on various cosmological constraints [29]. In contrast to the uncontrolled environment of space, the controlled environment of the laboratory can permit measurements with much higher precision. However, the time scales between two measurements in a laboratory is significantly shorter. Still, the laboratory measurements of $\Delta\mu/\mu$ started to compete with astronomical observations after the progress in laser stabilization techniques [33], optical frequency measurements [34] and cooling of atomic samples [35]. The cooling of multiple cold-atom samples has provided fractional frequency instabilities of 6×10^{-17} on the one second time scale [36]. Comparing different transitions types of high precision atomic clocks results in an upper limit of $|\Delta\mu/\mu| < 1.6 \times 10^{-16}\,\frac{1}{\mathrm{yr}}$ [37]. For our future measurements on the vibrational transition frequencies in OH, the implicit reference would be the SI second as determined by a collective of the best frequency standards on earth. This frequency is delivered to us with high precision through the global navigation satellite system (GNSS) and can be decoded with a high-end GNSS receiver. Since the second is defined based on hyperfine transitions in ^{133}Cs, a potential variation of the fundamental constants affects both systems simultaneously, but with a different rate (Table 1.1). Only the Rydberg constant cancels out in the ^{133}Cs system and the vibrational transition of OH. The final interpretation of varying constants depends on which terms are considered constant [38]. Therefore, the investigation of a potential variation of μ correlates frequently with the fine structure constant α, which also potentially varies [39]. The fundamental constant $\alpha \approx 1/137$ contains information

about the forces between charged objects, which determine the structure of atoms and molecules. The quest behind the investigation of these constants is the search for the mechanism that defines them. Every precision measurement on fundamental constants constrains theory beyond the SM, by setting a new upper limit for a potential variation. The pioneer work in this field brings us one step closer to understanding the universe.

1.3 Outline

This thesis describes the design of a precision laser system, that will ultimately be used in measurements to test physics beyond the SM. The first benchmark system for testing this apparatus are the $A^2\Sigma^+$, $v' = 0 \leftarrow X^2\Pi_{3/2}$, $v'' = 0$, $J'' = 3/2$ electronic transitions in OH and its deuterated isotopologue, OD.

Chapter 2 introduces the theory needed to describe the rich electronic structure of these molecules. Afterwards, Chapter 3 describes the complex laser system used in the measurement of these electronic transitions, with emphasis on the optical frequency comb (OFC). The OFC is required to phase stabilize the ultraviolet spectroscopy laser to an infrared reference laser, which has higher stability. Both of these lasers, as well as the OFC, rely on nonlinear optical conversion, which is explained in Chapter 4. Furthermore, this chapter introduces the optical parametric oscillator (OPO), which will be the core of future vibrational transition measurement in OH. Although no vibrational transitions are measured in this thesis, they are the long term goal of building the described laser system in this thesis. Chapter 5 completes the discussion of the involved lasers, by highlighting the various frequency standards used to stabilize the lasers. In particular, Doppler-free saturation spectroscopy is used to stabilize the laser system on a short time scale, introduced in Chapter 6. Although the laser system is stable, frequency shifts can still occur when measuring the molecules in a molecular beam. Thus, Chapter 7 gives a brief overview of molecular beams, potential frequency shifts of the measured transitions that can occur due to the Doppler-effect, and discusses ways to correct for these shifts.

Frequency shifts can also occur due to interactions with the electric field of the laser. Chapter 8 covers these shifts and introduces the theoretical model to fit the measured electronic transitions described in Chapter 9. A detailed analysis of the measured spectra and comparison to previous measurements is provided in Chapter 10. Although we succeeded in precisely measuring electronic transitions in OH, Chapter 11 emphasizes certain improvements to the measurement setup to make future measurements even more precise.

Chapter 2

The Hydroxyl Radical

This chapter introduces the rich electronic structure of the hydroxyl radical (OH). After explaining the term symbols of diatomic molecules, the Hund's case (a) basis is discussed, which is the most suitable for describing the OH electronic ground state. the ground state of OH is emphasized which is preferably described in Hund's case (a) basis. The later introduced Hund's case (b) basis simplifies the qualitative description of the first electronic excited state. The quantum numbers of the ground and the excited state provide selection rules for the electronic transitions between both states. Since this thesis also involves measurements on the deuterated hydroxyl radical (OD), it is convenient to clarify the differences between OH and OD.

2.1 Term Schema of Diatomic Molecules

The molecular structure of the OH depends on the motion of both nuclei and the nine electrons. In the Born-Oppenheimer approximation, the motion of the electrons is independent of the slow motion of the heavy nuclei[40]. This allows separating the wavefunction into an electronic and nuclear part. The description of the electronic states of a diatomic molecule is analogous to atomic energy states[41]. In an atom, the individual electronic angular momenta l_i of all electrons inside the atom couple to a total electronic angular momentum $\sum_i \mathbf{l}_i = \mathbf{L}$, with the associated good quantum number L. A diatomic molecule also has a total angular momentum $\mathbf{L}$, but L is no longer a good quantum number. In contrast to the spherical symmetry of an atom, the internuclear axis defines the symmetry of a diatomic molecule. Thus, the projection of $\mathbf{L}$ along the internuclear axis is a good quantum number. This projection is denoted with the quantum number $\Lambda = 0, 1, 2, \cdot\cdot$ and the corresponding molecular states are $\Sigma, \Pi, \Delta, \cdot\cdot$, in analogy to the atomic states $S, P, D, \cdot\cdot$. An important second degree of freedom is the total electron spin angular momentum $\mathbf{S} = \sum_i \mathbf{s}_i$, with the corresponding quantum numbers S (total electron spin angular momentum) and Σ (projection of $\mathbf{S}$ along the internuclear axis). Since Σ can range from $-\Sigma$ to Σ, the multiplicity $2S + 1$ describes the number of possible values for Σ. The term symbol $^{2S+1}\Lambda$ provides a

compact way of summarizing the values of S and Λ that define an electronic state. For example, the state $X^2\Pi$ means $S = 1/2$ and $\Lambda = 1$ (Section 2.2.1). The label 'X' in front of the symbol marks the state as the electronic ground state. The only different letter from 'X' appearing in this thesis is 'A', generally denoting the first electronic excited state with the same S as the ground state. A basis of the quantum mechanical state is chosen such that the resulting eigenvectors are as diagonal as possible. Consider at the moment only Hund's case (a) basis (Section 2.2). In this case, the projection of the total electron angular momentum along the internuclear axis $\Omega = \Lambda + \Sigma$ is a good quantum number and Ω can be added to the term symbol as a subscript, for instance, ${}^{2\Sigma+1}\Lambda_{|\Omega|}$. However, not all states will have nearly diagonal eigenvectors in Hund's case (a), and for these Ω will not be a good quantum number. In many cases, these states can be better described by a Hund's case (b) basis (Section 2.3). In such cases, Ω is left out in the term symbol. An example is the $A^2\Sigma^+$ state (Section 2.2.1), with the symmetry label '+' in the superscript. This symbol describes the potential sign change of the wave function after a reflection through a plane, containing the internuclear axis. If the sign of the wave function stays the same, then the label is '+', otherwise it is '−'.

2.1.1 Parity

The discussion of parity is often a source of confusion since more than one kind of symmetry operation is possible. For diatomic heteronuclear molecules, the plane through the internuclear axis is used to consider the effect of reflection on the sign of the wavefunction. However, reflection across planes is not the only possible symmetry operation. The inversion operation E^* is defined as a change of the sign of the space-fixed coordinates X, Y, Z and is equivalent to a combination of the previous reflection and an additional rotation of the molecular frame by 180° [42]. If the purely electromagnetic Hamiltonian H commutes with E^* such that $[H, E] = 0$, then simultaneous eigenstates of H and E^* exist. Consider the inversion operator acting on the wavefunction ones [42]

$$E^*\phi(X,Y,Z) = \phi(-X,-Y,-Z) \quad \text{and twice} \quad E^*E^*\phi(X,Y,Z) = \phi(X,Y,Z). \tag{2.1}$$

Applying E^* twice on the wavefunction sets the system back into its original state, meaning the square of the eigenvalue is 1. Therefore the eigenvalue of E^* must be ± 1. The sign of the wavefunction after transformation with E^* defines the parity of the state. The doubly degenerate states of

$$|\Lambda, \pm\rangle = \frac{1}{\sqrt{2}} \left(|\Lambda\rangle \pm (-1)^p |-\Lambda\rangle \right) \quad \text{for} \quad |\Lambda| > 0 \tag{2.2}$$

have different parities. While there are interactions that mix different electronic states and lift this degeneracy, the parity remains a good quantum number. The value of p in

Equation (2.2) is given by $J - S + s$ in Hund's case (a) basis (Section 2.2) and in Hund's case (b) (Section 2.3) by $N + s$. The parameter s is zero for $\Lambda > 0$ or Σ^+ states and one for Σ^- states. In order to more easily determine the energetic order of the levels in a nearly-degenerate doublet, it is convenient to define an alternative version formulation of parity, namely the e and f labeling scheme[43]. These labels depend solely on the parity and the total angular momentum J. For half-integral J, if $(-1)^{J-1/2}$ is the sign of the parity, then the state is labeled e, otherwise it is a f level. For integral J, if the sign of the parity is $(-1)^J$, then it is an e level, otherwise it is a f level. The lower level in each parity doublet will always have the same e/f label in a given electronic state.

2.2 Hund's Case (a)

Hund's coupling cases supply a basic understanding of the involvement of different angular momentum couplings in the final energy level distribution[44]. Each case presents an idealized view of the molecule, that closely approximates a certain set of electronic states. In Hund's case (a) the orbital angular momentum **L** is coupled to an electrostatic field, caused by the two nuclei of the diatomic molecule. Thus, the precession frequency of **L** about the nuclear axis reaches high values and the magnitude of **L** is unknown. In this case, the quantum number L is not good[45], but the projection of **L** along the internuclear axis, labeled with the quantum number Λ, is well defined and conserved in time. This makes Λ a good quantum number. Furthermore, a strong spin-orbit coupling exists, that couples the electron spin angular moment to the internuclear axis, making Σ a good quantum number. Thus, the projection of the total electron angular momentum along the internuclear axis $\Omega = \Lambda + \Sigma$ is also a good quantum number. The entire set of good quantum numbers of Hund's case (a) contains: n, v, Λ, S, Σ, J, Ω. The wavefunction is described by a linear combination of states with positive and negative Λ to form a definite-parity state[42]

$$\begin{aligned} &|n^{2S+1}\Lambda_{|\Omega|}; v; JM_J; \pm\rangle = \\ &\tfrac{1}{\sqrt{2}}\left(|n,\Lambda\rangle\,|S,\Sigma\rangle\,|J,\Omega,M_J\rangle \pm (-1)^{J-S+s}\,|n,-\Lambda\rangle\,|S,-\Sigma\rangle\,|J,-\Omega,M_J\rangle\right)|v\rangle\,. \end{aligned} \tag{2.3}$$

The separated basis wave functions contains the electronic orbital part $|n\Lambda\rangle$, the electronic spin part $|S\Sigma\rangle$, the vibrational part $|v\rangle$ and the rotational part $|J\Omega M_J\rangle$. M_J defines the projection of **J** along a space-fixed axis, with allowed values in the range $-J, -J+1, \cdot\cdot, J$. The M_J quantum number becomes important when considering the Hamiltonian of a molecule inside an external electric or magnetic field. Without an external field, each energy level is degenerate in M_J. In a perfect Hund's case (a) **L** and **S** are coupled along the internuclear axis. The projection of both onto the axis sums up to Ω (Figure 2.1). The total electron angular momentum couples with the angular momentum of the rotating nuclei **R** to produce the total angular momentum $\mathbf{J} = \mathbf{R}+\mathbf{L}+\mathbf{S}$. The general requirement for Hund's

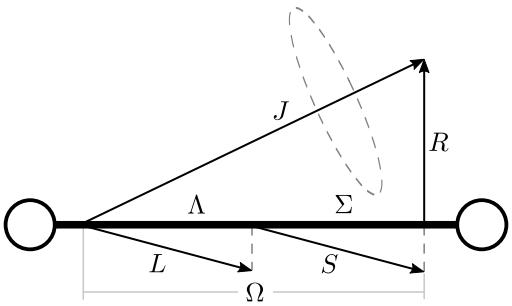

Figure 2.1: In a diatomic molecule, **R** is perpendicular to the internuclear, while characteristic for Hund's case (a) **L** and **S** are coupled to the internuclear axis. The resulting total angular momentum **J** is the sum of **L**, **S** and **R** (adapted from [42]).

case (a) to be a good approximation of the true eigenstates is that $A\Lambda \gg BJ$, where A is the spin-orbit coupling constant and B the rotational constant [42]. The Hamiltonian involving these two constants is

$$H = H_{\text{rot}} + H_{\text{SO}} = B\mathbf{R}^2 + A(\mathbf{L} \cdot \mathbf{S}), \tag{2.4}$$

with the rotational part H_{rot} and the spin-orbit part H_{SO}.

2.2.1 Ground State of OH

The Hund's case (a) basis is generally well suited to describe a 2-Pi state, which also happens to be the electronic ground state of OH. In a 2-Pi state, $\Lambda = \pm 1$ and $S = \frac{1}{2}$, yielding $\Sigma = \pm\frac{1}{2}$. Thus, four values are allowed for $\Omega = \Lambda + \Sigma$, namely $\Omega = -\frac{3}{2}, -\frac{1}{2}, \frac{1}{2}, \frac{3}{2}$. The two resulting definite-parity wave functions for $|\Omega| = \frac{1}{2}$ and $|\Omega| = \frac{3}{2}$ in Hunds's case (a) basis are

$$\begin{aligned} &|a\rangle = |n^2\Pi_{\frac{1}{2}}; v; JM_J; \pm\rangle = \\ &\tfrac{1}{\sqrt{2}}(|n,1\rangle\,|\tfrac{1}{2},-\tfrac{1}{2}\rangle\,|J,\tfrac{1}{2},M_J\rangle \pm (-1)^{J-\frac{1}{2}}\,|n,-1\rangle\,|\tfrac{1}{2},\tfrac{1}{2}\rangle\,|J,-\tfrac{1}{2},M_J\rangle)\,|v\rangle\,, \end{aligned} \tag{2.5}$$

$$\begin{aligned} &|b\rangle = |n^2\Pi_{\frac{3}{2}}; v; JM_J; \pm\rangle = \\ &\tfrac{1}{\sqrt{2}}(|n,1\rangle\,|\tfrac{1}{2},\tfrac{1}{2}\rangle\,|J,\tfrac{3}{2},M_J\rangle \pm (-1)^{J-\frac{1}{2}}\,|n,-1\rangle\,|\tfrac{1}{2},-\tfrac{1}{2}\rangle\,|J,-\tfrac{3}{2},M_J\rangle)\,|v\rangle\,. \end{aligned} \tag{2.6}$$

The quantum numbers are identified with Equation (2.3). The additional parameter $\pm$ denotes the parity of the doubly degenerate states of $|\Lambda| = 1$. The rotational and spin-orbit Hamiltonian of Equation (2.4) can be rewritten as [46]

$$\begin{aligned} H =& B\mathbf{R}^2 + A(\mathbf{L}\cdot\mathbf{S}) = B((\mathbf{J}-\mathbf{S})-\mathbf{L})^2 + A(\mathbf{L}\cdot\mathbf{S}) \\ \approx& B(\mathbf{J}^2 - 2J_zS_z + \mathbf{S}^2 - 2(J_z - S_z)L_z + L_z^2) - B(J_+S_- + J_-S_+) + AL_zS_z. \end{aligned} \tag{2.7}$$

All term containing the angular lowering and raising operators L_+ and L_- are neglected, since they are not well defined. In particular, these terms couple to other electronic states,

which is discussed later (Section 2.2.2). The secular determinant is

$$\begin{vmatrix} \langle b| H |b\rangle - E & \langle b| H |a\rangle \\ \langle a| H |b\rangle & \langle a| H |a\rangle - E \end{vmatrix} = 0 \quad \text{with} \quad \begin{array}{l} \langle b| H |b\rangle = B_v(J(J+1) - \frac{7}{4}) + \frac{1}{2}A_v, \\ \langle a| H |a\rangle = B_v(J(J+1) + \frac{1}{4}) - \frac{1}{2}A_v, \\ \langle a| H |b\rangle = \langle b| H |a\rangle = -B_v(J(J+1) - \frac{3}{4})^{\frac{1}{2}}. \end{array} \tag{2.8}$$

Only the first and the last term in Equation (2.7) contribute to the diagonal elements. The eigenvalues of the angular momenta are

$$\mathbf{J}^2 |J\Omega M_J\rangle = J(J+1) |J\Omega M_J\rangle , \quad \mathbf{S}^2 |S\Sigma\rangle = S(S+1) |S\Sigma\rangle , \tag{2.9}$$

$$J_z |J\Omega M_J\rangle = \Omega |J\Omega M_J\rangle , \quad S_z |S\Sigma\rangle = \Sigma |S\Sigma\rangle , \quad L_z |n\Lambda\rangle = \Lambda |n\Lambda\rangle . \tag{2.10}$$

The off diagonal elements are solely caused by the second term of Equation (2.7). The lowering and raising operators of the spin and the angular momentum couple different basis states with different Ω and Σ quantum numbers

$$\langle J\Omega \mp 1 M_J| J_\pm |J\Omega M_J\rangle = \sqrt{J(J+1) - \Omega(\Omega \mp 1)}, \tag{2.11}$$

$$\langle S\Sigma \pm 1| S_\pm |S\Sigma\rangle = \sqrt{(S(S+1) - \Sigma(\Sigma \pm 1)}. \tag{2.12}$$

Finally, solving the secular determinant yields the two eigenvalues[46]

$$E(^2\Pi; v; J) = B_v \left(\left(J - \tfrac{1}{2}\right) \left(J + \tfrac{3}{2}\right) \pm \tfrac{X}{2} \right) , \quad \text{with} \quad \begin{array}{l} X = \sqrt{4\left(J + \frac{1}{2}\right)^2 + Y\,(Y-4)}, \\ Y = A_v/B_v. \end{array} \tag{2.13}$$

The energy levels associated with the '+' sign are labeled with F_2 and the lower levels with F_1. Thus, the absolute ground state is always an F_1 state (Figure 2.2). Hund's case (a) is an approximation well suited to describe the lowest rotational levels of the $^2\Pi$ state. It becomes exact, if the off-diagonal contributions are zero which happens when $J = 1/2$. The off-diagonal values of the Hamiltonian increase with J while the difference between the diagonal values stays the same.

2.2.2 Lambda Doubling

As previously mentioned, states with positive Λ and negative Λ are degenerate and can be combined to form two states of definite parity. Exceptions are states with $\Lambda = 0$: each J, Ω level of a Sigma-state has a single parity. Λ-doubling originates in the coupling between different electronic states. In case of the OH ground state, the degenerate 2-Pi state couples to the non-degenerate 2-Sigma+ and 2-Sigma− states. However, the non-degenerate states only couple to one component of the degenerate state, especially the

component of the same parity. The rotational and spin-orbit Hamiltonian of Equation (2.7) neglects terms that couple to other electronic states. The omitted terms are[46]

$$\begin{aligned} H_1 &= -B(J_+L_- + J_-L_+) + (B + \tfrac{1}{2}A)(L_+S_- + L_-S_+), \\ &= -B(N_+L_- + N_-L_+) + \tfrac{1}{2}A(L_+S_- + L_-S_+), \end{aligned} \tag{2.14}$$

using the total angular momentum $\mathbf{N} = \mathbf{L} - \mathbf{S}$ (Section 2.3). The angular momentum lowering operators L_- and raising operators L_+ couple the Π and Σ states. Since the calculation of L_- and L_+ is not possible, it is convenient to absorb them into a phase factor such as[47][1].

$$\langle \Lambda = \pm 1 |\, e^{\pm 2i\phi} \,| \Lambda = \mp 1 \rangle = +1. \tag{2.15}$$

After performing a Van Vleck transformation[42,48] the Λ-doubling Hamiltonian is[47]

$$H_\Lambda \approx \tfrac{1}{2}o(S_+^2 e^{-2i\phi} + S_-^2 e^{2i\phi}) - \tfrac{1}{2}p(N_+S_+e^{-2i\phi} + N_-S_-e^{2i\phi}) + \tfrac{1}{2}q(N_+^2 e^{-2i\phi} + N_-^2 e^{2i\phi}). \tag{2.16}$$

The Λ-doubling parameters o, p and q are determined empirically, by comparison with the experiment. Thus, the Van Vleck transformation introduces additional perturbation parameters of the 2-Sigma state into the effective Hamiltonian. These parameters resemble a second-order perturbation, which includes a summation over all excited Σ states. However, the perturbation is dominated by the Σ state closest to the ground state $^2\Pi$. The limit in which only a single state is involved in the Λ-doublet creation, is called the 'unique perturber' hypothesis. This assumption is justified empirically[49]. The effect of Lambda-doubling on the eigenenergies can be determined by including Equation (2.16) into the Hamiltonian and solving the secular equation, as in Equation (2.8).

2.2.3 Hyperfine Structure and the Spherical Tensor Formalism

The effective Hamiltonian of the diatomic molecule is explained in more detail by Zare[46] and Brown[50]. This approach is appealing in its intuitive way of describing the interaction between the angular momenta of a quantum mechanical state. The essential elements are lowering and raising operators such as J_- and J_+, which are responsible for the off-diagonal elements in the Hamiltonian. However, as Klein[51] first noted, the commutation relations for J are different in the laboratory frame (coordinates X, Y, Z) and the molecular frame (x, y, z)[52].

$$[J_X, J_Y] = J_X J_Y - J_Y J_X = +iJ_z, \tag{2.17}$$

$$[J_x, J_y] = -iJ_z. \tag{2.18}$$

[1] Consider some authors use the opposite sign convention[42].

This reverses the effect of J_+ and J_- dependent on the frame. Thus, with increasingly complex quantum mechanical systems, the formalism becomes prone to errors. In general, the favored approach of describing the Hamiltonian uses spherical tensor operators[42]. One benefit of spherical tensor operators is the simple relationship between an operator in the space fixed frame $T^k_p(\mathbf{J})$ and one in the molecule fixed frame $T^k_q(\mathbf{J})$[42]

$$T^k_q(\mathbf{J}) = \sum_{p=0,\pm1} \mathfrak{D}^{(k)}_{p,q}(\omega) T^k_p(\mathbf{J}) \quad \text{and} \quad T^k_p(\mathbf{J}) = \sum_{q=0,\pm1} \mathfrak{D}^{(k)*}_{p,q}(\omega) T^k_q(\mathbf{J}). \tag{2.19}$$

The connection between both spaces is supplied by the Wigner D-matrix $\mathfrak{D}^{(k)}_{p,q}$. The M-state dependence of any matrix element described using a spherical tensor operator can be computed using the Wigner-Eckart theorem[53]

$$\langle J, M_J | \, T^k_p \, | J', M'_J \rangle = (-1)^{J-M_J} \begin{pmatrix} J & k & J' \\ -M_J & p & M'_J \end{pmatrix} \langle J || \, T^k \, || J' \rangle \,, \tag{2.20}$$

with the matrix like factor denoting the Wigner 3-j symbol and $\langle J || \, T^k \, || J' \rangle$ the reduced matrix element. The 3-j symbol is only non-zero if the triangle rule $|J-1| \leq J' \leq J+1$ is satisfied and the sum of the projection quantum numbers is $M_J = p + M'_J$. These selection rules are based on conservation of angular momentum. The selection rules concerning the parity are inside the reduced matrix element. The use of the Wigner-Eckart theorem reduces the computation of $3(2J+1)(2J'+1)$ first-order matrix elements to just one. Additionally, the anomalous commutator relation is taken care of in a rigorous way. However, computing matrix elements with more than one momentum operator and additional coupling terms still requires several extra steps. The explicit matrix elements are given elsewhere[54,55]. To eliminate the risk of errors associated with typing these formulae in by hand, this thesis relies on the program PGOPHER[56].

The hyperfine splitting introduces an additional splitting of the Λ-doublet parity states. It originates with the nuclear spin $\mathbf{I}$, resulting in a total angular momentum $\mathbf{F} = \mathbf{J} + \mathbf{I}$. The Hund's case (a) basis set can be expanded to include the I quantum number[42]

$$|n^{2S+1}\Lambda_{|\Omega|}; v; JI; FM_F\rangle = |n\Lambda\rangle \, |S\Sigma\rangle \, |J\Omega I\rangle \, |F, M_F\rangle \, |v\rangle \,, \tag{2.21}$$

with the total angular momentum part $|F, M_F\rangle$.

M_I is the projection of $\mathbf{I}$ along a space fixed axis. The allowed values are in the range $-I, -I+1, \cdot\cdot, I$, yielding to a multiplicity of $2I+1$. Assuming further the magnetic moment is generated by the electrons, but also partly by the nuclear spin resulting in possible couplings $\mathbf{I} \cdot \mathbf{L}$, $\mathbf{I} \cdot \mathbf{S}$ and $\mathbf{I} \cdot (\mathbf{J} - \mathbf{S})$. The full Hamiltonian in spherical tensor notation including this hyperfine interaction is found elsewhere[54,57]. There are sometimes slight variations of the spectroscopic constants used. For example, some references, when

describing the interaction between the electron spin and the nuclear spin, use the Fermi contact parameter b_F (with the operator $\mathbf{I}\cdot\mathbf{S}$) and the dipole-dipole coupling parameter c (operator $S_zI_z - \mathbf{I}\cdot\mathbf{S}/3$)[58]. Other references choose to simplify the operator for c to S_zI_z, which requires the Fermi contact parameter to be replaced with an effective parameter $b = b_F - c/3$[54]. The spectroscopic program PGOPHER knows only b and c.

Consider a coupling of $I = 1/2$ and $M_I = \pm 1/2$, with a multiplicity of two. Thus, the ground state $^2\Pi_{3/2}$ with $J = 3/2$, yields a total angular momentum of $F = 1$ and $F = 2$ (Figure 2.2). Every transition in this thesis starts from one of these levels.

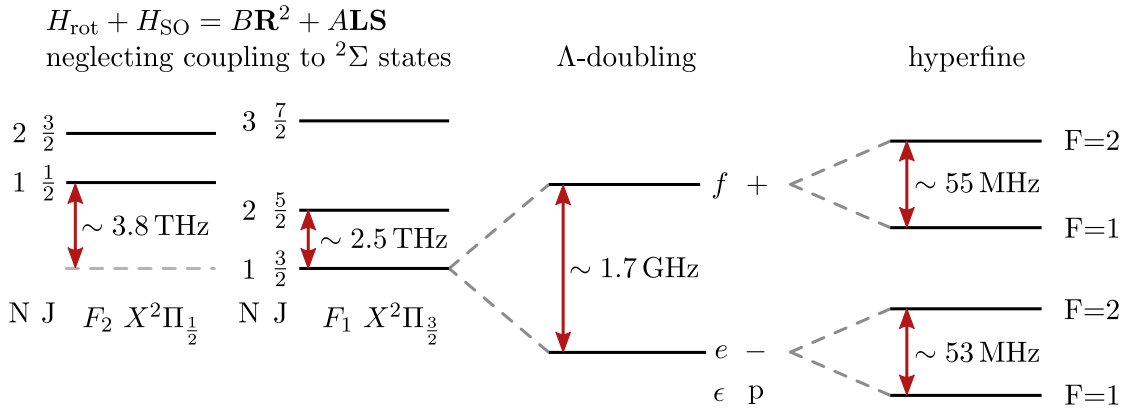

Figure 2.2: Schema of the OH electronic ground state structure. The left-hand side shows the splitting into two manifolds F_1 and F_2 caused by the spin-orbit interaction, but neglecting higher order coupling terms. Including this terms lifts the degeneracy of Λ and causes splitting into two different parity states (Section 2.2.2). The hyperfine splitting on the right is caused by an interaction between **L**, **S**, **J** and the nuclear spin **I** (Section 2.2.3).

2.2.3.1 Zeeman Effect

In most high-resolution experiments in which the earth's magnetic field has not been compensated, the Zeeman-effect needs consideration. The Zeeman effect consists of multiple parts. However, the most dominant parts are the electronic orbital Zeeman effect and the electronic spin isotropic Zeeman effect, yielding $H = g_L\mu_B\mathbf{B}\cdot\mathbf{L} + g_S\mu_S\mathbf{B}\cdot\mathbf{S}$[57]. The parameters g_L and g_S denote the electron orbital and the electron spin g-factors, respectively. Additionally, $\mu_B = e\hbar/(2m_e)$ is the Bohr magneton. Orienting the magnetic field along the space-fixed Z-axis simplifies this expression. The expectation value in Hund's case (a) basis and spherical tensor notation is[42]

$$\begin{aligned}&\langle n^{2S+1}\Lambda_{|\Omega|}; v; JI; FM_F|\, g_L\mu_B B_Z T^1_{p=0}(\mathbf{L}) + g_S\mu_B B_Z T^1_{p=0}(\mathbf{S})\, |n^{2S+1}\Lambda_{|\Omega|}; v; JI; FM_F\rangle \\ &= \mu_B B_Z(g_L\Lambda + g_S\Sigma)\frac{((F(F+1) + J(J+1) - I(I+1))\Omega M_F}{2F(F+1)J(J+1)}.\end{aligned} \tag{2.22}$$

In a pure Hund's case (a) at low magnetic field, the frequency shift of an individual Zeeman level changes linearly with the magnetic field. The ground state $^2\Pi_{3/2}$ with $J = 3/2$ has

hyperfine levels with $F = 1$ or $F = 2$, which are splitting into three or five Zeeman levels, respectively, according to the multiplicity of $2F + 1$. These levels are labeled with $M_F = F, F-1, \cdot\cdot, -F$. Thus each shifted level at M_F has a counterpart at $-M_F$, resulting in a symmetric splitting and a zero net shift. Considering the OH molecule inside a magnetic field of $B = 75\,\mu\text{T}$ yields a Zeeman splitting of the hyperfine $F = 1$ states of around 1.6 MHz. The splitting of the $F = 2$ states is around 1 MHz. The values are based on a calculation using PGOPHER[56], with ground states parameters from[49]. The effect of the Zeeman level splitting on the measured transition frequencies will be discussed later (Section 2.4).

2.3 Hund's Case (b)

In Hund's case (b) the spin-rotational part (**NS**) of the Hamiltonian has more weight relative to the spin-orbit (**LS**) coupling. Thus, the requirement of the Hund's case (b) basis set is $A\Lambda \ll BJ$[42]. Analog to Hund's case (a) the precession frequency of **L** about the internuclear axis is high, leaving the projection Λ as a good quantum number. The critical difference to Hund's case (a) is the non-coupling of the spin to the internuclear axis. Therefore, Ω is no longer a good quantum number. Instead, **L** couples to **R**, which results in the total angular momentum excluding spins $\mathbf{N} = \mathbf{J} - \mathbf{S}$ (Figure 2.3). The

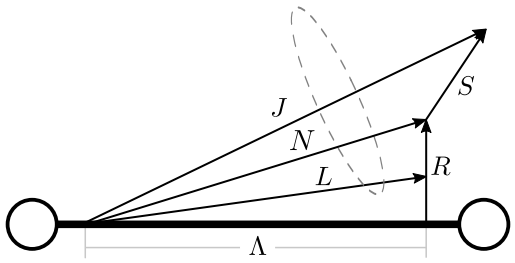

Figure 2.3: In Hund's case (b) **S** is not coupled to the internuclear axis. Thus, Ω is no good quantum number. **N** and **L** have the same projection onto the internuclear axis, such that $N = \Lambda$ (adapted from[42]).

coupling between **N** and **S** finally yields the total angular momentum excluding nuclear spin $\mathbf{J} = \mathbf{N} + \mathbf{S}$. The new good quantum numbers in Hund's case (b) are: n, v, N, Λ, S, J. Thus, the linear combination of the wavefunction into the parity basis sets is[42]

$$\begin{aligned} &|n^{2S+1}\Lambda; v; N\Lambda SJM, \pm\rangle = \\ &\tfrac{1}{\sqrt{2}}\left(|n\Lambda^s\rangle\,|N, \Lambda, S, J, M\rangle \pm (-1)^{N+s}\,|n, -\Lambda^s\rangle\,|N, -\Lambda, S, J, M\rangle\right)|v\rangle\,. \end{aligned} \tag{2.23}$$

However, Hund's coupling cases (a) and (b) are both approximations. Most states in light diatomic molecules are between both ideal cases, leading to an intermediate coupling. Still, choosing the right basis set of wavefunctions simplifies the labeling of the rotational levels. Generally, modern computer programs calculate everything in one Hund's case independent of the actual state. For example, the program PGOPHER, used in this thesis,

relies on a Hund's case (a) basis[56].

2.3.1 First Electronic Excited State of OH

A good example of the application of Hund's case (b) basis set is the state $^2\Sigma^+$, which also happens to be the first electronic excited state of OH. This means $\Lambda = 0$ and $S = \frac{1}{2}$. However, the projections Ω and Σ are no longer good quantum numbers in Hund's case (b). Due to $\Lambda = 0$, the inverted wave function is equal to the initial wave function. Thus, the parity phase factor $\pm(-1)^{N+s}$ must be $+1$ in order for the wavefunction in Equation (2.23) to not vanish. Therefore, the parity of each N-level is $(-1)^N$ for a 2-Sigma+ state where $s = 0$ (Section 2.1.1). The representation of the wave function as a linear combination of both parity states becomes unfeasible. The wave function is

$$|n^2\Sigma; v; N\Lambda SJM\rangle = |n, 0\rangle \, |N, 0, \tfrac{1}{2}, J, M\rangle \, |v\rangle \, , \tag{2.24}$$

with an adjusted normalization factor. For instance, Equation (2.23) assumes that both terms are orthonormal and the $1/\sqrt{2}$ factor accounts for it. The normalization changes accordingly for two identical terms, which is the case for the 2-Sigma+ state. Thus, rewriting the rotational Hamiltonian yields

$$H = B_v \mathbf{N}^2 + \gamma_v \mathbf{NS} = B_v \mathbf{N}^2 + \gamma_v \tfrac{1}{2} \left(\mathbf{J}^2 - \mathbf{N}^2 - \mathbf{S}^2 \right) . \tag{2.25}$$

Since only good quantum numbers remain, the eigenvalues follow instantly

$$E(^2\Sigma^+; NJ; \pm) = B_v N(N+1) + \tfrac{1}{2}\gamma_v \left(J(J+1) - N(N+1) - \tfrac{3}{4} \right) \tag{2.26}$$

Due to spin-rotational coupling, each N state consists of two closely spaced levels also referred as a ρ-doublet. They are only differing in J with the eigenvalues[46]

$$E(^2\Sigma^+; NJ; \pm) = B_v N(N+1) + \tfrac{1}{2}\gamma_v N \qquad \text{for } J = N + \tfrac{1}{2}, \tag{2.27}$$

$$E(^2\Sigma^+; NJ; \pm) = B_v N(N+1) - \tfrac{1}{2}\gamma_v (N+1) \qquad \text{for } J = N - \tfrac{1}{2}. \tag{2.28}$$

The exception is $N = 0$, which only consists of $J = \frac{1}{2}$ of parity $+$. To distinguish between both states, the state with $J = N + \frac{1}{2}$ is labeled F_1 and the state with $J = N - \frac{1}{2}$ is called F_2[46]. The separation between both states is

$$F_1(N) - F_2(N) = \tfrac{1}{2}\gamma_v (2N+1). \tag{2.29}$$

In general, γ_v is not necessarily positive. Thus, the state label with F_1 is not always higher in energy compared to the state F_2. It might even cause confusion, since the manifolds of the state $^2\Pi$ are also labeled F_1 and F_2, except the lowest level is always associated with F_1 (Section 2.2.1). The hyperfine splitting of the excited state $^2\Sigma^+$, with $I = 1/2$, is analogous

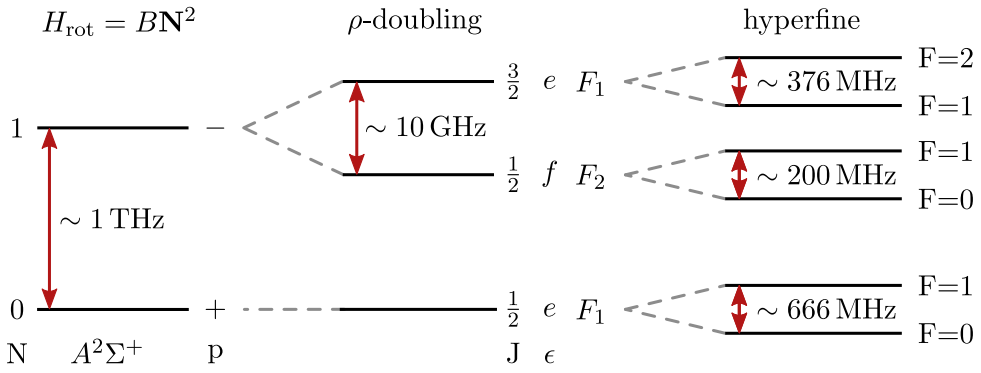

Figure 2.4: Schema of the OH first electronic excited state structure. The bare rotational states show no splitting. After coupling **N** with **S** the level structure splits into the ρ-doublets. Further coupling between **J** the nuclear spin **I** yields the hyperfine structure.

to the ground state (Section 2.2.3), except with different hyperfine parameters. Thus, the degeneracy of the M_I quantum number gets lifted, resulting into two levels with the total angular momentum $F = J \pm I$. Also, the Zeeman effect has already been explained (Section 2.2.3.1). In Hund's case (b) only one detail changes: the Zeeman splitting of Hund's case (a) converges to zero for increasing J values. With Hund's coupling case (b), however, the splitting converges to a constant value, which is dependent on the field strength [59].

2.4 Electron configuration

The electronic term symbols of OH for the ground state (Section 2.2.1) and the excited state (Section 2.3.1) can be predicted using molecular orbital theory. The electronic configuration of OH is $(1s\sigma)^2(2s\sigma)^2(2p\sigma)^2(2p\pi)^3$ in the united atom picture [41], with the superscripts 2 or 3 denoting the number of electrons in the σ-orbitals and the π-orbital, respectively. Comparing the electronic configuration of OH with oxygen (O) and hydrogen (H) shows that the energy of the hydrogen 1s electron is similar to the energy of the oxygen 2px, 2py and 2py electrons (Figure 2.5a). The spatial overlap of the 1s hydrogen orbitals

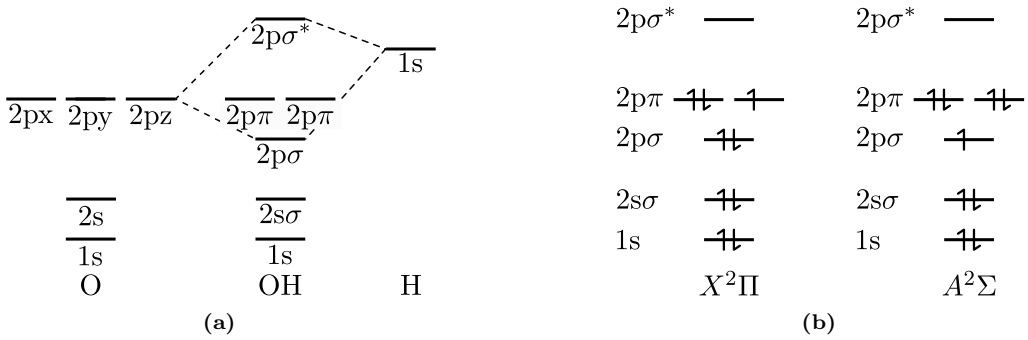

Figure 2.5: (a) Electronic configuration of an oxygen (O) and an hydrogen (H) atom forming the hydroxyl radical (OH). The dashed lines indicate the bonding oxygen 2pz orbital with the hydrogen 1s orbital. (b) Electronic configuration with the ground state $X^2\Pi$ and first electronic excited state $A^2\Sigma$ (adapted from [57]).

and the 2pz oxygen orbital forms the bonding- 2pσ and the anti-bonding 2pσ^* orbital of OH[57]. The 2px and 2py orbitals of oxygen have no spatial overlap with the 1s hydrogen orbital. Thus they are not involved in the bond. The corresponding unpaired electrons are the reason to denote the molecule as radical.

It is convenient to make the Russell-Saunders approximation to derive the term symbol. The antiparallel angular momenta λ_i and spins s_i of each electron along the internuclear axis are summed up to $\Lambda = \sum_i \lambda_i$ and $S = \sum s_i$, respectively[41]. Thus, the open $(2p\pi)^3$-orbital of the OH defines the term symbol of the electronic ground state. The three electrons lead to $\Lambda = 1$ and $S = 1/2$, with the term symbol $X^2\Pi$ (Figure 2.5b). The electronic transition of an electron from the lower $(2p\sigma)^2$ orbital into the $(2p\pi)^3$-orbital closes the π-orbital and opens the σ-orbital (Figure 2.5b). The term symbol of the first electronic excited state depends on the open $(2p\sigma)^1$-orbital. The remaining π-electron leads to the total spin of $S = 1/2$, while the σ-orbital implies $\Lambda = 0$. Therefore, the fist electronic state is labeled $A^2\Sigma$, with the configuration $(1s)^2(2s\sigma)^2(2p\sigma)^1(2p\pi)^4$.

2.5 Selection Rules

The observed transitions frequencies are dependent on the spectroscopic constants and the quantum numbers of the lower and upper state. The states $|\psi\rangle$ and $|\psi'\rangle$, respectively. A transition is allowed if the matrix element of the electric dipole moment $\langle\psi'|\,\boldsymbol{\mu}\,|\psi\rangle$ is non-zero. The dipole moment leads to selection rules that define the allowed transitions. The rules can be separated into three categories: a set of general selection rules, rules which can only be applied to specific Hund's cases and additional rules which emerge from the non-zero nuclear spin and the interaction with an external magnetic field (Table 2.1)[60]. The

Table 2.1: Selection rules of electric dipole allowed transitions, separated into three categories. Special care must be taken, considering the Zeeman selection rules. They are in general defined for unpolarized light.

I	General Rules $\Delta J = 0, \pm 1 \quad$ except $\quad J = 0 \leftrightarrow J = 0$ $\Lambda = 0, \pm 1 \quad$ except $\quad \Sigma^+ \leftrightarrow \Sigma^-$ $+ \leftrightarrow -$ $\Delta S = 0$	
II	Hund's case (a) $\Delta\Sigma = 0$	Hund's case (b) $\Delta N = 0, \pm 1 \quad$ except $\quad \Sigma \leftrightarrow \Sigma$
III	Hyperfine $\Delta F = 0, \pm 1 \quad$ except $\quad F = 0 \rightarrow F = 0$	Zeeman $\Delta M_F = 0, \pm 1$

general selection rules address the angular momentum J, the projection Λ, the parity $\pm$ and the electron spin S. The selection rule of most interest is $\Delta J = 0, \pm 1$, meaning an electronic excitation from the ground state $X^2\Pi$ with $J = 3/2$ is possible to A-states with $J = 1/2, 3/2, 5/2$. Since the quantum number N is only defined for Hund's case (b) the

selection rule $\Delta N = 0, \pm 1$ is less stringent considering the $X - A$ transitions. It is mostly $N = 1$, but partly also $N = 2$ for the ground state. Additionally, the non zero nuclear spin $I = 1/2$ of the OH proton causes the hyperfine splitting, leading to the selection rule $\Delta F = 0, \pm 1$ between different hyperfine levels.

The degeneracy of the M_F states is lifted inside a magnetic field, leading to the Zeeman selection rule $\Delta M_F = 0, \pm 1$ [61]. In more detail, the transition dipole moment matrix element in spherical tensor notation after applying the Wigner Eckart theorem is

$$\langle F, M_F | \, T_p^1(\boldsymbol{\mu}) \, | F' M_F' \rangle = (-1)^{F - M_F} \begin{pmatrix} F & 1 & F' \\ -M_F & p & M_F' \end{pmatrix} \langle F || \, T^1(\boldsymbol{\mu}) \, || F' \rangle \, . \tag{2.30}$$

This 3-j symbol leads to the selection rule $M_F = M_F' + p$, in which p has to be -1, 0 or 1. Including now the interaction between the electric dipole moment and the electrical field, yields [55]

$$H_e = -\boldsymbol{\mu} \cdot \mathbf{E} = -T^1(\boldsymbol{\mu}) \cdot T^1(\mathbf{E}) = - \sum_{p=0,\pm 1} (-1)^p T_p^1(\boldsymbol{\mu}) T_{-p}^1(\mathbf{E}). \tag{2.31}$$

The index p is referring to the space fixed components E_X, E_Y, E_Z and the rank-1 spherical tensor are defined by

$$T_0^1(\mathbf{E}) = E_Z \quad \text{and} \quad T_{\pm 1}^1(\mathbf{E}) = \mp \frac{1}{\sqrt{2}} E_{\pm} = \mp \frac{1}{\sqrt{2}} (E_X \pm i E_y). \tag{2.32}$$

Light is an electromagnetic wave and in vacuum, it has no field component along its propagation direction. Thus, defining the propagation direction along the Z-axis yields $T_0^1(\mathbf{E}) = 0$, which saves the computation of all product terms with $p = 0$ and results in the selection rule $\Delta M_F = \pm 1$. This is a particular example, for the detected ΔM_F transitions in this thesis. Considering vibrational transitions, no strict selection rules exist, although the most pronounced transition strengths are at $\Delta v = \pm 1$ [60]. Sometimes it is even possible to measure transitions, which are not allowed by the selection rules. This has two possible reasons. First, the selection rule is only in approximation true, for instance, $\Delta v = \pm 1$. Second, the transition is not an electric dipole transition, but instead a magnetic dipole, an electric quadrupole or a two-photon transition.

2.6 Isotope Measurements

Measuring transitions opens the possibility of determining the spectroscopic constants of a molecule. To find the true spectroscopic constants, it is sometimes necessary to make measurements on different isotopes. This is caused by an indeterminacy of some parameters, which is inherent to the theoretical model. In the OH $X^2\Pi$ ground state, it is well known that spin-rotation and spin-orbit centrifugal distortion operators have very

similar effects on the eigenenergies, making it difficult to determine the values of γ and A_D independently [62]. Consider the Hamiltonian [42]

$$H = H_{\text{rot}} + H_{\text{so}} + H_{\text{sr}} = B\mathbf{N}^2 + (A + A_D\mathbf{N}^2)(\mathbf{L}\cdot\mathbf{S}) + \gamma(\mathbf{N}\cdot\mathbf{S}), \tag{2.33}$$

with the four parameters B, A, A_D and γ. Calculating the secular determinant and extracting the eigenvalues shows three different dependencies on the angular momentum J [42], which is overconstrained by four parameters. Building a system of equations around the dependencies makes at least two parameters impossible to determine uniquely. One solution is to fit the spectroscopic data assuming $\gamma = 0$, which results in an effective value for A_D. This effective constant is related to the true constants by defining an effective parameter $\tilde{A}_D = A_D - 2B\gamma/(A-2B)$ [63]. The terms inside $\tilde{A}_D$ are proportional to different powers of the reduced mass $\mu = (M_1M_2)/(M_1+M_2)$, with M_i denoting the masses of the two atoms. Measuring different isotopes makes it possible to resolve the indeterminacy and assign values to γ and A_D.

The different dependency of the reduced mass on the $\tilde{A}_D$ parameter is shared with various other effective Hamiltonian parameters, although indeterminacy is not an issue. As an example, the effective rotational constant $B_v = B_v^{(1)} + B_v^{(2)}$ includes contributions of different order. The first order contribution $B_v^{(1)}$ is only concerned with the rotation of the two bare nuclei. The second order contribution $B_v^{(2)}$ takes the electron cloud into account, which is outside the Born-Oppenheimer approximation. An analysis shows, the first order contribution is proportional to μ^{-1}, but the second order contribution is proportional to μ^{-2} [42]. The effective parameters B_v absorb these effects, thus using the Dunham formalism dismantles all higher order contributions on the effective parameters [64]. However, the Dunham model requires measurements on different isotopes including vibrational states, to construct a more complete picture of the electronic state, including effects due to the breakdown of the Born Oppenheimer approximation.

2.6.1 Difference between OH and OD

In the Born Oppenheimer approximation, the electron cloud is independent of the mass of the two nuclei. The nucleus of the hydrogen atom (H) consists only of one proton and adding a neutron changes only the mass. Thus, replacing the proton with a deuteron (D) does not affect the electronic structure. Also, the charge distribution of a single proton is spherical. However, the additional neutron in the deuteron deforms it and causes a quadrupole moment. Describing the effect of the quadrupole moment on the energetic structure requires extra parameter eQq_0 and eQq_2 in the effective Hamiltonian of OD, which are not included in the OH Hamiltonian.

Additionally, the spin $\mathbf{I}$ of the deuteron is different from that of the proton, which affects the hyperfine splitting (Section 2.2.3). The spin is integral or half-integral, dependent if

the mass number is even or odd[42]. The proton and the neutron have both a nuclear spin of $I = 1/2$, which couple through nuclear interaction. The resultant nuclear spin angular momenta couple antiparallel, resulting in $I = 0$, or parallel, resulting in $I = 1$. The latter one is lower in energy and defines the ground states, while $I = 0$ is much higher in energy. This leads to a nuclear spin multiplicity of three. Compared with the OH nuclear spin multiplicity of two, more hyperfine transitions are observable with OD. Additionally, the nuclear spin defines, together with the nuclear gyromagnetic ratio γ_I, the magnetic moment $\mu_I = \gamma_I \hbar \mathbf{I} = g_I \mu_N \mathbf{I}$. The gyromagnetic ratio is the product of the nuclear g-factor g and the nuclear magneton $\mu_N = e\hbar/(2M_p)$, with the proton mass M_p. The magnetic hyperfine parameters are proportional to the magnetic moment. Thus, most hyperfine parameters between OH and OD are approximately scaled by the gyromagnetic ratio of both molecules. These parameters are for OD a factor 6.514 smaller, than for OH[42]. Exceptions are, for instance, c_I and related parameters, which have an additional scaling factor involving the reduced mass. This scaling greatly complicates the evaluation of OD spectra because all hyperfine levels move closer together. For example, in the case of a Gaussian line broadening with a full width at half maximum (FWHM) $w_G = 7\,\mathrm{MHz}$, the individual transitions in OD are not resolved. To illustrate this issue, a typical hyperfine transitions cluster of OD has been calculated with PGOPHER[56] (Figure 2.6a upper). The transitions are from the ground states $X^2\Pi_{3/2}$ with $J'' = 3/2$, $F'' = 1/2, 3/2, 5/2$

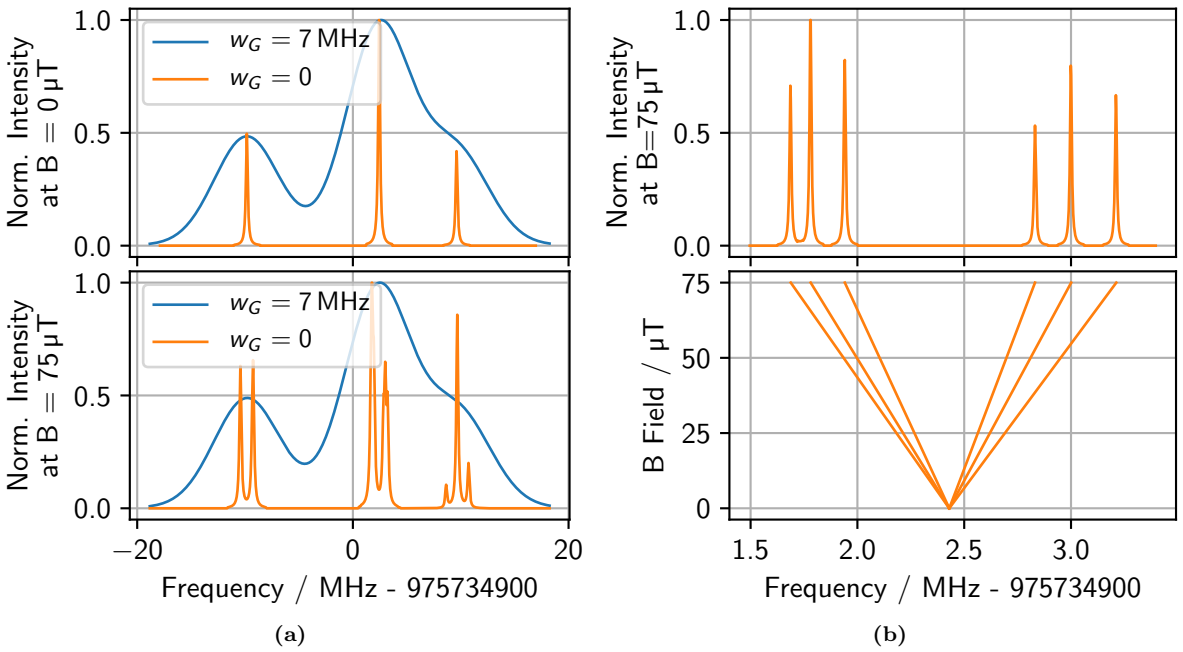

Figure 2.6: (a) Calculated transitions to the excited $A^2\Sigma^+$ state with $N' = 1, J' = 3/2, F' = 3/2$ and e-parity from the ground state $X^2\Pi_{3/2}$ with $J'' = 3/2$, $F'' = 1/2, 3/2, 5/2$ and f-parity. The effect of an external magnetic field becomes visible after setting $w_G = 0$. (b) Showing the Zeeman effect in more detail, by reducing the Lorentzian linewidth parameter to 10 kHz.

and f-parity to the excited state $A^2\Sigma^+$ with $N' = 1, J' = 3/2, F' = 3/2$ and e-parity. Setting the Gaussian line broadening to $w_G = 0$ highlights three distinct peaks with a

remaining Lorentzian linewidth setting of 200 kHz. Additionally, an external magnetic field of $B = 75\,\mu\text{T}$ lifts the degeneracy of the M_F quantum number (Figure 2.6a lower). In order to resolve this splitting, the Lorentzian linewidth is set to 10 kHz, and the focus is on the transitions starting at $F'' = 3/2$, corresponding to the central peak at $B = 0\,\mu\text{T}$ (Figure 2.6a upper). Increasing the magnetic field shows the expected linear trend of the Zeeman effect (Figure 2.6b lower). Six transitions are observable, as an example, for the transitions measured in this thesis (Figure 2.6b upper).

Considering the ratio of selected hyperfine parameters between OH and OD, results in ratios $a : 6.469$, $b : 6.535$, $c : 6.492$ and $d : 6.458$[65]. The discrepancy between those and the ratio of the gyromagnetic moment ratios of 6.514 is rooted in vibrational averaging effects and a break down of the Born-Oppenheimer approximation[42,66].

2.7 Definition of the Hamiltonian

The effective Hamiltonian in this thesis follows the 1994 international union of pure and applied chemistry (IUPAC) recommendation for the fine and hyperfine structure parameters of the linear molecule terms[47]. The quantum numbers follow the conventions in molecular spectroscopy based on the 1997 IUPAC recommendation[67]. Additionally, the rotational part of the Hamiltonian follows the $\hat{N}^2$ convention

$$\hat{H}_{\text{rot}} = B\mathbf{N}^2 - D\mathbf{N}^4 + H\mathbf{N}^6 + L\mathbf{N}^8 + M\mathbf{N}^{10} + P\mathbf{N}^{12} + Q\mathbf{N}^{14}. \tag{2.34}$$

In analogy, for the spin-orbit part of the Hamiltonian follows

$$\hat{H}_{\text{so}} = A\Lambda\Sigma + A_D[\mathbf{N}^2, \Lambda\Sigma]_+ + A_H[\mathbf{N}^4, \Lambda\Sigma]_+. \tag{2.35}$$

To understand the motivation for this definition, consider the pure rotational part of the Hamiltonian $H_{\text{rot}} = B\mathbf{R}^2$, with the nuclear rotational angular momentum $\mathbf{R} = \mathbf{N} - \mathbf{L}$ (Section 2.2.1). One expects a clear representation of the nuclear rotation, without effects associated with the angular momentum of the electrons. This Hamiltonian leads to the first order contribution[42]

$$H_{\text{eff}}^{(1)} = |0\rangle \langle 0| B(R)(\mathbf{N} - \mathbf{L})^2 |0\rangle \langle 0| = B^{(1)}(\mathbf{N}^2 - L_z^2), \tag{2.36}$$

with the first order rotational constant $B^{(1)}$. In analogy to the Lambda doubling, the higher order interaction arises from the coupling of the zero order state $|0\rangle$ to higher electronic states $|\eta\rangle$. The coupling operators are denoted with L_+ and L_-. Thus, the

second order Hamiltonian is[42]

$$H_{\text{eff}}^{(2)} = \sum_{\eta \neq 0} \frac{\langle 0| - B(N_+L_- + N_-L_+) |\eta\rangle \langle \eta| - B(N_+L_- + N_-L_+) |0\rangle \langle 0|}{(V_0 - V_\eta)} \approx B^{(2)}(\mathbf{N}^2 - N_z^2), \tag{2.37}$$

with terms forming the Lambda doubling omitted (Section 2.2.2). Comparing both Hamiltonians $H_{\text{eff}}^{(1)}$ and $H_{\text{eff}}^{(2)}$, shows the same operator form, namely a $H_{\text{eff}} = B_{\text{eff}}(\mathbf{N}^2 - N_z^2)$ dependence. Therefore, the effective Hamiltonian absorbs contributions of the electronic angular momentum into the second order rotational constant $B^{(2)}$. Since some terms have been already omitted and the N_z^2 is the same for all levels in the electronic state, it is justified to omit this term as well. The approximation of a $\mathbf{N}^2$ dependent Hamiltonian greatly simplifies the evaluation. For instance, using $\mathbf{R}^2$ instead of $\mathbf{N}^2$ requires consideration of the coupling of different electronic states, introduced by $\mathbf{L}$. Spectroscopic data cannot determine these contributions, and excluding them has no effect on the relative level positions.

The Comparison between the spectroscopic parameters determined in this thesis, with the $\mathbf{N}^2$ Hamiltonian, to the parameters given by previous works, with the $\mathbf{R}^2$ Hamiltonian[54], requires a parameter transformation. Although in case of the OH excited 2-Sigma state, L_z and N_z are both zero, leading to the relation $\mathbf{N} = \mathbf{R}$ (Equation (2.36)-(2.37)). However, the effective Hamiltonian parameters of the 2-Pi ground state are different. Since the measurement of the OH ground states is no concern in this thesis, it is not necessary to deal with most transformation rules. The exception is the band origin[42]

$$T' = T'_{\text{prev}} + \Lambda^2 B''_{\text{prev}} + \Lambda^4 D''_{\text{prev}}, \tag{2.38}$$

with the superscripts $'$ and $''$ denoting the excited and ground state, respectively. The subscript 'prev' for previous, denotes parameters expressed in the $\mathbf{R}$ formalism. The transformation rule simplifies further for the OH $^2\Pi$ ground state, with $\Lambda = 1$. Some authors use an additional Λ-doubling parameter o in their definition of the Hamiltonian, which shifts the band origin[50]

$$T' = T'_{\text{prev}} + \Lambda^2 B''_{\text{prev}} + \Lambda^4 D''_{\text{prev}} - o''_{\text{prev}}/2. \tag{2.39}$$

The o parameter can only be calculated dependent on the p parameter[25], thus excluding it has no effect on the relative level positions. Inside an effective Hamiltonian, it loses its physical meaning and can as well be directly absorbed into the effective band origin T. In addition to the different $\mathbf{R}$ and $\mathbf{N}$ formalism, some authors prefer to define the centrifugal distortion parameters for γ in terms of $\mathbf{J}^2$ instead of $\mathbf{N}^2$. This Hamiltonian

takes the form [27]

$$\begin{aligned} H = T + B\mathbf{N}^2 - D(\mathbf{N}^2)^2 + H(\mathbf{N}^2)^3 - L(\mathbf{N}^2)^4 + M(\mathbf{N}^2)^5 \\ + (\gamma + \gamma_D \mathbf{J}^2 + \gamma_H (\mathbf{J}^2)^2)(\mathbf{N} \cdot \mathbf{S}), \end{aligned} \tag{2.40}$$

with the rotational constants B, D, H, L, M and the centrifugal parameters γ, γ_D γ_H. In this thesis, each parameter is defined relative to $\mathbf{N}^2$. Thus a transformation of the $\mathbf{J}^2$ parameters is necessary, for comparison reasons. The transformation rules are most easily extracted by evaluating the matrix elements of the state of interest. In a 2-Sigma molecule, which is diagonal in Hund's case (b), the matrix element using the $\mathbf{J}^2$ convention is given by [27]

$$\begin{aligned} \langle {}^2\Sigma^+ | {}^2\Sigma^+ \rangle = T + Bx(x \pm 1) - Dx^2(x \pm 1)^2 + Hx^3(x \pm 1)^3 - Lx^4(x \pm 1)^4 \\ + Mx^5(x \pm 1)^5 - \tfrac{1}{2}[\gamma + \gamma_D J(J+1) + \gamma_H J^2(J+1)^2](1 \pm x), \end{aligned} \tag{2.41}$$

with $x = J + S = J + 1/2$. The matrix element is given for both e- and f-parity sublevels, with the upper sign referring to the f-parity. It is convenient to note that the term $x(x \pm 1) = N(N+1)$. Now rewriting the explicit J dependent terms, aiming to introduce the $x(x \pm 1)$ term, leads to

$$J(J+1) = (x - \tfrac{1}{2})(x + \tfrac{1}{2}) = x^2 - \tfrac{1}{4} = x(x \pm 1) \mp x - \tfrac{1}{4}, \tag{2.42}$$

$$(J(J+1))^2 = x^2(x \pm 1)^2 \mp 2x \cdot x(x \pm 1) + \tfrac{1}{2}x(x \pm 1) \mp \tfrac{1}{2}x + \tfrac{1}{16}. \tag{2.43}$$

Inserting these terms into Equation (2.41) and sorting out the expression leads to the transformation rules

$$B = B_{\text{prev}} + \gamma_{D,\text{prev}}/2 + \gamma_{H,\text{prev}}/4, \tag{2.44}$$

$$D = D_{\text{prev}} - \gamma_{H,\text{prev}}, \tag{2.45}$$

$$\gamma = \gamma_{\text{prev}} - \gamma_{D,\text{prev}}/4 + \gamma_{H,\text{prev}}/16 \tag{2.46}$$

$$\gamma_D = \gamma_{D,\text{prev}} + \gamma_{H,\text{prev}}/2. \tag{2.47}$$

These are important for comparing the measured spectroscopic parameters in this thesis to previous measurements expressed in a different formalism.

Chapter 3

Precision Laser System

The three essential components of a laser are always an active medium, a resonator and something pumping the population inversion. Dependent on the application, there are many different variants of these three components. The spectroscopy in this thesis requires a laser system with high stability and a wide tuning range that enables readout of the absolute emission frequency of the spectroscopy lasers. A single laser is not able to meet these demands, but instead, a combination of different lasers does. Each involved laser has a different field of application.

3.1 CW Lasers

The potentially narrow linewidth in single mode emission makes continuous wave (CW) lasers the primary choice for high-resolution spectroscopy. This thesis relies on two CW lasers: the spectroscopy laser excites the hydroxyl radical (OH) transitions for detection, and the reference laser is a narrow-linewidth source used to stabilize the other lasers.

3.1.1 Spectroscopy Laser

To investigate the electronic transitions of OH from the rovibronic ground state $X^2\Pi_{3/2}$, $v'' = 0$, $J'' = -3/2$ to the lowest levels of $A^2\Sigma^+$, $v' = 0$, we use an ultraviolet (UV) laser around 308 nm. The standard approach for producing coherent UV light is by non-linear conversion of visible light, for instance using second-harmonic generation (SHG) (Chapter 4). For this, a laser with an emission wavelength of around 616 nm is required.

A semiconductor laser was used first in this thesis to produce light at 616 nm. Electric current pumps the active medium, and the cavity mirrors are the uncoated crystal surfaces[68]. In a simplified picture, the active medium is a p-n semiconductor diode. Applying current into the conducting direction leads to population inversion of electrons at the p-n junction. The n part has an electron surplus and the p part an electron deficiency referred to as holes. The process of electron-hole recombination leads to the emission

of light. Unfortunately, there are no laser diodes available which operate single mode at 616 nm. The closest wavelengths offered are around 633 nm using diodes with aluminium gallium indium phosphide (AlGaInP) semiconductor material. The emission wavelength of the 633 nm diodes can be shortened by cooling them to low temperatures and increasing the band gap. While the lower temperature forces the laser to operate at 616 nm, it also decreases the lasers ability to operate with a single mode. An additional weakness of a diode laser is the limited tuning range. The efforts toward cooling the laser diode are discussed in Section 9.4.1.

A dye laser can cover, in contrast to a semiconductor laser, nearly the whole visible spectral range and is used for the spectroscopy presented in this thesis. The specific tuning range depends on the choice of dye and pump laser [68]. Laser dyes consist of rather large molecules with a multiplicity of ground and excited states. The interaction with the solvent leads to a broadening of the transitions frequencies, that exceeds the average level distance, resulting in a continuum of possible lasing transitions. Pumping these states with a CW laser of high intensity leads to fluorescence light from this continuum. A cavity with frequency-selective elements reduces the gain for all frequencies except one, the lasing frequency. All frequency-selective optics used can potentially contribute to the instability of the laser frequency. Each mechanical element can potentially move and introduce noise. Compensating the noise requires control over the cavity length. This control enables laser stabilization as well as frequency tuning. Both things are necessary for high-resolution spectroscopy. The dye laser in this thesis is stabilized to a reference laser.

3.1.2 Reference Laser

The free running dye laser is not a stable laser system, due to the amount of associated optical components inside the laser and the large size of the optical cavity. Therefore, a laser system without any optics inside the cavity, which is as small as possible, shows superior stability. A single monolithic crystal of neodymium-doped yttrium aluminum garnet (Nd:YAG), with a length of just a few millimeters, acts as both the cavity and the gain medium of the non-planar ring oscillator (NPRO) [69]. The unique shape of the crystal allows total internal reflection at the facets and simultaneously provides ring oscillation [70]. An early measurement in 1987 of the beat note between two NPRO lasers showed a full width at half maximum (FWHM) of less than 3 kHz [71]. No other laser design until today matches this level of stability. NPROs are an essential part of the interferometers used in the observation of gravitational waves [72]. The bare NPRO laser design is the best possible starting point for further stabilization, with an external ultra-low expansion (ULE) cavity [73] or an iodine-based frequency reference reducing frequency fluctuations on timescales longer than a few milliseconds [74]. In order to stabilize the NPRO to these references, it is essential to be able to control its frequency. Slow control can be achieved

by changing the crystal temperature, which leads to thermal expansion and a change of the refractive index while compressing the laser crystal with a piezoelectric transducer (PZT) supplies a faster change of the cavity length. Both methods shift the frequency of the longitudinal modes. The emission wavelength of a Nd:YAG NPRO is around 1064 nm, and the maximum tuning range is around 30 GHz. Thus, a direct optical lock with the dye laser at 616 nm is not possible, and an additional step is necessary.

3.2 Mode-Locked Laser

The narrow linewidth and high stability of a NPRO is perfectly suited for spectroscopy (Section 3.1.2), but its application potential is limited by a small tuning range. Conversely, the dye laser has a large tuning range, but a less-stable emission frequency. On top of both issues, a precise determination of the optical frequency is necessary. A mode-locked laser is a tool that makes it possible to transfer the high stability of the solid-state laser onto the dye laser and enables a precise determination of the optical frequency. Normally, in a continuously-pumped laser, the intensity of the radiation traveling through the cavity is constant, and the laser emits continuously. In a mode-locked laser, the cavity is configured such that the energy in the cavity coalesces into a short pulse, which results in a train of pulses being emitted (Section 3.2.1). A train of equally spaced pulses in the time domain leads to an optical frequency comb (OFC) in the frequency domain. Such a spectrum is essentially an optical ruler, which allows direct optical frequency comparisons with other lasers, by measuring the beat note (Section 3.2.3). The OFC makes it possible to measure an optical frequency with the same precision as a radio frequency. One system that generates ultrashort optical pulses is the Kerr-lens mode-locked Ti:sapphire laser [75]. This laser relies on self-focusing inside the active medium, with an aperture selecting the corresponding mode. Dependent on the level of dispersion correction, pulse duration of fewer than 6 fs are possible [76,77], leading to a one-octave span of the spectrum [78]. The OFC revolutionized metrology and is the center of each frequency measurement in this thesis.

3.2.1 Mode-Locking

The basis of pulse generation is the longitudinal mode structure of the laser cavity. In general, laser operation is possible on a large number of modes and even desired for a pulse train. The frequency of each mode satisfies the condition [79]

$$\omega_m = (2\pi m + \Delta\Phi)\frac{c}{Ln(\omega_m)}, \tag{3.1}$$

with the mode number m, the effective frequency dependent refractive index n and the round-trip path Length L. An additional Gouy phase $\Delta\Phi$ is caused, if the beam goes

through a focus, which is for the sake of simplicity ignored at the moment, along with dispersion. Thus, the spacing of two adjacent comb modes is described by the free spectral range $\Delta\nu = c/(nL)$. The frequency of mode m is $\omega_c = \omega_l + m2\pi\Delta\nu$, centered around a carrier frequency ω_c. The resulting electric field is[80]

$$E(t) = \frac{1}{2}E_0 e^{i\omega_c t} \sum_{m=(1-M)/2}^{(M-1)/2} e^{i(m2\pi\Delta\nu t+\phi_m)} + c.c., \tag{3.2}$$

with M oscillating modes. For simplicity, these modes have the same amplitude E_0. The phase factor ϕ_m is random for a free-running laser. Mode-locking forces an equal phase $\phi_0 = \phi_m$ onto all modes. Rewriting the electric field, by applying the geometric series yields[80]

$$E(t) = \frac{1}{2}E_0 e^{i\phi_0} e^{i\omega_c t} \frac{\sin(M\pi\Delta\nu t)}{\sin(\pi\Delta\nu t)}. \tag{3.3}$$

The intensity $I(t) \propto |E(t)|^2$ shows well separated maxima at integer multiples of the time $1/\Delta\nu$. At these points in time, the waves inside the laser cavity add up constructively and create a short pulse of light. The width is linked to the number of interacting cavity modes M and is approximately $1/(M\Delta\nu)$. After each round trip inside the cavity, a fraction of this pulse gets coupled out, so keeping the cavity length constant and shielding it from acoustic noise and temperature fluctuations is crucial to obtain an equally spaced pulse train in the time domain.

3.2.2 Frequency Spectrum

A Fourier transform of the time-domain pulse train from a mode-locked laser results in a comb of evenly spaced modes in the frequency domain. These modes are separated by the repetition rate of f_r, which is associated with the time difference between two subsequent pulses $T = 1/f_r$.

If there were no dispersion inside the laser cavity, the absolute frequency of each mode would be a multiple of f_r, but with dispersion, all modes are shifted in frequency by an offset. Consider a decomposition of a single pulse $E(t) = A(t)e^{\omega_c t}$ into two factors, consisting of an envelope function $A(t)$ and a previously used carrier wave with frequency ω_c (Section 3.2.1). Introducing dispersion leads to a changing phase difference between the carrier wave and the envelope function, which have different velocities inside the laser cavity. The carrier wave propagates with the phase velocity $v_{ph}(\omega_c) = c/n(\omega_c)$ while the envelope propagates with the group velocity

$$v_g(\omega_c) = \left(\frac{\partial k(\omega)}{\partial\omega}\right)^{-1}\Bigg|_{\omega_c} = \left(\frac{\partial}{\partial\omega}\left(\frac{\omega}{v_{ph}}\right)\right)^{-1}\Bigg|_{\omega_c} = \left(\frac{n(\omega_c)}{c} + \frac{\omega_c}{c}\frac{\partial n(\omega)}{\partial\omega}\right)^{-1}\Bigg|_{\omega_c}, \tag{3.4}$$

resulting in different round-trip times inside the laser cavity. The round-trip carrier-envelope phase difference yields[79]

$$\Delta\phi = \omega_c \Delta T = \omega_c \left(\frac{L}{v_g} - \frac{L}{v_{ph}} \right) = \frac{\omega_c^2 L}{c} \frac{\partial n(\omega)}{\partial \omega}\bigg|_{\omega_c} = -2\pi L \frac{\partial n}{\partial \lambda}\bigg|_{\lambda_c} . \tag{3.5}$$

Every optical element within the laser cavity contributes to this shift. However, the periodic nature of waves limits the range to $0 \leq \Delta\phi \leq 2\pi$. The carrier-envelope phase shift changes by $\Delta\phi$ from one pulse to the next. In the time domain, the phase difference between the peak of the envelope $A(t)$ and the closest maximum of the carrier wave define $\Delta\phi$ (Figure 3.1a). In the frequency domain, this phase shift results in a frequency offset

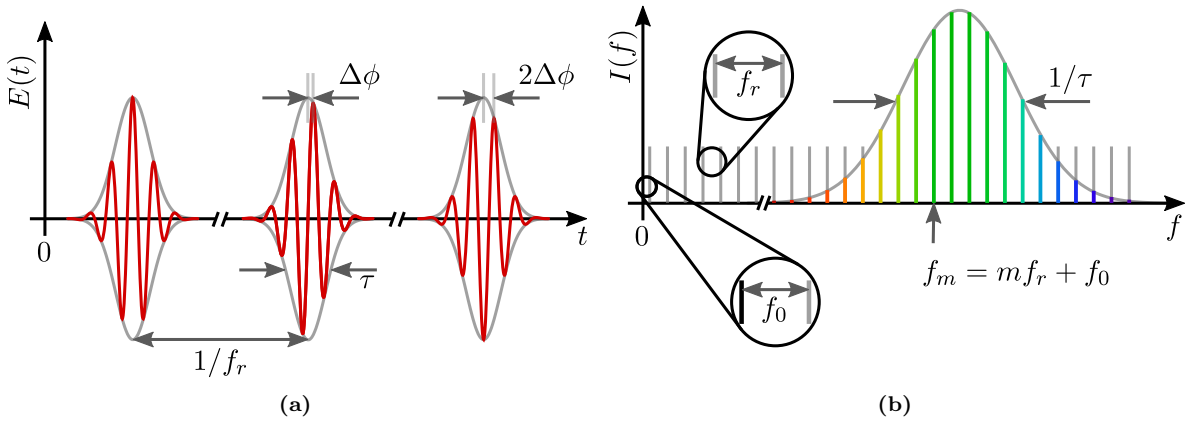

Figure 3.1: (a) Pulse train of a mode-locked laser in the time domain, with the electric field in red and the envelope function in gray. The phase shift between two neighboring pulses is constant. (b) The Fourier transform of the pulse train leads to equally spaced frequencies f_m. An extrapolation of the comb to low frequencies shows a frequency offset f_0 when $m = 0$.

$f_0 = \Delta\phi/(2\pi T)$ for all modes in the comb spectrum[81]. Thus, the optical frequency of a single comb tooth is described by

$$f_m = m f_r + f_0, \tag{3.6}$$

with a mode number m starting at zero and an offset frequency $|f_0| < f_r/2$. Essentially, each of these modes acts as an individual single mode laser with a frequency difference of f_r from its neighboring modes. A hypothetical pulse train with $f_r = 1\,\text{GHz}$ and a pulse duration of $\tau = 20\,\text{fs}$ leads to 5×10^4 interacting cavity modes. If the central wavelength is 800 nm, the span corresponds to ca. 100 nm. The frequency of a laser under test must be within the span of the OFC. If the span is too narrow, it is convenient to broaden it using a photonic crystal fiber (PCF), which creates additional comb modes using the nonlinear conversion of four-wave mixing (Section 4.0.4). The design of the PCF deviates from conventional optical fibers, by microscopic air tunnels along its length[82]. Such a structure supplies strong guiding of the light field[83], which can control dispersion to keep the fs pulses bunched, as well contributes to a strong activity of nonlinear processes.

The actual frequency measurement of a CW laser with the OFC requires a heterodyne detection of both laser beams [34,84].

3.2.3 Optical Beat Note

Optical heterodyne detection is based on the superposition of two monochromatic electromagnetic fields $E_1(t)$ and $E_2(t)$ of different frequencies ω_1 and ω_2 (Figure 3.2a and 3.2b), leading to

$$\begin{aligned} I(t) &= |E_1(t) + E_2(t)|^2 \propto |e^{i\omega_1 t} + e^{i\omega_2 t} + c.c.|^2 \\ &= 2e^{i(\omega_1-\omega_2)t} + \underbrace{2e^{i(\omega_1+\omega_2)t} + e^{i2\omega_1 t} + e^{i2\omega_2 t}}_{\xrightarrow{\text{LP}} 0} + \underbrace{4}_{\xrightarrow{\text{DC}} 0} + c.c. \approx 4\cos((\omega_1-\omega_2)t). \end{aligned} \tag{3.7}$$

After eliminating the high frequency components and the direct current (DC) part, only

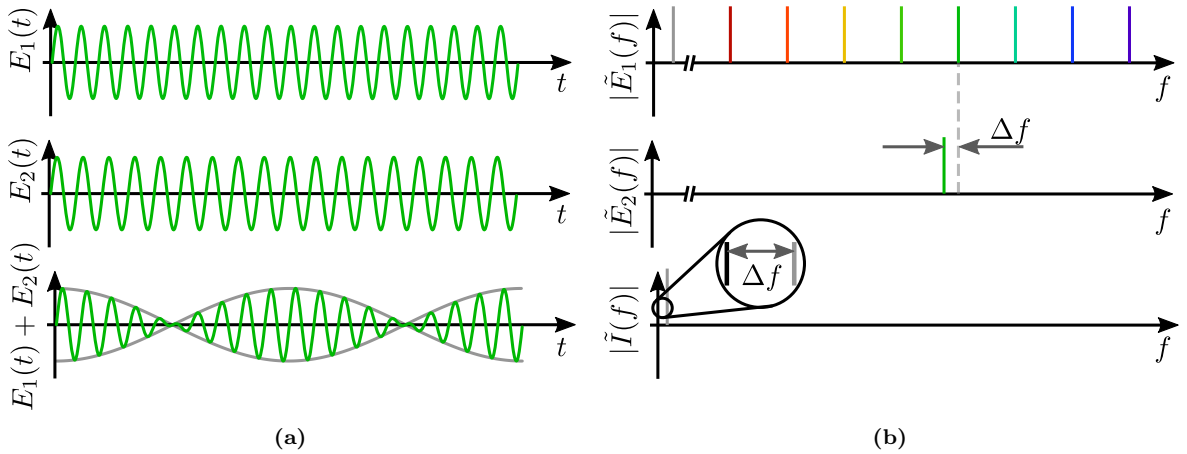

Figure 3.2: (a) Time domain representation of two electromagnetic fields $E_1(t)$ and $E_2(t)$ with nearly identical optical wavelengths. $E_3(t)$ displays an envelope function with a much larger wavelength. (b) The beat note between a single mode CW laser and the nearest comb tooth is at a frequency $\Delta f < f_r/2$.

the low frequency signal at $\Delta\omega = \omega_1 - \omega_2$ remains, resulting in a beat note frequency at $\Delta f = \frac{1}{2\pi}|\Delta\omega|$. A photodiode detects the intensity $I(t) \propto |E(t)|^2$ with a certain electronic bandwidth. Since optical frequencies are always outside this bandwidth, the beat note causes the only remaining detectable frequency. An OFC supplies multiple optical frequencies. The superposition of the OFC beam with an arbitrary CW laser beam, within the frequency span of the OFC yields an optical beat note between both lasers. A repetition rate of $f_r = 1\,\text{GHz}$ results in a beat note with $\Delta f < 500\,\text{MHz}$, which is within the range of conventional radio frequency technology. Thus, a fully characterized OFC supplies a high precision measurement of the CW laser's frequency

$$f_{cw} = m f_r + f_0 \pm \Delta f. \tag{3.8}$$

The only uncertainties are the mode number m and the sign of the beat note frequency, which changes depending on whether the closest comb tooth is higher or lower in frequency. Observing the progression direction of the beat note, dependent on the frequency change of the CW laser, allows identifying the sign. If Δf increases with the CW laser frequency, then the nearest comb tooth is lower in frequency and vice versa. The mode number can be most easily determined using an independent measurement of the CW laser frequency with a precision better than 500 MHz. In the experiment, a well-calibrated wavemeter satisfies this condition. Determining the absolute frequency of the comb tooth requires radio frequency measurements of f_r and f_0. The repetition rate f_r can be measured directly by counting the pulses with a fast photodiode. A measurement of the carrier to envelope offset frequency f_0 is possible by two different techniques.

3.2.4 OFC Parameter Control

Self-referencing of the OFC is the most utilized technique of measuring the parameter f_0. A one-octave span of the OFC greatly simplifies this measurement [85]. In this case, the highest frequencies are a factor of two larger than the lowest frequencies. A heterodyne setup between the original blue end of the OFC and the frequency-doubled red end leads to an optical beat note (Figure 3.3a), which allows a direct readout of the carrier to envelope offset frequency. For simplicity, doubling the frequency on the red end to $2(mf_r + f_0)$ and comparing it to the mode at the blue end of the spectrum $2mf_r + f_0$ leads to the beat note [85]

$$\Delta f = |2f_m - f_{2m}| = |2mf_r + 2f_0 - 2mf_r - f_0| = f_0. \tag{3.9}$$

In detail, the modes are not only doubled, but also added up such that the mode spacing

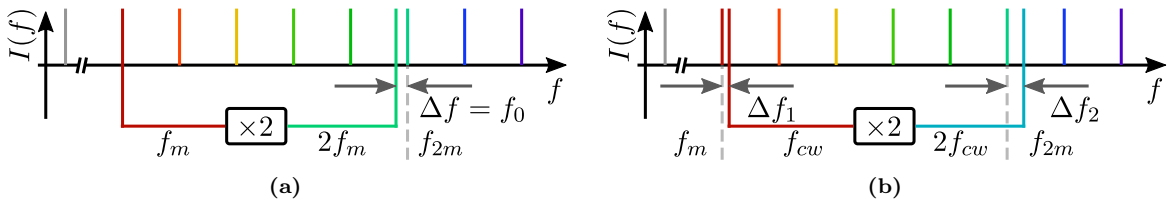

Figure 3.3: (a) Self referencing of OFC by SHG of a low frequency f_m and a beat note measurement between $2f_m$ and the closest comb tooth at f_{2m}. For the sake of clarity, only one beat note is draw, even more exist. (b) The measurement of two beat notes with a CW laser at the low frequency and the high frequency part of the comb, leads also to a read-out of the carrier to envelope offset frequency.

remains f_r instead of $2f_r$. Also f_0 is produced by multiple pairs of comb lines, which increases the signal to noise ratio (SNR).

A CW-Laser based extraction is more convenient in the apparatus used in this thesis. Instead of frequency doubling the OFC, a CW laser at the red end of the comb spectrum is frequency-doubled. Afterwards, two optical beat notes are detected. The first beat

note with Δf_1 is between the CW laser at f_{cw} and the closest comb tooth at f_m. The beat note at the high-frequency part of the comb spectrum with Δf_2 is between the frequency doubled CW laser at $2f_{cw}$ and the comb tooth at f_{2m}. Subtracting both beat notes frequencies leads to

$$|2\Delta f_1 - \Delta f_2| = |2(f_{cw} - f_m) - (2f_{cw} - f_{2m})| = f_0, \tag{3.10}$$

$$|\Delta f_1 - \Delta f_2| = |(f_{cw} - f_m) - (2f_{cw} - f_{2m})| = |mf_r - f_{cw}|. \tag{3.11}$$

An appropriate weighting allows directly to extract the carrier envelope offset frequency, independent of the interacting CW laser frequency (Equation 3.10). Weighting both beat notes equally provides the frequency difference between the CW laser frequency and a high harmonic of the repetition rate f_r (Equation 3.11). The OFC parameters can be tuned using pump power and cavity size, but their effects are not entirely independent of each other. The repetition rate f_r, for example, is associated with the round trip time of a pulse inside the laser cavity. Shortening the cavity length with a mirror on a piezoelectric transducer reduces the round trip time, increasing the repetition rate f_r. The OFC behaves like a rubber band, with a fixed anchor at zero frequency for changes of the cavity length (Figure 3.4a). The frequency change of a mode m is $\Delta f = m\Delta f_r$, resulting in a negligible

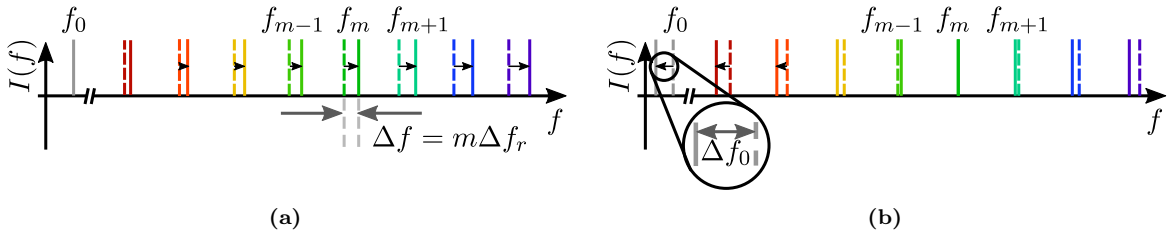

Figure 3.4: (a) Reducing the cavity length increases the repetition rate f_r. Thus, the comb spacing increases and shifts the frequency f_m by Δf. The carrier to envelope offset frequency f_0 is nearly unaffected. (b) Changing the pump power affects both f_r and f_0, but tends to leave a mode somewhere near the center of the spectrum fixed in frequency. This leads to a large frequency change of f_0 for a small change in f_r.

change of f_0. The pump power influences the phase and the group velocities differently which allows the control of f_0 [86]. In general, also the repetition rate f_r is dependent on the pump power [87,88]. For small changes of power, the relation between the pump power and f_0 shows a linear trend. In a simplified picture, the OFC gets stretched again, but this time with a different anchor point. A particular comb tooth near the center of the spectrum will be independent of the power, and the highest frequency change is experienced at f_0 (Figure 3.4b). Utilizing the independent controls of the OFC parameters, it is now convenient to stabilize them.

3.2.5 OFC Stabilization

If the two beat notes described in the previous section can be held at constant frequencies, all degrees of freedom of the comb will be constrained relative to the CW laser, and f_0 and

f_r will be fixed. Since the invention of the frequency modulation (FM) radio (1933) by Armstrong[89], modulating and demodulating signals in a frequency range up to 300 GHz is a technology used in our daily lives. Many modern radio receivers employ in-phase and quadrature modulation and demodulation schemes[90]. The same technology is adapted to demodulate the beat note signal into an in-phase $I(t)$ and a quadrature component $Q(t)$ relative to the reference frequency. In IQ modulation, the signal waveform is expressed in the form

$$x(t) = A(t)\cos(\omega t + \phi(t)) = \underbrace{A(t)\cos\phi(t)}_{I(t)}\cos(\omega t) - \underbrace{A(t)\sin\phi(t)}_{Q(t)}\sin(\omega t), \tag{3.12}$$

with the amplitude $A(t)$, the phase $\phi(t)$ and the reference waveforms $\cos(\omega t)$ and $\sin(\omega t)$. Multiplying the waveforms by $\cos(\omega t)$ leads directly to the in-phase component

$$x(t)\cos(\omega t) = \frac{1}{2}I(t) + \underbrace{\frac{1}{2}I(t)\cos(2\omega t)}_{\xrightarrow{\text{LP}}0} - \underbrace{\frac{1}{2}Q(t)\sin(2\omega t)}_{\xrightarrow{\text{LP}}0} \approx \frac{1}{2}I(t). \tag{3.13}$$

The 2ω frequency components are eliminated using a low-pass filter, leaving only the in-phase component. Analogous to the in-phase component, multiplying the waveform by $-\sin(\omega t)$ results in the quadrature component

$$-x(t)\sin(\omega t) = \frac{1}{2}Q(t) - \underbrace{\frac{1}{2}I(t)\sin(2\omega t)}_{\xrightarrow{\text{LP}}0} - \underbrace{\frac{1}{2}Q(t)\cos(2\omega t)}_{\xrightarrow{\text{LP}}0} \approx \frac{1}{2}Q(t) \tag{3.14}$$

The I and Q demodulation signals can be represented as a vector in a plane, with the amplitude $A(t) = \sqrt{I(t)^2 + Q(t)^2}$ and the angle $\phi(t) = \text{atan2}(Q(t), I(t))$. The I and Q signals can be digitized to calculate the angle $\phi(t)$ in software, which is then used as the error signal in a feedback loop (Section 5.3). One of the lasers is controlled by the feedback loop, which brings $\phi(t)$ back to zero. The stabilization of the OFC in this thesis requires two such feedback loops. The first feedback loop stabilizes the beatnote at 1064 nm (with frequency Δf_{1064}) to a $f_{\text{ref}} = 100$ MHz reference frequency (Figure 3.5a). The constraining equation for this can be written as

$$|f_{\text{ref}} - \Delta f_{1064}| = |\underbrace{100\,\text{MHz} - f_{1064}}_{\text{constant}} + \underbrace{f_0}_{f_0 \ll m f_r} + m f_r| \stackrel{!}{=} 0. \tag{3.15}$$

The dominant factor in this equation is the repetition rate f_r, since other factors are not determined by the frequency comb or are negligibly small. Thus, the beat note at 1064 nm is well suited to feedback using the cavity length and the associated f_r. To stabilize the beat note at 100 MHz, a reference waveform at 200 MHz is divided by two

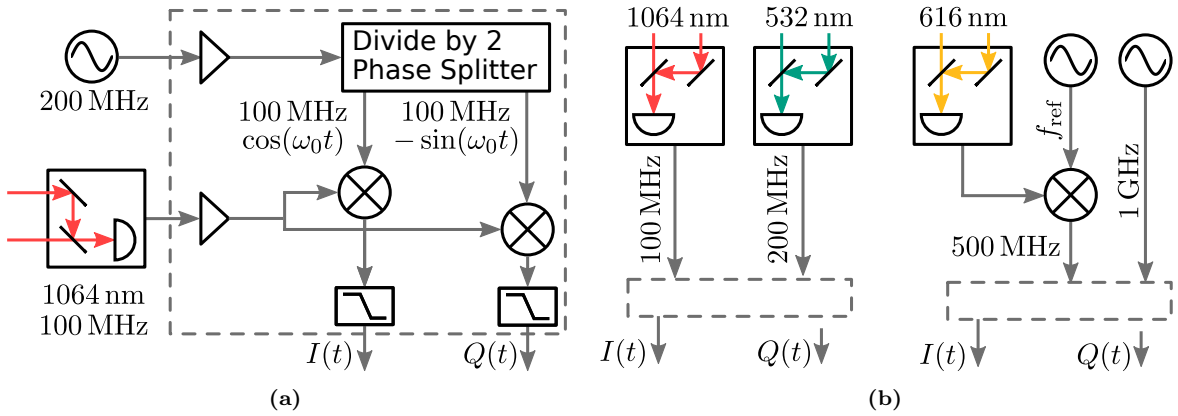

Figure 3.5: (a) Stabilization scheme of $\Delta f_{1064} = 100\,\text{MHz}$ to a reference waveform at 200 MHz. The I/Q-demodulation unit, depicted as dashed gray box, returns the in-phase $I(t)$ and the quadrature $Q(t)$ component of the waveform. The following calculated phase $\phi(t)$ is used to stabilize primary f_r (b) The scheme on the left shows the demodulation between two beat notes to stabilize f_0. In analogy, the scheme on the right is the requirement to lock an arbitrary laser, for example at 616 nm, to the OFC.

using a phase splitter, which produces two waveforms with 90° phase difference. These are mixed with the beat note signal and filtered, generating the I and Q signals described in Equations (3.13)-(3.14). A subsequent proportional-integral (PI) controller uses $\phi(t)$ calculated from $I(t)$ and $Q(t)$ as an input error signal to generate a control signal. Finally, the control signal is amplified before being applied to a PZT, that adjusts the cavity length. The cavity control keeps Δf_{1064} and the associated f_r constant. A second control loop is used to stabilize f_0. Here the 532-nm beat note is used as the reference input of a second phase splitter and compared to the 1064-nm beat note at $\Delta f_{1064} = 100\,\text{MHz}$. Instead of an external reference, the beat note frequency Δf_{532} is set to 200 MHz (Figure 3.5b left). Since the phase splitter divides by two, the feedback loop will force the 532-nm beat note frequency to $\Delta f_{532} = 200\,\text{MHz}$. According to Equation (3.10), this behavior of the phase splitter results in $I(t)$ and $Q(t)$ having a frequency of $f_0/2$

$$|\frac{1}{2}\Delta f_{532} - \Delta f_{1064}| = |\frac{1}{2}(f_{532} - (f_0 + 2mf_r) - f_{1064} + (f_0 + mf_r)| = \frac{1}{2}f_0 \stackrel{!}{=} 0. \qquad (3.16)$$

Therefore, extracting the phase $\phi(t)$ and setting it to zero with a feedback loop forces f_0 to zero. The control parameter used in this feedback loop is the laser pump power, which most just changes the beat note frequency of Δf_{532}. It was determined experimentally that the fixed point in the comb spectrum for changes of the pump power is around 900 nm, so the beat note at Δf_{1064} and its control loop experiences negligible disturbance from this second control loop. The OFC is now fully constrained, the frequency of an additional CW laser can be precisely determined by measuring the beat note between the OFC and the CW. Additionally, it is possible to transfer the stability of the OFC onto this laser, which is, for example, a 616-nm laser with a beat note frequency Δf_{616} (Figure 3.5b right). As an example, if we want to stabilize the beat note at $\Delta f_{616} = 100\,\text{MHz}$, we mix it with a 400-MHz reference frequency f_{ref}, to have the sum at 500 MHz. The reference

input for the phase splitter is fixed at 1 GHz, resulting in two 500-MHz waveforms with a 90-degree phase difference, which are then mixed with the frequency-shifted beat note. The constraining equation for the feedback loop based on the beat note with the new CW laser is

$$|500\,\mathrm{MHz} - (\Delta f_{616} + f_{\mathrm{ref}})| = |\underbrace{500\,\mathrm{MHz} - f_0 - m f_r}_{\text{constant}} - \underbrace{f_{\mathrm{ref}}}_{\text{adjustable}} + f_{616}| \stackrel{!}{=} 0, \tag{3.17}$$

and the feedback loop sets $\phi(t)$ to zero by controlling the cavity length of the 616-nm laser. In other words, the CW laser frequency changes, while the OFC parameters remain constant. Since the locking condition is satisfied for each f_{ref}, the frequency of the CW laser can be changed by changing f_{ref}. Details on the experimental setup of the OFC, as well the electronic components involved in the stabilization are in Section (9.3).

Chapter 4

Nonlinear Optics

The transmissive medium is one of the essential tools in the manipulation of light. A prism, for example, changes the propagation direction of a single light ray. The direction changes for light at different frequencies, but the frequency stays the same. In analogy, some optical media keep the direction of propagation but change the frequency of the light wave. The latter is the consequence of the light wave potentially altering the optical properties of the medium. Essential for light conversion between two different frequencies is the nonlinear dependence between an optical property of the medium and the power of the electric field. One simple case of power dependent change of optical properties is nonlinear absorption inside the medium. The spectroscopic setup described in this thesis relies heavily on nonlinear processes. We use second-harmonic generation (SHG) to convert a neodymium-doped yttrium aluminum garnet (Nd:YAG) laser at 1064 nm to 532 nm (Section 4.0.1). The wave at 532 nm is used to stabilize the frequency of the laser to an absorption line in molecular iodine with modulation transfer spectroscopy, which is based on a nonlinear four-wave mixing process (Section 4.0.4). Essentially, the same process inside an optical fiber leads to the spectrum broadening of the femtosecond laser (Section 4.0.2). The resulting optical frequency comb (OFC) serves as a reference between the various laser systems of the setup. These are all relevant nonlinear processes allowing the measurement of the electronic transitions of the hydroxyl radical (OH) in this thesis. One requirement for prospective vibrational excitation of the OH is mid-infrared light. For this, we have developed an optical parametric oscillator (OPO) (Section 4.0.3), that makes use of second-order non-linearity to convert the amplified wave of the Nd:YAG laser at 1064 nm into a light wave around 2.9 µm. This chapter gives an introduction of nonlinear optics, based on Boyd [91], before going into more detail in explaining the OPO.

The polarizability of a medium is the most used optical property for nonlinear conversion of light, in particular, the nonlinear dependence of the polarization of a material on

the electric field strength [91]

$$P(t) = \epsilon_0 \left[\chi^{(1)} E(t) + \chi^{(2)} E^2(t) + \chi^{(3)} E^3(t) + \cdots\right], \tag{4.1}$$

$$\equiv P^{(1)}(t) + P^{(2)}(t) + P^{(3)}(t) + \cdots . \tag{4.2}$$

The polarization $P(t)$ depends on the permittivity of free space ϵ_0, the susceptibility $\chi^{(i)}$ of order $i \in \mathbb{N}$ and the strength of the electromagnetic field $E(t)$. In the case of linear optics only the first order of the susceptibility $\chi^{(1)}$ is considered. Non-linear processes are dependent on the second order susceptibility $\chi^{(2)}$ or the third order susceptibility $\chi^{(3)}$. The corresponding nonlinear polarizations of order two or three are denoted $P^{(2)}(t)$ or $P^{(3)}(t)$, respectively. The Maxwell equations describe the light propagation through a nonlinear medium [91]

$$\nabla \mathbf{D} = \rho, \tag{4.3}$$

$$\nabla \mathbf{B} = 0, \tag{4.4}$$

$$\nabla \times \mathbf{E} = -\frac{\partial \mathbf{B}}{\partial t}, \tag{4.5}$$

$$\nabla \times \mathbf{H} = \frac{\partial \mathbf{D}}{\partial t} + \mathbf{J}, \tag{4.6}$$

with the electric displacement field $\mathbf{D} = \epsilon_0 \mathbf{E} + \mathbf{P}$. Thus, the polarization vector $\mathbf{P}$ causes a nonlinear relation between $\mathbf{D}$ and $\mathbf{E}$. The Maxwell equations simplifies, considering no free charges ($\rho = 0$) and no free current ($\mathbf{J} = 0$) inside the nonlinear medium. Additionally, the material is nonmagnetic ($\mathbf{B} = \mu_0 \mathbf{H}$). The derived optical wave equation is [91]

$$\nabla^2 \mathbf{E} - \frac{1}{\epsilon_0 c^2} \frac{\partial^2}{\partial t^2} \mathbf{D} = 0. \tag{4.7}$$

The only included approximation refers to infinite plane waves with $\nabla E = 0$. It is convenient to separate the electric displacement field into a linear and a nonlinear part, yielding to [91]

$$\mathbf{D} = \mathbf{D}^{(1)} + \mathbf{P}^{\mathrm{NL}} = \epsilon_0 \mathbf{E} + \mathbf{P}^{(1)} + \mathbf{P}^{\mathrm{NL}} \approx \epsilon_0 \boldsymbol{\epsilon}^{(1)} \mathbf{E} + \mathbf{P}^{\mathrm{NL}}. \tag{4.8}$$

The included approximation is valid for a lossless and dispersionless medium. In detail, the frequency independent dielectric tensor $\boldsymbol{\epsilon}^{(1)}$ connects $\mathbf{D}^{(1)}$ and $\mathbf{E}$. Inside an isotropic medium, it is replaced by the relative permittivity $\epsilon^{(1)} = n^2$, with the linear index of refraction n. Finally, the wave equation is [91]

$$\nabla^2 \mathbf{E} - \frac{n^2}{c^2} \frac{\partial^2 \mathbf{E}}{\partial t^2} = \frac{1}{\epsilon_0 c^2} \frac{\partial^2 \mathbf{P}^{\mathrm{NL}}}{\partial t^2}, \tag{4.9}$$

with the vacuum speed of light $c = 1/\sqrt{\epsilon_0 \mu_0}$. The second time derivative of the nonlinear polarization makes the wave equation inhomogeneous. This additional time-varying polarization creates new field components. The polarization change is a representation of an acceleration process of charges inside the medium. This process is analogous to one of the fundamental theorems of electromagnetism pointed out by Lamour, namely that an accelerated charged particle generates electromagnetic radiation. The frequencies of this radiation are calculated using the general description of polarization of Equation (4.2). For simplicity, further calculations assume an instantaneous interaction between the electric field and the medium.

4.0.1 Second Harmonic Generation

One of the most common nonlinear processes is the second harmonic generation (SHG). A monochromatic electromagnetic field describes the initial laser beam

$$E(t) = Ee^{-i\omega t} + c.c.. \tag{4.10}$$

The nonlinear second order interaction with a medium demands a non-vanishing susceptibility $\chi^{(2)}$. Inserting Equation (4.10) into the second order polarization of Equation (4.2) leads to [91]

$$P^{(2)} = 2\epsilon_0 \chi^{(2)} EE^* + \left(\epsilon_0 \chi^{(2)} E^2 e^{-2i\omega t} + c.c.\right). \tag{4.11}$$

With respect to Equation (4.9), only terms with a second derivative are important. Therefore, the constant prefactor does not create an electric field. However, the second part generates an electric field of twice the initial frequency ω, the second harmonic frequency. Dependent on the experimental setup, SHG can reach high efficiencies of nearly a full conversion. Sometimes this process is visualized regarding photon creation and annihilation (Figure 4.1a). In one quantum mechanical process, two photons of energy ω get

Figure 4.1: (a) Schema of geometric beam propagation after SHG. (b) Schema of the SHG energy level diagram. The virtual levels are represented by dashed lines (adapted from [91]).

destroyed in exchange for one photon at frequency 2ω. The dashed lines in Figure 4.1b are not energy eigenstates, but instead, virtual levels induced by the electric field. The cause of their existence are several real eigenstates, which are potentially far away from the virtual level. However, for simplicity consider a single real level. Based on the energy

difference δE between the real and the virtual state, Heisenberg's uncertainty principle grants the atom a time $\hbar/\delta E$ to reside in this state. The incoming photon makes use of multiple of these virtual levels without transferring population between two real levels. The final and initial quantum mechanical state of the atom are identical. Such a process is denoted as parametric.

4.0.2 Sum- and Difference-Frequency Generation

In analogy to SHG, the sum frequency generation (SFG) and the difference frequency generation (DFG) is driven by two photons, but of different frequencies ω_1 and ω_2. Therefore, the electromagnetic field is

$$E(t) = E_1 e^{-i\omega_1 t} + E_2 e^{-i\omega_2 t} + c.c.. \tag{4.12}$$

After inserting this field into the second order polarization of Equation (4.2) one obtains [91]

$$P^{(2)}(t) \propto \epsilon_0 \chi^{(2)} \left[E_1^2 e^{-i2\omega_1 t} + E_2^2 e^{-i2\omega_2 t} + 2E_1 E_2 e^{-i(\omega_1+\omega_2)t} + 2E_1 E_2^* e^{-i(\omega_1-\omega_2)t} + c.c. \right], \tag{4.13}$$

neglecting constant terms. The terms with $2\omega_1$ and $2\omega_2$ correspond to SHG, while the two additional terms describe the components of the polarization at the sum $\omega_1 + \omega_2$ and the difference $\omega_1 - \omega_2$. Dependent on the phase matching condition (Section 4.1), one of the four electromagnetic fields dominates the others. The phase matching condition is set by the polarization of the incident beam and the specifics of the nonlinear medium. SFG is particularly useful in generating a tunable, narrow linewidth light source in the ultraviolet (UV). As an example, the SFG of a violet and an infrared (IR) laser diode supplies light at 309 nm for OH spectroscopy [92]. In contrast to sum-frequency generation, difference frequency generation is better suited to produce a tunable laser source in the IR. The energy level diagram is a good approach to clarify this process (Figure 4.2b). One

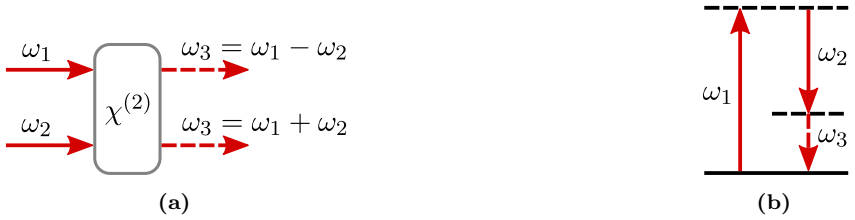

Figure 4.2: (a) Schematic of beam propagation of the difference-frequency generation. (b) Energy level diagram of difference frequency generation, with dashed virtual levels (adapted from [91]).

of the incident photons with frequency $\omega_1 > \omega_2$ is destroyed inside the nonlinear medium. Afterwards, the atom is in the highest virtual state. Simultaneously, two new photons at frequency ω_2 and $\omega_3 = \omega_1 - \omega_2$ get created, stimulated by the incident electromagnetic field at frequency ω_2. Therefore, the input electromagnetic field at lower frequency ω_2

gets amplified. This effect is denoted as optical parametric amplification (OPA). However, what is happening without an electromagnetic field at ω_2?

4.0.3 Optical Parametric Oscillator

The process of spontaneous conversion of a photon into two lower energy photons is denoted as parametric fluorescence [93,94]. On its own, it is a weak process compared to other nonlinear effects, but this changes when it is combined with an optical cavity. Placing the nonlinear medium into a cavity, resonant to a wave at frequency ω_2, traps the fluorescence light. This is the basic setup of the Optical Parametric Oscillator (OPO) (Figure 4.3). A

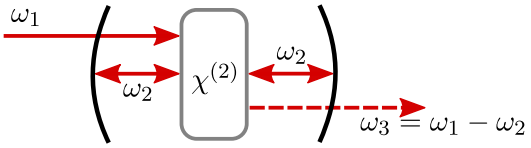

Figure 4.3: Schematic setup of an OPO cavity, which is resonant at a frequency ω_2. The OPO converts the initial pump wave at ω_1 into the low frequency idler wave at ω_3 (adapted from [91]).

detailed description, concerning the cavity design, follows later (Section 4.4). Consider for now solely the conversion process. The electromagnetic field at ω_2 builds up inside the cavity. Simultaneously, the generated field at $\omega_3 = \omega_1 - \omega_2$ increases. The trapped electric field inside the cavity at $\omega_2 < \omega_1$ is selected by the phase matching condition, which is part of a later discussion (Section 4.1).

4.0.4 Third Order Interaction

In this thesis, a third order interaction is a significant process for two different applications. It supplies the generation of the OFC, which is essential to compare lasers at largely different optical frequencies (Section 3.2.2). Additionally, it is the basis for the short term laser stabilization by modulation transfer spectroscopy (MTS) (Section 6.3.3).

The OFC is based on a mode-locked lasers (Section 3.2). The spectrum of such a laser consists of multiple closely spaced modes, separated by ω_{rep}. The third order interaction takes place inside a nonlinear crystal fiber behind the laser. Since it is a third order process, three photons get destroyed in exchange for one new photon. For simplicity, consider two photons at ω_1 and a third at $\omega_2 = \omega_1 + \omega_{\text{rep}}$. The nonlinear medium converts the three incoming photons into a photon at $\omega_3 = 2\omega_1 - \omega_2 = \omega_1 - \omega_{\text{rep}}$. The four involved electrical fields give it also the name four-wave mixing. Subsequently, this process repeats itself with all frequencies inside the spectrum, including the newly generated. Finally, the spectrum behind the crystal fiber consists of many equally spaced modes over a large spectral range, the supercontinuum.

The MTS setup relies on the saturation of a transition line inside a gas cell. The power dependent change of the absorption ensures a nonlinear interaction between the electromagnetic field and the medium. In analogy to the third order interaction inside the OFC crystal fiber, the two forward propagating photons at ω_1 and $\omega_2 < \omega_1$ interact with an additional counter propagating photon at ω_1 (Figure 4.4a). Energy conservation of

Figure 4.4: (a) Schematic of the four wave mixing process in the MTS setup. Three collinear photons get destroyed in favor of a fourth photon at $\omega_3 = \omega_2$. (b) Energy level diagram of the four wave mixing process, with dashed virtual levels (adapted from [91]).

this third order process requires the generation of a fourth photon at frequency $\omega_3 = \omega_2$ (Figure 4.4b). This new photon is also counter propagating towards the initial two photons, which is the basis of an error signal for laser stabilization.

4.1 Phase Matching

The electromagnetic field generated by a nonlinear interaction is described by the wave Equation (4.9). If multiple electromagnetic waves at different frequencies are involved, then a variety of frequency combinations is imaginable for the newly generated field. However, the involved electromagnetic waves at different frequencies have different phase velocities. Additionally, the relative phases of the interacting waves potentially differ based on the point in space. Only if the phase difference between the involved fields adds up to zero, nonlinear conversion takes place. Thus, usually, one frequency is dominating the generated field, which is defined by this phase matching condition. Consider the concrete example of SFG using plane waves. The spatial dependence of each electromagnetic field component is given by

$$E_j(z,t) = E_j e^{i(k_j z - \omega_j t)} + c.c., \tag{4.14}$$

with the wave number $k_j = n_j \omega_j / c$ and propagation along the z direction. The initial waves are denoted with the indices $j = 0, 1$ and the generated wave with $j = 3$. The resulting wave frequency is $\omega_3 = \omega_1 + \omega_2$ (Section 4.0.2), which leads with Equation 4.13 to the nonlinear polarization

$$P_3(z,t) = P^{(2)}(\omega_1 + \omega_2)[e^{i(k_1+k_2)z} + e^{-i(k_1+k_2)z}] = 4\epsilon_0 d_{\text{eff}} E_1 E_2 e^{i[(k_1+k_2)z - \omega_3 t]} + c.c., \tag{4.15}$$

Only the combination of the electric fields $E_1(z,t)$ and $E_2(z,t)$ responsible for SFG is considered. Additionally, the susceptibility $\chi^{(2)}$ has been replaced, for simplicity, with the effective susceptibility $2d_{\text{eff}}$, which assumes a fixed polarization, a fixed propagation and the Kleinman symmetry condition [91,95]. Inserting $E_3(z,t)$ and $P_3(z,t)$ into the wave Equation (4.9) and using the slowly varying amplitude approximation $|\frac{\partial^2 E_3}{\partial z^2}| \ll |k_3 \frac{\partial E_3}{\partial z}|$ leads to the differential equation [91]

$$\frac{\partial E_3}{\partial z} = \frac{2id_{\text{eff}}\omega_3^2}{k_3 c^2} E_1 E_2 e^{i\Delta k z}, \tag{4.16}$$

where $\Delta k = k_1 + k_2 - k_3$ is the wave vector mismatch. This equation describes the spacial change of the generated wave amplitude E_3 as a function of the wave amplitudes E_1 and E_2. In general, these amplitudes also have a spatial variation. However, for now, they are assumed to be constant. The intensity after passing a nonlinear medium is calculated by integration of Equation (4.16) from $z = 0$ to $z = L$, with L denoting the length of the medium. Squaring the expression of the amplitude yields the intensity [91]

$$I_3 \propto \text{sinc}^2\left(\frac{\Delta k L}{2}\right) = \text{sinc}^2\left(\frac{L}{L_{\text{coh}}}\right), \tag{4.17}$$

with the coherent build up length $L_{\text{coh}} = 2/\Delta k$. If the length of the nonlinear medium exceeds L_{coh}, then the phase mismatch between the driving waves and the generated wave becomes significant. After this distance, the generated wave gets converted back into the initial waves. Thus, maintaining the phase matching condition $\Delta k = 0$ is crucial, with

$$\Delta k = \frac{n_1\omega_1}{c} + \frac{n_2\omega_2}{c} - \frac{n_3\omega_3}{c} = 0. \tag{4.18}$$

However, normal dispersion makes it challenging. In this case, the refractive index increases monotonically for waves at a higher frequency, so $n_1 > n_2 > n_3$. The phase matching condition of Equation (4.18) can be written as

$$(n_3 - n_2)\omega_3 = (n_1 - n_2)\omega_1. \tag{4.19}$$

This obviously has no solution, because the left-hand side is negative and the right-hand side is positive. In an isotropic medium, phase matching is only possible for anomalous dispersion, like near an absorption feature. One way around this limitation is to make use of the birefringence displayed by some crystals. The refractive index is now not only dependent on the frequency of the wave, but also on the direction of the polarization. According to Equation (4.19) the refractive index n_1 at highest frequency is supposed to be smaller than n_2. The polarization providing this condition is dependent on the orientation of the crystal.

4.1.1 Angle Tuning

The following discussion is limited to a negative uniaxial crystal, which is characterized by two equivalent optical axes, labeled $\hat{a}$ and $\hat{b}$, and a third optical axis, $\hat{c}$. Light polarized along the $\hat{a}$ and $\hat{b}$ axes has a refractive index given by n_o, and light polarized along the $\hat{c}$ axis has a refractive index given by $n_e < n_o$. The axis $\hat{c}$ defines the orientation of the crystal relative to the propagation vector of the light $\mathbf{k}$. If the propagation $\mathbf{k}$ is along $\hat{c}$, then no birefringence is displayed, and no phase matching is possible. For a non-zero angle theta between $\mathbf{k}$ and $\hat{c}$, the polarization of the light determines the refractive index experienced by it. If the polarization is perpendicular to the plane containing $\mathbf{k}$ and $\hat{c}$, then the beam is denoted as ordinary, with a refractive index n_o. Conversely, a beam with polarization parallel to this plane is extraordinary with the refraction index $n_e(\theta)$, dependent of the angle θ. For a negative uniaxial crystal, the refractive index $n_e(\theta)$ is smaller then n_o. In the case of SHG, with two incoming waves at frequency ω, the generated wave at higher frequency 2ω must experience the refractive index $n_e(\theta)$. This relation is described by [91]

$$\frac{1}{n_e(\theta)^2} = \frac{\sin^2(\theta)}{\bar{n}_e^2} + \frac{\cos^2(\theta)}{n_o^2}. \tag{4.20}$$

The two limits of the refractive index are $n_e(0°) = n_o$ and $n_e(90°) = \bar{n}_e$, with the principal value $\bar{n}_e$. Therefore, the initial waves have ordinary polarizations and the generated wave extraordinary polarization (Figure 4.5). In general, the polarizations of the two waves

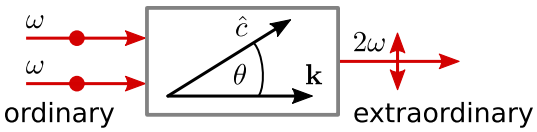

Figure 4.5: Schematic of SHG for an uniaxial crytal, with an angle θ between the propagation vector $\mathbf{k}$ and the optical axis $\hat{c}$ (adapted from [91]).

at lower frequencies define the phase matching type. If both low-frequency waves have the same polarization, it is denoted as type I phase matching [95]. The phase matching condition is in this case

$$n_e(2\omega, \theta) = n_o(\omega), \tag{4.21}$$

with Equation (4.20) leaving at most one solution for θ. For an angle between 0° and 90°, the Poynting vector and the propagation vector are not parallel for waves experiencing the extraordinary refractive index. Thus, the Poynting vectors of the ordinary beam and the extraordinary beam are different. The angle θ controls the phase matching condition and the walk-off between the two beams, which is always non-zero between 0° and 90°. Only a finite range of angles supplies sufficient phase matching at an accepted walk-off angle;

this is the critical phase matching condition. The exception of no walk-off is an angle of $\theta = 90°$, denoting the non-critical phase matching condition. Thus, it is popular to fix the angle at $\theta = 90°$ and tune the temperature instead of the angle for phase matching without the walk-off effect. Practically, this necessitates a strongly temperature dependent birefringence of the crystal, like in lithium niobate.

4.2 Quasi-Phase-Matching

Consider the case of non-critical phase matching (Section 4.1.1), with the optical axis $\hat{c}$ perpendicular to the propagation direction of the wave (Figure 4.6a). Since the sign

Figure 4.6: (a) Schematic of a homegeneous medium with one optical axis $\hat{c}$. (b) Schematic of a periodically poled medium with an alternating optical axis and the period length Λ (adapted from [91]).

of the nonlinear coupling coefficient d_{eff} depends on the orientation of $\hat{c}$, it stays the same for an uniaxial crystal. In general, it is not feasible to achieve the temperature required for non-critical phase matching, which leads to a finite coherent buildup length. The newly generated wave gets converted back before reaching the end of the nonlinear medium. However, the walk-off effect can still be avoided, using a technique known as quais phase matching (QPM). The basis of QPM is a nonlinear material, with an optical axis $\hat{c}$, inverted multiple times along the propagation direction of the wave, with the period length Λ (Figure 4.6b). The change of the $\hat{c}$ orientation flips the sign of d_{eff}, which arrests the back conversion of the nonlinear process. Thus, the sign of the coupling coefficient becomes spatial dependent with a square-wave function and its Fourier representation

$$d(z) = d_{\text{eff}} \operatorname{sign}\left(\cos(2\pi z/\Lambda)\right) = d_{\text{eff}} \sum_{m=-\infty}^{\infty} G_m \exp(ik_m z). \tag{4.22}$$

In order to maximize the coupling coefficient, the Fourier coefficient

$$G_m = \operatorname{sinc}(m\pi/2) \quad \text{with} \quad G_0 = 0, \tag{4.23}$$

needs to be as large as possible. The maximum is obtained at $m = 1$, with the fundamental amplitude $G_1 = (2/\pi)$. Additionally, the periodic structure of the material allows defining a grating vector $k_m = 2\pi m/\Lambda$, which adds to the phase matching condition. The grating vector supplies QPM, where phase matching is not possible solely based on the involved field vectors.

4.2.1 SHG Inside a Periodically-Poled Medium

As an example, consider the case of SHG inside a periodically-poled crystal. The coupled differential equations for SHG can be derives the same manner as Equation (4.16), yielding

$$\frac{dE_1}{dz} = \frac{2id_{\text{eff}}\omega_1^2}{k_1 c^2} \sum_m G_m E_2 E_1^* e^{-i(\Delta k_Q - 2k_m)z}, \tag{4.24}$$

$$\frac{dE_2}{dz} = \frac{id_{\text{eff}}\omega_2^2}{k_2 c^2} \sum_m G_m |E_1|^2 e^{-i\Delta k_Q z}, \tag{4.25}$$

with the quasi wave vector mismatch of the SHG

$$\Delta k_Q = 2k_1 - k_2 + k_m. \tag{4.26}$$

The grating vector k_m has to compensate the wave vector mismatch caused between $2k_1$ and k_2. Since maximum conversion is achieved at $m = 1$, the poling-period is customized to satisfy the condition $\Delta k_Q = 0$, resulting in a period length of $\Lambda = 2\pi/(2k_1 - k_2)$. In the case of SHG inside a periodically-poled lithium niobate (PPLN) crystal with a pump wave at 1064 nm, this results in $\Lambda \approx 7\,\mu\text{m}$. It took around 30 years from the first suggestion of fabricating this structures 1962 [96] to an experimental breakthrough around 1993 [97], by applying an external electrical field. Figure 4.7a shows a solution to Equations (4.24) and (4.25) with the initial conditions $E_1(0) = 1$ and $E_2(0) = 0$. Characteristic for this

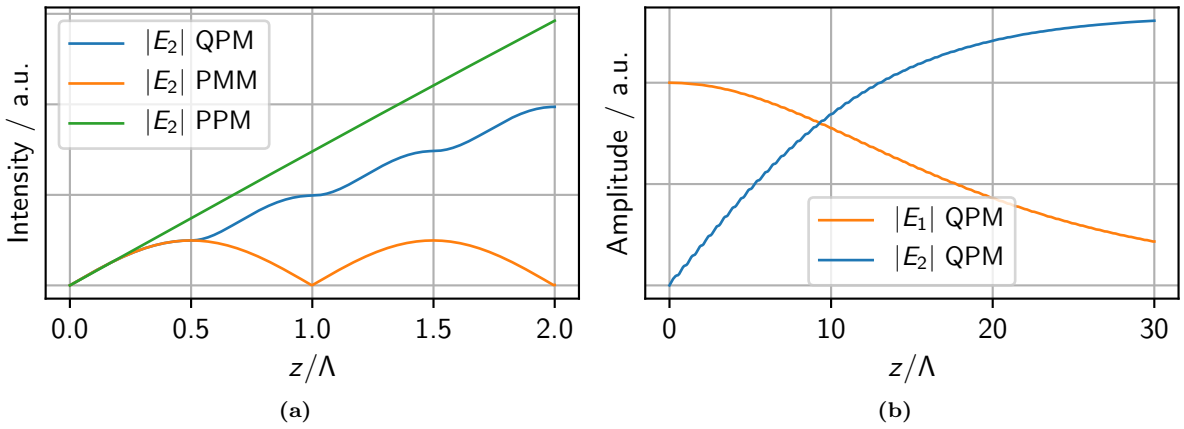

Figure 4.7: (a) Calculated field intensities based on the different phase matching conditions. Perfect phase matching (PPM) results in a linear increase of the intensity with growing propagation distance. Quasi phase matching (QPM) increases monotonic with a periodic structure. Phase mismatching (PMM) results in no gain of the intensity. (b) QPM case for a large number of poling periods shows a nonlinear decrease of the incoming field amplitude $|E_1|$ and an increase of the generated amplitude $|E_2|$.

process is a wavelike gain of the field strength. The period Λ is here twice the coherent buildup length L_{coh}. After the distance L_{coh}, the relative phases of the involved waves have shifted such that the E_2 field would convert back to E_1 if no change were made to the medium, as shown in the phase mismatching (PMM) curve. Because the sign of

the nonlinear coefficient $d(z)$ changes at $z = 0.5\Lambda$, though, the relative phases are now correct for additional conversion of E_1 to E_2. The gain is less than in the perfectly phase matched (PPM) case, where $2k_1 = k_2$ and $k_m = 0$, but the sign change of the nonlinear coefficient ensures a monotonic growth of the amplitude. The periodic structure of the SHG amplitude growth is negligible, considering several more periods (Figure 4.7b). The more interesting effect is the nonlinear rise of the amplitude $|E_2|$, due to a depletion of the incoming field amplitude $|E_1|$. This behavior is the same, independent of QPM in a periodic poled crystal or PPM in a single uniaxial crystal. At the limit $z \to \infty$, the input field amplitude $|E_1|$ gets completely converted into $|E_2|$, following a $\tanh(z)$ function[96].

4.2.2 DFG and Parametric Amplification with QPM

The basis of an OPO is DFG and parametric amplification. Due to the benefits of zero walk-off and high efficiency, the PPLN crystal is one of the most common nonlinear media to generate light in the mid-IR. One of the differential equations for DFG has been derived previously (Section 4.1). The following additional differential equations are derived analog and expanded for a periodic crystal, with

$$\frac{dE_1}{dz} = \frac{2id_{\text{eff}}\omega_1^2}{k_1c^2}\sum_m G_m E_3 E_2^* e^{-i(\Delta k_Q - 2k_m)z}, \tag{4.27}$$

$$\frac{dE_2}{dz} = \frac{2id_{\text{eff}}\omega_2^2}{k_2c^2}\sum_m G_m E_3 E_1^* e^{-i(\Delta k_Q - 2k_m)z}, \tag{4.28}$$

$$\frac{dE_3}{dz} = \frac{2id_{\text{eff}}\omega_3^2}{k_3c^2}\sum_m G_m E_1 E_2^* e^{-i\Delta k_Q z}, \tag{4.29}$$

and the quasi wave vector mismatch of DFG

$$\Delta k_Q = k_3 - k_1 - k_2 + k_m. \tag{4.30}$$

In contrast to SHG, the aim is to generate a field with a lower frequency. For simplicity, consider an undepleted pump wave with the constant amplitude $|E_3|$ at highest frequency $\omega_3 > \omega_2 > \omega_1$. Furthermore, spontaneous down-conversion yields a field amplitude $|E_1| > 0$. The effect of parametric amplification is illustrated by setting the field amplitude $|E_2| = 0$. Solving the differential equations with this boundary conditions shows an exponential growth for both field amplitudes $|E_1|$ and $|E_2|$ (Figure 4.8a). An energy level diagram helps to understand this process (Figure 4.8b). The initial field with frequency ω_3 pumps the highest virtual state. Energy conservation is now possible by two path ways, either through DFG between ω_3 and ω_1 to produce ω_2 or between ω_3 and ω_2 to produce ω_1. Therefore, photons at ω_1 stimulate the generation of photons at ω_2 and vice versa. This process is denoted as parametric amplification. In the case of an OPO, the wave at the frequency ω_1 is trapped inside the cavity, which is denoted as signal. Building up

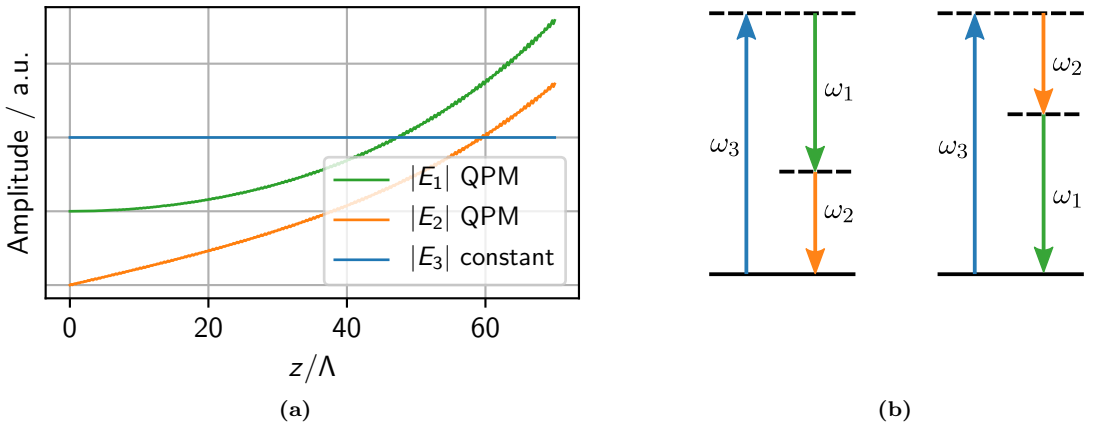

(a) (b)

Figure 4.8: (a) Calculated exponential parametric amplification of both generated field amplitudes. The pump field amplitude $|E_3|$ experiences for the sake of simplicity no depletion. (b) Energy level diagram of DFG, with dashed virtual levels.

the signal wave after several round trips inside the cavity leads to an amplification of the mid-IR at ω_2, which is denoted as idler. It is convenient to couple the idler directly out of the cavity (Section 4.0.3).

4.3 Focused Beams

The previous sections assumed an infinite plane wave interacting with the nonlinear medium. This is a simplification. In reality, all beams have a finite transverse extent. The situation is again described with the wave Equation (4.9). However, this time, the transverse variation of the field $\mathbf{E}(\mathbf{r},t)$ and $\mathbf{P}(\mathbf{r},t)$ are also considered. The paraxial approximation neglects the contribution $\partial^2 E/\partial z^2$, since the wave is propagating along the z-axis, and yields the paraxial wave equation of a freely-propagating wave ($\mathbf{P}=0$)[91]

$$2ik\frac{\partial \mathbf{E}}{\partial z} + \nabla_T^2 \mathbf{E} = 0. \tag{4.31}$$

Furthermore, it is convenient to express the field vector as a scalar $E(r,\phi,z)$, as well the transverse Laplace operator in cylindrical coordinates $\nabla_T^2 = (1/r)(\partial/\partial r)(r\partial/\partial r) + (1/r)^2\partial^2/\partial\phi^2$. A solution for this differential equation is the scalar approximation[98]

$$E(r,z) \propto \frac{w_0}{w(z)} \exp\left(-\frac{r^2}{w^2(z)}\right) \exp\left(-\frac{ikr^2}{2R(z)}\right) \exp\left(-i[kz+\phi(z)]\right), \quad \text{with} \tag{4.32}$$

$$w(z) = w_0\sqrt{1+\left(\frac{z}{z_R}\right)^2} \tag{4.33}$$

A vector solution of Equation 4.31 can be found elsewhere[99]. The scalar solution of the differential equation introduces the minimum waist w_0, the Rayleigh length z_R, the radius of curvature of the wavefront $R(z) = z(1+(z_R/z)^2)$ and the Gouy phase $\phi(z) =$

$-\arctan(z/z_R)$. In general, the waist $w(z)$ is associated with the radius of the beam, at which the field amplitude decays to $1/e$ of its maximum value (Figure 4.9a). The transverse

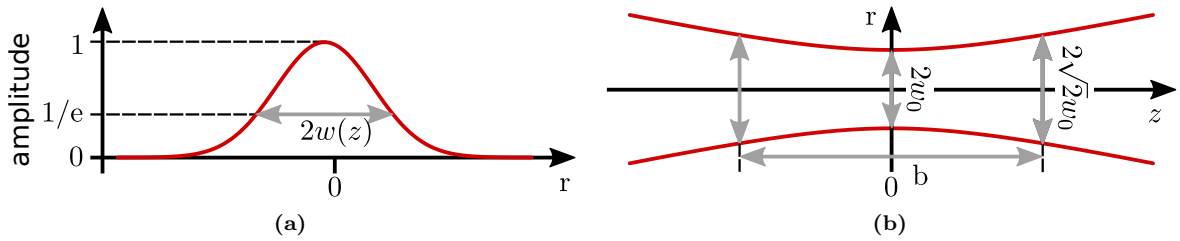

Figure 4.9: (a) Transverse Gaussian field amplitude with the waist $w(z)$. (b) The minimum beam radius of a Gaussian laser beam at $z = 0$ is described by the waist ω_0. The associated longitidunal parameter is the confocal parameter b.

intensity distribution of this wave is everywhere Gaussian. Considering the propagation of the wave along the z-axis, $z = 0$ marks the focal point. The minimum waist w_0 increases by a factor of $\sqrt{2}$ after reaching the Rayleigh length $z_R = \pi w_0^2/\lambda$ (Figure 4.9b). Twice this distance denotes the confocal parameter $b = 2z_R$.

The Gouy phase represents the phase difference between the Gaussian beam and an infinite plane wave[100]. Along the propagation of a Gaussian beam from $z = 0$ to $+\infty$ the phase difference increases to the limit $\phi = -\pi/2 \to \infty$. The wavefront curvature reaches a minimum at this plane wave limit. However, in the limit of $z \to -\infty$, ϕ goes to $+\pi/2$. The phase change of a Gaussian beam passing the focal point can influence the conversion inside a nonlinear medium. The evolution of the Gouy phase through the waist modifies the wavevector slightly. The wavevectors are all parallel for plane waves. Thus, a positive wavevector mismatch reduces the efficiency of the nonlinear process (Figure 4.10a). However, a Gaussian beam contains a spread of nonparallel wavevectors

Figure 4.10: (a) Schematic of the SHG wavevector mismatch $\Delta k > 0$, for plane waves. (b) Schematic of one possible case of SHG wavevector mismatch $\Delta k > 0$, for a Gaussian beam (adapted from [91]).

(Figure 4.10a). This spread allows an efficient nonlinear conversion at positive wavevector mismatch. In contrast, a negative wavevector mismatch reduces the conversion efficiency. Thus, it is convenient, if the evolution of a SHG wave is slower compared to the initial wave. Analytical solutions are only possible for special cases, such as plane waves, which generally means the Gouy phase gets neglected. A more detailed analysis can be done by separating a nonlinear medium into a grid and solving Equation (4.31) at different grid points using the finite element method (FEM). One parameter emerging from theoretical predictions for maximum nonlinear conversion is $\xi = L_c/b$, with the length of the nonlinear medium L_c[101]. Studying this parameter for SHG or DFG is done elsewhere[101,102]. Justifiable

values are typically in the range $1 < \xi < 7$. The Gouy phase shift, pushes the optimum ξ parameter at maximum nonlinear conversion to slightly larger values, compared to simulations not involving the Gouy phase[103,104]. A series of optical elements along the propagation of the Gaussian beam are defining the ξ paramter.

4.3.1 ABCD Matrix Formalism for Gaussian Beams

Focusing a Gaussian beam into a nonlinear medium requires an optical element like a lens or a curved mirror. The most powerful tool calculating the beam properties after passing these optics is the ABCD matrix formalism. It allows theoretical predictions of the ξ parameter inside a nonlinear medium, as well as the determination of stable cavity dimensions. The basis for this formalism is the paraxial ray theory[105]. In this idealized picture, a light ray is described using the slope of its propagation relative to the optical axis, dr/dz, and its transverse offset, $r(z)$. The free space propagation of a ray preserves the slope, but changes the transverse offset to $r_2 = r_1 + L dr/dz$ after a distance L (Figure 4.11a). In contrast, the propagation through a thin lens with focal length f preserves the transverse

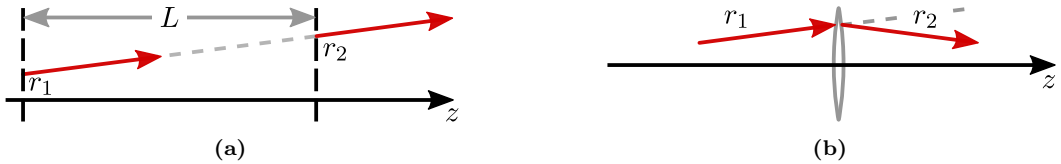

Figure 4.11: (a) Schematic of free ray propagation over a distance L, changing the transverse distance r to the optical axis z. (b) Schematic of refraction of a ray at a lens, changing the slope dr/dz (adapted from[105]).

offset $r_2 = r_1$, but changes the slope to $dr_2/dz = -(1/f)r_1 + dr_1/dz$. The goal is to describe these transformations in matrix form[105]

$$\mathbf{r}_2 = \begin{bmatrix} r_2 \\ r_2' \end{bmatrix} = \begin{bmatrix} A & B \\ C & D \end{bmatrix} \times \begin{bmatrix} r_1 \\ r_1' \end{bmatrix} = M\mathbf{r}_1, \tag{4.34}$$

with the reduced slope $r' \equiv n dr/dz$, containing the local refractive index n at the ray position. This definition leads to the free space propagation matrix F and the thin lens matrix L given by

$$F(L,n) = \begin{bmatrix} 1 & L/n \\ 0 & 1 \end{bmatrix} \quad \text{and} \quad L(f) = \begin{bmatrix} 1 & 0 \\ -\frac{1}{f} & 1 \end{bmatrix}, \text{ respectively.} \tag{4.35}$$

In general, one important property of all ray matrices is $\mathrm{M} = AD - BC = 1$. The thin lens matrix L is an approximation. A product of multiple matrices supplies a more-accurate description. For example, a biconvex lens requires an incidence matrix at a curved interface I_c and free space propagation F inside the medium until the next curved interface I_c. The resulting matrix is $M = I_c \cdot F \cdot I_c$, with the curved interface matrix I_c listed in Table 4.1. A flat interface is described at the limit $R \to \infty$. The incidence angle is denoted as θ. The

Table 4.1: Ray matrices for curved interfaces with respect to incidence angle. If the ray stays in the plane of incidence, it is denoted as tangential. If it is perpendicular to the plane of incidence, it is called sagittal [105].

	tangential	sagittal
Curved Mirror M_c	$\begin{bmatrix} 1 & 0 \\ \frac{2}{R}(\cos\theta)^{-1} & 1 \end{bmatrix}$	$\begin{bmatrix} 1 & 0 \\ \frac{2}{R}\cos\theta & 1 \end{bmatrix}$
Curved Interface I_c	$\begin{bmatrix} \frac{\cos\theta_2}{\cos\theta_1} & 0 \\ \frac{n_2\cos\theta_2 - n_1\cos\theta_1}{R\cos\theta_1\cos\theta_2} & \frac{\cos\theta_1}{\cos\theta_2} \end{bmatrix}$	$\begin{bmatrix} 1 & 0 \\ \frac{n_2\cos\theta_2 - n_1\cos\theta_1}{R} & 1 \end{bmatrix}$

angles θ_1 and θ_2 between two media with the refraction indices n_1 and n_2 are described by Snell's law. Thus, complicated optical systems including multiple lenses and mirrors are easily modeled using the mentioned matrices. After evaluating the product, one obtains a single ABCD matrix. The ABCD matrix formalism can also be used to describe the effect of an optical system on a Gaussian beam with [105]

$$\frac{n_f}{q_f} = \frac{A\frac{q_i}{n_i} + B}{C\frac{q_i}{n_i} + D}, \quad \text{with} \quad \frac{1}{q} = \frac{1}{R} - i\frac{\lambda_0}{\pi n \omega^2}. \tag{4.36}$$

The parameters q_i and q_f describe the properties of the Gaussian beam before and after passing the optical system, respectively. The parameter q_i can be estimated by measuring the Gaussian waist at different positions along the optical axis. Frequently, the optical system is designed to produce a specific q_f parameter, corresponding to a specific ξ parameter inside a nonlinear crystal. This adjustment is necessary to get maximum conversion efficiency. A particular case is the design of an OPO cavity. The lasing mode inside the cavity is defined by the cavity dimension independent of the pump beam.

4.4 Optical Parametric Oscillator

Spontaneous down conversion inside an OPO cavity is an extremely weak process on its own, which requires a resonant cavity for parametric amplification (Section 4.2.2). In general, the trapped signal wave inside the cavity drives the nonlinear conversion. The highest frequency wave serves as a pump and passes the nonlinear medium only a single time. However, both beams are focused inside at the center of the nonlinear medium. The resulting ξ-parameter of the pump and the signal wave control the efficiency of the nonlinear conversion (Section 4.3) In detail, maximum conversion is achieved for a slightly smaller ξ_p parameter relative to the ξ_s parameter [102]. Thus, shaping the laser beam with optics based on predictions of the ABCD matrix formalism is crucial.

4.4.1 Bow Tie Resonator

One strength of this ABCD matrix formalism is the analysis of periodic focusing systems, for example, a set of optics that direct a beam along a closed path [105]. This system can be as simple as the two curved mirrors of an optical resonator. The periodic system of an optical cavity is characterized by the eigenvalues of the ABCD matrix describing one round trip. These are particularly helpful in analyzing the stability of the resonator. When building an OPO, one must choose an appropriate cavity design. The preferred design for maximum stability is a ring resonator in bow-tie configuration, which works without an optical diode. In a ring resonator, the signal beam passes the nonlinear medium only once by one round trip, while in a linear cavity, the beam passes the nonlinear medium twice, which might cause potential thermally induced instabilities (Section 4.4.2).

The cavity design consists of two curved and two flat mirrors (Figure4.12). The gen-

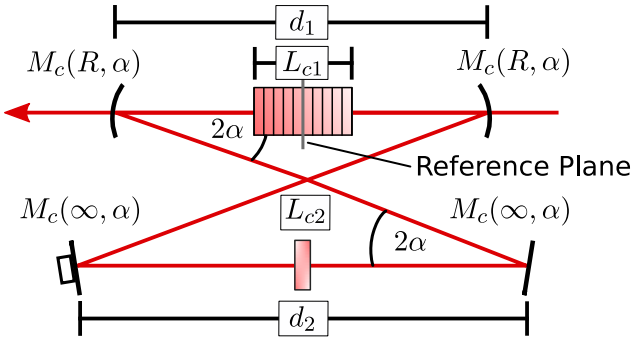

Figure 4.12: (a) Schematic bow tie rig cavity design, with a periodic poled nonlinear medium of length L_{c1} and an etalon of thickness L_{c2}. The plane of reference is placed in the center of the nonlinear medium.

erated signal wave propagates collinear with the pump wave, except it stays inside the cavity. One round trip is completed after the reflection at the first curved, the first flat, the second flat and the second curved mirror. The two curved mirrors focus the signal wave at two points inside the cavity, at $d_1/2$ and $d_2/2$. The cavity angle α defines the incidence angle of the signal wave at the mirrors. It is large enough to let the laser beam pass the nonlinear crystal but as shallow as possible to keep astigmatism small. Between the two curved mirrors, at $d_1/2$, is the nonlinear medium resting, for instance a PPLN with refraction index n_{c1}. An etalon with the refractive index n_{c2} is placed at $d_2/2$, for additional frequency selectivity of the OPO (Section 4.4.3).

The resonator matrix describes the propagation of a light ray, starting at a reference plane and ending after one round trip on the same plane. The reference plane is placed

in the center of the nonlinear medium by the matrix

$$M = F(\tfrac{L_{c1}}{2}, n_{c1}) \cdot F(\tfrac{d_1-d_2}{2}, 1) \cdot M_c(R) \cdot F(d_3, 1) \cdot M_c(\infty) \cdot F(\tfrac{d_2-L_{c2}}{2}, 1) \cdot \tag{4.37}$$

$$F(L_{c2}, n_{c2}) \cdot F(\tfrac{d_1-d_2}{2}, 1) \cdot M_c(\infty) \cdot F(d_3, 1) \cdot M_c(R) \cdot F(\tfrac{d_1-L_{c1}}{2}, 1) \cdot F(\tfrac{L_{c1}}{2}, n_{c1}), \tag{4.38}$$

with the path way $d_3 = (d_1 + d_2)/(2\cos(2\alpha))$ between the curved and the flat mirror. The beam is characterized only at the reference plane. For analyzing the stability, the location of the reference plane is unimportant. However, for later consideration, it is convenient to know the beam waist at this position. The eingenvalues of a general ABCD matrix are[105]

$$\lambda_\pm = m \pm \sqrt{m^2 - 1}, \quad \text{with} \quad m = \frac{A + D}{2}. \tag{4.39}$$

Assuming $-1 \leq m \leq 1$ leads to the complex eigenvalues $\lambda_\pm = \cos\theta \pm i \sin\theta = e^{\pm i\theta}$ of magnitude one, with $m \equiv \cos\theta$. If a ray vector inside the cavity is expressed as a linear combination of eigenvectors, for example, $\mathbf{r}_0 = c_+\mathbf{r}_+ + c_-\mathbf{r}_-$, the resulting ray vector after n round trips can be computed using[105]

$$\mathbf{r}_n = M^n\mathbf{r}_0 = M^n(c_+\mathbf{r}_+ + c_-\mathbf{r}_-) = c_+\lambda_+^n\mathbf{r}_+ + c_-\lambda_-^n\mathbf{r}_-. \tag{4.40}$$

Inserting the eigenvalues λ_+ and λ_- leads to $\mathbf{r}_n = c_+\mathbf{r}_+e^{i\theta} + c_-\mathbf{r}_-e^{-i\theta}$. Therefore, the ray oscillates about the optical axis. It does not pass the same transversal point in the reference plane after each round trip, but it stays confined. Thus, a cavity with $|m| < 1$ is stable. A Gaussian beam is a cluster of multiple light rays. The dimensions of the cavity determine the values of the Gaussian beam parameter q that are unchanged after one round trip through the cavity. In general, the initial Gaussian beam at the reference plane with q_i is described after one round trip by q_f on the same plane (Equation 4.36). If the beam is self-consistent, then it returns after one round trip to its initial value $q_f = q_i$. The two stable Gaussian modes in a resonator are determined from the eigenvectors of the resonator matrix[105]

$$\frac{n}{q_\pm} = \frac{D - A}{2B} \pm \frac{1}{B}\sqrt{m^2 - 1} = \frac{D - A}{2B} \pm \frac{i}{B}\sqrt{1 - m^2} = \frac{n}{R} - i\frac{\lambda_0}{\pi n w^2}. \tag{4.41}$$

One of these solutions represents a confined Gaussian beam, in case of a stable resonator, which means the waist w of the Gaussian beam has a real and positive value. In contrast, the other eigenvalue represents a nonphysical solution. Thus, the two Gaussian beam parameters of the real and geometrically stable resonator ($|m| < 1$) are[105]

$$R = \frac{2Bn}{D - A} \quad \text{and} \quad w^2 = \frac{|B|\lambda_0}{\pi}\sqrt{\frac{1}{1 - m^2}}. \tag{4.42}$$

As an example, consider a cavity angle of $\alpha = 9°$, a radius of curvature for the two focusing mirrors of $R = 100\,\text{mm}$, an yttrium aluminum garnet (YAG) etalon thickness of 3 mm and a PPLN of 50 mm length. The beam profile is only for a distinct combination of d_1 and d_2 circular at the center of the nonlinear medium (Figure 4.13a). Thus, setting

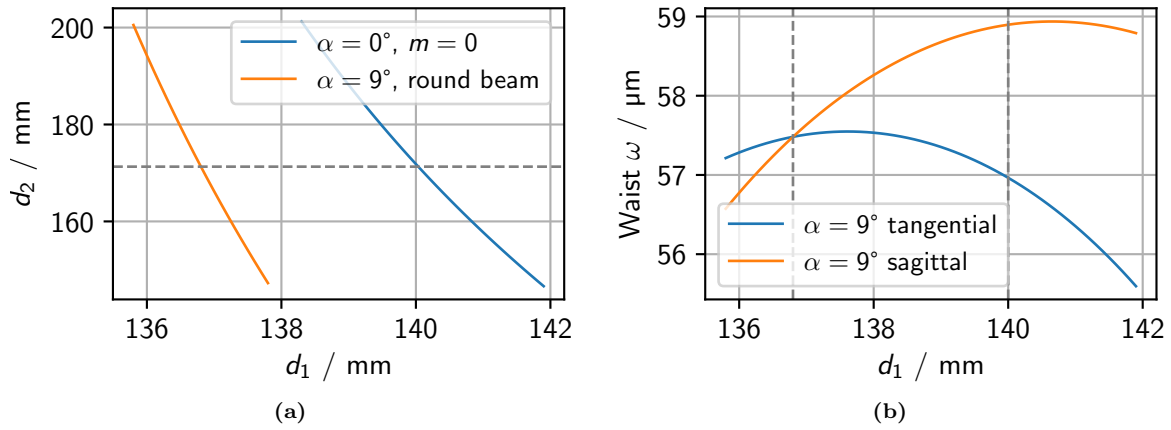

Figure 4.13: (a) Calculated example of possible bow tie cavity dimensions, for a radius of mirror curvature of $R = 100\,\text{mm}$ and an etalon thickness of $L_{c2} = 3\,\text{mm}$ (Equation (4.37)). The criterion is maximum stability $m = 0$ or a round beam profile at the center of the nonlinear medium. (b) Calculated tangential and sagittal beam waists for a fixed cavity parameter $d_2 = 171.3\,\text{mm}$.

the dimension $d_2 = 171.3\,\text{mm}$ allows only one value $d_1 = 136.8\,\text{mm}$. The beam waist is, in this case, $w = 57.5\,\mu\text{m}$. For any other value, the beam is elliptical. The tangential and sagittal waist inside the reference plane is calculated separately (Figure 4.13b). The stability parameter for this cavity dimension is $m_s = -0.1$ and $m_t = -0.3$ for the sagittal and the tangential component, respectively. This is inside the allowed range of a stable cavity of $|m| < 1$, but apparently with a tendency to negative m values. It is convenient, for comparison, to take also a look at a cavity design closest to $m = 0$. Astigmatism prevents $m = 0$ on both beam axis, thus further calculation considering an ideal cavity with no astigmatism where $\alpha = 0°$ (Figure 4.13a). Keeping the dimension $d_2 = 171.3\,\text{mm}$ fixed leads to a cavity parameter $d_1 = 140\,\text{mm}$. The resulting stability parameters are now $m_s = 0.17$ and $m_t = -0.08$ for $\alpha = 9°$. The beam is no longer circular at the cavity design point, but the astigmatism increases only to $(w_{\text{sag}} - w_{\text{tan}})/w_{\text{sag}} \approx 4\%$. The maximum level of astigmatism is reached between the two flat mirrors with $(w_{\text{sag}} - w_{\text{tan}})/w_{\text{sag}} \approx 12\%$. Small astigmatism also justifies the cavity design based on $\alpha = 0°$, which is the design choice for the OPO in this thesis.

4.4.2 Thermal Effects

The previous consideration of the OPO stability left out absorption inside the nonlinear medium. This effect causes a rise in temperature along the propagation axis of the Gaussian laser beam. Regions of the crystal exposed to a higher field intensity have a higher temperature than those exposed to a lower intensity. This temperature gradient

leads to a radially changing index of refraction. Instead of a free propagation inside the nonlinear medium, the beam gets focused by the thermal lens. The ABCD matrix associated with this duct is[105]

$$D(\gamma, z, n) = \begin{bmatrix} \cos(\gamma z) & (n_0\gamma)^{-1} \\ -(n_0\gamma)\sin(\gamma z) & \cos(\gamma z) \end{bmatrix} \quad \text{with} \quad \begin{matrix} n(r) = n_0 - \frac{1}{2}n_2 r^2, \\ \gamma = \sqrt{n_2/n_0}. \end{matrix} \tag{4.43}$$

The ray propagating along the z axis experiences the refraction index n_0, while a ray at an off-axis transverse position r experiences a different index of refraction, which depends on the second derivative $n_0'' = n_2$. In general, it is challenging to determine the axial temperature dependence of this matrix. Thus, some authors[106] prefer instead to use a thin lens matrix (Equation (4.35)) in the middle of the crystal with the focal length[106,107]

$$f_T = \frac{\pi K_c}{\alpha P_c (dn_s/dT)} \frac{w^2}{L_c}. \tag{4.44}$$

Crystal heating measurements give an estimation for the absorption coefficient $\alpha \approx 0.08\,\%$ of a PPLN crystal at $\lambda_s = 1611\,\text{nm}$[106,108]. The thermal conductivity of a MgO-doped (5 mol%) lithium niobate crystal is $K_c = 4.02\,\text{W/mK}$[106] and the temperature dependence of the crystal refractive index is $dn_s/dT = 5 \cdot 10^{-6}/\text{K}$[109]. Assuming a signal power of $P_c = 50\,\text{W}$ and a crystal length of $L_c = 50\,\text{mm}$ results in a focal length about $f_T \approx 4\,\text{mm}$. In the case of linear cavities, this might cause bi-stability[106]. A precaution against the thermal lens is a tightly focused beam ($\xi \approx 2$) for higher pump depletion[106]. This method is counter-intuitive since a large waist decreases the power density and increases the focal length of the lens (Equation (4.44)). Additionally, the dimension d_1 might be chosen slightly larger relative to the cold cavity stability center, to consider the thermal lens in advance[110]. However, a thermal lens is of less importance for ring cavities, due to a lower temperature increase. This statement is valid as long as the absorption of the idler beam is negligibly small. Consider a MgO-doped (5 mol%) PPLN for spectroscopy in the mid infrared between 2.5 µm and 4 µm, with a discrete set of poling periods of different length Λ_n. A typical set of seven poling periods for a mid-IR OPO goes, for example, from $\Lambda_1 = 31.5\,\mu\text{m}$ to $\Lambda_7 = 28.5\,\mu\text{m}$ in steps of 0.5 µm (Figure 4.14a). Estimating the phase matching condition for planes waves with Equation (4.30) yields

$$\frac{1}{\Lambda_n} = \frac{n(\lambda_p, T)}{\lambda_p} - \frac{n(\lambda_s, T)}{\lambda_s} - \frac{n(\lambda_i, T)}{\lambda_i}, \tag{4.45}$$

where $n(\lambda, T)$ is the wavelength and temperature dependent refraction index of a MgO-doped (5 mol%) PPLN crystal[111]. The pump wavelengths $\lambda_p = 1064\,\text{nm}$ leads to a signal wavelength of $\lambda_s = (1/\lambda_p - 1/\lambda_I)^{-1}$. For producing the 2.7 µm to 2.9 µm light needed to excite the fundamental vibrational transitions of OH, only the two longest poling periods with $\Lambda_1 = 31.5\,\mu\text{m}$ and $\Lambda_2 = 31.0\,\mu\text{m}$ satisfy the phase matching condition at reasonable

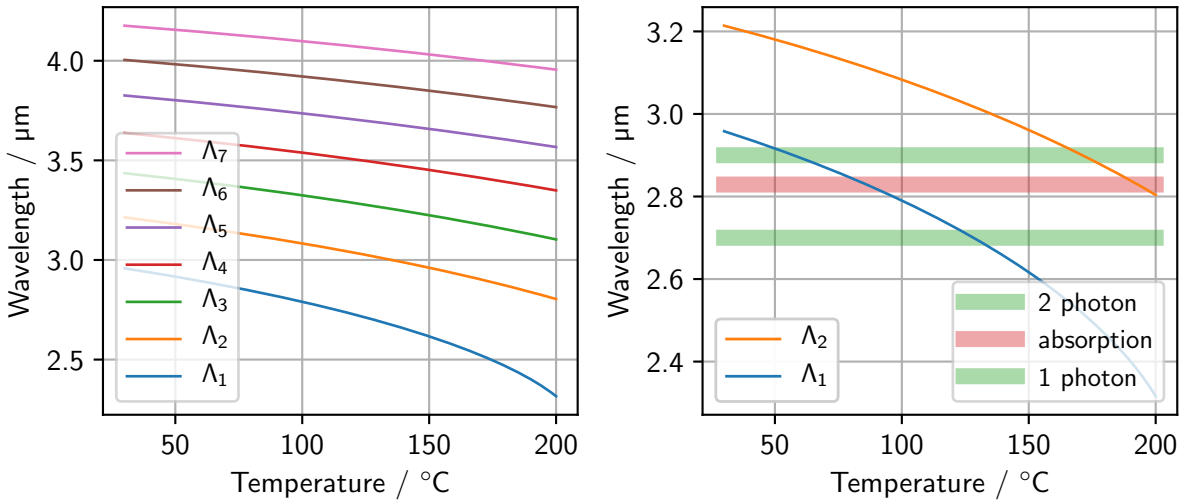

Figure 4.14: (a) Theoretical temperature dependence of the phase matching condition of a MgO-doped (5 mol%) PPLN crystal[111]. The congruent poling periods are $\Lambda_n = 32\,\mu\text{m} - n \cdot 0.5\,\mu\text{m}$ with $n \in [1, 2, \cdot\cdot, 7]$. (b) Only two poling periods are suited for nonlinear conversion to target wavelengths around 2.7 µm and 2.9 µm driving a 1 photon and 2 photon transition in the OH, respectively. In the vicinity of the target wavelengths, there is also an absorption feature in the crystal around 2.829 µm[106].

temperatures (Figure 4.14b). Concerning the idler absorption inside the PPLN crystal, two wavelength regions are worth mentioning, the phonon absorption above 4 µm and an absorption peak around 2.829 µm[106]. At the peak of the absorption feature, a 5 cm long crystal absorbs more than 80 %[106]. Without the MgO-doping of the crystal the absorption peak would overlap with the wavelength needed for two-photon vibrational spectroscopy on OH[112] (Figure 4.14b). Fortunately, the MgO-doping shifts the absorption line in between the two wavelengths of interest for OH spectroscopy.

4.4.2.1 Spectral Instabilities

The temperature distribution inside the crystal plays an important role in selecting the phase matching bandwidth. Additionally, a temperature rise caused by absorption leads to spectral instabilities. Above a critical pump level, the OPO signal line width might experience a broadening[113]. Increasing the pump power further, the OPO starts to emit multiple modes over a frequency range larger than the bandwidth of the gain profile. One reason is spontaneous Raman scattering, caused by phonons inside the crystal[114,115]. At high powers, this leads to a stimulated Raman scattering of the signal wave, adding satellite peaks to the spectrum[113]. The frequency shift of Raman lines relative to the signal frequency is constant and independent of the poling period. However, some modes change monotonically with the poling period of the PPLN crystal. These modes are associated with cascade optical parametric oscillations[116]. The ideal OPO operation describes the conversion of a pump wave λ_p into an idler $\lambda_i^{(1)}$ and a signal wave $\lambda_s^{(1)}$ (Section 4.0.3). The wave vectors of the pump and the idler wave are both in the forward

direction (Figure 4.15a). At high powers, however, the signal acts as pump wave itself,

Figure 4.15: (a) Schema of the quasi wave vector mismatch for the ideal OPO operation. (b) Conversion to an additional wave with $\mathbf{k}_s^{(2)}$ caused by backward oscillation of an idler wave with $\mathbf{k}_i^{(2)}$ (adapted from [116]).

which is converted into a second signal wave with $\lambda_s^{(2)}$ (Figure 4.15b). The frequency difference between the initial and the additional signal waves depends on the phase matching condition. In contrast to the previous wave vector orientations, the idler can also propagate in the direction opposite to the signal and pump, denoted as a parametric backward oscillation (Figure 4.15b). As an example, for $\lambda_s^{(1)} = 1.7\,\mu\text{m}$ and a period length of $\Lambda_2 = 31\,\mu\text{m}$, the secondary wavelengths of signal and idler are around $\lambda_s^{(2)} = 2.8\,\mu\text{m}$ and $\lambda_i^{(2)} = 4.3\,\mu\text{m}$. Those wavelengths are in general unwanted. A simple solution to this issue along with the Raman scattering is the reduction of the intra-cavity signal power. It is convenient to couple the signal power out with one partly transmissive mirror. Optimum OPO operation of a bow tie cavity has been observed at a signal wave output of around 3 % [108]. The suggested signal output of a linear cavity is 4 % or larger, to ensure reliable single mode operation [106]. The limit of the circulating power inside the cavity additionally increases the idler power, as well enhances the beam quality factor M^2, corresponding to an ideal Gaussian beam [108].

4.4.3 Frequency Selection

Consider the OPO cavity is stable at single-mode emission. Now it is convenient for spectroscopic measurements, to tune the lasing frequency. A coarse way to change the emission frequency is increasing or lowering the temperature of the PPLN crystal. One approximation of the phase matching gain profile is

$$I = \text{sinc}^2\left(\frac{2\pi L_c}{\Lambda(\lambda_p, \lambda_s, T)} - \frac{2\pi L_c}{\Lambda_2}\right). \tag{4.46}$$

The following calculations assume the bow tie cavity design of Section 4.4.1, a PPLN crystal of length $L_c = 5\,\text{cm}$ and a period length $\Lambda_2 = 31\,\mu\text{m}$. The temperature and wavelength dependent period length $\Lambda(\lambda_p, T)$ is calculated with Equation (4.45). Thus, the resulting phase matching gain profile has a full width at half maximum (FWHM) around 100 GHz (Figure 4.16a). A stable single-mode OPO lases at the cavity mode closest

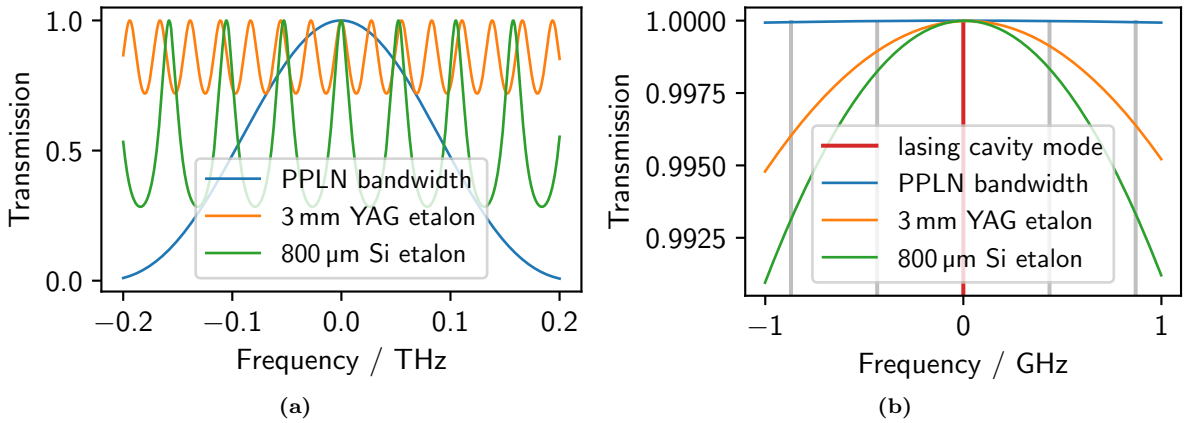

Figure 4.16: (a) Schema of the frequency selectivity inside an OPO cavity. The phase matching profile of the PPLN crystal allows a coarse tuning of the lasing wavelength. (b) A more precise frequency selectivity is supplied by a thin etalon. The material and the thickness of the etalon determines the final gain profile.

to the highest gain. The cavity modes are separated by the free spectral range

$$\mathrm{FSR} = \frac{c}{n d_{\mathrm{total}}} = 428.46\,\mathrm{MHz}, \tag{4.47}$$

with the refraction index in air $n \approx 1$ and the total optical round trip path length $d_{\mathrm{total}} = 699.7\,\mathrm{mm}$.

The phase matching condition of the PPLN supplies nearly no frequency selectivity (Figure 4.16b). Without frequency selective elements inside the cavity, the lasing mode is defined by parasitic etalon effects or absorption features caused by impurities of the nonlinear medium. These spurious frequency selective losses modify the gain profile and create local maxima and minima[106]. The lasing mode can stay at the absorption related maximum of the gain medium and resist temperature fluctuations of the PPLN crystal of as much as 100 mK[106]. Thus, thermal-locking cancels noise fluctuations induced by temperature changes, but also prevents tuning of the OPO signal frequency. However, frequency tuning can be achieved by adding an etalon into the OPO cavity[117]. The low etalon thickness d allows a significant spacing between the transmitted interference fringes. The second important parameter of a Fabry-Perot interferometer like the etalon or OPO cavity is the coefficient of finesse $F = 4R/(1-R)^2$, which is a measure of the spectral width of the modes inside the interferometer and increases with the reflectivity R. A higher reflectivity of the cavity mirrors leads to a narrower mode profile. The reflectivity at the etalon surfaces is dependent on the refraction index n of the material and the polarization state of the light wave. In the case of p-polarized light, the reflection coefficient is given by the Fresnel equation

$$R_p = \left| \frac{\cos\theta_o - n\cos\theta_i}{\cos\theta_o + n\cos\theta_i} \right|^2 . \tag{4.48}$$

Snell's law $\sin\theta_o = n\sin\theta_i$ describes the relation between the angle outside the medium θ_o and the angle inside the medium θ_i. Since the reflectivity of the etalon surfaces is much lower than the reflectivity of the cavity mirrors, the finesse of the etalon is several orders of magnitude smaller than that of the cavity. It is convenient to calculate the transmission profile of an etalon to illustrate the influence of different etalon materials and thicknesses. The transmission of an etalon is described in approximation by the Airy function [118]

$$I = \frac{1}{1 + F\sin^2(\phi/2)} \quad \text{with} \quad \phi = \frac{4\pi}{\lambda} nd\cos(\theta_i). \tag{4.49}$$

However, to study the etalon in more detail, it is necessary to calculate the transmission for a Gaussian electromagnetic field (Equation (4.32)). First, the incident beam gets refracted at the etalon surface. The propagation direction inside the etalon changes according to Snell's law. Some fraction of the beam experiences a back and forth reflection inside the etalon, which introduces the walk-off $X = 2d\sin(\theta_t)$ relative to the initial beam. The magnitude of the walk-off depends critically on the etalon thickness d and the internal reflection angle θ_i of the etalon. Multiple $m \in \mathbb{N}$ of this steps lead to the total transmitted electric field [118]

$$E_t(x, y, z) = \sum_{m=0}^{\infty} (1 - R)R^m E_m(x_m, y, z_m), \tag{4.50}$$

with $x_m = x - mX$ and $z_m = z + 2md\cos(\theta_i)$. As an example, the transmissions curves have been calculated for a 800 µm thick silicon etalon and a 3 mm thick YAG etalon at a zero incidence angle (Figure 4.16a). The higher refractive index $n_{\mathrm{Si}} \approx 3.4$ [119] of silicon relative to the refractive index $n_{\mathrm{YAG}} \approx 1.8$ [120] of YAG leads to a higher finesse of the silicon etalon. Thus, transmission fringes are more pronounced (Figure 4.16a). However, the smaller $\mathrm{FSR}_{\mathrm{YAG}} = c/(2nd) = 27\,\mathrm{GHz}$ of the YAG etalon relative to the silicon etalon $\mathrm{FSR}_{\mathrm{Si}} \approx 54\,\mathrm{GHz}$ partly compensates for it. The resulting mode selection inside the cavity improves with both etalons (Figure 4.16b). The silicon etalon is here superior to the YAG etalon.

Assuming the lasing mode is successfully selected with the etalon, the next step is to find a way to tune the frequency of the etalon's transmission maximum. One possibility is tiling the etalon, which changes the optical pathway inside. For example, the calculated frequency tuning of the YAG etalon is around $8\,\mathrm{GHz/degree^2}$, and the frequency tuning of the silicon etalon is around $2.2\,\mathrm{GHz/degree^2}$. Therefore, the silicon etalon is slightly better suited for angle tuning. However, with increasing incidence angle the transmission of the etalon decreases. The beam walk-off inside the etalon causes the lower transmission. It becomes critical for thick etalons and small beam waists. A one percent reflection level is reached at an incidence angle of 2.4° for the YAG etalon, while the thinner silicon etalon reaches the same reflectivity at 6.8°. Considering a power of around 100 W is circulating

inside the cavity, a one percent reflection at the etalon would result in an additional Watt of power being coupled out of the cavity. Additionally, the etalon tilt distorts the beam profile and slightly changes the alignment of the cavity. Thus, it is convenient to avoid potential large reflections and alignment issues by changing the etalon temperature instead of the tilt angle. This calculation requires consideration of the temperature dependent change of thickness give by the refraction index dn/dT of YAG[121] and silicon[119], respectively. Equally important is the change of the thermal expansion coefficient $\alpha(T)$ for YAG[121] and silicon[122], respectively. The approximate temperature tuning coefficient for the YAG etalon is around 2 GHz/K and for the silicon etalon around 9.4 GHz/K. The frequency selectivity of the OPO, in this thesis, relies on the 3 mm thick YAG etalon (Section 9.5).

Chapter 5

Frequency Stability and Stabilization

The frequency stability of the laser system relies on the neodymium-doped yttrium aluminum garnet (Nd:YAG) reference laser (Chapter 3) and the various other frequency references used to stabilize it further. In this chapter, I will first define stability and then introduce the various frequency standards required for stabilizing and monitoring of the laser frequency. Transferring the stability from a frequency standard onto the Nd:YAG laser depends on the bandwidth of the used feedback loop. Although this bandwidth limitation is no issue for the inherent stable reference laser, it is important for a further stability transfer onto the optical frequency comb (OFC). Two techniques of measuring the feedback bandwidth are presented at the end of this chapter.

5.1 Definition of Stability

Almost any oscillator suffers an irregular variation of the amplitude or frequency. Understanding the origin of potential noise sources is a cornerstone of building a high-resolution measurement system. In general, the output signal of a modulated real oscillator is expressed as[123]

$$U(t) = U_0(t)\cos\varphi(t) = [U_0 + \Delta U_0(t)]\cos\left(2\pi\nu_0 t + \phi(t)\right), \tag{5.1}$$

with the nominal amplitude U_0 and its small perturbation $\Delta U_0(t)$. For simplicity, the perturbation of the amplitude $\Delta U_0(t)$ is assumed to be zero. The derivative of the phase $\varphi(t)$ determines the instantaneous frequency[123]

$$\nu(t) = \frac{1}{2\pi}\frac{d\varphi(t)}{dt} = \frac{1}{2\pi}\frac{1}{dt}\left[2\pi\nu_0 t + \phi(t)\right] = \nu_0 + \frac{1}{2\pi}\frac{d\phi(t)}{dt} = \nu_0 + \Delta\nu(t). \tag{5.2}$$

Thus, the instantaneous frequency deviation from the ideal oscillator at frequency ν_0 is $\Delta\nu(t)$. It is convenient to replace the small value of $\Delta\nu(t)$ with the instantaneous fractional

frequency deviation

$$y(t) = \frac{\nu(t) - \nu_0}{\nu_0} = \frac{\Delta\nu(t)}{\nu_0}. \tag{5.3}$$

A perfect, instantaneous measurement of $y(t)$ is generally not possible. A frequency counter, for example, must measure multiple periods of the waveform, resulting in a sample time τ. Therefore, the fractional frequency deviation becomes a discrete series of consecutive measurements

$$y_i(t) = \frac{1}{\tau}\int_{t_i}^{t_i+\tau} y(t)dt. \tag{5.4}$$

The individual measurements differ from each other and are, for simplicity, uncorrelated. The mean value is

$$\bar{y} = \frac{1}{n}\sum_{i=1}^{N} y_i \tag{5.5}$$

and the N-sample variance is given by[124]

$$\sigma^2(N,\tau) = \frac{1}{N-1}\sum_{i=1}^{N}\left(y_i - \frac{1}{N}\sum_{j=1}^{N} y_j\right)^2 \tag{5.6}$$

with the ensemble size N of consecutive measurements y_i, corresponding to an measurement time τ of each sample. The dead time between individual measurements y_i is zero.

However, if the measurement time τ is shorter than the correlation time between two consecutive measurements y_i, the calculation of the mean value and the variance leads to difficulties. Concerning the description of a frequency standard, consecutive measurements are potentially correlated due to a frequency drift, which increases the variance with the sample size. In contrast, the correlation of two consecutive measurements reduces the variances for short data sets. Thus, the sample size N is crucial in describing the stability of the system.

5.1.1 Allan Variance

An important statistic in frequency analysis is the two sample variance, with $N = 2$ (Equation 5.6), proposed by Dave Allan[125]

$$\sigma_y^2(\tau) = \left\langle \sum_{i=1}^{2}\left(y_i - \frac{1}{2}\sum_{j=1}^{2} y_j\right)^2 \right\rangle = \frac{1}{2}\left\langle (y_{k+1} - y_k)^2 \right\rangle, \tag{5.7}$$

It is based on the analysis of two averaged adjacent frequency samples y_{k+1}, y_k of length τ. Thus, to define the variance for τ the total measurement time must be at least 2τ.

It is convenient, for analysis purposes, to rewrite the Allan variance (AVAR) as[126]

$$\sigma_y^2(\tau) = \left\langle \left(\int_{-\infty}^{\infty} y(t') w_A(t - t') dt' \right)^2 \right\rangle \quad \text{with} \quad w_A(t) = \begin{cases} -\frac{1}{\sqrt{2\tau}} & 0 < t < \tau \\ \frac{1}{\sqrt{2\tau}} & \tau < t < 2\tau \\ 0 & \text{elsewhere} \end{cases}. \tag{5.8}$$

The weighting function $w_A(t)$ is a rectangle function acting as a filter on the frequency fluctuation $y(t)$ (Figure 5.1a). The operation of the filter on the signal becomes more

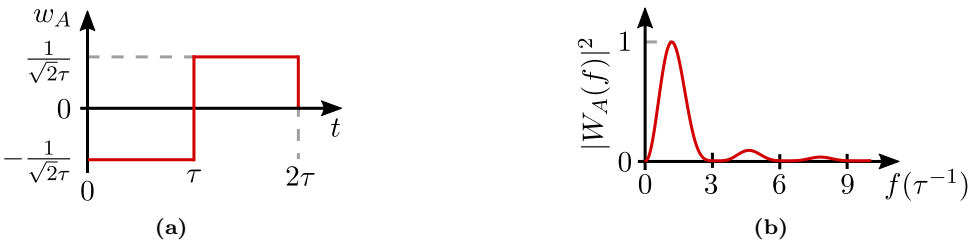

Figure 5.1: (a) Illustration of the rectangle filter function $w_A(t)$ of the AVAR. (b) The calculated squared absolute value $|W_A(f)|^2$ of the associated Fourier transform of $w_A(t)$ in units τ^{-1} (adapted from[123]).

evident by changing into the frequency domain. The Fourier transform of the filter function $w_A(t)$ is[123]

$$W_A(f) = \mathcal{F}\{w_A(t)\} = \int_0^{2\tau} w_A(t) e^{i2\pi f t} dt \quad \text{leading to} \quad |W_A(f)|^2 = 2\frac{\sin^4(\pi\tau f)}{(\pi\tau f)^2}. \tag{5.9}$$

In the frequency domain it acts as a bandpass filter with a center peak at $f \approx 1/(2\tau)$ and minor peaks at multiples $(2n+1)f$ with $n \in \mathbb{N}$ (Figure 5.1b). Thus, the frequency dependent representation of the AVAR is[123]

$$\sigma_y^2(\tau) = \int_0^{\infty} |W_A(f)|^2 S_y(f) df = 2 \int_0^{\infty} \frac{\sin^4(\pi\tau f)}{(\pi\tau f)^2} S_y(f) df, \text{ where} \tag{5.10}$$

$$S_y(f) = \int_{-\infty}^{\infty} \langle y(t+\tau) y(t) \rangle e^{i2\pi f t} dt \tag{5.11}$$

is the power spectral density, which is according to the Wiener-Khintchine theorem the Fourier transform of the autocorrelation function of $y(t)$. Inserting the power spectral density for white phase noise $S_y \propto f^2$ into Equation (5.10) leads to the power law $\sigma_y^2(\tau) \propto \tau^{-2}$. The condition is an integral limit by the cutoff frequency f_h, which corresponds to a low-pass filter in an experiment. The precise values for different noise contributions are summarized in Table 5.1. The relation between the power spectral density $S_y(f) \propto f^\alpha$ and the AVAR is unambiguous for $\alpha = -2, -1, 0$. However, the contributions of flicker phase noise $\alpha = 1$ and white phase noise $\alpha = 2$ to the AVAR are indistinguishable. This

Table 5.1: Comparison between the AVAR $\sigma_y^2(\tau)$ and the MVAR mod $\sigma_y^2(\tau)$ for different types of phase noise (PM) and frequency noise (FM) expressed with the power spectral density $S_y(f)$ (adapted from [126]).

Noise type	$S_y(f)$	σ_y^2	mod σ_y^2
White PM	$h_2 f^2$	$3f_h h_2/(2\pi)^2\tau^{-2}$	$3f_h\tau_0 h_2/(2\pi)^2\tau^{-3}$
flicker PM	$h_1 f$	$(1.038h_1 + 3h_1\ln(2\pi f_h\tau))/(2\pi)^2\tau^{-2}$	$0.084h_1\tau^{-2}$
White FM	h_0	$(1/2)h_0\tau^{-1}$	$(1/4)h_0\tau^{-1}$
Flicker FM	$h_{-1}f^{-1}$	$2\ln(2)h_{-1}$	$(27/20)\ln(2)h_{-1}$
Random walk FM	$h_{-2}f^{-2}$	$((2\pi)^2/6)h_{-2}\tau$	$0.824((2\pi)^2/6)h_{-2}\tau$
drift		$(1/2)\dot{y}^2(t)\tau^2$	$(1/2)\dot{y}^2(t)\tau^2$

limitation of the AVAR can be solved by introducing a slight modification of it.

5.1.2 Modified Allan Variance

The modified Allan variance (MVAR) is defined as [127]

$$\text{mod } \sigma_y^2(\tau_0 n) = \frac{1}{2}\left\langle\left(\frac{1}{n}\sum_{i=1}^{n}\left(\frac{1}{n}\sum_{k=1}^{n} y_{i+k+n} - \frac{1}{n}\sum_{k=1}^{n} y_{i+k}\right)\right)\right\rangle, \tag{5.12}$$

where the samples y_k are averaged over the interval τ_0, while the two sums average the samples over the interval $n\tau_0 = \tau$. For clarification, consider MVAR at the limit of $\tau_0 \to 0$ in the alternative notation [126]

$$\text{mod } \sigma_y^2(\tau) = \left\langle\left(\int_{-\infty}^{\infty} y(t) w_M(t) dt\right)^2\right\rangle \text{ with } w_M(t) = \begin{cases} -\frac{1}{\sqrt{2\tau^2}}t & 0 < t < \tau \\ \frac{1}{\sqrt{2\tau^2}}(2t - 3\tau) & \tau < t < 2\tau \\ -\frac{1}{\sqrt{2\tau^2}}(t - 3\tau) & 2\tau < t < 3\tau \\ 0 & \text{elsewhere} \end{cases}. \tag{5.13}$$

The weighting of the frequency fluctuations is defined by a triangle function $w_M(t)$ (Figure 5.2a). This alternative notation keeps the basic definition of the Allan variance the

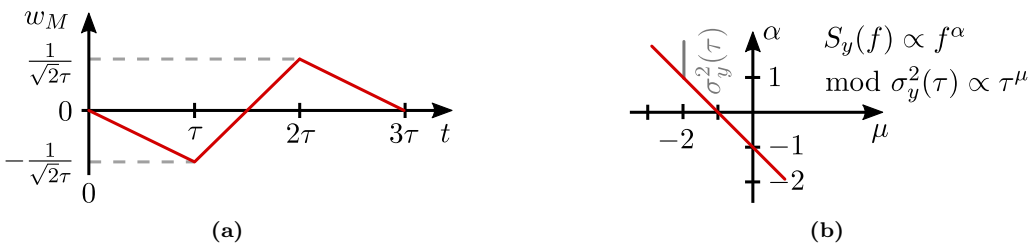

Figure 5.2: (a) Schema of the triangle filter function $w_M(t)$ of the modified Allan variance mod $\sigma_y^2(\tau)$ (adapted from [126]). (b) The relation between the power spectral density $S_y \propto f^\alpha$ and mod $\sigma_y^2(\tau)$ (adapted from [125]).

same, with only a change to $w_M(t)$. The squared absolute value of the Fourier transformed

filter function is[127]

$$|W_M(f)|^2 = 2\frac{\sin^6(\pi f\tau)}{(\pi f\tau)^4}, \tag{5.14}$$

The MVAR is now calculated in analogy to Equation (5.10) for different power spectral densities by replacing $|W_A(f)|^2$ with $|W_M(f)|^2$, which completes Table 5.1. The convolution integral of the MVAR converges more rapidly for increasing frequencies and therefore provides higher sensitivity for white phase noise $S_y(f) \propto f^2$ compared to the AVAR. In fact, the calculation of the MVAR for $S_y(f) \propto f^2$ leads to the power law mod$\sigma_y^2(\tau) \propto \tau^{-3}$ while the standard AVAR only scales with τ^{-2} (Table 5.1). A power spectral density $S_y(f) \propto f^\alpha$ with $\alpha = -3, -2, -1, \cdot\cdot$ leads to a modified variance mod $\sigma_y^2(\tau) \propto -\alpha - 1$ (Figure 5.1b). Thus, the MVAR solves the previous ambiguity between white phase noise ($\alpha = 2$) and flicker phase noise ($\alpha = 1$). The disadvantage of the MVAR is a poor efficiency in detecting slow variations of $y(t)$, since the filter function spans 3τ, while filter function of the AVAR spans 2τ. Thus, a total measurement Time of T results in a maximum of $\tau = T/3$ instead of $\tau = T/2$. The parabolic variance (PVAR) addresses this disadvantage[128]. The filter function of the PVAR is based on a parabolic function with length 2τ, but the PVAR still shows a scaling τ^{-3} for white phase noise. In this way, it combines the benefits of both Allan variances. However, in this thesis, the MVAR deemed sufficient for most long term stability measurements. Additionally, the most dominant noise contribution at large time scales is the frequency drift of the oscillator, which is the same for both Allan variances.

5.2 Frequency Standards

The precise measurement of time is probably one of the oldest ambitions of humanity. Historically, the first laboratory device was the pendulum clock. The oscillation frequency dependents solely on the length of the pendulum, disregarding environmental factors like temperature and humidity, as well as, mechanics keeping the pendulum in motion. All these components are worsening the clock's stability. Additionally, the period of the clock is an arbitrary value without proper calibration to an external standard. In the early days, a reference clock would have been calibrated such that it records 86400 seconds in a mean solar day, which could be determined by astronomical observations[129]. Later, in 1956, the SI definition of a second was revised to a fraction of the length of the year 1900. Around this time, electrical circuits and quartz oscillators replaced the pendulum clock in metrology laboratories. The frequency of these electrical oscillators is typically much higher than in pendulum clock but can still be transferred into a clockwork device using a suitable frequency divider. For example, a typical quartz crystal inside a wrist watch is designed with a resonance frequency at $32\,768\,\mathrm{Hz} = 2^{15}\,\mathrm{Hz}$, making it possible to divide

the frequency down to $1\,\mathrm{Hz} = 1\,\mathrm{s}^{-1}$ by dividing by two 15 times. The stability of the quartz oscillator is several orders of magnitude higher than the pendulum clock, but it still suffers due to temperature variations and aging of the crystal. Finally, the breakthrough for high-precision time measurements came with atomic frequency standards. The year 1958 marks the first publication on the atomic definition of the second. Since 1967, one SI-second has been defined as the duration of 9 192 631 770 periods of the radiation corresponding to the ground state hyperfine transition of the cesium atom (^{133}Cs)[130]. The cesium clock defines since 1967 until today the prevailing standard of the SI-second. However, not every laboratory is equipped with a cesium clock. For those laboratories, the global navigation satellite system (GNSS) allows a convenient means of comparison between the local frequency standard and the frequency standards operated by metrology laboratories around the planet. The local general purpose frequency standard used in our lab is the rubidium oscillator.

5.2.1 Rubidium Standard

The rubidium standard is based on the hyperfine transition at 6.83 GHz inside the ^{87}Rb electronic ground state $5S_{1/2}$. The nuclear spin of $I = 3/2$ and the total angular momentum $J = 1/2$ couple from two hyperfine states with $F = 1$ and $F = 2$[123]. The degeneracy of the m_F quantum number is lifted inside a magnetic field, resulting in a splitting of $m_F = -1, 0, 1$ and $m_F = -2, -1, -, 1, 2$ of the $F = 1$ and the $F = 2$ state, respectively. Since the shift is, to first order, proportional to the m_F quantum number, the $m_F = 0$ states display the smallest dependency on magnetic field strength, which makes them ideal candidates for the clock transition. The technical realization requires a glass cell containing ^{87}Rb located inside a microwave cavity (Figure 5.3). Both ground states $F = 1$ and $F = 2$

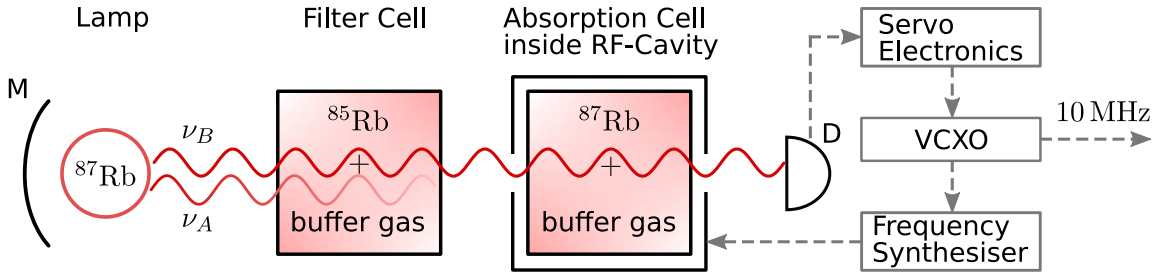

Figure 5.3: Schematic of a rubidium oscillator. The optical pump is realized with an ^{87}Rb lamp and ^{85}Rb filter combination, causing population inversion between the two hyperfine states $F = 1$ and $F = 2$. A microwave source is probing the population and set on resonance with a feedback loop. (adapted from [123]).

are nearly equally populated at room temperature. Therefore, optical pumping is used to create population imbalance between the two states. In general, a ^{87}Rb discharge lamp excites both $5S_{1/2}$ ground state hyperfine components to the higher electronic states $5P_{1/2}$ and $5P_{3/2}$. To create an asymmetry between the light exciting $F = 1$ and $F = 2$, a filter cell containing ^{85}Rb is placed after the discharge lamp. By coincidence, one of the ^{85}Rb

lines coincides with the transition from $F = 2$, so the filtered light preferentially excites $F = 1$, depleting this state. Finally, the population of the $F = 2$ state in the final ^{87}Rb cell is interrogated with microwave radiation. The microwave radiation on resonance with the ground state transition between $F = 2$ and $F = 1$ at 6.83 GHz leads to a repopulation of the state $F = 1$. Consequently, the absorption inside the ^{87}Rb gas cell increases transition from $F = 1$. A photodetector measures the decrease of transmitted optical power, which is less than 1 %. The signal becomes part of a feedback loop, which includes servo electronics, a voltage-controlled crystal oscillator (VCXO), and a frequency synthesizer, keeping the microwave radiation on resonance at 6.83 GHz. One possible design is to operate the VCXO at 10 MHz, which clocks the frequency synthesizer and simultaneously supplies the output signal. This 10-MHz radio frequency output is the primary reference used in this thesis for measuring optical beat notes and the repetition rate of the OFC.

5.2.2 Iodine Standard

Similar to the rubidium, the hyperfine-resolved transition frequencies in molecules are also suited as frequency standards. For example, the iodine molecule is a prominent absorber used for calibration of optical frequencies. The bureau of weights and measures (BIPM) recommends multiple molecular iodine transitions as the frequency standard for the practical realization of the meter. Since the meter is defined through the speed of light in vacuum $c = 299\,792\,458$ m/s, it is related by $c = \lambda f$ with the optical frequency of the light wave. The BIPM recommends in total 28 different optical frequency standards, 8 of which are transitions in molecular iodine. These iodine frequency standards mostly fall in the tuning ranges of various common lasers, from the argon ion laser at 515 nm [131] to the helium neon laser at 633 nm [132]. The laser system in this thesis is built around a Nd:YAG laser at 1064 nm. After frequency doubling, the accessible $^{127}I_2$ transitions are limited to the region near 532 nm [133]. All visible transitions of molecular iodine refer to the system $B^3\Pi_{0+u} \leftarrow X^1\Sigma_g^+$. The individual transitions are distinguished by their rovibrational quantum numbers v'', J'' and v', J' of the electronic ground state $X^1\Sigma_g^+$ and the second electronic excited state $B^3\Pi_{0+u}$, respectively. The selection rule $\Delta J = J' - J'' = -1, 0, 1$ defines whether the transition is part of the P branch ($\Delta J = -1$) or the R branch ($\Delta J = 1$). Consequently, the ro-vibrational transitions are labeled as P(J'') $v' - v''$ or R(J'') $v' - v''$. Additionally, the nuclear spin of the iodine molecule causes each rovibrational level to split into multiple hyperfine states. The corresponding hyperfine transitions are labeled a_n with $n \in \mathbb{N}$. Thus, the BIPM recommends the a_{10} component of the $R(56)$ 32-0 transition cluster in $^{127}I_2$ [134], at

$$f = 563\,260\,223\,513\,\text{kHz} \quad \text{or} \quad \lambda = 532\,245\,036.104\,\text{fm}. \tag{5.15}$$

The standard uncertainty is 8.9×10^{-12}, which is at the 5 kHz level. The standard also specifies the conditions under which this frequency was measured, such as the cold-finger temperature and saturating beam intensity. Details on the optical stabilization of a laser to a molecular absorption line follow later (Chapter 6). Already an early measurement in 1995 of a frequency doubled Nd:YAG laser locked to the iodine standard by modulation transfer spectroscopy (MTS) showed the promising result of an Allan deviation of smaller than 1×10^{-13} at the 1 s timescale[135]. The small pressure shift of 1.3 kHz/Pa and power dependent frequency shift of 2.1 kHz/mW are crucial factors in choosing $^{127}I_2$ as the frequency standard. One of the most promising prospective applications of the iodine standard is in the Laser Interferometry Space Antenna (LISA) for the detection of gravitational waves. Modern iodine standards reach Allan deviations of $< 3 \times 10^{-14}$ at the 1 s timescale[74,136,137], though the highest stability is reached at 200 s with an Allan deviation of $< 5 \times 10^{-15}$. At higher time scales the stability of the system decreases due to long term drifts.

5.2.3 GNSS Standard

The primary objective of the GNSS is to find the position of a receiver on earth. This goal is accomplished by one of the largest networks of different frequency standards. The most prominent networks are the US NAVSTAR GPS, the Russian GLONASS, and the European GALILEO system. The global positioning system (GPS), for example, includes 24 satellites orbiting the earth at a height of 20 200 km[138]. Each satellite is equipped with multiple frequency standards, including rubidium and cesium clocks. These clocks are adjusted by ground stations, which use clocks of higher stability. The ground stations supply the coordinated universal time (UTC) measured at the united states naval observatory (USNO) agree with UTC measured at national institute of standards and technology (NIST) to within < 100 ns. The time measurements at USNO and NIST both contribute to the international atomic time (TAI). The TAI is a weighted average of the measured time by approximately 50 metrology laboratories including 250 clocks calculated at the BIPM[139]. The TAI is the most precise measurement of time, though no clock can track it in real time. The closest estimates of the TAI are provided by the NIST and USNO which agree within a few nanoseconds. The pulse per second (PPS) provided by a GNSS receiver is also synchronized to the TAI second with an accuracy sufficient for many laboratory applications, though long term high precision measurements often require post-processing of the data recorded from the satellites to improve the uncertainty.

To understand the operation of the GNSS, it is convenient to consider first an individual satellite. It tasks are limited to the continuous transmission of its precise time and position. The assignment of the receiver is to process the incoming information from multiple satellites, evaluate the time and estimate the distance to each satellite. For simplicity, consider a two dimensional world, with a receiver at positions $\mathbf{P} = (X, Y)$ and two

satellites at $\mathbf{R_i} = (x_i, y_i)$, with $i = 1, 2$. The emitted signal of each satellite expands homogeneously in all directions. The position $\mathbf{P}$ is at one of the two intersection points by the two circles of radius d_i (Figure 5.4). Thus, the distances $d_i = |\mathbf{R}_i - \mathbf{P}|$ of both satellites

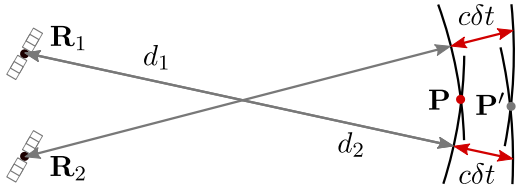

Figure 5.4: Schema of the position determination based on two satellites. The time offset δt between the satellite time and the receiver time leads to a wrong position P'. (adapted from [123]).

defines the position of the receiver. Ideally, d_i correspond to the traveling time required by the signal $\Delta t = d_i/c$, with the speed of light c. However, the satellite time T_{GNSS} is in general not synchronized with the receivers time T. A unaccounted time difference of $\delta t = T - T_{\mathrm{GNSS}} = 1\,\mu\mathrm{s}$ corresponds to an error in the position of around 300 m [123]. Thus, more information is required to determine δt, which is provided by an additional third satellite at $\mathbf{R_3} = (x_3, y_3)$. The pseudo range $D_i = d_i + c\delta t$ takes δt into accounts and leads to the set of equations [123]

$$(x_i - X)^2 + (y_i - Y)^2 = (D_i - c\delta t)^2, \text{ where } i = 1, 2, 3. \tag{5.16}$$

The three equations allow to determine the unknowns X, Y and δt. A third spatial dimension requires a minimum number of four satellites. Each further satellite is beneficial for error correction. For use as a frequency standard, δt is the crucial parameter for referencing a local laboratory oscillator. Because the GNSS receiver measures the offset to GNSS time as part of its operation, a rubidium oscillator referenced with the GNSS suffers no long term frequency drift. Referencing might be an active or a passive technique: the GNSS receiver might correct the clock of the rubidium oscillator as part of a feedback loop, or it could simply record the difference as a function of time for later post-correction. Active stabilization can result in frequency jumps, though these are negligible in most applications. Even if the rubidium oscillator is actively stabilized to GNSS time, the offset between the two is always monitored during the experiment, enabling post-processing of the rubidium frequency if necessary.

5.2.4 Comparison of Frequency Standards

The most convenient representation of frequency stability is the AVAR (Section 5.1.1), though the MVAR is preferred at short integration times (Section 5.1.2). Stability of an oscillator can only be measured relative to a reference oscillator, so any determinations of the AVAR contain the instabilities of both involved clocks. Thus, it is convenient to measure the AVAR of two identical clocks: since both clocks contribute the same instabil-

ities, the AVAR of a single clock can be easily determined. The alternative technique is to use a reference clock which is superior in stability to the oscillator under test, making it possible to neglect the additional noise of the reference oscillator when determining the AVAR. All following ADEV measurements (ADEV=$\sqrt{\text{AVAR}}$) follow this second approach. Figure 5.5 shows the ADEVs for the frequency standards previously introduced in this section, namely the rubidium, iodine, and the GNSS. In addition to the frequency standards, the ADEV of the free-running reference Nd:YAG laser is depicted [140] (Section 3.1.2).

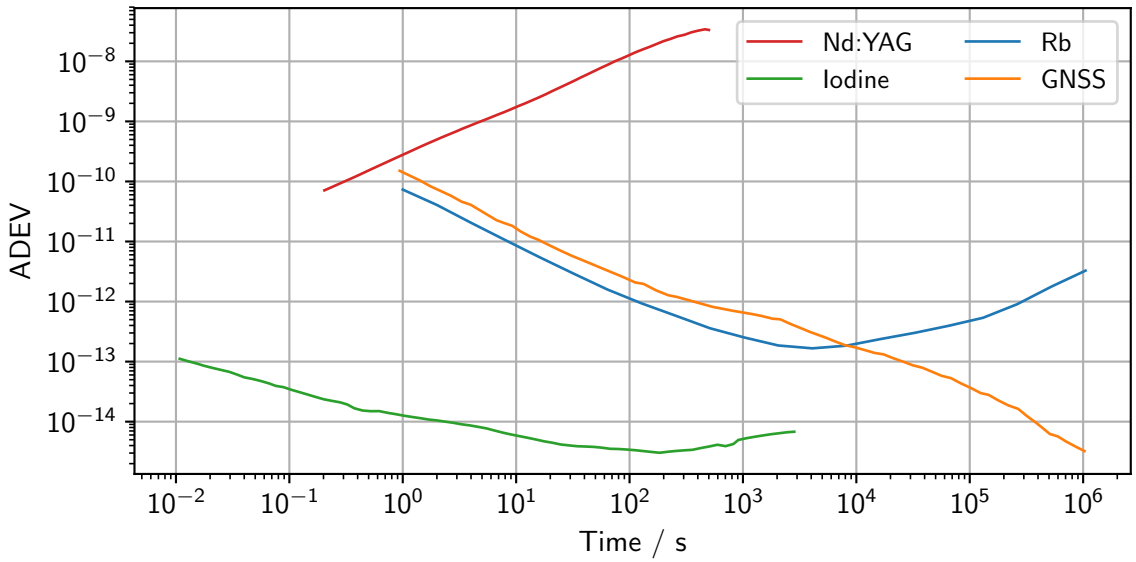

Figure 5.5: ADEV comparison of different frequency standards. (Nd:YAG) Free-running NPRO laser at 1064 nm [140]. (Iodine) Frequency doubled Nd:YAG laser stabilized with MTS to molecular Iodine [137]. (Rb) Free running rubidium oscillator. (GNSS) Stability of the PPS signal of the GNSS [141].

The stabilization of the Nd:YAG laser to the iodine is provided by means of saturated absorption spectroscopy, which is the topic of Chapter 6. If the Nd:YAG laser is stabilized to the iodine standard such that the iodine curve in Figure 5.5 corresponds to the stabilized laser, then on time scales up to 3×10^3 s, this laser provides the highest stability compared to all other mentioned frequency standards. The stability of the reference laser is transferred onto the OFC which provides it to the spectroscopy lasers (Section 3.2.5), and by monitoring the repetition rate of the OFC, the frequency of the reference laser can be compared relative to the rubidium standard. According to Figure 5.5, any potential frequency drifts at the 3×10^3 s timescales are more likely due to drifts of the rubidium oscillator than the iodine. However, a rubidium oscillator stabilized with a PPS signal from the GNSS surpasses the stability of the iodine standard at large time scales, such as 1×10^6 s, and makes each frequency measurement absolute.

This thesis relies on frequency standards comparable to the ones depicted in Figure 5.5 with ADEV curves that are to be expected at the same order of magnitude. The question of whether the stabilization schema introduced here applies in our experiment is investigated

in Section 9.2.

5.3 Feedback Bandwidth

Feedback loops provide a means to transfer of stability from a frequency standard onto a laser. Their ability to compensate environmental noise, for example, acoustic vibrations, depends on the frequency bandwidth of the feedback. If a loop attempts to cancel noise past a certain frequency limit, then the feedback starts to amplify the noise inside the loop instead of counteracting on it. The maximum bandwidth achievable in a feedback loop determines how precisely a frequency can be stabilized and provides motivation in measuring the bandwidth of the lasers used in the experiment.

5.3.1 Feedback Loop

A free running oscillator at frequency ν_i will experience changes of its oscillation frequency caused by environmental changes or aging effects. Therefore, a feedback loop is required which monitors potential changes of the oscillator frequency and takes counteractions. Ideally, the frequency ν_s of the oscillator inside the loop is compared to a reference oscillator at ν_0. The challenge of the loop is to keep the difference $\delta\nu = \nu_s - \nu_0$ as small as possible[123].

The core component of a phase-locked loop (PLL) is a phase detector which provides the difference in phase between the oscillator output and the reference. This is equivalent to $\int \delta\nu dt$ or $\delta\nu/(2\pi i f)$ in the frequency domain. Amplification and filtering of this error signal results in a feedback signal $g(f)\delta\nu/(2\pi i f)$, with the frequency dependent gain $g(f)$. Applying the feedback signal on a suitable control element of the oscillator, for instance, a mirror attached to a piezoelectric transducer (PZT) inside a laser cavity, changes the oscillation frequency. The response curve $D(f)$ of the PZT assembly also is frequency dependent, resulting in a combined frequency dependent transfer function $D(f)g(f)/(2\pi i f)$. Thus, the frequency of the oscillator inside the control loop is $\nu_s = \nu_i - D(f)g(f)\delta\nu/(2\pi i f)$. Negative feedback from the control loop aims to shift the laser from its free-running oscillation frequency ν_i to ν_s. The residual error is given by[123]

$$\delta\nu = \frac{\Delta\nu}{1 + D(f)g(f)/(2\pi i f)} \quad \text{with} \quad \Delta\nu = \nu_i - \nu_0. \tag{5.17}$$

The frequency deviation between the stabilized oscillator and the set frequency $\delta\nu$ converges to zero when the loop transfer function is large, but there are issues that can arise due to the frequency dependence of $g(f)$ and $D(f)$. In particular, if $(2\pi i f)^{-1}D(f)g(f)$ approaches -1, $\delta\nu$ can approach infinity. The transfer function generally decreases as a function of frequency, and the phase shift increases. However, if the phase shift reaches 180 degrees before the magnitude drops below 1, the sign of the feedback changes and the

feedback loop will start to oscillate.

5.3.2 Phase Shift Measurement

The transfer function of a laser cavity is mostly determined by the mounting block of the PZT which controls one of the cavity mirrors. The lowest resonance frequency inside this block determines the maximum feedback bandwidth. A direct measurement of the PZT response curve $D(d)$ is most easily accomplished outside the optical cavity of the laser. The following self-referenced measurement setup relies on the splitting and recombination of one single mode continuous wave (CW) laser beam (Figure 5.6). In particular, the

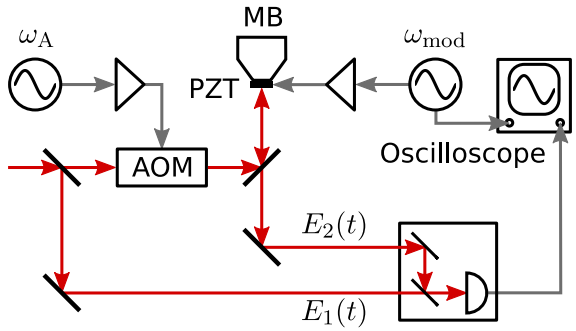

Figure 5.6: Self-referenced setup of the PZT phase response. The laser beam gets split into two parts: one part experiences modulation of the phase while the other part stays undisturbed. The modulation signal probes potential resonances inside the mounting block (MB) of the PZT assembly, which are analyzed after a homodyne detection of both beams.

electric field is separated in two parts

$$E_1(t) = Ae^{i(\omega_{cw}t+\phi_1)} + c.c., \tag{5.18}$$

$$E_2(t) = Ae^{i((\omega_{cw}+\omega_A)t+\phi_2)} + c.c., \tag{5.19}$$

where $E_1(t)$ stays unchanged while $E_2(t)$ passes an acoustic-optical modulator (AOM) that shifts the optical frequency by $\omega_A = 2\pi \times 40\,\text{MHz}$. Both electric fields have different phases of ϕ_1 and ϕ_2, due to unequal path lengths. For simplicity, the amplitudes A of both fields are assumed to be equal. Superimposing both fields and detecting the intensity with a photodiode leads to

$$I(t) = (E_1(t) + E_2(t))^2 = 2A^2e^{i(\omega_A t+\phi)} + \underbrace{A^2e^{i(2\omega_{cw}t+2\phi_1)} + ..}_{\xrightarrow{LP}0} + \underbrace{4A^2}_{\xrightarrow{DC}0} + c.c.. \tag{5.20}$$

The direct current (DC) part of the signal is removed by differential detection, discussed later in Section 9.3.1, and the high frequency components experience low-pass (LP) filtering. These cancellations leave only the low frequency part of the signal at ω_A, containing the phase difference $\phi = \phi_2 - \phi_1$. Recording the waveform on an oscilloscope allows digital processing and extraction of the phase difference $\phi \in [0, 2\pi]$. One way to do this is using

digital multiplication with $e^{-i\omega_A t}$, which leads to

$$I(t) \cdot e^{i\omega_A t} \approx (2A^2 e^{i(\omega_A t+\phi)} + c.c.) \cdot e^{i\omega_A t} = 2A^2 e^{i\phi} + \underbrace{2A^2 e^{-i(2\omega_A t+\phi)}}_{\xrightarrow{\text{LP}} 0} \approx 2A^2 e^{i\phi}. \quad (5.21)$$

The low-pass filter is realized fully digitally using a fast Fourier transform (FFT), removing the high frequency parts and finally calculating the inverse FFT. The argument of the complex number is extracted with the $\arg(e^{i\phi}) = \phi$ function. Modulating the PZT with the voltage $U(t) = \Delta U e^{i(\omega_{\text{mod}} t+\phi_1')} + c.c.$ leads simultaneously to a modulation of $\phi_2(t)$. The modulation propagates on to the phase $\phi(t) = \Delta\phi e^{i(\omega_{\text{mod}} t+\phi_2')} + c.c.$. Note, both signals have potentially different phase shifts ϕ_1' and ϕ_2', respectively. The modulation frequency is in both cases the same, allowing demodulation of ϕ_2' using $\phi(t) \cdot e^{i\omega_{\text{mod}} t}$ in analogy to the previously demodulation at ω_A (Equation (5.21)). Since ϕ_2' does not change during the measurement, averaging $\phi(t) \cdot e^{i\omega_{\text{mod}} t}$ for all values in the measurement trace results in $\Delta\phi e^{(i\phi_2')}$, and ϕ_2' can be extracted as before.

To obtain the phase difference $\phi' = \phi_2' - \phi_1'$, a demodulation of $U(t)$ is also necessary, which yields ϕ_1'. An ideal PZT system would show $\phi' = 0$ at every modulation frequency ω_{mod}, but the real PZT always has a delay in its response, making $\phi' < 0$. A full spectrum of the PZT response curve is obtained after repeating the described procedure at different modulation frequencies. An experimental application, measuring the bandwidth of the optical parametric oscillator (OPO) cavity PZT mirror is provided later (Section 9.5.2).

5.3.3 Frequency Shift Measurement

The luxury of investigating the PZT mounting block outside the laser cavity is often not provided. In such cases, the frequency response of the PZT mirror can be determined without moving it out of the cavity by measuring changes induced in the laser's frequency instead. The setup described here is designed for use with a mode-locked oscillator, but a similar measurement could be done with a CW laser. First, the pulses from the mode-locked laser are measured with a photodiode and band-pass filtered around the repetition rate frequency. For simplicity, assume the output is described by $E_1(t) = Ae^{i\omega_{\text{rep}} t} + c.c.$, with the repetition rate $\omega_{\text{rep}} \approx 2\pi \cdot 1\,\text{GHz}$. The signal $E_1(t)$ is split into two parts, with roughly equal amplitudes (Figure 5.7). One signal is sent through a long cable, which leads to a temporal delay Δt in this path. Combining both signals again with an electronic mixer gives

$$\begin{aligned} E_2(t) = E_1(t) \cdot E_1(t+\Delta t) &= A^2 e^{i\omega_{\text{rep}}\Delta t} + c.c. + \underbrace{A^2 e^{i(2\omega_{\text{rep}} t+\omega_{\text{rep}}\Delta t)} + c.c.}_{\xrightarrow{\text{LP}} 0}, \\ &\approx A^2 \cos(\phi) = \tilde{E}_2(\phi) \quad \text{with} \quad \phi = \omega_{\text{rep}}\Delta t. \end{aligned} \quad (5.22)$$

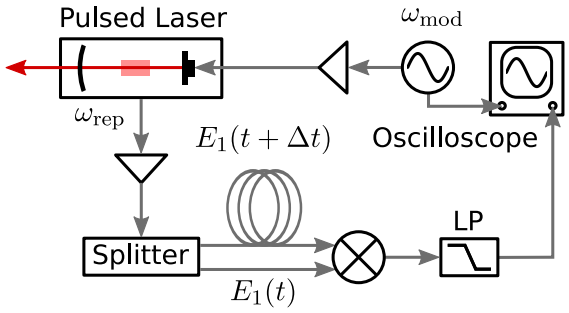

Figure 5.7: The pulsed laser signal at ω_{rep} gets split into two parts. After the temporal delay of one signal, an electronic mixer superimposes both signals again. An Oscilloscope displays the modulation signal of the PZT and the low-pass (LP) filtered signal after the mixer for further analysis..

An analog low-pass filter removes the high frequency component at $2\omega_{\mathrm{rep}}$, leaving only the low frequency component of the signal. The cable length is chosen to correspond approximately to a phase $\phi_n = (2n-1)\frac{\pi}{2}$ with $n \in \mathbb{N}$, thus the Taylor expansion of $\tilde{E}_2(\phi)$ around ϕ_n yields

$$\begin{aligned} \tilde{E}_2(\phi) &\approx \tilde{E}_2(\phi)|_{\phi=\phi_n} + \tfrac{\partial \tilde{E}_2(\phi)}{\partial \phi}|_{\phi=\phi_n}(\phi-\phi_n), \\ &= A^2(-1)^n(\omega_{\mathrm{rep}}\Delta t - (2n-1)\tfrac{\pi}{2}). \end{aligned} \tag{5.23}$$

Changing the cavity length with the PZT affects the round trip time of the pulse and consequently the repetition rate ω_{rep}. Thus, a modulation of the PZT with the voltage $U(t) = \Delta U e^{i(\omega_{\mathrm{mod}}t+\phi_1')} + c.c.$ leads simultaneously to a modulation of ω_{rep}. The frequency modulation is approximately $\omega_{\mathrm{rep}} = \omega_{\mathrm{rep}}' + \Delta\omega_{\mathrm{rep}} e^{i\omega_{\mathrm{mod}}t} + c.c.$ with the mean repetition frequency $\omega_{\mathrm{rep}}' = (2n-1)\frac{\pi}{2}/\Delta t$. Inserting the new repetition rate into Equation (5.22) yields

$$E_2(t) \approx A^2(-1)^n \Delta\omega_{\mathrm{rep}} \Delta t e^{i(\omega_{\mathrm{mod}}t+\phi_2')} + c.c.. \tag{5.24}$$

The digital demodulation of the signal with $e^{i\omega_{mod}t}$ is analog to the previous description in Section 5.3.2, leading to the phase difference between the signal modulating the PZT and the response of the repetition frequency of the mode-locked laser. The response curve of the OFC used in this thesis is discussed later (Section 9.3.2).

Chapter 6

Saturated Absorption Spectroscopy

The short term stability of the precision laser system in this thesis is provided by the iodine standard, previously discussed in Section 5.2.2. This chapter explains the transfer of stability from a hyperfine-resolved iodine transition onto the reference laser by introducing first the concept of saturation as the basis for Doppler-free spectroscopy. Laser modulation is the next step, to make use of the Doppler-free absorption signal and generate a control signal for a feedback loop resulting in the laser stabilization (Section 5.3.1). The laser system is ultimately stabilized by modulation transfer spectroscopy (MTS), which is gradually introduced in this chapter by explaining fundamental laser modulation techniques.

6.1 Einstein's Rate Equations

Einstein's rate equations provide general introduction into absorption, stimulated emission and spontaneous emission of discrete light photons of energy $h\nu$. Each interaction is associated with an Einstein coefficient. Spontaneous emission has the coefficient $\pm A_{12}$, and stimulated processes are labeled with $\pm B_{12}$ where the indices correspond to the affected states of the transition. The sign represents the loss or the gain of atoms populating a particular state. A simple two-level atom is described by the rate equations [142]

$$\frac{dN_2}{dt} = -A_{21}N_2 - B_{21}\rho(\omega)N_2 + B_{12}\rho(\omega)N_1, \tag{6.1}$$

$$\frac{dN_1}{dt} = A_{21}N_2 + B_{21}\rho(\omega)N_2 - B_{12}\rho(\omega)N_1, \tag{6.2}$$

where $\rho(\omega)$ is the field energy density. The total density number $N = N_1 + N_2$ is constant, with N_1 associated with the ground state and N_2 with the excited state. Not-degenerate energy levels are simplified with $B_{12} = B_{21}$, meaning the rates for emission and absorption are equal. Setting the change of the populations to zero $dN_1/dt = 0$ and $dN_2/dt = 0$ leads

to the steady state solution

$$\frac{N_2}{N_1} = \frac{1}{A_{21}/(B_{21}\rho) + 1}. \tag{6.3}$$

At the limit of a strong electromagnetic field $\rho(\omega) \to \infty$ the populations are equal $N_1 = N_2$ and no population inversion is possible. Therefore, in a two-level system, no laser operation takes place. In absorption spectroscopy, this is also the basis of saturation. The opposite limit of a weak field leads to a proportional relation between N_2/N_1 and $\rho(\omega)$. A more general description of saturation requires considering degenerate energy levels to derive relations between the Einstein coefficients. The number of the degeneracy of a specific state is described by the factors g_1 and g_2. Additionally, the atoms are non-interacting and are in thermal equilibrium. Therefore, the average distribution is given by Maxwell-Boltzmann statistics, which leads to the general steady-state solution of[142]

$$\frac{N_2}{N_1} = \frac{g_2}{g_1} e^{-\hbar\omega/k_B T} = \frac{B_{12}\rho(\omega)}{A_{21} + B_{21}\rho(\omega)}. \tag{6.4}$$

Solving this equation for $\rho(\omega)$ is essentially Planck's distribution of black body radiation[143]

$$\rho(\omega) = \frac{8\pi\hbar}{\lambda^3} \frac{1}{e^{\hbar\omega/k_B T} - 1}, \tag{6.5}$$

after identifying the relations

$$g_2 B_{21} = g_1 B_{12} \quad \text{and} \quad A_{21}/B_{21} = 8\pi\hbar/\lambda^3. \tag{6.6}$$

These relations will be used soon in one of Einstein's rate equations. First, it is convenient to redefine the energy density $\rho(\omega) = s(\omega)\rho = s(\omega)I/c$ with the line shape function $s(\omega)$. In case of spontaneous emission $s(\omega)$ is a Lorentzian function with the natural linewidth $\Delta\omega = A_{21}$ describing the probability of spontaneous emission around resonance ω_0. Inserting Equation (6.6) and the line shape function into Equation (6.1) yields[142]

$$\frac{dN_2}{dt} = -A_{21}N_2 - \frac{\sigma(\omega)I}{\hbar\omega}\left[N_2 - \frac{g_2}{g_1}N_1\right], \tag{6.7}$$

where $\sigma(\omega) = A_{21}\lambda^2 s(\omega)/4$ denotes the absorption cross section. The resonance condition $\omega = \omega_0$ leads to the cross section $\sigma = \lambda_0^2/(2\pi)$. Therefore, the dimension is an area and $I\sigma(\omega)$ describes the absorbed power by a single atom. Introducing the absorption coefficient[68,144]

$$\frac{dI}{dz} = -\alpha(\omega)I, \quad \text{leads to the identity} \quad \alpha(\omega) = \sigma(\omega)\left[N_2 - \frac{g_2}{g_1}N_1\right] = \sigma(\omega)\Delta N, \tag{6.8}$$

where ΔN denotes the population density difference, and this leads to Beer's law

$$I(z) = I_0 e^{-\alpha(\omega)z}. \tag{6.9}$$

This equation describes the exponential decay of the initial intensity of a light field after propagating a distance z through an absorbative medium (Figure 6.1a). However, $\alpha(\omega)$ is not independent of the intensity, which can be seen by calculating the steady-state solution of the rate equations again. For simplification, it is assumed the degeneracies are $g_1 = g_2$, and the field is on resonance. Thus, the absorption coefficient is[142]

$$\alpha(\omega_0) = \sigma(\omega_0)\frac{N}{1+\frac{I}{I_{sat}}}, \quad \text{with} \quad I_{sat} = \frac{\hbar\omega_0 A_{21}}{2\sigma(\omega_0)}. \tag{6.10}$$

At small intensities the absorption coefficient is nearly constant with $\sigma(\omega_0)N$, while at high intensities the absorption coefficient converges to zero. The saturation intensity I_{sat} corresponds to the intensity at which $\alpha(\omega_0)$ decreases by a factor of two. Saturation effects are a double-edged sword in spectroscopy. Increasing the laser field intensity does not increase the absorption and the associated signal strength linearly. At some intensity the line profile gets distorted and the signal to noise ratio (SNR) decreases. On the other hand, these effects open the field of Doppler-free saturation spectroscopy.

6.2 Doppler Free Saturation Spectroscopy

Two things have been mentioned in Section 6.1 without pointing out the consequences. First, the line shape function $\sigma(\omega)$ of spontaneous emission is a Lorentzian function, with a narrow linewidth of $\Delta\omega = A_{21}$. Second, the atoms satisfy the Maxwell-Boltzmann velocity distribution, meaning most molecules are at a velocity of $v \neq 0$. The resonance condition is satisfied, if the absorption frequency is within the narrow line shape function $s(\omega)$. However, due to the velocity spread of the molecules, the frequency inside the moving frame of the molecule differs from the frequency outside in the laboratory frame. According to the Doppler effect, a molecule moving with a velocity v towards the wave vector of an electromagnetic field experiences a higher frequency

$$\omega = \omega_0(1 + \frac{v}{c}). \tag{6.11}$$

Conversely, a molecule moving away experiences a lower frequency. Each velocity class inside the Maxwell-Boltzmann distribution satisfies the resonance condition for a specific field frequency. Exciting molecules with an off-resonant frequency $\omega < \omega_0$ 'burns' a hole into the ground state velocity distribution at $v > 0$[145]. The width of this hole is associated with the natural linewidth in the velocity interval Δv (Figure 6.1a). Based on a single frequency it is impossible to tell if the actual resonance frequency is matched. A

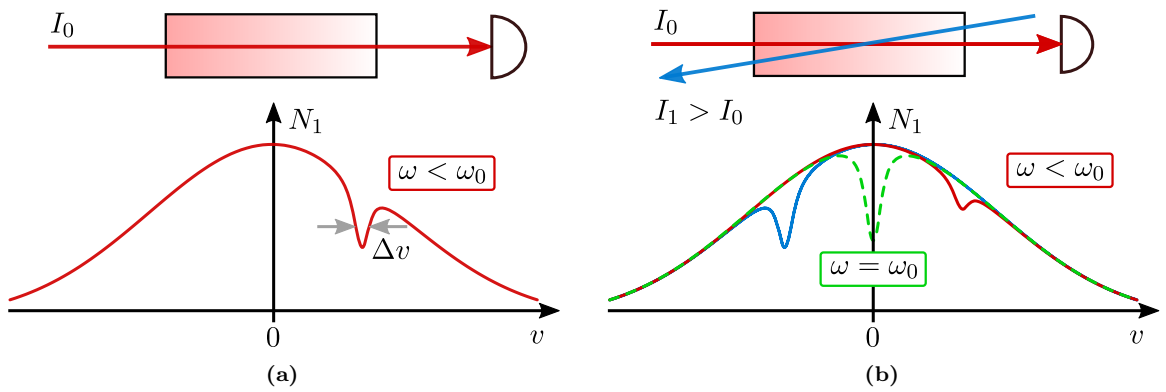

Figure 6.1: (a) A single red detuned wave interacts with a single velocity group $v > 0$. (b) Two counter propagating waves, with the same frequency excite two different velocity groups. Both waves interact with the zero velocity group at resonance.

scan over the full Doppler broadened ground-state velocity distribution provides clarity. The total width is a convolution of all Lorentzian lines with the Gaussian Maxwell-Boltzmann distribution. The core of saturated absorption spectroscopy is to introduce a second counterpropagating laser beam, which can be generated by reflecting the first one. The frequencies of both waves are identical, but the amplitudes generally differ. The counterpropagating beam with $I_1 > I_0$ is denoted as the pump. Its primary purpose is to saturate the transition. The second beam is probing the level of saturation. Assuming the case of $\omega \neq \omega_0$, leads to an excitation of different velocity groups, due to the counter propagation of both beams. Thus, two holes are burned into the velocity distribution of the ground state (Figure 6.1b). Tuning the field frequency into the direction of resonance leads to an approach of both holes. At resonance, both beams interact with the same velocity group namely $v = 0$. The pump beam depletes the population of the ground state so that the absorption coefficient reaches a minimum, and the probe beam experiences less absorption through the medium to the detector. The final signal results in a narrow intensity peak on top of the Doppler-broadened background.

6.3 Laser Modulation Techniques

Consider a saturated absorption experiment where the laser frequency is tuned to the center of the Doppler-free saturation peak. If the laser frequency deviates from this center position, the saturation signal will decrease, but the signal will contain no information about the direction of the frequency change. Modulating the frequency of the laser provides this information, which can be used for laser stabilization.

6.3.1 Wavelength Modulation Spectroscopy

Wavelength modulation (WM) spectroscopy is strongly coupled to tunable diode laser absorption spectroscopy (TDLAS). This high-resolution spectroscopy is based on the ease

of changing the emission frequency of a diode laser. A change of the injected current or the ambient temperature changes the physical properties of the diode, which leads to a shift in the frequency of the emitted electromagnetic field. Around 1970 [146], it opened a new field of spectroscopy and was further improved by adding a fast sinusoidal modulation on to the slow scan [147]. In these experiments, the frequency of the electric field is given by

$$\omega = \omega_0 + \delta\omega \cos(\omega_m t), \tag{6.12}$$

with the modulation frequency ω_m and the modulation amplitude, or depth $\delta\omega$. The ratio between $\delta\omega$ and the width of the absorption feature Γ is defined as the modulation index M. The following consideration assumes a small modulation depth $\delta\omega \ll \Gamma$ and a small modulation frequency of $\omega_m \ll \Gamma$. This modulated electromagnetic field experiences absorption inside a gas cell following Beer's law. At the limit of low absorption $NL\sigma \ll 1$, the intensity change is approximated by the first term of the Taylor series [148]

$$\Delta I(\omega) = I_0 e^{-NL\sigma(\omega)} \propto \sigma(\omega), \tag{6.13}$$

leaving only the absorption cross section $\sigma(\omega)$. A second Taylor series around ω_0 is now applied on the cross section and Equation (6.12) is inserted, yielding [148]

$$\begin{aligned} \Delta I(\omega) &\propto \sigma(\omega_0) + \delta\omega \cos(\omega_m t)\frac{d\sigma(\omega_0)}{d\omega} + \delta\omega^2 \cos^2(\omega_m t)\frac{1}{2}\frac{d^2\sigma(\omega_0)}{d\omega^2} + ..., \\ &= \sigma(\omega_0) + \delta\omega \cos(\omega_m t)\frac{d\sigma(\omega_0)}{d\omega} + \delta\omega^2 \cos(2\omega_m t)\frac{1}{4}\frac{d^2\sigma(\omega_0)}{d\omega^2} + ..., \end{aligned} \tag{6.14}$$

using $\cos^2(x) = (1 + \cos(2x))/2$ in the last line. One obtains a series of oscillating terms at $n\omega_m$, with $n \in \mathbb{N}$. The term oscillating at ω_m is associated with the first derivative of the cross-section. Higher oscillating terms $n\omega_m$ contain the information of the cross section derivative of order n (Figure 6.2). Essentially, the small frequency modulation $\delta\omega$

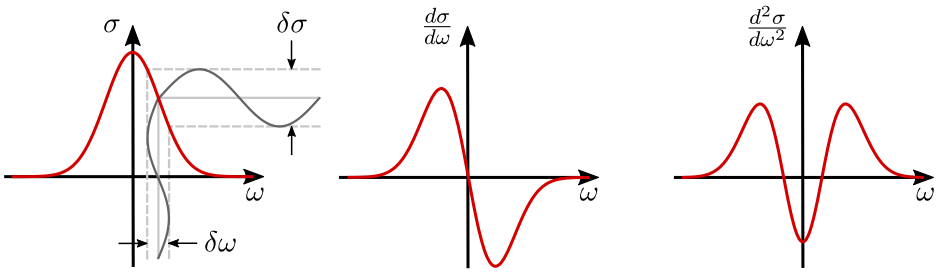

Figure 6.2: Schematic representation of wavelength modulation spectroscopy. The first derivative of the absorption line shows a zero crossing right at the center of the transition frequency, while higher orders increase the slope at this frequency.

gets converted into an amplitude modulation, which is proportional to $\delta\sigma$. The derivative signal of interest gets separated by using a lock-in amplifier; therefore, this technique is denoted as derivative spectroscopy or harmonic detection. Choosing, for example, the

second derivative filters out noise components outside the range around $2\omega_m$. This filtering leads to an improvement of the SNR compared to absorption spectroscopy without fast modulation. Also, the baseline of the signal becomes flat, because all constant and linear components of σ are removed. The second derivative scales with $\delta\omega^2$. Increasing the modulation depth to $\delta\omega \gg 1$ improves the SNR even further. However, the simple picture of a Taylor-expansion is now no longer valid. Instead, the intensity after absorption is described by a Fourier expansion

$$I(\omega) \propto \sum_{n=0}^{\infty} H_n(\omega_0)\cos(n\omega_m t), \text{ where} \tag{6.15}$$

$$H_n(\omega_0) = \frac{2}{\pi}\int_0^{\infty} \sigma(\omega_0 + \delta\omega\cos\Theta)\cos(n\Theta)d\Theta. \tag{6.16}$$

The detection of the individual harmonic terms is analog to derivative spectroscopy and the shape of the individual signals is qualitatively similar[149,150]. This is referred to as WM spectroscopy, with an modulation depth $\delta\omega > \Gamma$. Further reduction of the SNR requires higher modulation frequencies.

6.3.2 Frequency Modulation Spectroscopy

The heart of frequency modulation (FM) spectroscopy is a fast phase modulation realized by an electro-optic modulator (EOM). This device consists of an electro-optic material between two electrodes. Applying a voltage changes the refractive index of the material, allowing fast frequency modulations $\omega_m > \Gamma$. The electric field of a single mode laser is

$$E_1(t) = \widetilde{E}_0 \sin(\omega_c t) = E_0 e^{i\omega_c t} + c.c., \tag{6.17}$$

where ω_c describes the carrier frequency, which is in the frequency domain depicted as a delta peak (Figure 6.3). Modulating the electric field sinusoidally at the frequency ω_m

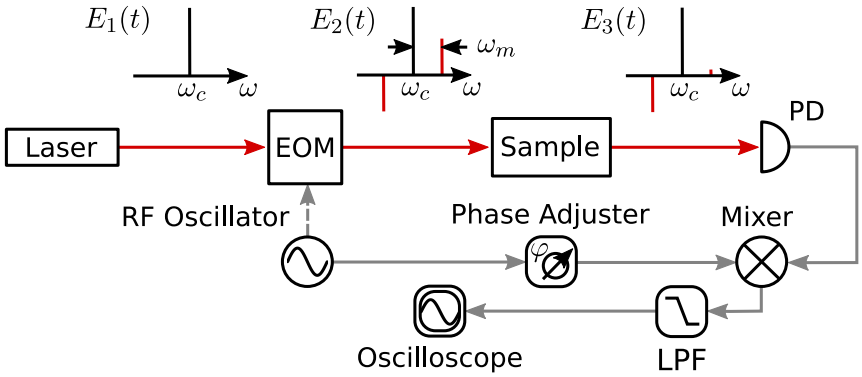

Figure 6.3: Schematic setup of FM spectroscopy. The modulated sidebands are depicted as delta peaks at $\omega \pm \omega_m$. The different phase is illustrated by flipping one of the sidebands upsides down. After the interaction with the sample, the sum of both sidebands doesn't cancel out. This results in optical beating, which is measured with a PD (adapted from[151]).

and propagating the laser beam through the EOM, leads to

$$E_2(t) = E_0 \sin\left(\omega_c t + M \sin(\omega_m t)\right), \tag{6.18}$$

with the modulation index M. Expressing the amplitudes of the sidebands with Bessel-functions $J_n(M)$ of order n[152,153], in analogy to FM in audio spectra[154], leads to

$$E_2(t) = E_0 \sum_{n=-\infty}^{\infty} J_n(M) e^{i(\omega_c + n\omega_m)t} + c.c.. \tag{6.19}$$

The side bands are an infinite series of multiples of the modulation frequency ω_m, though for small modulation indices $M \ll 1$ only $n = -1, 0, 1$ are significant. This narrow band-band FM yields $J_0(M) \approx 1$ and $J_{\pm 1}(M) = \pm M/2$. Also, the signs of the sidebands are opposite, leading to cancellation on a square law detector. After sending the laser beam through an absorbative gas cell the amplitudes are attenuated, and the phase experiences a shift. The different interactions of the side bands at $\omega_c - \omega_m$ for $n = -1$ and at $\omega_c + \omega_m$ for $n = +1$ with the absorption profile is essential for FM spectroscopy. It is convenient to describe a function $T_n = e^{-\delta_n - i\phi_n}$ which takes the individual attenuation of the amplitude δ_n and the phase shift ϕ_n into account. The electric field after the sample is[153]

$$E_3(t) = E_0 \left(T_0 e^{i\omega_c t} + T_1 \frac{M}{2} e^{i(\omega_c + \omega_m)t} - T_{-1} \frac{M}{2} e^{i(\omega_c - \omega_m)t} \right). \tag{6.20}$$

The optical PD after the sample can only detect the field intensity $I_3 \propto |E_3(t)|^2$. The difference between FM and WM is the size of the modulation frequency ω_m. Low-frequency modulations of the EOM lead to the same observations one would obtain in WM spectroscopy. In the case of classical FM spectroscopy[152] the modulation frequency is usually higher than the spectral range of the absorption profile, therefore only one sideband is absorbed. The carrier and the other sideband experience no attenuation and no phase shift, and are called background-amplitude and -phase. The interaction of only one of the sidebands generates the intensity at the PD[151]

$$I_3(t) \propto E_0^2 e^{-2\delta_0} \left(1 - \Delta\delta M \cos(\omega_m t) + \Delta^2 \phi M \sin(\omega_m t)\right), \tag{6.21}$$

where $\Delta\delta = \delta_1 - \delta_0$ and $\Delta\phi = \phi_1 - \phi_0$ are the deviations from background phase and amplitude, respectively. In this representation, the sideband higher in frequency $\omega_c + \omega_m$ is absorbed, and the intensity $I_3(t)$ oscillates with the modulation frequency ω_m, while the direct current (DC) offset contains the amplitude of the carrier signal. The information about the change of the amplitude $\Delta\delta$ and the change of the phase $\Delta\phi$ is obtained by demodulating the signal with an electronic mixer which means mathematically to multiply the signal with $\cos(\omega_m t + \varphi)$, where φ is the variable phase. Afterwards, all the oscillating

terms are filtered out by a low-pass filter so that the DC signal is only phase dependent

$$I_3(t)\cos(\omega_m t+\varphi) \overset{\text{LP}}{\propto} \Delta\delta\frac{M}{2}\cos(\varphi)+\Delta\phi\frac{M}{2}\sin(\varphi). \tag{6.22}$$

The component containing the amplitude is in case of $\varphi = 0$ the only surviving term. It is denoted as the in-phase component, while the other component is called the quadrature. By altering the phase φ, it is possible to obtain the change of the amplitude $\Delta\delta$ or the change of the phase $\Delta\phi$, separately. The high-frequency modulation causes a convergence of the amplitude noise to the shot noise level. By combining this technique with saturated absorption spectroscopy (Section 6.2), one approaches the domain of high-resolution spectroscopy[155,156]. Unfortunately, the signal requires an active subtraction of the background, making it less than ideal for laser stabilization.

6.3.3 Modulation Transfer Spectroscopy

The previous sections aimed to give a basic understanding of fundamental modulation techniques, carrying the message that high modulation frequencies reduce the amplitude noise[157,158] which results in a higher SNR.

However, independent of the modulation frequency a complete cancellation of the amplitude background noise is not possible by design. A laser is a very coherent light source, thus placing optics inside the path of a laser beam always results in spurious interferometric fringes. The linear absorption of these unwanted parts of the electromagnetic field adds up to a noisy background. The solution for this issue is to make the detection schema insensitive to linear absorption features. Modulation transfer spectroscopy (MTS) can cancel the background and increases the sensitivity close to the shot-noise limit[158]. The setup of MTS (Figure 6.4) looks at first sight very similar to FM spectroscopy (Figure 6.3) with the obvious addition of a counter propagating beam. However, the mechanism behind

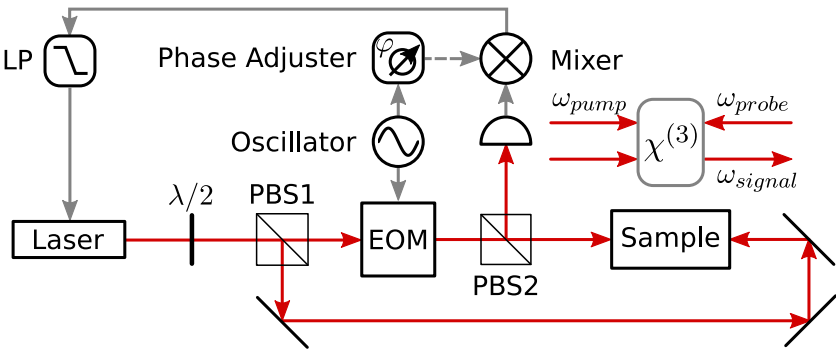

Figure 6.4: Schema of a MTS setup. The saturation beam coming from the left interacts nonlinearly with a counterpropagating probe beam inside the absorbing sample. The modulation of the saturating beam is transferred onto the probe beam for phase sensitive detection.

it is described by a nonlinear process of the third order, called four-wave mixing[157,159] (Section 4.0.4). The modulated laser beam saturates the transition. It contains the carrier

frequency and two sidebands like in the case of FM spectroscopy (Equation 6.19). The counterpropagating probe beam is also at the carrier frequency but is unmodulated and at lower power. The saturation of the transition causes the nonlinear power dependence of both beams, which results in a nonlinear interaction and a transfer of the modulation frequency of the pump beam onto the probe beam. Modulation transfer happens only at resonance. Therefore, the background noise becomes independent of linear absorption effects and leads to a zero baseline. The mathematical description makes use of third order perturbation theory, which leads to the signal[160–163]

$$S(\omega_m) = \frac{c}{\sqrt{\Gamma^2+\omega^2}} \sum_{n=-\infty}^{\infty} J_n(\delta) J_{n-1}(\delta) \times \left[\left(L_{(n+1)/2} + L_{(n-2)/2} \right) \cos(\omega_m t + \phi) + \left(D_{(n+1)/2} + D_{(n-2)/2} \right) \sin(\omega_m t + \phi) \right], \tag{6.23}$$

with the Bessel functions J_n of order n, the phase modulation index M and the Lorentzian resonance functions

$$L_n = \frac{\Gamma^2}{\Gamma^2 + (\Delta - nM)^2} \quad \text{and} \quad D_n = \frac{\Gamma\,(\Delta - nM)}{\Gamma^2 + (\Delta - nM)^2}. \tag{6.24}$$

These functions describe the absorption for a detuning Δ away from the resonance for a natural linewidth δ and a modulation frequency ω_m. The detection of the signal is dependent on the phase of the demodulation signal ϕ which is one of the possible tuning parameters to maximize the signal[163]. Demodulating the signal with $\cos(\omega_m t + \varphi)$ leads again to a in-phase and a quadrature part of the signal (Section 6.3.2). The maximum signal is found at $\varphi > 0$, which requires a linear combination of both parts. However, sometimes it is convenient to generate either the pure in-phase or quadrature signal. Maximizing the signal is not necessarily the target. In case of laser locking, one might prefer a signal with a large slope at zero crossing over a signal with a larger amplitude. Considering a modulation index $M < 1$ simplifies the evaluation of the signal because only the first order sidebands contribute[164]. For a small modulation $\omega_m/\Gamma \approx 0.5$ the quadrature and in-phase signals have the same line shape (Figure 6.5a and 6.5b). The in-phase component consists of Lorenzian functions L_n describing the absorption and the quadrature component describes the dispersion with D_n. This characteristic is analog to the case of FM spectroscopy in Equation (6.22). Therefore, the in-phase component is proportional to the first derivative of the absorption, and the quadrature component is proportional to the second derivative of the dispersion[153]. The maximum gradient is reached at $\omega_m/\Gamma = 0.35$ and at $\omega_m/\Gamma = 0.67$ for the in-phase and the quadrature component, respectively. A further increase of the modulation frequency ω_m raises only the peak to peak amplitude, and the slope starts to decrease after passing a modulation frequency of $\omega/\Gamma \approx 1.4$. Much larger MTS signals are achieved by increasing the modulation index

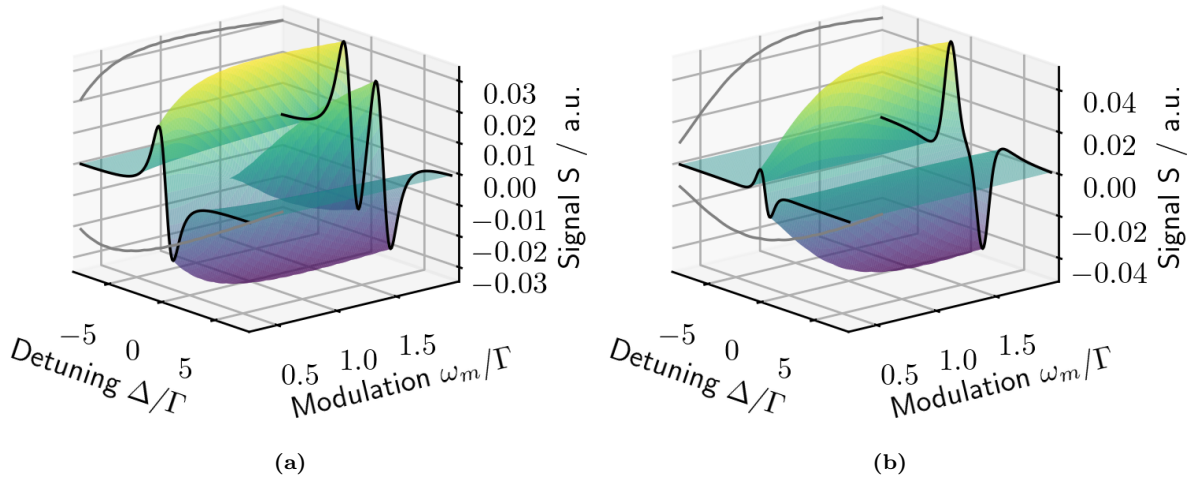

Figure 6.5: Calculation of the MTS (a) in phase and (b) quadrature signal after demodulating with $\cos(\omega_m t + \varphi)$. The modulation index is set to $M = 0.5$.

$M > 1$. Essentially, the behavior of the in-phase and quadrature component are the same, as in the case of $M < 1$. The difference is a faster decline of the signal amplitude with respect to the modulation frequency ω_m (Figure 6.6a-6.6b). Choosing an ideal signal based

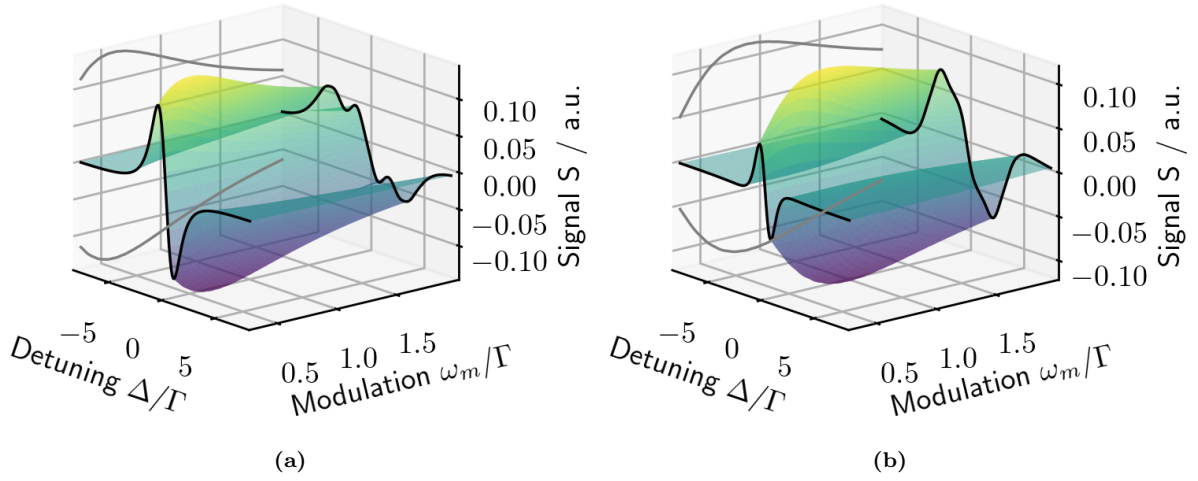

Figure 6.6: Calculation of the MTS (a) in phase and (b) quadrature signal after demodulating with $\cos(\omega_m t + \varphi)$. The modulation index is set to $M = 3$.

on this theoretical curves, one should select the in-phase signal. The modulation index should be $M > 1$ and the modulation frequency w_m smaller than the natural linewidth Γ.

Chapter 7

Spectroscopy on a Molecular Beam

The molecules are prepared in a highly-collimated molecular beam of the hydroxyl radicals (OH), which is crossed perpendicular by the spectroscopy laser. Afterwards, electronically excited OH molecules emit fluorescence light on a microsecond timescale, which is detected with a photomultiplier tube (PMT). Unfortunately, the excitation frequency of the molecules is shifted, due to the Doppler-effect (Section 7.2). The same effect dominates the line broadening of the transition frequencies. For instance, the natural linewidths of the $A^2\Sigma^+$, $v' = 0 \leftarrow X^2\Pi_{3/2}$, $v'' = 0$ transitions in hydroxyl radical (OH) are $\Delta\nu = 1/(2\pi\tau) \approx 231\,\mathrm{kHz}$[165], based on a lifetime of $\tau \approx 688\,\mathrm{ns}$[166]. Saturation broadening increases the linewidth to $\Delta\nu' = \Delta\nu\sqrt{1+S_0} \approx 400\,\mathrm{kHz}$ for an overestimated saturation parameter $S_0 = 2$, which corresponds to twice the light intensity required for steady state absorption and emission[123]. Now, in contrast, the full width at half maximum (FWHM) due to the Doppler effect is approximately 8 MHz. Individual transitions start to blend and make the determination of their center frequencies challenging. The Zeeman-effect (Section 2.6.1), as well as laser field dependent effects (Chapter 8) are within the line broadening. Therefore, this chapter explains the molecular beam and its relation to the first order Doppler-effect.

7.1 Molecular Beam

Doppler broadening is a general problem when determining the center frequency of a transition. Decreasing the velocity distribution along the propagation direction of the laser beam reduces the Doppler width. The narrower velocity distribution is the most substantial benefit of a collimated molecular beam, which propagates perpendicular to the laser axis. All molecules are contained inside a reservoir and satisfy the Maxwell-Boltzmann velocity distribution. The pressure inside the container is for example $P_0 \approx 1\,\mathrm{atm}$. A hole at the container allows the molecules to exit into a space of lower pressure P_b. The molecules escape collision-free if the hole diameter is smaller than the mean free path of the gas. Outside the container, the velocity distribution and the rotational and vibrational

degrees of freedom stay the same as inside, which is characteristic for an effusive beam. However, a hole diameter larger than the mean free path of the gas introduces collisions. Escaping molecules frequently collide, which leads to adiabatic cooling of all degrees of freedom in the expansion region[167]. Sometimes it is also referred to as an isentropic expansion since it is adiabatic and reversible. The collisions contribute mainly to a cooling of the rovibrational states of the molecules, while the expansion is cooling the translational motion by narrowing the velocity distribution[168]. Clustering of the molecules at small velocity distributions limits the cooling. Thus a noble carrier gas counteracts the clustering. Good choices are heavy noble gases like krypton or xenon. Their main advantage is the reduction of the velocity of the molecular beam. The translational temperature T_{tr} is mostly determined by the carrier velocity distribution Δv_{tr}. Thus, the temperature of the ideal gas is described by $k_B T_{tr} = \frac{1}{2} m \Delta v_{tr}^2$ [169]. Typical translational temperatures of diatomic molecules are below 1 K. The rotational and vibrational temperatures are around 10 K and 100 K, respectively[45]. The velocity of the molecules is described by the Mach number $M = u/a$, with the mass flow velocity u and the local speed of sound $a = \sqrt{\gamma k_B T_{tr}/m}$ [45]. The critical constant is the ratio of the heat capacities of constant pressure and constant volume $\gamma = C_P/C_V \approx 5/3$, as an example of a monatomic gas. In terms of Mach numbers, the molecules start at $M \ll 1$ and reach $M \approx 1$ at the source exit (Figure 7.1a). This includes the assumption of a pressure ratio $P_0/P_b > 2.1$ [170]. In

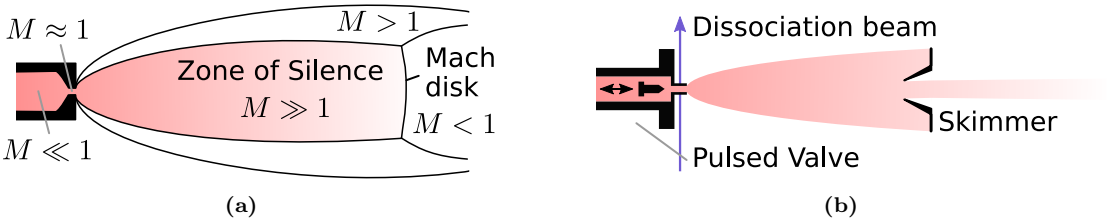

Figure 7.1: (a) Supersonic expansion of a molecular beam, with an isentropic core independent of the boundary condition of P_b. This zone of silence is surrounded by shock waves, depicted as black lines around the zone of silence. The ideal position of a skimmer is before the Mach disk inside the isentropic expansion (adapted from [170]).

this range, the pressure at the exit becomes independent of P_b and is roughly $P_0/2 > P_b$. Due to the pressure difference at the exit, the beam starts to expand. The flow velocity reaches values of $M \gg 1$. Thus, it is called a supersonic expansion. An exciting feature of particles moving at this velocity is the lack of information transfer. Information travels with the speed of sound, but the molecules move faster. Therefore, they are not affected by the boundary condition of P_b, and the Mach number continues increasing. The molecular beam even starts to overexpand, until it gets adjusted by shock waves. They are thin non-isentropic regions, in which all beam parameters experience a large gradient. The Mach number decrease in regions beyond the shock waves. The location of the Mach disk brakes the expansion in the forward direction to $M < 1$ and is estimated at [170]

$$x_m = 0.67 d \sqrt{P_0/P_b}. \tag{7.1}$$

A background pressure $P_b \approx 10^{-4}$ mbar and a hole diameter $d = 1$ mm lead, for example, to a distance of $x_m \approx 2$ km. Thus, shock waves are negligible in the pulsed molecular beam in this thesis. The molecules passing the skimmer into the second vacuum chamber have a high Mach number, but a narrow velocity distribution in all dimensions. The maximum flow velocity is[169]

$$v_0(T_0) = \sqrt{\frac{2k_B T_0}{m} \frac{\gamma}{\gamma - 1}}, \tag{7.2}$$

with the stagnation temperature $T_0 = 293.15$ K, correspondig to the start temperature of the molecules. The resulting velocity of the perfect isentropic expansion for an ideal gas of xenon is around $v_0 = 304$ m/s. The actual value in an experiment will be slightly higher at 340 m/s. A detailed calculation includes the pressure and temperature dependence of γ[169]. As important as understanding the expansion of the molecular beam, is the creation of sample molecules. This thesis focuses only on the generation of an OH molecular beam. The most prominent techniques for producing OH are photolysis[171], chemical reactions[172] and electrical discharge[173]. However, the chemical reaction of $H + NO_2 \longrightarrow OH + NO$ is limited to a continuous molecular beam. A modern electrical discharge source, which creates cold and intense OH beams[174] seems to be the most straightforward approach, though building such a device is a small project of its own.

7.1.1 Photodissociation of Nitric Acid

In this thesis, we used photodissociation of nitric acid to generate the OH. A mixture of gaseous nitric acid (HNO_3) and the carrier gas xenon at 1 atm fill the pulsed valve. Opening the valve lets the gas mixture flow first into an evacuated fused silica tube, which produces into the expansion chamber (Figure 7.1b). A perfectly timed laser pulse around 193 nm dissociates the nitric acid molecules inside the quartz tube

$$HNO_3 \longrightarrow NO_2 + OH. \tag{7.3}$$

The OH radicals then undergo supersonic expansion, along with the carrier gas and NO_2. In contrast to an ideal supersonic expansion, the quartz tube confines the molecules over a distance of a few millimeters. By the time, the first molecules reach the exit of the tube, the pressure difference to the vacuum chamber has already decreased. However, the cooling of the supersonic expansion is not endangered as long the relation $P_0/P_b > 2.1$ is satisfied. Effects like a potential tail of the supersonic expansion, due to the quartz tube are neglected. The most significant drawbacks of nitric acid dissociation are of technical nature. The vacuum pumps can handle only a limited amount of acid before they start to degrade, making a cold finger at liquid nitrogen temperature necessary. The cold finger takes frequent maintenance. It is emptied by bringing it to room temperature, purging

it with nitrogen and neutralizing the emerging acid with an alkaline solution inside a bubbler, for instance, sodium bicarbonate ($NaHCO_3$)

$$2\,H^+ + CO_3{}^- \rightleftharpoons H^+ + HCO_3{}^- \longrightarrow H_2O + CO_2\uparrow . \tag{7.4}$$

Both ions are in aqueous solution and experience an equilibrium reaction, which results in water and CO_2. The CO_2 gas leaves the solution together with the purging nitrogen. Due to an excess of $NaHCO_3$ inside the solution, all HNO_3 gets neutralized.

7.2 Doppler-Shift

The basis of the Doppler effect is the relative velocity mismatch between the observer and the molecule. In the system of the molecule, the wavelength of an electromagnetic wave appears shorter if the molecule is moving towards the origin of the wave. Therefore, the molecule experiences a higher optical frequency. In contrast, a molecule moving alongside the laser beam in the same direction observes a lower frequency. The actual laser induced fluorescence (LIF) experiment takes place in the laboratory system. If a molecule which is propagating towards the laser beam absorbs, it will absorb at a lower laser frequency than if it were at rest. The absorbed light is, therefore, red detuned relative to the transition frequency. The frequency observed inside the laboratory system is

$$\nu = \nu' \left(1 - \frac{v}{c}\right), \tag{7.5}$$

with the molecule velocity v, the speed of light c and the emitted frequency ν'. Additionally, the molecules satisfy in general the Maxwell-Boltzmann velocity distribution. Thus, each velocity class absorbs light at a different optical frequency. The velocity distribution of the molecules inside a gas cell is symmetric, which leads only to a broadening of the absorption feature. However, the velocity distribution of a collimated molecular beam is different, with a narrow velocity distribution but a large forward velocity in the propagation direction. Thus, the velocity distribution perpendicular to the propagation direction depends on the collimation. Assuming a perpendicular Gaussian velocity distribution of the molecules with a FWHM of $\Delta v_\perp = 2.5\,\mathrm{m/s}$ which is parallel to the laser beam, yields a narrow Doppler FWHM around $\Delta v/\lambda \approx 8\,\mathrm{MHz}$ at $\lambda = 308\,\mathrm{nm}$. It is practically tricky, to align the laser beam perfectly perpendicular to the propagation axis of the molecular beam, and this results in a shift of the velocity distribution and hence a shift of the absorbed laser frequency. A solution to this problem is to use two counter-propagating laser beams of the same power and wavelength, created by retroreflection of the first beam. The two laser beams cause essentially two shifts, which are equal in opposite directions. The center of the ideal superimposed absorption frequency distribution is Doppler-free, and only the Doppler-broadening remains.

7.3 Geometric Back Reflection Quality

It remains a technical challenge to achieve a precise back reflection. A standard approach is to use an aperture close to the laser, reflect the laser beam off a mirror and pass it a second time from the opposite direction through the same aperture (Figure 7.2a). The

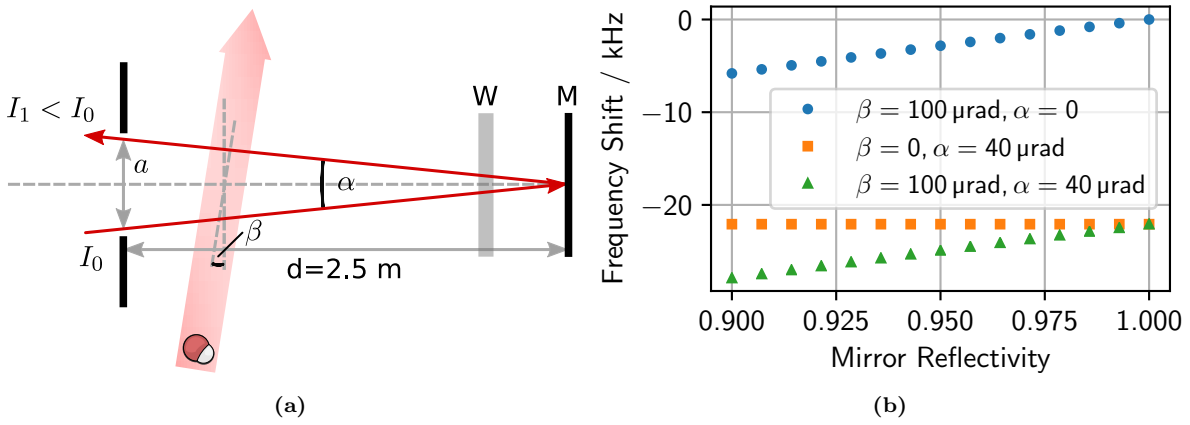

(a) (b)

Figure 7.2: (a) Schema of laser beam reflection at a mirror M passing a window W. This results in a intensity difference between the outgoing and the reflected laser beam. The angles α and β define the back reflection quality. (b) Frequency shift dependent of the mirror reflectivity, including losses from the window. At high mirror reflectivity the back reflection mostly relies on α.

resulting frequency shift is defined by two angles. The angle α is between the outgoing and incoming laser beam, while the deviation angle β of the molecular beam orientation is defined relative to the tilt of the mirror. Setting both angles at zero degrees and the mirror reflectivity at one results in a zero net shift. The net Doppler shift only remains zero, if both laser beams are identical. Thus, introducing additional optics, like a vacuum chamber window or a mirror reduces the intensity of the counterpropagating beam. This is severe for a small tilt of the molecular beam $\beta = 100\,\mu\text{rad}$, which yields a frequency shift of 7 kHz at a mirror reflectivity around 90 % (Figure 7.2b). Thus, it is crucial to use a mirror of high reflectivity and well transmissive windows. However, even a perfectly aligned molecular beam or an identical counter-propagating laser beam do not prevent a possible frequency shift caused by $\alpha > 0$. Assuming, both beams are within $a = 200\,\mu\text{m}$ at the aperture after a distance of 2.5 m, results in $\alpha = 40\,\mu\text{rad}$ and the interaction with slightly different velocity classes inside the molecular beam. The frequency shift is in this example around 22 kHz. In an experiment, both uncertainties of the angles α and β add up. The worst case net shift in this example is close to 30 kHz, with an unpredicted direction in the experiment, which leads to an uncertainty of ± 30 kHz.

The impact of the mode structure in geometric back reflection can also shift the laser frequency. As previously mentioned, both laser beams need to be identical. The best suited spatial mode is the fundamental transverse electromagnetic mode (TEM_{00}), which is the lowest order mode, coupled out of a confocal laser cavity. The measured light intensity is

the basis for the geometric back reflection setup. The procedure is to maximize first the intensity I_0 of the initial beam through the aperture and afterwards the power I_1 of the reflected beam through the same hole (Figure 7.2a). This technique minimized the angle α if both beams correspond to the TEM_{00} mode. However, additionally optics inside the cavity or windows after the cavity potentially generate higher order Hermite-Gaussian modes TEM_{0n}. Aligning the laser beam now on maximum intensity is no guarantee of superimposing both beam centers. The potential displacement of both beams introduces a frequency shift of the observed transition.

7.4 Recoil Shift

The translational motion of the molecules is in general not independent of the interaction with the electromagnetic wave, or more convenient in this case a photon. Assume that, the energy of the photon matches the resonance condition. An absorbing molecule is not putting all the energy of the incoming photon into the transition; some of this energy gets transformed into motion. The derivation of the recoil shift only relies on the conservation of energy and momentum [175].

$$h\nu_0 + \frac{1}{2}mv'^2 = h\nu + \frac{1}{2}mv^2 \tag{7.6}$$

$$mv' = mv - \frac{h\nu}{c} \tag{7.7}$$

After squaring the second equation and inserting it into the first, one gets an expanded Doppler-equation

$$\nu = \nu_0 \left(1 + \frac{v}{c} - \frac{h\nu_0}{2mc^2}\right). \tag{7.8}$$

The new additional part after the Doppler-shift is the recoil shift, which is usually in the range of kHz. A recoil is associated with the loss of photon energy into momentum. Therefore, the recoil shift has a negative sign, and the observed frequency is always redshifted. For the sake of clarification let's take a look at the following thought experiment (Figure 7.3a). A resting molecule in the ground state absorbs a photon of energy $h\nu$, gets exited with energy $h\nu_0$ and gains a momentum $p = h\nu/c$. Writing this energy equation out and repeating this for the case of a resting exited molecule emitting a photon leads to

$$h\nu = h\nu_0 + \frac{1}{2m}\left(\frac{h\nu}{c}\right)^2, \tag{7.9}$$

$$h\nu_0 = h\nu' + \frac{1}{2m}\left(\frac{h\nu'}{c}\right)^2. \tag{7.10}$$

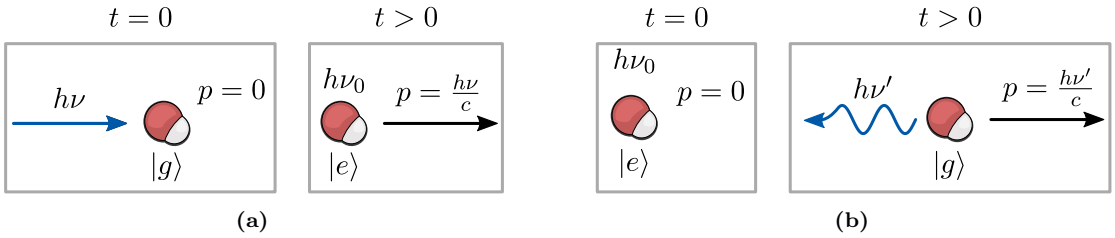

Figure 7.3: (a) The resting ($p = 0$) ground state OH molecule absorbs the photon $h\nu$ and gets excited, which results in the momentum $p = h\nu/c$. (b) The resting and excited OH molecule emits the photon $h\nu'$ and experiences simultaneously the recoil $p = h\nu'/c$.

The gain of kinetic energy after absorbing a photon is in the same order of magnitude as the recoil energy. Based on this assumption, the transition frequency is approximately

$$\nu_0 \approx \frac{1}{2}(\nu + \nu')\,. \tag{7.11}$$

Therefore, neither the frequency absorbed nor the emitted is of interest, but instead, the average sum of both frequencies. The recoil shift increases with decreasing mass of the molecules and increases quadratically with frequency, making it an essential contribution to the overall frequency shift of ultraviolet (UV) transitions in the rather light OH molecule.

Chapter 8

Molecule Field Interaction

The most crucial question of spectroscopy is the interaction between the molecule and the electric field. The coupling between the electric field and the molecule always influences the observed transition frequency. For clarification of these effects, it is convenient to first look at the atom-field interaction in a two-level system. In this simple picture, it makes no qualitative difference whether the particle involved in the interaction is an atom instead of a molecule. It is also a prominent canonical problem in quantum mechanics, which is described in detail by Daniel Steck[142]. This chapter summarizes the introduction by Steck before it proceeds to more complicated systems, involving momentum states of the atom inside an optical lattice (Section 8.4) or complex simulations of a laser induced fluorescence (LIF) spectra (Section 8.5).

8.1 Atom-Field Coupling strength

A two-level system consists of a ground state $|g\rangle$ and an exited state $|e\rangle$. The energy difference between the two states is ω_0 in frequency units. A laser with a frequency ω is applied to the system, and the detuning from the resonance is described with $\Delta = \omega - \omega_0$. In the case of no electric field, one can describe the free evolution Hamiltonian as

$$H_A = \hbar\omega_0 |e\rangle \langle e| = \hbar\omega_0 \sigma^\dagger \sigma. \tag{8.1}$$

The operator $\sigma = |g\rangle \langle e|$ on the right side is the atomic lowering operator. For the interaction between the atom and the field, it is convenient to make the dipole approximation, which assumes a constant electric field over the spatial extent of the particle. This leads to the atom-field interaction Hamiltonian[142]

$$H_{AF} = -\mathbf{dE} = -\langle g| \mathbf{d} |e\rangle \left(\sigma^\dagger + \sigma\right) \mathbf{E} \tag{8.2}$$

with the dipole operator $\mathbf{d}$ and the electric field $\mathbf{E}$. The decomposition of $\mathbf{d}$ is possible by multiplying it with the identity $(|e\rangle \langle e| + |g\rangle \langle g|)$ on both sides. Inserting the time

dependent electric field $\mathbf{E}(t) = E_0 \cos(\omega t)$ into Equation (8.2) yields

$$H_{AF} = \hbar\Omega \left(\sigma^\dagger + \sigma\right) \quad \text{with} \quad \Omega = -\frac{\langle g| \mathbf{d} |e\rangle E_0}{\hbar}. \tag{8.3}$$

The new parameter Ω is defined as the Rabi-frequency, which describes the coupling strength between the atom and the electric field.

8.2 Solving the Schrödinger Equation

The Schrödinger equation describes the time evolution of the system

$$i\hbar\partial_t |\psi\rangle = H |\psi\rangle = (H_A + H_{AF}) |\psi\rangle . \tag{8.4}$$

The ansatz of solving this equation is possible by using the general description of the state $|\psi\rangle = c_g |g\rangle + c_e |e\rangle$, with the complex parameters c_e and c_g taking the time dependence into account. Rewriting the Schrödinger equation in matrix notation yields

$$\partial_t \begin{bmatrix} c_e \\ c_g \end{bmatrix} = -i \begin{bmatrix} \omega_0 & \Omega\cos(\omega t) \\ \Omega\cos(\omega t) & 0 \end{bmatrix} \begin{bmatrix} c_e \\ c_g \end{bmatrix} = -\frac{i}{\hbar} H \begin{bmatrix} c_e \\ c_g \end{bmatrix} . \tag{8.5}$$

This is essentially a set of coupled differential equations containing oscillating terms at optical frequencies ω and ω_0. Instead of solving them directly, it is convenient to change the point of view into the frame of this fast oscillating field, which is the rotating-frame transformation (RFT). The RFT simplifies the problem further, by making the interaction of the atom with an alternating electric field to an interaction with a time-independent constant field. Essential for this transformation is that both the transformed state $|\widetilde{\psi}\rangle = U |\psi\rangle$ and the original state $|\psi\rangle$ satisfy the Schrödinger Equations (8.4)

$$i\hbar\partial_t |\widetilde{\psi}\rangle = \widetilde{H} |\widetilde{\psi}\rangle , \tag{8.6}$$

with $\widetilde{H}$ describing the transformed Hamiltonian. Based on this, the time-dependent unitary transformation of the Hamiltonian H is

$$\widetilde{H} = UHU^\dagger + i\hbar \left(\partial_t U\right) U^\dagger, \tag{8.7}$$

In the case of a two level system the transformation operator looks like

$$U = \exp\left(i\omega t |e\rangle \langle e|\right) = \begin{bmatrix} e^{i\omega t} & 0 \\ 0 & 1 \end{bmatrix} . \tag{8.8}$$

After performing this unitary transformation on the full system of Equation (8.5), the Schrödinger equation simplifies to the time independent form

$$\partial_t \begin{bmatrix} \widetilde{c}_e \\ c_g \end{bmatrix} = -i \begin{bmatrix} -\omega + \omega_0 & \frac{\Omega}{2}(1 + e^{2i\omega t}) \\ \frac{\Omega}{2}(1 + e^{-2i\omega t}) & 0 \end{bmatrix} \begin{bmatrix} \widetilde{c}_e \\ c_g \end{bmatrix} \overset{\text{RWA}}{\approx} -i \begin{bmatrix} -\Delta & \frac{\Omega}{2} \\ \frac{\Omega}{2} & 0 \end{bmatrix} \begin{bmatrix} \widetilde{c}_e \\ c_g \end{bmatrix} \tag{8.9}$$

with the detuning $\Delta = \omega - \omega_0$, which corresponds to the bare state energies $E_g = 0$ and $E_e = -\hbar\Delta$ in the uncoupled system (i.e. when $\Omega = 0$). The fast oscillating terms $e^{2i\omega t}$ and $e^{-2i\omega t}$ in Equation (8.9) are neglected using the rotating-wave approximation (RWA). Calculating the eigenvalues of the coupled system leads to

$$E_\pm = -\frac{\hbar\Delta}{2} \pm \frac{\hbar\widetilde{\Omega}}{2}, \tag{8.10}$$

with the generalized Rabi-frequency $\widetilde{\Omega} = \sqrt{\Omega^2 + \Delta^2}$. These new energies don't cross each other at $\Delta = 0$ anymore since the optical field lifts the degeneracy. However, for a large detuning Δ the coupling to the electric field is weak and the eigenvalues converge to E_g and E_e, respectively (Figure 8.1). The new eigenstates emerging from this two-level

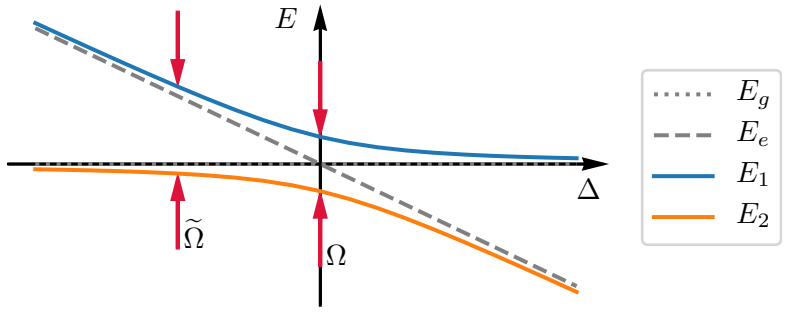

Figure 8.1: The coupling of the two states $|g\rangle$ and $|e\rangle$ with an AC electrical field lifts the degeneracy of the energies E_g and E_e at zero detuning.

system are[176]

$$|1\rangle = \sin\Theta\,|g\rangle + \cos\Theta\,|e\rangle\,, \tag{8.11}$$

$$|2\rangle = \cos\Theta\,|g\rangle - \sin\Theta\,|e\rangle\,, \tag{8.12}$$

with $\tan(2\Theta) = -\frac{\Omega}{\Delta}$. These new dressed states $|1\rangle$ and $|2\rangle$ mix the uncoupled bare states $|e\rangle$ and $|g\rangle$.

8.3 Dressed States

The bare states are no longer eigenstates of the coupled Hamiltonian, but expressing them as a superposition of dressed states is possible. Especially at resonance $\Delta = 0$, when both

dressed states are equally mixed, they simplify to

$$|g\rangle = \tfrac{1}{\sqrt{2}}(|1\rangle + |2\rangle), \tag{8.13}$$

$$|e\rangle = \tfrac{1}{\sqrt{2}}(|1\rangle - |2\rangle). \tag{8.14}$$

The time evolution of the wavefunction is calculated with the operator [142]

$$U(t) = \sum_{n=1}^{2} \exp\left(-\frac{i}{\hbar} E_n t\right) |n\rangle \langle n| . \tag{8.15}$$

If the wavefunction at $t = 0$ consists only of the ground state $|g\rangle$, applying the time evolution operator on $|g\rangle$ leads to [142]

$$|\psi(t)\rangle = U(t)\,|g\rangle = e^{-iE_1 t/\hbar}\,|1\rangle + e^{-iE_2 t/\hbar}\,|2\rangle \tag{8.16}$$

$$= e^{-i\Omega t/2}\,|1\rangle + e^{i\Omega t/2}\,|2\rangle \approx |1\rangle + e^{i\Omega t}\,|2\rangle\,, \tag{8.17}$$

neglecting the normalization, as well as the overall phase. At the time $\Omega t = \pi$ the wavefunction changes to $|\phi\rangle = |e\rangle$, while at the time $\Omega t = 2\pi$ the wavefunction is again $|\phi\rangle = |g\rangle$. Thus, the wavefunction is oscillating between the ground and the excited state with the Rabi-frequency Ω. This effect is named Rabi-flopping.

The momentum of the atom changes after absorbing or emitting a photon (Section 7.4). These momentum changes can correspond with frequency shifts, caused by the radiation pressure or the dipole force. The radiation force is defined by

$$\mathbf{F}_{rad} = \hbar \mathbf{k} R_{sc}, \tag{8.18}$$

with the photon scattering rate R_{sc}. It can be used to explain Doppler-cooling of atoms in fields of counterpropagating laser beams. With low laser power, cooling is achieved by red detuning the laser frequency relative to the resonant frequency. The dressed state model can be used to explain this effect [177]. In this picture, the Hamiltonian associated with the energy in the electric field is described by [142]

$$H_R = \hbar\omega a^\dagger a, \quad \text{with} \quad a = \sum_{n=1}^{\infty} \sqrt{n}\,|n-1\rangle \langle n| \tag{8.19}$$

where a is the field annihilation operator lowering the photon number n in the photon state $|n\rangle$ by one. The photon number is the most significant quantity of a state. In case of no atom-field coupling, the bare states in one manifold ε_n are $|g, n+1\rangle$ and $|e, n\rangle$ (Figure 8.2a). The manifolds are separated by the laser frequency ω, and the two states inside one manifold are separated by the detuning Δ. If an atom moves into an electric

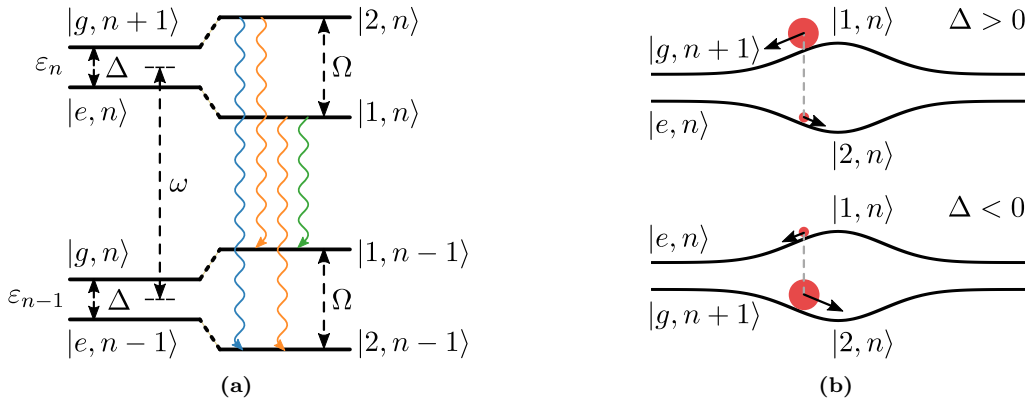

Figure 8.2: (a) Energy schema of dressed states bunched into to separate manifolds. (b) Geometric representation of the dressed states energy level across a spatially-varying laser field. The atom experiences a force into the direction of maximum field intensity, if the initial state is $|g, n+1\rangle$ and the detuning is $\Delta < 0$ (adapted from [177]).

field, the bare states start mixing. The dressed states are labeled $|1, n\rangle$ and $|2, n\rangle$. Since a transition involves only one photon, only transitions between manifolds with n differing by 1 are possible. Since both dressed states contain a ground and an excited state, four possible transitions are allowed. Two of these transitions have nearly the same frequency, which leads to a tripled structure in the fluorescence spectrum, denoted as a Mollow-triplet [178]. The atom experiences forces proportional to ∇E_i inside an electric field which average to [177]

$$\mathbf{F}_{dip} = -\Pi_1^{st} \nabla E_1 - \Pi_2^{st} \nabla E_2, \tag{8.20}$$

with the probabilities of occupation Π_i^{st} of the states $|i, n\rangle$ for $i \in [1, 2]$. A reason for the change in the electric field E_i can be as simple as the Gaussian intensity distribution of a laser beam. For example, atoms passing perpendicular a laser beam experience a rise and fall of the mean electric field amplitude. The probability of occupation Π_i^{st} depends on the detuning of the laser. If the frequency of the electric field is blue detuned $\Delta = \omega - \omega_0 > 0$ and the atom starts in the ground state $|g, n+1\rangle$, than according to Figure 8.2a, the state $|g, n+1\rangle$ is higher in energy than the state $|e, n\rangle$. Inside the electric field, both dressed states $|1, n\rangle$ and $|2, n\rangle$ are a linear superposition of the bare states (Figure 8.2b upper). The state $|1, n\rangle$ is more strongly populated than $|2, n\rangle$ because it adiabatically transits to $|g, n+1\rangle$ outside of the field. The population Π_1^{st} of the state $|1, n\rangle$ dominates the dipole force (Equation (8.20)) and the atoms get expelled from the high-intensity region of the electric field. In the case of a field with a red-detuned frequency $\Delta = \omega - \omega_0 < 0$, the energies of the bare states outside the electric field are reversed (Figure 8.2b lower). Therefore, the population of the dressed state $|2, n\rangle$ is higher than the state $|1, n\rangle$, and the atoms are attracted to the high-intensity region of the field. For atoms passing perpendicular a laser beam, this region is usually in the center of the beam. High-resolution spectroscopy often requires correction for potential Doppler-shifts.

A standard technique to achieve this involves two counter-propagating laser beams created by the reflection of the initial laser beam on a mirror. However, this creates a new spatial intensity distribution which deviates from that of a single laser beam.

8.4 Momentum States in Optical Lattices

Deriving the spatial field distribution of two counterpropagating laser beams starts with two electromagnetic waves with the same amplitude E_0 moving in opposite directions

$$E(t) = E_0(e^{i(\omega t - kx)} + e^{i(\omega t + kx)} + c.c.) = \underbrace{(e^{i\omega t} + e^{-i\omega t})}_{=2\cos(\omega t)} \underbrace{(e^{ikx} + e^{-ikx})}_{=2\cos(kx)} \tag{8.21}$$

The periodic spatial structure of this standing wave is defined by the wavenumber k. The periodicity leads to an intensity distribution of equally-spaced regions of high and low field intensity, namely an optical lattice. The light force shift, the atoms experience inside this structure, affects their momentum (Section 8.3). During the interaction time inside a resonant electric field, the atom changes its internal state. Such transitions can be accompanied by a change of the momentum. The abstract wave function of an atom is described by the wavefunction $\Psi_{i,k} = |\Psi_i\rangle\,|k\rangle$, with the internal state $|\Psi_i\rangle$ and the external momentum state $|k\rangle = e^{ikx}$. A transition between two different states requires a non-vanishing transition dipole moment

$$\langle\Psi_{i_1,k_1}|\,(-\mu E(t))\,|\Psi_{i_2,k_2}\rangle \propto \langle\Psi_{i_1}|\,(\mu\cos(\omega t))\,|\Psi_{i_2}\rangle\,\langle k_1|\cos(kx)\,|k_2\rangle\,. \tag{8.22}$$

Here, the wave function of the atom has been separated into two parts. The first part describes the internal transition of the atom. The second part takes the spatial variation of the interaction potential and the momentum into account and leads to

$$\frac{\langle k_1|\cos(kx)\,|k_2\rangle}{\sqrt{\langle k_1|k_1\rangle\,\langle k_2|k_2\rangle}} = \lim_{a\to\infty}\sum_{q=\pm1}\frac{\int_{-a}^{a} e^{i(k_2-k_1+qk)x}dx}{2\int_{-a}^{a}dx} = \begin{cases} 1/2 & \text{if} \quad k_2-k_1+k=0 \\ & \text{or} \quad k_2-k_1-k=0 \\ 0 & \text{otherwise} \end{cases} \tag{8.23}$$

The much lager spatial distribution of the atom beam compared to the node spacing of the lattice is taken into account by the approximation $a \to \infty$. According to this equation, only momentum changes of $\Delta k = \pm k$ are allowed. In the photon picture, this is equivalent to noting that a change of internal state is always accompanied by the emission or absorption of a recoil photon with momentum $kr = k$. The quantization of the momentum allows the construction of the quantum mechanical operator

$$\tilde{\mathbf{p}} = \hbar\sum_{n=-N}^{N}|n\rangle\,\langle n|\,(nk_r + k_0)\,, \tag{8.24}$$

The initial momentum of the atom k_0 can only change by an integer multipe of the recoil momentum k_r. N defines the size of the momentum space for the momentum states $|n\rangle$, with the momentum number n. The corresponding Hamilton operator is

$$H_p = \frac{\tilde{\mathbf{p}}^2}{2m} = \frac{\hbar^2 k_r^2}{2m} \sum_{n=-N}^{N} |n\rangle \langle n| \left(n + \frac{k_0}{k_r}\right)^2 = \hbar\delta p^2, \tag{8.25}$$

where $p = \tilde{\mathbf{p}}/(\hbar k_r)$ is the new momentum operator and δ is the angular frequency of the recoil energy. The free-space Hamiltonian H_A in Equation (8.9) can be adapted to include the RFT (Section 8.2) by substituting the detuning $\Delta = \omega - \omega_0$ for ω_0

$$H_A = \Delta\hbar\sigma^\dagger\sigma. \tag{8.26}$$

The atom-field interaction Hamiltonian from Equation (8.3) is adapted to include the momentum states:

$$H_{AF} = \mu E(\sigma + \sigma^\dagger)(b + b^\dagger), \tag{8.27}$$

with the ladder annihilation operator b. This operator reduces the momentum number n of a state by one $b\,|n\rangle = |n-1\rangle$, while its adjoint, the creation operator $b^\dagger$ increases the momentum number by one $b^\dagger\,|n\rangle = |n+1\rangle$. This description completely neglects any interaction between atoms. A transition between momentum states of the atom is only possible by interaction with the electric field. For example, an interaction caused by $\sigma^\dagger b^\dagger$ describes the absorption of one photon and the increase of the momentum number n by one. Reducing or increasing the momentum number describes the direction of the recoil momentum along one axis. Finally, putting all terms of the Hamiltonian together and transforming all energies into angular frequencies leads to the full Hamiltonian

$$H = H_A + H_p + H_{AF} = \Delta\sigma^\dagger\sigma + \delta p^2 + \frac{\mu E(t)}{\hbar}(\sigma + \sigma^\dagger)(b + b^\dagger). \tag{8.28}$$

The beauty of this representation is its complete independence from spacial coordinates. The atom is delocalized inside the field of the standing wave (Figure 8.3a). To study the

Figure 8.3: (a) Schematic of a laser retroreflected at a mirror M, with a atom beam moving perpendicular through the light field. The individual atom is delocalized inside the standing wave. (b) The field distribution of the standing wave has a Gaussian line shape along the propagation direction of the atoms.

influence of the electric field on the momentum distribution of the atom, one has to look

at the time evolution of the system. The atom has a perpendicular velocity component to the Gaussian beam, which limits the interaction time. The time dependence of the electric field is approximated by a Gaussian function, with an interaction time defined by the velocity of the atom beam and the diameter of the laser beam (Figure 8.3b).

8.4.1 Lindblad Master Equation

The Schrödinger equation describes, in general, the time evolution of a closed quantum mechanical system and can be solved by transforming the system into a matrix representation and solving the coupled differential equations (Section 8.2). For the sake of clarity, the previous discussion greatly simplified the problem by assuming a two-level system with pure states. The Hamiltonian including momentum (Equation (8.28)) involves more than just two states. Also, pure states are only valid for a closed system. As soon as dissipation is involved, the system is open. One major dissipation process in the systems of interest here is spontaneous emission. It is the basis of LIF and the associated light force shift. Therefore, a more-complete theoretical description is necessary, which the density matrix formalism provides. The general expression of the density operator is

$$\rho = \sum_i P_i \left|\psi_i\right\rangle \left\langle\psi_i\right| , \tag{8.29}$$

with the pure states $|\psi_i\rangle$ and the probability P_i assigned to this state. An operator with multiple probabilities P_i describes a mixed state. The particular case of $\rho = |\psi\rangle \langle\psi|$ describes a pure state. The ability to describe both pure states and incoherent superpositions of different states is the strength of the density matrix formalism. The evolution of the density operator without dissipation follows out of the time-dependent Schrödinger equation and is called the von Neumann equation

$$\frac{\partial \rho}{\partial t} = -\frac{i}{\hbar} \left[H, \rho\right] . \tag{8.30}$$

So far the system is still closed. The generalized form of the von Neumann equation is the Lindblad master equation [179]

$$\frac{\partial t}{\partial \rho} = -\frac{i}{\hbar} \left[H, \rho\right] - \frac{1}{2} \sum_n \left[L_n^\dagger L_n \rho(t) + \rho(t) L_n^\dagger L_n - 2 L_n \rho(t) L_n^\dagger\right] , \tag{8.31}$$

with the Lindblad operators L_n, which introduce dissipation [180,181]. In case of spontaneous emission, one can describe a Lindblad operator as the product $L_n = \sqrt{\gamma_n} Q_n$ of the decay rate γ_n and the coupling operator Q_n to an external reservoir.

The following discussion uses a three-level system with a dark state $|d\rangle$, an excited state $|e\rangle$ and a ground state $|g\rangle$ as a model for the intrinsic atom state $|\psi_i\rangle$ (Section 8.4). Additionally, the momentum states $|n\rangle$ are included in the wavefunction. The total wave-

function is described by

$$\psi_{\text{tot}} = |\psi_i\rangle \otimes |n\rangle \,. \tag{8.32}$$

Therefore, all operators of the momentum Hamiltonian (Equation (8.28)) need to address both factors in this tensor product. Mostly, one needs to differentiate between operators affecting the internal state of the atom and operators changing the momentum. This leads to using $\sigma \otimes I_{2N+1}$ instead of σ, $I_3 \otimes b$ instead of b and $I_3 \otimes \tilde{p}$ instead of $\tilde{p}$. A new set of dissipative coupling operators Q_n describe decays from the excited internal state to the dark state and are defined by $Q_n = |d\rangle \langle e| \otimes |n\rangle \langle n|$. Note that each momentum number state $|n\rangle$ decays independently. Now everything is ready to calculate the time evolution of the system. The starting point is the absolute ground state $|\psi_0\rangle = |g\rangle \otimes |0\rangle$. The state $|0\rangle$ for the momentum number $n = 0$ doesn't mean the initial momentum of the molecule is zero, but simply refers to the initial momentum state with momentum k_0 (Equation (8.24)). The term of interest is the amount of spontaneous emission after the interaction with the electric field, which is proportional to the final population of the dark state $|d\rangle$. This can be computed by summing the $|d\rangle \langle d| \otimes |n\rangle \langle n|$ elements of the density matrix after the interaction with the electric field. A single solution of the Lindblad equation leads to a population of the dark state for a specific set of initial parameters, which are designed to approximate a molecular beam of hydroxyl radical (OH) (Section 8.4.2). The Lindblad equation is solved multiple times, using the open-source Python QuTiP library[182,183], to obtain a whole spectrum. After superimposing all solutions as a function of the detuning Δ from resonance, one obtains a typical Doppler broadened spectrum (Figure 8.4a). The

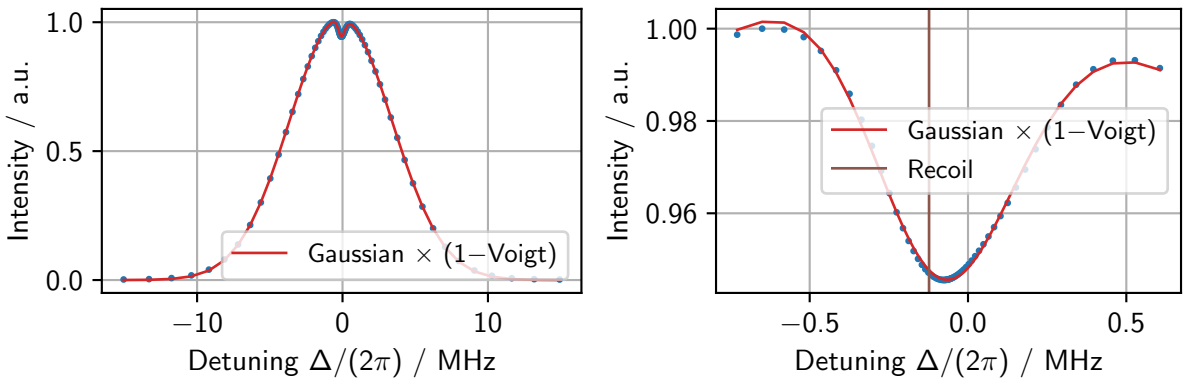

Figure 8.4: (a) Simulated fluorescence spectrum after the time evolution of the Lindblad equation using a Gaussian velocity distribution of OH molecules. (b) Zooming in on the resonance frequency $\Delta = 0$ shows a shift of the Lamb dip, which is displaced from the recoil frequency at the center of the profile.

center of this profile is always red shifted by the OH recoil frequency of 123 kHz. The spectrum can be fit with the product of a Gaussian function and a pseudo-Voigt dip on a uniform background (red curves in Figure 8.4b). The Gaussian function matches the expected Doppler broadening distribution and recoil shift, while the pseudo-Voigt

function approximates the saturation dip (Figure 8.4b). Zooming in on the Lamb dip shows not only a discrepancy of the fit but also a shift away from the recoil frequency. This observation is an essential conclusion when considering saturation spectroscopy in molecular beams, and is part of a later discussion (Section 8.4.3).

8.4.2 Discussion of Simulation Parameters

The size of the individual simulation parameters is roughly oriented on the OH molecule investigated in this thesis. Each value of the detuning Δ and the initial momentum k_0/k_r need a separate solution of the Lindblad equation. A whole spectrum is created by solving the Lindblad equation multiple times and superimposing the individual results. The range of the detuning depends on the momentum distribution of the molecules. In general, most of the molecule's momentum is along the propagation direction of the molecular beam, and only a small fraction is along the electric field axis. Both the perpendicular $p_\perp$ and the parallel component $p_\parallel$ of the momentum are important. The interaction of the standing wave with the momentum of the molecules is determined by $p_\parallel$. Therefore, the initial momentum k_0/k_r always refers to $p_\parallel$. The momentum $p_\parallel$ is assigned a Gaussian probability distribution with a maximum at zero momentum and a full width at half maximum (FWHM) corresponding to 2.5 m/s ($k_0/k_r \approx 13.9$). To calculate the full spectral range Δ, the initial momentum k_0/k_r should at least cover the range Δ/δ. A minimum step size of $\Delta k_0/k_r = 0.1$ is recommended. The second momentum component $p_\perp$ defines the interaction time inside the electric field. The calculations assume a constant velocity around 340 m/s and a full width ($1/e$) of the laser beam diameter of 1 mm and determine the time evolution of the electric field strength based on this (Figure 8.3b). With the velocity and beam width given above the molecules spend around 3 µs inside the high-intensity region of the field. This duration is more than four times the lifetime of the excited state $\tau = 0.688\,\mu s$[184]. The coupling strength of the molecule field interaction is defined by the electric field E and the transition dipole moment μ, which are fixed at $\mu E/h = 0.05$ MHz. Finally, the number of momentum states needs a limitation to keep the time evolution solvable. In general, multiple steps of absorption and emission of photons are possible, and each step corresponds to a change of the momentum state. However, the counter-propagating beams reduce the probability of gaining a net momentum change greater than one recoil. This yields an exponential decay of finding a molecule in a momentum state greater one. In all simulations, the momentum space is limited to $N = 3$. This last definition completes the list of all parameters involved in simulating saturated fluorescence spectra of OH inside a molecule beam, with emphasis on the light force shift (Figure 8.4a-8.4b).

8.4.3 Shift of the Saturation dip

The position of the Doppler-broadened fluorescence signal is always red-shifted by one recoil, while the position of the saturation dip shows a somewhat different behavior. To investigate this effect further, it is convenient to eliminate the Doppler-background. One possibility for removing the background is by replacing the initial Gaussian momentum spread with a rectangular function and weighting all momentum classes equally. Each momentum class contributes to the background by emitting light described approximately by a Lorentzian function, with a width corresponding to the natural linewidth. The background is approximated with

$$I_b(f) = a\frac{f_c}{\pi(f_c^2 - (f - f_0)^2)} + b, \tag{8.33}$$

where a is a scaling parameter, b an offset parameter, f_0 the center frequency and f_c the cutoff frequency of the background. Fitting only the points furthest away from the saturation feature and subtracting the fit from the whole profile leads to a proper saturation dip (Figure 8.5a). All attempts of fitting an analytical function to this dip failed. Neither

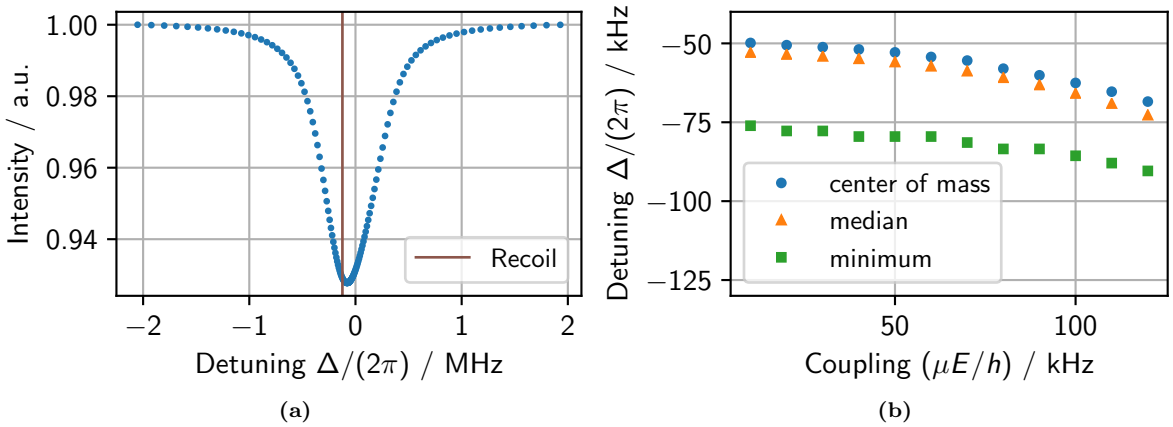

Figure 8.5: (a) Background free saturation dip at $\mu E/h = 50\,\text{kHz}$ (b) Extracted saturation dip positions at different coupling strengths $\mu E/h$. Dependent on the method extracting the dip position, one obtains different answers.

an asymmetric pseudo-Voigt function [185] nor a multi Lorentzian function, consisting of 20 individual Lorentz functions can produce consistent results. Only non-fit-based techniques, involving the extraction of the center of the Lamb dip, remain. Furthest away from the recoil frequency are the center of mass and the median of the Lamb dip. The minimum of the saturation dip is closest to the recoil frequency. The profile is asymmetric and makes the determination of a precise frequency within this range vague. Furthermore, increasing the coupling strength between the field and the molecule shifts the dip position (Figure 8.5b). For example, an increase of the coupling from $\mu E/h = 50\,\text{kHz}$ to $\mu E/h = 100\,\text{kHz}$ shifts the dip by around 10 kHz closer to the recoil frequency. A general conclusion from this analysis is that the Lamb dip is always located between the resonance frequency $\Delta = 0\,\text{Hz}$

and the recoil frequency $\delta/(2\pi) = -123\,\mathrm{kHz}$, nearly independent of the field strength.

Considering only single momentum classes helps to understand this effect. Most important is again the subtraction of the background. The fluorescence of a single momentum class is represented by a Lorentzian function. In the case of two counter-propagating beams, two Lorentzian functions are associated with one momentum class. They are centered around the recoil frequency: one at $(-1 + 2k_0/k_r)\delta/(2\pi)$ and the other at $(-1 - 2k_0/k_r)\delta/(2\pi)$. The periodicity of the standing wave gets averaged away for high momentum classes. However, fluorescence peaks of low momentum classes move closer together until they are indistinguishable. In this range, saturation occurs in conjunction with a growing light force shift. Especially at low coupling strength, for instance, $\mu E/h = 10\,\mathrm{kHz}$, the change of amplitude is small compared to the overall size of the fluorescence peak. A proper subtraction of the individual fluorescence peaks excluding interaction becomes crucial. The separation of the two counterpropagating beams is possible, by removing the terms $\sigma b^\dagger + \sigma^\dagger b$ or the terms $\sigma b + \sigma^\dagger b^\dagger$ from the interaction Hamiltonian (Equation (8.28)). Calculating the fluorescence from each of the individual beams and adding the results describes the fluorescence background. The background resolved saturation dip minimum is close to the recoil frequency for the zero momentum class $k_0/k_r = 0$. At higher momentum classes $k_0/k_r > 0$ the minimum moves towards the resonance frequency $\Delta = 0\,\mathrm{Hz}$ and ultimately passes it (Figure 8.6a). Simultaneously, the

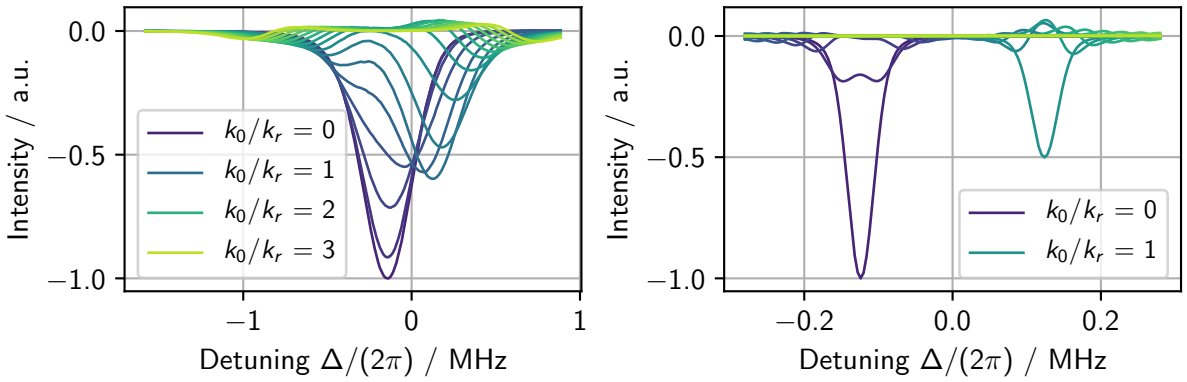

Figure 8.6: (a) Frequency shift of one broad saturation dip for different momentum classes. (b) Two pronounced saturation dips at defined momentum classes after reducing the natural linewidth by a factor of 10.

amplitude decreases until nearly zero at $k_0/k_r = 3$. The wave-like behavior around zero is rooted in interference effects involving both interacting laser beams.

To investigate this effect further, the fluorescence peaks are artificially narrowed. The rate of spontaneous emission used thus far corresponds to a natural linewidth of 231 kHz. Increasing the lifetime of the excited state by a factor of 10 reduces the linewidth by the same amount. Simultaneously, the interaction time of the molecule inside the electric field is also increased by 10. The resulting saturation dips are now well separated at the recoil

frequencies $\pm\delta/(2\pi)$. The first dip only appears for the zero momentum class $k_0/k_r = 0$ and the second just for $k_0/k_r = 1$, with an amplitude half as strong. Thus, a system with a broad natural linewidth would result in a single minimum in between those dips. Simultaneously, it opens a question, why are two Lamb dips present?

In general, saturation only happens if both counterpropagating beams are interacting with the same momentum class. This condition is satisfied under two sets of circumstances. First, if the photon energy is at one recoil higher, then both laser beams interact with the zero momentum ground state, which will be depleted. This depletion is the expected case and would result in a Lamb dip precisely at the center of the Doppler-broadened background. Second, if the photon energy is lower by one recoil, a certain velocity class of molecules against the direction of the wave vector are excited and end up at rest with zero momentum. This leads to a center peak in the momentum distribution of excited molecules. The rate of spontaneous emission is equal for all momentum classes, but stimulated emission driven by the other laser depletes the peak in the excited state momentum distribution and leads to a saturation dip at the recoil frequency $\delta/(2\pi)$. A quasi-classical prediction of this effect by Wigner functions is known since 1969 [186]. The first measurements followed 1973 on methane [187,188] and later on iodine [189].

Going into more detail and analyzing the exact position of the Lamb dip at $k_0/k_r = 1$ shows a small deviation from the prediction. The actual saturation dip is asymmetric with a center of mass shifted dependent on the size of the coupling parameter μE. This linear shift is around 1 kHz for $\Delta\mu E/h = 10$ kHz, which is associated with the light force. Going back to the overall shift of the saturation peak with a natural linewidth of 231 kHz leads to a shift more than twice as large (Figure 8.4a-8.4b). The light force shift contributes to it, but the second and more dominant effect is the saturation of the $k_0/k_1 = 1$ momentum class. The LIF spectra in this thesis are dominated by the Doppler-broadened background, which stays unaffected by the investigated shifts. Thus, it is justified to avoid the treatment of momentum state related shifts in subsequent analysis.

8.5 Quantum-Mechanical Simulation of LIF Spectra

The Lindblad master equation has proven to be a reliable tool in describing the time evolution of multiple momentum states (Section 8.4.1). However, another important application is calculating the evolution of a molecular wavefunction when multiple quantum-mechanical states are involved. For all spectra measured in this thesis, an analysis has been performed using the Lindblad master equation, which has been implemented in the open-source Python framework QuTiP [182,183]. The following description assumes an effective Hamiltonian that describes the $A^2\Sigma^+$, $v' = 0$ and $X^2\Pi_{3/2}$, $v'' = 0$, $J'' = 3/2$ states in OH and the deuterated hydroxyl radical (OD) as well as the transition dipole moments between two electronic states. The spectroscopic parameters are either known

from previous works or estimated from rudimentary fits of the spectra, and the effect of the external magnetic field of 75 µT is also included in the Hamiltonian (Section 9.8.2). The Hamiltonian matrix is calculated using the program PGOPHER and extended to include the effect of the electric field from the two counter-propagating laser beams. The extended Hamiltonian is then inserted into the Lindblad master equation and used to calculate the evolution of the density matrix. The density matrix can be used to determine the LIF spectrum that would result from a molecule with a specific trajectory, and combining spectra from all possible trajectories can be used to construct a composite spectrum. The fit of these simulated LIF spectra to the measured spectra is discussed in Section 10.1.

The Hamilton matrix is calculated with the program PGOPHER for an effective Hamiltonian parameter set in a 75 µT magnetic field and zero electrical field. The eigenstates from this calculation are used as the basis states for further calculations, so the eigenenergies correspond to the diagonal elements of the Hamilton matrix. PGOPHER can compute the transition dipole moment between the space-fixed basis states but requires the molecule-fixed transition dipole moment as a scaling factor. This factor is determined using the lifetime of the first electronic excited state $v' = 0$, $N' = 0$ of $t_{21} = 688\,\mathrm{ns}$, which corresponds to the Einstein coefficient $A_{21} = 1/t_{21}$ [184]. Thus, the normalization factor for all $A - X$ transitions is [190]

$$|\langle A, v' = 0|\, T^1_{q=\pm1}(\vec{\mu})\, |X, v'' = 0\rangle| = \sqrt{\frac{A_{21}}{g_2}\frac{3\epsilon_0 hc^3}{2\omega_{21}^3}} = 0.26\,\mathrm{D}, \tag{8.34}$$

with the angular transition frequency $\omega_{21} = 2\pi c/308\,\mathrm{nm}$ and the degeneracy factor $g_2 = 2$. The degeneracy is caused by two decay channels, namely from $\Lambda = 0$ ($A^2\Sigma^+$) to $\Lambda = \pm1$ ($X^2\Pi$). Another requirement of the Lindblad master equation are the radiative decay rates of all M state resolved transitions. These rates are equal to the Einstein A coefficients and can be calculated from the transition dipole moments [190]

$$\gamma_i = \frac{2\omega_{21}^3 \mu_i^2}{3\epsilon_0 hc^3}, \tag{8.35}$$

In general, the relevant number of basis states for the simulation depends on the number of transitions in the cluster being measured. In these calculations only transitions, which are within 2 GHz of the measured transitions are included. Since the LIF measurement depends on the reemitted fluorescence light, it is important to include all ground state levels X, $v'' = 0$ with allowed transitions to the A states already included. Since large matrices result in long computation time, the number of basis states is reduced by considering only transitions satisfying the selection rule $J = \pm1$ and 0. All other transitions are extremely weak, which justifies the procedure. After the reduction, there are a maximum of 84 left for OH and 126 basis states for OD (Table 8.1), though some transitions clusters require

fewer basis states. The bare Hamilton matrix H_0 can now be defined as a diagonal matrix

Table 8.1: Maximum number of basis states involved in the calculation of the LIF spectra in this thesis. The ground state X, $v'' = 0$ is separated into initial states and final states after decay.

	Number of basis states for	
	OH	OD
X, $v'' = 0$, $\Omega'' = 3/2$, $J'' = 3/2$ initial states	8	12
A, $v' = 0$ excited levels	12	18
X, $v'' = 0$ to which the A states potentially decay	64	96

which contains the eigenenergies of the basis states. In the next step, we consider the interaction with the electric field of the laser.

Two counterpropagating Gaussian beams with equal intensity create a time and space dependent electrical field

$$E_x(x, y, z, t) = 2\sqrt{\frac{\mu_0 c P_0}{\pi \omega_0^2}} \exp\left(-\frac{x^2 + z^2}{\omega_0^2}\right) \cos\left(\frac{2\pi\nu y}{c}\right) \times \left[\exp(2\pi i\nu t) + \exp(-2\pi i\nu t)\right], \tag{8.36}$$

with the impedance of free space $\mu_0 c \approx 377\,\Omega$, the laser power in one propagation direction P_0, the laser frequency ν and the waist $w_0 = 0.5\,\mathrm{mm}$, which corresponds to the $1/e^2$ beam radius. The propagation direction of both laser beams is along the y-axis, with a linear polarization along the x-axis. The electric field and the off-diagonal transition dipole moment matrix μ_x couple the hyperfine states with $\Delta M_F = \pm 1$, leading to the total Hamilton matrix

$$H = H_0 - E_x \mu_x. \tag{8.37}$$

As in the previous calculations (Section 8.2), the large optical frequency in Equation (8.36) results in a fast oscillation of the density matrix, which makes the numerical evaluation challenging. Therefore, it is convenient to apply a time-dependent unitary transformation again and invoke the RWA. The transformation of H is identical to before (Equation (8.7)), while the transformations of ρ and A are

$$\widetilde{\rho} = U^\dagger \rho U \quad \text{and} \quad \widetilde{A}_i = U^\dagger A_i U. \tag{8.38}$$

The transformed matrices preserve the form of the Lindblad master Equation (8.28). The transformation operator itself $U = \exp(2\pi i\nu t \left|A\right\rangle \left\langle A\right|)$ is identical to the transformation operator of the two level system (Equation (8.8)), except the dimension is expanded. The ground state $|g\rangle$ and the excited state $|e\rangle$ correspond now to the multiple X and A states, respectively. Finally, the time-independent Hamiltonian after the unitary transformation

and the RWA is given by

$$\widetilde{H} = \widetilde{H}_0 - 2\mu_x \sqrt{\frac{\mu_0 c P_0}{\pi \omega_0^2}} \exp\left(-\frac{x^2+z^2}{\omega_0^2}\right) \cos\left(\frac{2\pi\nu y}{c}\right). \tag{8.39}$$

The difference between $\widetilde{H}_0$ and H_0 is a frequency shift of all A levels by $-h\nu$.

The Lindblad master equation with the new Hamiltonian operator $\widetilde{H}$ determines the evolution of the density operator for a single molecule, passing the electric field E_x of the two counter-propagating laser beams. At the beginning of the simulation, the molecule resides in an incoherent mixture of the ground states X, $v'' = 0$, $\Omega'' = 3/2$, $J'' = 3/2$, with an equal population in each state. During the time evolution of the Lindblad equation, the molecule passes the electric field and emits fluorescence light. Calculating the weighted sum over the populations of all A states, with the weighting factor of the total fluorescence decay rate of each A state, leads to an approximation of the fluorescence light. The total decay rate of an individual A state is the sum over all decay rates to the multiple X, $v'' = 0$ states. The motion of the molecules along the z-axis of the magnetic field corresponds to the mean forward velocity of the molecular beam at $v_z = 340\,\mathrm{ms}$. The velocity v_z limits the interaction time with the laser which propagates along the y-axis (Figure 8.7a). Ignoring the polarization state of the field leaves the molecule motion along the x and

Figure 8.7: (a) Schema of a single molecule passing perpendicular a standing wave, with a well defined position of the molecule along the y-axis. (b) Schema of the Gaussian power distribution of the electric field along the x-axis.

z-axis equivalent. Since both axes are equivalent and $v_z \gg v_x$, v_x is fixed at 0. However, the velocity of the molecule along the laser axis v_y remains an adjustable parameter, along with its coordinates x, y, the laser power P_0 and laser frequency ν. In the following, the y coordinate at closest approach to the center of the molecular beam ($z = 0$) is y_0 and the x parameter is merged with the laser power to $\widetilde{P}_0(x) = P_0 \exp(-2x^2/\omega_0^2)$. Thus, the fluorescence light of a single molecule passing the laser beam corresponds to $I(\nu, \widetilde{P}_0, v_y, y_0)$. Considering the spatial extent of the molecular beam requires an integral over all possible positions y_0, x and velocities v_y of the individual molecule. Therefore, the total fluorescence

intensity in the experiment is proportional to

$$S(\nu, P_0, \sigma) = \int_0^\infty \int_0^\infty \int_0^{\frac{c}{4\nu}} \exp\left(-\tfrac{\Delta_\nu^2}{2\sigma^2}\right) I\left(\nu, \widetilde{P}_0(x), \tfrac{c\Delta_\nu}{\nu}, y_0\right) dy_0 d\Delta_\nu dx, \tag{8.40}$$

with the substitution $\Delta_\nu = \nu v_y/c$. The line-broadening σ accounts for the velocity distribution along the y-axis. Finally, the whole spectrum can be determined by calculating $S(\nu, P_0, \sigma)$ at each frequency ν in a region around the transition frequency. However, it is convenient to approximate the expensive calculation of $S(\nu, P_0, \sigma)$.

For the numerical evaluation the inner integrals are separated into different ranges of $\Delta\nu$, which correspond to a molecule's velocity along the laser beam. In the range of Δ_ν from 0 to 2 MHz the integral over Δ_ν is replaced by a sum with a 50 kHz interval size. If Δ_ν reaches values > 400 kHz the velocity v_y of the molecule dominates the integral over the specific position y_0. Therefore, a fast-moving molecule experiences a frequent alternation of nodes and anti-nodes of the standing wave. The starting point of the molecule becomes arbitrary, which justifies the evaluation of the integral at a single coordinate $y_0 = 0$. In contrast, if $\Delta_\nu \leq 400$ kHz, the integral over y_0 is approximated by averaging the values at $y_0 = 0$ and $y_0 = c/(4\nu)$. Finally, if $\Delta_\nu > 2$ MHz, the molecule interacts with only one of the two counterpropagating beams, and the fluorescence signal simplifies to

$$I\left(\nu, \widetilde{P}_0(x), \tfrac{c\Delta\nu_y}{\nu}, 0\right) \approx I\left(\nu + \Delta_\nu, \tfrac{1}{2}\widetilde{P}_0(x), 0, 0\right) + I\left(\nu - \Delta_\nu, \tfrac{1}{2}\widetilde{P}_0(x), 0, 0\right). \tag{8.41}$$

The last integral over x is calculated for fixed values of $\widetilde{P}_0(x)$ corresponding to $\widetilde{P}_0(x_n) = 1\,\mathrm{mW} \times 10^{n/5}$, with the integer number n. Since the calculation of the fluorescence spectra serves mainly a fitting routine, the particular laser powers correspond to the values measured during a frequency scan. The largest value of $\widetilde{P}_0(n_{\max})$ corresponds to the largest measured laser power of a transition in OH or a transition cluster in OD. The smallest laser power $\widetilde{P}_0(n_{\min})$ is chosen to get into the approximately linear regime of the single-molecule fluorescence signal. These fixed power values are the basis for integrating over x by using a linear interpolated function between two adjacent values in $\widetilde{P}_0(x)$. Potentially smaller power values $< 1\,\mathrm{mW} \times 10^{n_{\min}/5}$ are linear extrapolated to zero.

Chapter 9

Experiment

This chapter describes the experimental setup, in which all previously mentioned components come together. It starts with a general overview of the laser system, before going into more detail by describing the experimental setup of each involved laser and the molecular beam. Finally, precision spectra of the $A^2\Sigma^+$, $v' = 0 \leftarrow X^2\Pi_{3/2}$, $v'' = 0$, $J'' = 3/2$ electronic transitions in the hydroxyl radical (OH) and the deuterated hydroxyl radical (OD) are measured as a benchmark test of the system.

9.1 Complete Measurement Setup

The precision spectroscopy on OH requires a laser system which is referenced to multiple frequency standards. The basis of this precision laser system is an inherently stable nonplanar ring oscillator (NPRO) based on a neodymium-doped yttrium aluminum garnet (Nd:YAG) crystal operating at 1064 nm (Coherent Mephisto 1000 NE). Afterwards, second-harmonic generation (SHG) inside a periodically-poled lithium niobate (PPLN) waveguide (NTT Electronics) converts the wavelength to 532 nm (Figure 9.1). The green 532-nm beam is coupled into an iodine modulation transfer spectroscopy (MTS) setup, which provides an error signal for the stabilization of the Nd:YAG laser (Section 9.2). The Nd:YAG-laser is now stable at short timescales, but its exact frequency is still unknown. The measurement of the absolute emission frequency of the Nd:YAG-laser requires an optical frequency comb (OFC). The OFC is based on a mode-locked Ti:sapphire femtosecond oscillator (Laser Quantum Taccor-6) and a photonic crystal fiber module (NKT Femtowhite 800), resulting in a one-octave wide spectrum (Section 9.3).

The superposition of the OFC laser beam and the Nd:YAG-laser at 1064 nm and at 532 nm results in two beat notes. The frequencies of the two beat notes depend on the repetition rate f_r and the carrier envelope offset frequency f_0 of the OFC. Two phase-locked loops (PLLs) stabilize the 1064-nm and 532-nm beat notes at exactly 100 MHz and 200 MHz, respectively. Therefore, the OFC mode at 532 nm is exactly a factor of two higher in frequency than the OFC mode at 1064 nm. The OFC is now fully constrained

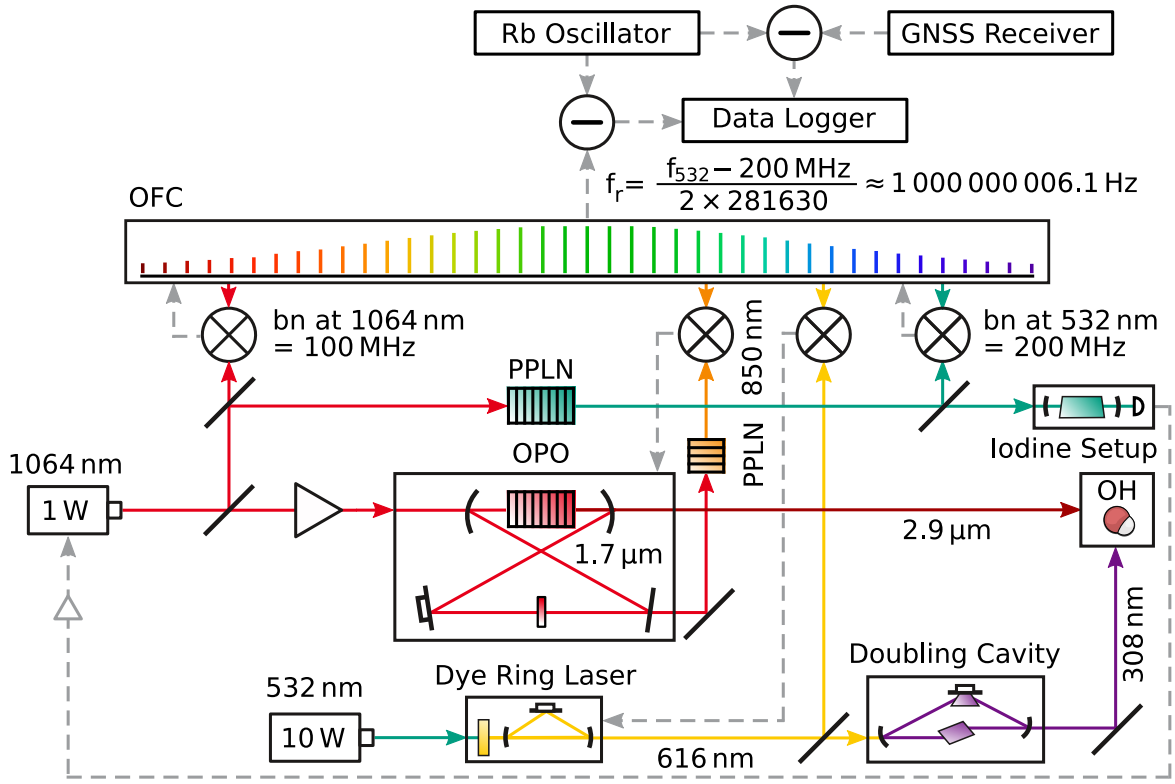

Figure 9.1: Schema of the precision laser system. The Nd:YAG laser supplies beams at 1064 nm and 532 nm, allowing the stabilization of the laser to an iodine reference. The short-term stability of the Nd:YAG laser is then distributed, through an OFC, to the spectroscopy lasers, a mid-IR OPO and a UV frequency doubled dye laser. Additionally, OFC repetition rate is recorded relative to the local rubidium oscillator and a GNSS receiver. Thus, the beat notes of the individual lasers provide a reading of their absolute optical frequencies.

with $f_0 = 0$ and

$$f_r(n) = \frac{f_{532} - 200\,\mathrm{MHz}}{2n}. \tag{9.1}$$

The integer mode number n corresponds to the number of OFC modes between 1064 nm and 532 nm. It is convenient to set the repetition rate as close as possible to 1 GHz. In the experiment, the repetition rate used is either

$$f_r(281630) = 1\,000\,000\,006.1\,\mathrm{Hz}, \quad \text{or} \tag{9.2}$$

$$f_r(281631) = \quad 999\,996\,455.3\,\mathrm{Hz}. \tag{9.3}$$

Due to potential drifts of the iodine reference, the exact value of f_r can slightly change over time. To account for this, the repetition rate of the OFC is recorded with a dead time free counter which is referenced to the rubidium oscillator (Stanford Research Systems PRS10).

A global navigation satellite system (GNSS) receiver (Septentrio PolaRx4TR PRO) supplies a pulse per second (PPS) to stabilize the rubidium oscillator and counteract potential long term drifts. Additionally, the GNSS receiver records data corresponding to

the phase error of the rubidium oscillator relative to GNSS time. A number of services are available that will process this data[1], enabling post-correction of the frequency offset. However, since the estimated relative root-mean-square (RMS) value of this correction is less than 1.5×10^{-12} for 1000 s (corresponding to a typical measurement time in this thesis), the post-correction was neglected in the calculation of the laser frequencies.

The rubidium oscillator is also used as a reference for measuring and stabilizing the optical beat note frequencies. The lasers are stabilized by PLLs, which rely on the phase error between the optical beat note and a reference signal. These reference signals, such as the 200 MHz signal required for the stabilization of the OFC or the tunable radio frequency synthesizers used for stabilizing the spectroscopy lasers to the OFC, derive their frequency from the rubidium oscillator. The spectral overlap between the OFC and the spectroscopy lasers is the requirement for the optical beat notes between both laser systems.

The electronic excitation of the OH requires an ultraviolet (UV) laser around 308 nm, which is outside the OFC spectrum. Therefore, we use a continuous wave (CW) dye laser at 616 nm (Sirah GmbH Matisse 2 DR) within the spectrum of the OFC and subsequently double the frequency by nonlinear conversion. For this, the wave at 616 nm is coupled into an enhancement cavity and converted by SHG inside a beta barium borate (BBO) crystal to 308 nm (Sirah WaveTrain).

The vibrational excitation of OH requires a mid infrared (IR) laser around 2.9 µm, which is also outside the OFC spectrum. This laser is produced using an optical parametric oscillator (OPO), which is pumped with the already stabilized and now amplified (Nufern NUA-1064-PD-0015-C2) 1064-nm beam of the Nd:YAG laser with up to 15 W. The nonlinear conversion inside the magnesium-doped PPLN crystal (Castech PPMCLN 5mol%) of the OPO generates a resonant signal wave at 1.7 µm and an idler wave at 2.9 µm, which is immediately coupled out. Approximately two percent of the signal wave in the cavity is also coupled out, and frequency doubled in a single pass through another magnesium-doped PPLN crystal (Covesion MSHG1650-0.5-10). The SHG inside the second PPLN leads to a wave at 850 nm, which is also inside the OFC spectrum. Now that optical beat notes between the spectroscopy lasers and the OFC are available, phase locked loops adjust the cavity length of each laser to keep the beat note frequency stable at the reference frequency. Frequency tuning is achieved by changing the reference frequency provided by the computer controlled frequency synthesizer.

A frequency scan over a single electronic transition line of the OH is performed in steps of 200 kHz with a typical span of 32 MHz. The richer hyperfine structure of OD requires occasionally scans over 50 kHz. The available scan range is limited between 50 MHz and 450 MHz, even though the beat notes can fall anywhere between 0 MHz and

[1] For example: https://www.nrcan.gc.ca/earth-sciences/geomatics/geodetic-reference-systems/18766

$f_2/2 = 500\,\text{MHz}$. The reason is the ambiguity in assigning the correct laser frequencies. If the beat note frequency is close to 0 MHz, it is hard to determine whether the CW laser frequency is higher or lower than the OFC mode frequency. Similarly, a beat note frequency close to 500 MHz is right in between two OFC modes producing two beat notes with similar frequencies. The PLL behaves unpredictably in the ambiguous frequency regions, and it is generally better to avoid them. Fortunately, the OFC can be stabilized to a different repetition rate defining mode (Equation 9.2) before the scan of the spectroscopy laser. Choosing the right mode in advance makes it possible to avoid dead frequency zones during the scan. For example, if the OFC is stabilized at the mode $n = 281630$, some electronic transitions will fall into the dead frequency zone, but usually, these transitions will have more favorable beat note frequencies when the OFC is stabilized to the mode $n = 281631$.

9.2 Iodine Reference

Building on the introduction to MTS presented in Section 6.3.3 and the basics of the iodine standard presented in Section 5.2.2, this section concentrates on the technical details realizing the MTS setup. The core design of our MTS setup is inspired by previous work, mostly from the group of A. Peters at the Humboldt University in Berlin[74,136,137,191].

Our iodine reference is built on a commercial optics honeycomb breadboard. A heat mat under the breadboard opens the possibility of active temperature control, although it is currently turned off. The core of the iodine reference is the gas cell. Our iodine cell is 500 mm long with wedged fused silica windows that are coated for 532 nm on all surfaces (ISI Brno). The cold finger at the center of the cell is 30 mm long and cooled to $-15\,^\circ\text{C}$, which follows the recommendation of the bureau of weights and measures (BIPM) This temperature corresponds to a vapor pressure of 0.76 Pa[137] or 0.83 Pa[192,193]. The two counterpropagating pump and probe beams pass the cell four times (Figure 9.2a), resulting in a total optical path length of 2000 mm. The superposition of the two beams is achieved and maintained by using precision kinematic mirror mounts (Thorlabs Polaris).

Long term pointing stability is possible with a control loop, involving piezoelectric transducer (PZT) on the mirrors and quadrature photodiodes. Each quadrature photodiode consists of four separated detector areas, and attached electronics produce three output signals (Figure 9.2b). In detail, the sum output is proportional to the total laser intensity on the photodiode, while the horizontal and vertical error outputs are proportional to the intensity difference between one half of the photodiode and the other. The ideal transverse electromagnetic mode (TEM) mode for alignment of the pointing and also MTS is the TEM_{00} mode. To filter out potential higher order modes, two single-mode optical fibers are used in the pump and probe beam paths. Pointing instabilities at the entrances to these fibers can change the field strength after the fiber, so an acoustic-optical

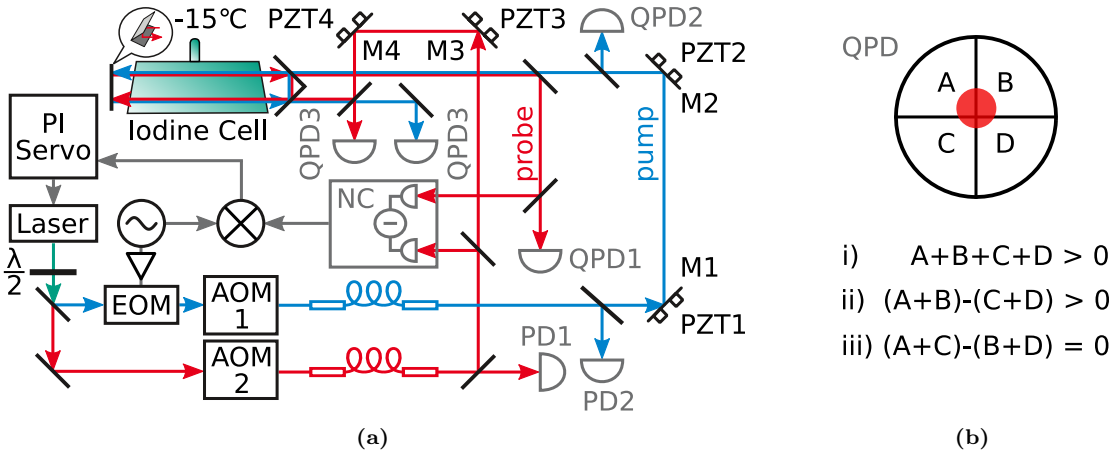

Figure 9.2: (a) Schema of the MTS iodine reference setup, which involves an electro-optic modulator (EOM), two acousto-optic modulators (AOM), two photodiodes (PD), four quadrature photodiodes (QPD), two piezo transducer (PZT) at each relevant mirror (M), and finally a noise canceling detector (NC). (b) Schema of the QPD outputs: i) sum, ii) vertical error, iii) horizontal error.

modulator (AOM) (IntraAction Corp. 402AF1) is used in front of each fiber, adjust the beam intensities and cancel out potential residual amplitude modulation (RAM). A traveling acoustic wave inside the AOM diffracts some part of the incoming light into the first diffraction order, depleting it from the undiffracted beam. The amount of light transferred is determined by the intensity of the radio-frequency signal applied to the PZT driving the acoustic wave. Thus, amplitude control of either the diffracted or the undiffracted light component into the optical fiber is possible. A photodiode behind the fiber detects the light intensity after the fiber, and a control loop can be used to keep this intensity constant.

Additionally, the fiber setup reduces RAM from the electro-optic modulator (EOM) which drives the MTS[194]. The RAM leads to frequency fluctuations and shifts. It is convenient to reduce it, though the RAM contribution compared to the broad OH UV transitions in this thesis is negligibly small. One of the AOMs is used to shift the frequency of the pump beam by a constant 40-MHz offset while the frequency of the probe is left unchanged. Doing this ensures that any back-reflected beams will have a different frequency from the beam that should be traveling in that direction and will not interact with the same molecules.

9.2.1 Iodine Spectrum near 532 nm

The inherently stable NPRO laser based on a Nd:YAG crystal is the starting point for the MTS (Coherent Mephisto). After frequency doubling the 1064-nm output using a waveguide PPLN, some portion of the 532-nm light is coupled into a polarization maintaining optical fiber. The 532 nm wave is collimated again on the breadboard containing the iodine setup (Section 9.2). A combination of $\lambda/2$-waveplate and polarizing beam splitter separates and sets the relative intensities of the pump and the probe wave. The

optimal pump and probe intensities before entering the absorption cell are 24.4 mW and 12.7 mW, respectively. The frequency synthesizer that modulates the pump frequency has two outputs supplying a cosine and a sine waveform (Figure 9.2a). The sine waveform is amplified to ±8 V before being transformed up to ±320 V and applied to the EOM. The EOM (Qioptic PM-C BB) requires 100 V to reach a modulation of $\lambda/10$ at 1064 nm, which implies a modulation of $\lambda/5$ at 532 nm with the same voltage. Thus, the phase modulation of the pump wave is

$$\Delta\varphi(t) \approx \frac{1}{5} 2\pi \frac{320\,\mathrm{V}}{100\,\mathrm{V}} \sin(2\pi\nu_m t) = 2\pi 0.64 \sin(2\pi\nu_m t) \quad \text{at} \quad 532\,\mathrm{nm}. \tag{9.4}$$

The definition of the instantanious frequency (Equation (5.2)) leads to the modulation index

$$\delta = \frac{\Delta\nu}{\nu_m} = \frac{1}{2\pi}\frac{1}{\nu_m}\frac{d\varphi(t)}{dt} = \frac{1}{2\pi}\frac{1}{\nu_m}\lim_{\Delta t\to 0}\frac{\Delta\varphi(t)}{\Delta t} = 2\pi 0.64 \approx 4, \tag{9.5}$$

which is independent of the modulation frequency $\nu_m = 161\,\mathrm{kHz}$ of the EOM. After the saturation experiment, a noise-canceling detector measures variations of the probe wave[195]. This signal gets amplified, filtered and sent to an electrical mixer. The sine phase modulation applied using the EOM results in a cosine frequency shift, which becomes the primary modulation in the probe signal. Thus, the cosine wave from the frequency synthesizer is used as the local oscillator frequency of the mixer, resulting in a pure in-phase MTS signal at the mixer output. The Nd:YAG laser emission frequency can be tuned by changing the temperature or cavity length, enabling measurement of the region around the a_{10} component of the $R(56)$ 32-0 transition cluster (Figure 9.3a). The spectrum

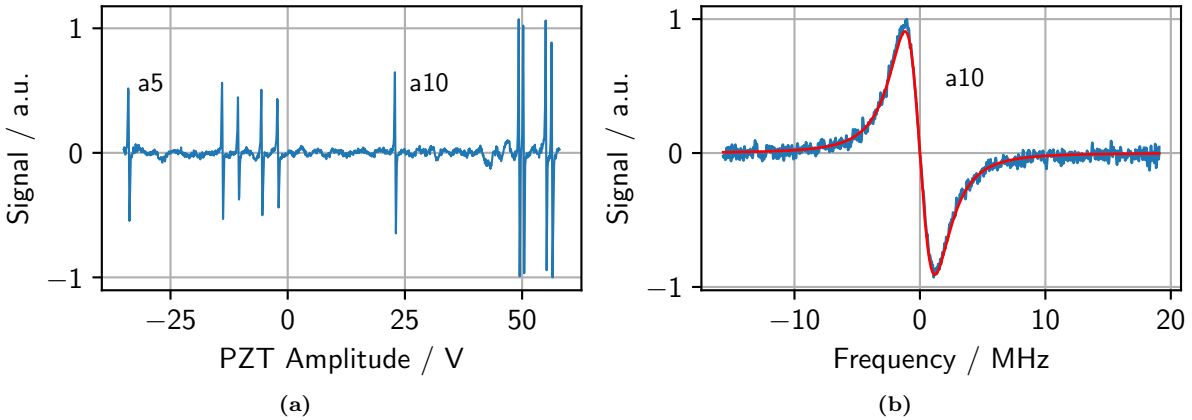

Figure 9.3: (a) Measurement of the a_5 to a_{14} hyperfine lines of the $R(56)$ 32-0 transition cluster in molecular iodine around 532 nm. (b) Fit of the in-phase MTS signal to the hyperfine component a_{10}, with the fixed parameters $\delta = 4$, $f_m = 161\,\mathrm{kHz}$ and $\phi = 0$.

shown in Figure 9.3a was produced by ramping the voltage on the cavity PZT between −35 V and 58 V. The frequencies of the individual hyperfine components are well known relative to the a_{10} reference line. Based on the relative frequencies of the other hyperfine

components provided by the BIPM[134], the transfer function of the PZT is determined to be approximately linear with a slope of 4.67 MHz/V. The purely in-phase MTS signal around the a_{10} component is shown in Figure 9.3b, with the frequency axis determined using this scaling factor. The MTS signal is then fit using Equation (6.23). Fixing the parameters $\delta = 4$, $f_m = 161\,\text{kHz}$ and $\phi = 0$ results in a linewidth of $\gamma \approx 2\,\text{MHz}$. For comparison, the expected linewidth of the a_{10} component is around $\Gamma = 350\,\text{kHz}$ at a vapor pressure of 0.83 Pa[193]. Thus, the iodine gas cell is probably contaminated, resulting in much higher vapor pressure, probably $> 100\,\text{Pa}$. The larger linewidth decreases the slope of the MTS signal at zero crossing, which decreases the short-term stability of the laser stabilized to the iodine MTS setup. However, the MTS signal measured with the current modulation parameters is still found to be sufficient (Section 6.3.3), and the potential decrease of short-term stability is negligible at the measurement time scales and linewidths in this thesis.

9.2.2 Frequency Stability of Iodine Reference

The stabilization of the Nd:YAG laser is the primary purpose of the MTS signal. The laser is roughly tuned to the center of the a_{10} line by adjusting the temperature of the Nd:YAG crystal, and afterward the MTS signal serves as an error signal for a proportional-integral (PI) controller (New Focus LB1005 High-Speed Servo Controller), which is directly connected to the PZT of the Nd:YAG laser. This stabilizes, the Nd:YAG laser to the MTS of the iodine reference, but measuring the stability of this frequency reference still requires an independent reference oscillator. The rubidium standard (Stanford Research Systems PRS10) is a suitable oscillator, but because its output frequency is at 10 MHz and the iodine-stabilized laser is at an optical frequency, an OFC is needed to bridge the two different frequency domains. Therefore, the Nd:YAG laser is used to stabilize the OFC, transferring its stability onto the OFC (Section 3.2.5). The repetition rate of the OFC is measured on a frequency counter, which is referenced to the rubidium standard. Frequency noise originating in the iodine MTS setup is mapped onto the repetition rate of the OFC. In this way the iodine MTS setup is compared to the rubidium oscillator (I_2-Rb). A ten-hour measurement shows a maximum phase difference of approximately 13 ns if the initial and the final phase differences are chosen to be zero (Figure 9.4a). Since the overall phase offset is arbitrary and the phase difference between the start and end of the measurement is related to the average frequency assumed, these points can be fixed without loss of generality. Based on the data shown in Figure 5.5, the modified Allan deviation (MDEV) of the iodine standard should be smaller than the MDEV of the rubidium standard at all time scales. Therefore, calculating the MDEV of the OFC repetition rate phase change contains mostly the instability of the rubidium standard (Figure 9.4b). The third reference available in our laboratory is the GNSS receiver. Simultaneously to the previous comparison of I_2-Rb, the GNSS receiver was monitoring the phase difference between

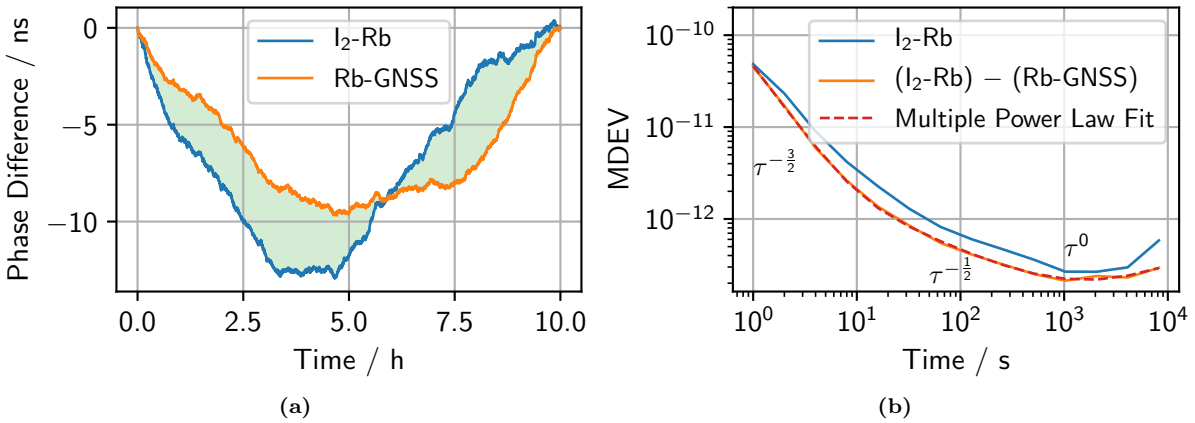

Figure 9.4: (a) Long term measurement of the phase difference between the iodine MTS setup and the rubidium standard (I_2-Rb), as well as the phase difference between rubidium oscillator and GNSS receiver (Rb-GNSS). (b) Corresponding calculations of the MDEV.

the rubidium oscillator and its measurement of GNSS time (Rb-GNSS) (Figure 9.4a). The maximum phase difference between I_2-Rb and Rb-GNSS is less than 5 ns, indicating that the I_2 and the GNSS references are more stable than the Rb reference. Calculating the MDEV of the phase difference (I_2-Rb − Rb-GNSS) should be free of the frequency instability of the rubidium oscillator (Figure 9.4b). It is indeed lower than the MDEV of the rubidium oscillator, but higher than the expected MDEV based on comparable setups[136]. Thus, either the stability of the iodine reference is poor, or an additional noise source has not been considered yet. The truth is probably in between. For example, a random error in each individual measurement of the I_2-Rb and Rb-GNSS phase difference will not cancel out when the two curves are subtracted. Performing a multiple power law fit on the I_2-Rb − Rb-GNSS MDEV curve makes it possible to distinguish between white phase noise ($\tau^{-3/2}$), white frequency noise $\tau^{-1/2}$ and other noise contributions ($\geq \tau^0$). The white phase noise is largely caused by technical limitations of the frequency counter and the GNSS receiver and, in particular, random, uncorrelated noise in their measurements of the phase difference. The fit of the white phase noise corresponds to a total RMS jitter of 27 ps on each measurement at one-second intervals. These noise contributions are not present in the iodine stability measurement cited in Figure 5.5 which is based on a comparison to an ultra-low expansion (ULE) cavity[136]. The white frequency noise depends on the signal to noise ratio (SNR) of the MTS signal. The broader linewidth caused by the high vapor pressure inside the reference cell likely contributes to this noise by decreasing the quality of the error signal. Higher noise contributions lead to a minimum MDEV of around 10^{-13} at 1000 s and finally an increase of the MDEV after an integration time of 2000 s. The calculated MDEV gives an upper limit on the noise of the iodine reference, although the true stability is probably at least somewhat better.

9.3 OFC Setup

The general characterization of the OFC has been discussed previously (Section 3.2). In this section, I will discuss the technical details related to the specific OFC in this thesis. The basis of the OFC is a mode-locked femtosecond oscillator (Laser Quantum Taccor-6), with a repetition rate of 1 GHz and an output power around 1.4 W. The central wavelength is around 800 nm with a bandwidth of around 32 nm and a pulse duration around 22 fs.

The first optical element after the laser output is a periscope, which increases the height of the propagating beam (Figure 9.5). The following $\lambda/2$-waveplate and a Glan-

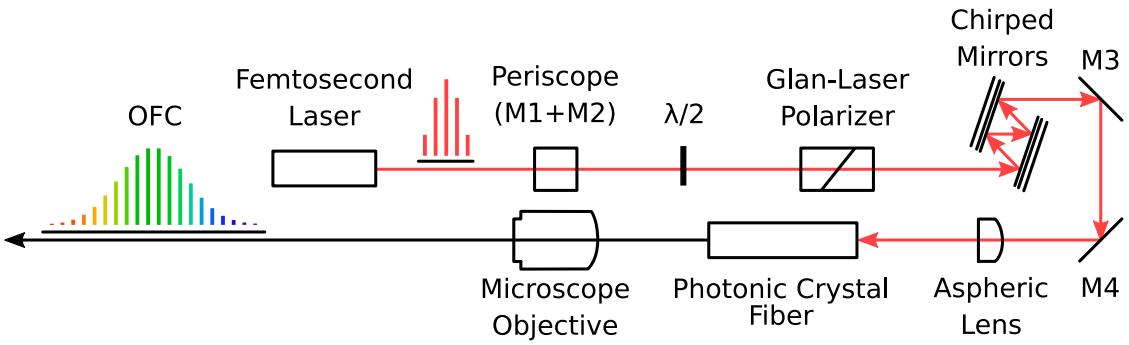

Figure 9.5: Schema of the OFC setup with silver coated mirrors M1-M4. The $\lambda/2$-waveplate and the Glan-Laser polarizer control the optical power, while the chirped mirrors compensate dispersion. An aspheric lens couples the laser beam into a photonic crystal fiber, which broadens the spectrum. Finally, a microscope objective collimates the beam.

Laser calcite polarizer (Thorlabs GL10-B) enable fine adjustment of the laser power. All optical elements until this point introduce dispersion, meaning the red and blue frequency components of the pulse experience different group delays. This temporally broadens the individual pulses, resulting in less-efficient spectral broadening in the subsequent nonlinear fiber. Therefore, the individual pule experiences temporal broadening, which results in a narrower overall spectrum. A pair of chirped mirrors (Layertec 106658) introduces a group delay to the red component of the pulse, which allows the blue component to catch up. In total, seven reflections at each chirped mirror are required to compensate for dispersion. The laser is then focused using an aspheric lens (Thorlabs C230TMD-B) into the photonic crystal module (NKT Femtowhite 800). A high precision flexure stage (Elliot Scientific MDE122) provides the necessary stability and adjustment precision for the lens. Afterwards, the $\chi^{(3)}$ nonlinear process inside the crystal module broadens the spectrum (Section 4.0.4). The spectrum spans behind the fiber over one octave, at least from 500 nm to 1100 nm. An Olympus plan fluorite microscope objective (Thorlabs RMS40X-PF) with 40x magnification collimates the laser beam again, after which it continues to the beat note detection unit.

9.3.1 Beat Note Unit Setup

Superimposing the beam of the OFC with a CW laser beam within the OFC spectrum leads to an optical beat note (Section 3.2.3). The beat note contains the radio frequency difference between the CW laser and the nearest comb tooth. The nearest comb tooth is always within $f_{\mathrm{rep}}/2 = 500\,\mathrm{MHz}$. However, the intensity of the individual beat note depends on the field strengths of both involved waves. The total output power of the OFC behind the setup in Figure 9.5 is around 400 µW. Unfortunately, each frequency tooth is, on average, much weaker. Over the span from 532 nm to 1064 nm, there are approximately 280000 modes, and dividing the total output power of the OFC beam over these modes results in 1.4 µW average power per tooth. Thus, the available field strength from the OFC is the limiting factor of the beat note signal strength.

The setup in Figure 9.6 introduces one possibility to increase the weak signal of the optical beat note and simultaneously reduce the noise. In total, this thesis relies on

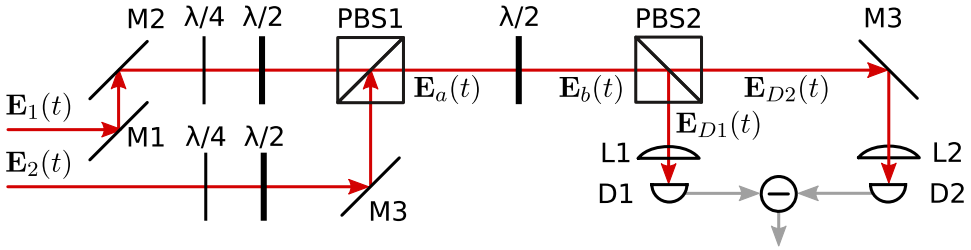

Figure 9.6: Schema of a beat note unit for differential detection. The incoming light waves are first superimposed with the polarizing beam sampler (PBS1). A set of $\lambda/2$- and $\lambda/4$-waveplates optimizes the optical power. The PBS2 separates the beam again into two equally intense components. Each component is focused through a lens L and detected on a photodiode D.

four such setups at 532 nn, 616 nm, 850 nm and 1064 nm. It is convenient to design one compact breadboard setup as a way of assembling a set of optics, that is copied four times. The dielectric coating on the mirrors, the waveplate design and the anti-reflective (AR) coatings on all transmissive optics match the individual target wavelength of each such beat note unit. The core of this setup are polarizing beam splitters (PBSs), which separate vertical and horizontal polarized components in the incoming beam. This process is used in reverse at PBS1 where the two light waves of vertical and horizontal polarization are superimposed. The polarization state of the incidence waves is controlled with a $\lambda/4$ and a $\lambda/2$ waveplate and optimized for maximum intensity of the superimposed wave behind PBS1. In detail, the PBS1 transmits horizontally polarized light to the incidence plane and reflects vertically polarized light. The superimposed electromagnetic field behind PBS1 is

$$\mathbf{E}_a(t) = T\mathbf{E}_1(t) + R\mathbf{E}_2(t) = A_1' e^{i\omega_1 t}\,|H\rangle - A_2' e^{i\omega_2 t}\,|V\rangle + c.c.. \tag{9.6}$$

This field exhibits two different optical frequencies ω_1, ω_2 and amplitudes A_1', A_2' of the initial fields. The horizontal and vertical polarization states are denoted with $|H\rangle$ and $|V\rangle$, respectively. The following differential detection technique uses two photodiodes for

further refinement of the signal. Thus, a $\lambda/2$-waveplate is used to turn the electric field vector by 45°, resulting in the field $E_b(t)$, given by

$$\mathbf{E}_b = A_1 e^{i\omega_1 t}\left(|H\rangle + |V\rangle\right) + A_2 e^{i\omega_2 t}\left(|H\rangle - |V\rangle\right) + c.c.. \tag{9.7}$$

The separated fields behind the PBS2 are $\mathbf{E}_{D1}(t)$ and $\mathbf{E}_{D2}(t)$ corresponding to the horizontal and the vertical polarized components, respectively. Two lenses ($F = 50\,\mathrm{mm}$) focus each field on two separate photodiodes. The corresponding intensities are

$$I_{D1}(t) \propto (\mathbf{E}_{D1}(t))^2 = 2A_1A_2e^{i(\omega_1-\omega_2)t} + \underbrace{2A_1^2 + 2A_2^2}_{\mathrm{DC}} + \underbrace{A_1^2e^{2i\omega_1 t} + ..}_{\xrightarrow{\mathrm{LP}}0} + c.c., \tag{9.8}$$

$$I_{D1}(t) \propto (\mathbf{E}_{D1}(t))^2 = -2A_1A_2e^{i(\omega_1-\omega_2)t} + \underbrace{2A_1^2 + 2A_2^2}_{\mathrm{DC}} + \underbrace{A_1^2e^{2i\omega_1 t} + ..}_{\xrightarrow{\mathrm{LP}}0} + c.c., \tag{9.9}$$

where the high frequency components are filtered out by a low-pass (LP) filter. To improve the SNR, both intensities are subtracted electronically

$$I_{D1}(t) - I_{D2}(t) = 4A_1A_2e^{i(\omega_2-\omega_1)t} + c.c.. \tag{9.10}$$

The intensity of the beat note is proportional to the product of both amplitudes A_1 and A_2. Thus, the larger amplitude of the CW laser compensates the weaker amplitude of the OFC. The cancellation of the direct current (DC) components A_1^2 and A_2^2 reduces potential amplitude noise. Simultaneously, the signal increases by a factor of two compared to the single photodiode signal.

9.3.2 Bandwidth of the OFC

An optical beat note between the OFC and a CW laser is the basis for the phase stabilization between both lasers. The success of the stabilization depends on the feedback bandwidth of the OFC laser system since only noise contributions within this bandwidth can be compensated. Section 5.3.3 described one possibility to measure the response of the repetition rate to the modulation of the fast PZT as a function of frequency.

The repetition rate output of the OFC is filtered (BP 800 MHz-1050 MHz), amplified (Mini-Circuits ZFL-1000LN) and coupled into a splitter. One output of the splitter is connected directly to an electrical mixer, and the other part propagates through a 17 m long coaxial cable (Ecoflex 15 Plus), before entering the second input of the same mixer. Afterwards, the signal gets filtered (LP 1.9 MHz), amplified (x560) and connected to the first channel of a digital oscilloscope. This signal contains the phase information of the PZT response as a function of the modulation frequency, while the temporal delay of $\Delta t \approx 66.8\,\mathrm{ns}$ scales the signal strength (Equation 5.24). A frequency synthesizer (AnalogDevices AD9854) directly modulates the fast PZT of the OFC with an amplitude

of ±2 V, and the modulation signal is also recorded on the second oscilloscope channel. The modulation frequency is scanned in discrete steps between 10 kHz and 100 kHz, and the phase and amplitude of the repetition rate response are determined at each frequency using a fast Fourier transform (FFT). The frequency dependent amplitude and phase difference relative to the reference signal are displayed in Figure 9.7a and 9.7b. As expected, the

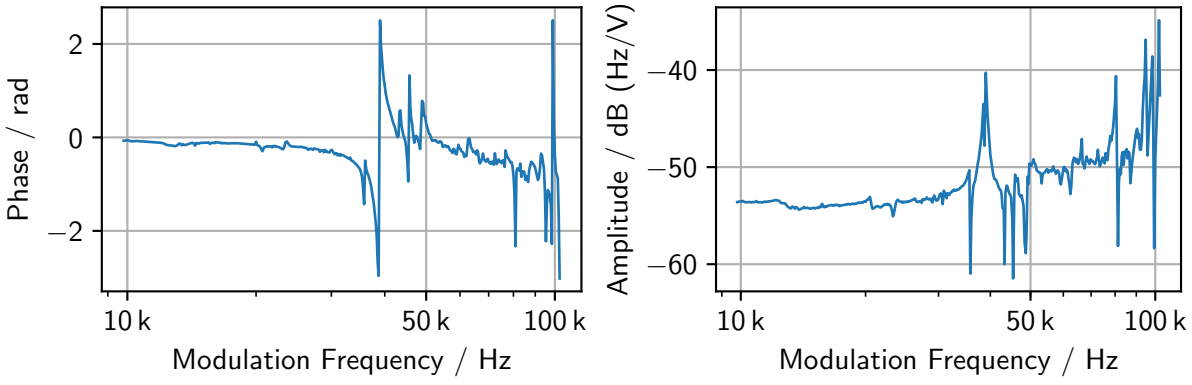

Figure 9.7: (a) Frequency shift measurement of the phase difference between the PZT response and a cosine modulation signal. (b) Corresponding amplitude difference, with a resonance peak at 40 kHz.

phase difference is approximately zero at low frequencies. However, a strong mechanical resonance of the PZT setup at a frequency of 40 kHz introduces a large phase delay and rise of the amplitude response. The resonance peak limits the bandwidth of the feedback loop using this PZT.

9.3.3 Stabilization of the OFC

The stabilization of the OFC requires two independent control loops, which stabilize the repetition rate and the carrier envelope offset frequency, respectively. The control of the repetition rate is based on the beat note at 1064 nm between the OFC and the CW reference laser (Coherent Mephisto 1000 NE) (Section 3.2.4). The 200 MHz reference signal for the I/Q-demodulation is derived from the rubidium oscillator (Stanford Research PRS10) (Section 3.2.5). In detail, the 10 MHz output of the rubidium oscillator gets multiplied in a chain (Wenzel Associates, Inc. $\times 4 \times 5 \times 5$) up to 1 GHz. Each multiplication adds noise, and the final 1 GHz output has residual sidebands at ±10 MHz offset. These effects are minimized by using a PLL, based on a narrow bandwidth surface acoustic wave (SAW) oscillator, which is stabilized to the output of the multiplier chain with a 1-kHz feedback bandwidth. The clean 1 GHz reference signal is now divided down to 200 MHz. The difference between the beat note and the new 200 MHz reference, divided by two, results in the in-phase signal $I(t)$ and the quadrature signal $Q(t)$. Mathematically, the phase difference between both lasers is $\phi(t) = \text{atan2}(Q(t), I(t))$. The task of the control loop is to keep $\phi(t)$ at all times at zero. To do this, the $I(t)$ and $Q(t)$ components need to

be processed into a phase, which serves as an error signal for a PI controller, stabilizing the PZTs of the OFC cavity.

The response time of the control loop adds a potential bandwidth limitation. Thus a fast processing speed is of the essence. This thesis relies on a single device (Red Pitaya STEMlab125-14), which contains two 14-bit 125 MSPS analog-digital converters, two 14-bit 125 MSPS digital-analog converters, and a field-programmable gate array (FPGA) for implementing digital logic that interacts with these inputs and outputs. The largest benefit of this device is the re-programmability: since the inputs and outputs are connected to a FPGA, the board can be modified to suit a specific application. Some features are already implemented, such as the two-channel oscilloscope for monitoring the $I(t)$ and $Q(t)$ signals with a bandwidth of 40 MHz and the PI controller. However, the computation of the phase requires a custom implementation based on the coordinate rotation digital computer (CORDIC) algorithm for the efficient calculation of the atan2-function. Afterwards, the PI output signal is delivered through the two outputs of the board, with a frequency range of 0 MHz-50 MHz. Only the amplification of this servo signal requires an additional device. The input and output signals can be monitored on a computer screen using a web-based interface.

The stabilization schema of the OFC using the 532-nm and the 1064-nm beat notes has been discussed in Section 3.2.4.

9.4 UV Spectroscopy Laser System

The high short-term stability of the iodine reference can be distributed to any CW laser whose frequency is within the comb spectrum using the OFC as a transfer oscillator. The PLL based on the beat notes between the CW laser and the OFC can be used to narrow the optical linewidth of the CW laser. The required wavelength for electronic excitation of the OH at 308 nm is outside the comb spectrum, so the spectroscopy laser in this thesis is based on a dye laser at 616 nm (Sirah GmbH Matisse 2 DR) which is frequency doubled by SHG to 308 nm. The nonlinear conversion takes place inside a BBO crystal, which is placed within an optical enhancement cavity (Sirah GmbH WaveTrain 2). The enhancement cavity is stabilized with the Pound-Drever-Hall (PDH) technique in order to track changes of the frequency of the input wave at 616 nm[196]. The beat note at 616 nm is used in a PLL which controls the fast and the slow PZTs of the dye laser cavity (Section 3.2.4).

Before purchasing this dye laser system, we tried to construct a 308-nm spectroscopy laser based on a diode laser. The following sections detail the results of these efforts.

9.4.1 Laser Diode 1st Setup

There are no commercially-available laser diodes that emit in the wavelength region around 308 nm. Despite this, two laser diode based techniques for generating light around 308 nm for OH spectroscopy have been implemented. The first technique involves cooling a laser diode specified for operation at 635 nm to a low temperature. The band gap of the semiconductor increases at lower temperatures, resulting in emission at a shorter wavelength [197]. The target wavelength is 616 nm, which is afterwards frequency doubled to 308 nm. The second technique involves the sum frequency generation of a violet diode laser at 404 nm and a distributed feedback (DFB) laser diode at 1320 nm inside a BBO crystal [92]. The generated wave around 308 nm is tuned continuously by ramping the current or the temperature of the DFB laser diode. However, both laser diodes require sufficient stability for precision spectroscopy.

In preliminary tests, this thesis followed the approach of cooling a single mode laser diode (Oclaro HL63163DG). The output wavelength at room temperature is 633 nm with a maximum output power of 100 mW with a current of 230 mA. The recommended operating temperature range is between −10 °C and +40 °C, but this is violated with the following setup. The laser diode is mounted inside a copper block, which is attached through a polytetrafluoroethylene (PTFE) insulator at the bottom of a liquid nitrogen container (Figure 9.8a). An additional resistor at the copper mount is used for temperature control of the laser diode. Evacuating the region around the laser diode thermally insulates the liquid nitrogen container, which is resting on three glass spheres at the bottom, and prevents condensation on the cooled components. The laser light is collimated with an aspherical lens and coupled out through a Brewster window. The temperature dependent wavelength shows approximately a linear trend (Figure 9.8b). However, the decreasing

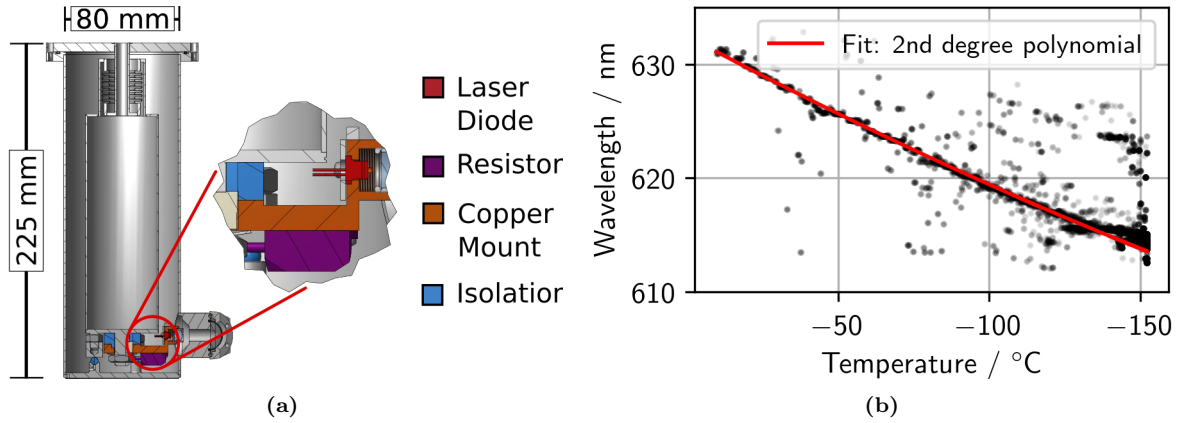

(a) (b)

Figure 9.8: (a) Dewar vessel for liquid nitrogen with a laser diode placed inside the evacuated space. (b) The laser diode emission wavelength decreases with temperature along with its ability to operate on a single mode.

temperature moves the laser diode operation further away from its design temperature. The laser diode becomes less stable with decreasing temperature, and it operates on multiple longitudinal modes at low temperatures. The wavelength meter (HighFinesse

WS7) tends to misinterpret the wavelength during multimode operation, which results in a large spread of the wavelength readings at low temperatures. The general trend is highlighted with a 2nd-degree polynomial fit (Figure 9.8b). However, even without single mode emission, this setup demonstrates the emission of 616 nm light with an intensity of around 200 mW (200 mA) at a temperature of −130 °C. Encouraged by this measurement, we constructed a second setup with the goal of increasing the stability of the laser diode.

9.4.2 Laser Diode 2nd Setup

The previous laser diode setup displayed poor wavelength stability along with insufficient liquid nitrogen reservoir size requiring a refill approximately once each hour. Increasing the size of the dewar vessel addresses both issues (Figure 9.9a). The larger volume of

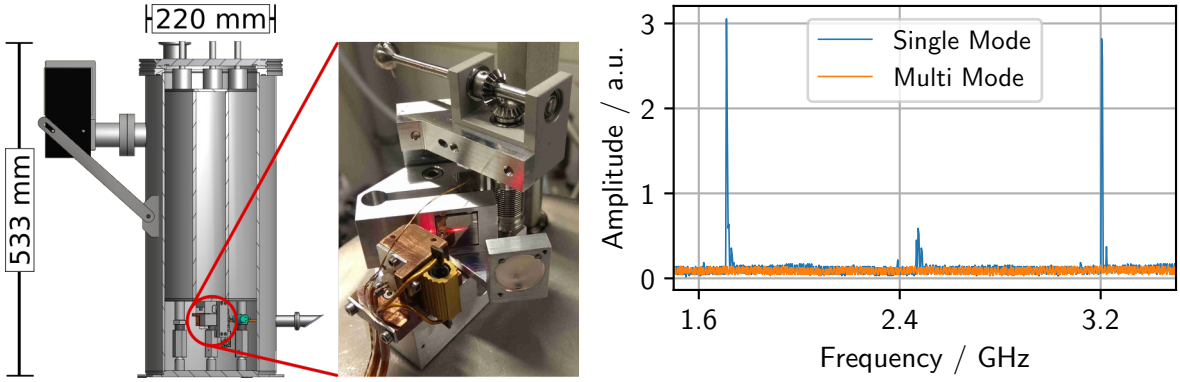

(a) (b)

Figure 9.9: (a) Dewar vessel for liquid nitrogen with an ECDL placed inside the evacuated space. The vacuum is maintained with the help of an ion pump. (b) Successful measurement of single mode emission behind a scanning Fabry-Perot interferometer, although at most ECDL settings, the emitted light remains multi mode.

the nitrogen reservoir allows operation of the laser diode for approximately 7 h without refill. Additionally, the area below the reservoir provides enough space to implement an external cavity diode laser (ECDL)[198–201]. A grating is placed in front of the laser diode in Littrow configuration, meaning the first order diffracted beam is coupled back into the diode. The efficiency of the holographic grating (Throlabs GH13-24V) is approximately 17 % for parallel polarized light at 616 nm. The coarse alignment of the grating requires two rotational feedthroughs into the vacuum for the vertical and the horizontal tilt of the grating (Figure 9.9a). An additional stacked PZT (Throlabs PK4DMP2) allows fine-tuning of the horizontal tilt with a travel range of 9.2 µm. All electrical components inside the evacuated region of the dewar vessel are connected through vacuum-compatible Kapton-insulated wires. The additional ion pump improves the vacuum inside the dewar vessel. For the following measurements, the laser diode is operated at 200 mA and cooled down to −137 °C. The laser beam is coupled into a scanning Fabry-Perot interferometer (FPI) (FSR=1.5 GHZ). At single mode emission, two distinct interference peaks separated by the free spectral range (FSR) are detected with a photodiode behind the FPI (Figure 9.9a).

Thus, single mode emission around 616 nm is possible, although the grating decreases the output power to approximately 130 mW. However, after a small change of the laser diode current (≈ 1 mA), the signal after the FPI disappears, indicating multimode operation. Active stabilization of the ECDL current relative to the grating position might permit conditions which allow a large tuning range at hight laser diode output powers[202,203]. However, instead of pursuing this challenge, we instead replaced the diode laser with a dye laser and used that for the spectroscopy presented in this thesis.

9.5 IR Spectroscopy Laser System

Based on previous considerations (Section 4.4), the parallel mirror distances of the OPO bow-tie ring cavity design are set to $d_1 = 140$ mm and $d_2 = 171.3$ mm, targeting a laser incidence angle at the mirrors of $\alpha = 9°$. These cavity dimensions correspond approximately to the stability center of the cold cavity around $m = 0$. The OPO cavity consists of three different types of mirrors. The curved ($r = 100$ mm) incoupling mirrors (Layertec 102102) are AR coated for the pump and idler wavelengths ($< 2\,\%t$ reflection) and high-reflective (HR) for the signal ($> 99\,\%$). The planar PZT mirror (5 mm × 5 mm) reflects the full signal wave ($> 99.9\,\%$) (Layertec 102101), while the signal outcoupling mirror transmits some small fraction ($< 2\,\%$) (Layertec 109761). Additionally, a 3 mm thick YAG etalon (Layertec 107984) inside the cavity optimizes the frequency selectivity of the OPO. The etalon is mounted into a copper block glued to a circular Peltier element, which itself is glued to a 1 inch aluminum heat reservoir inside an ordinary mirror mount (Figure 9.10a). The 50 mm long magnesium-doped PPLN crystal (Castech PPMCLN

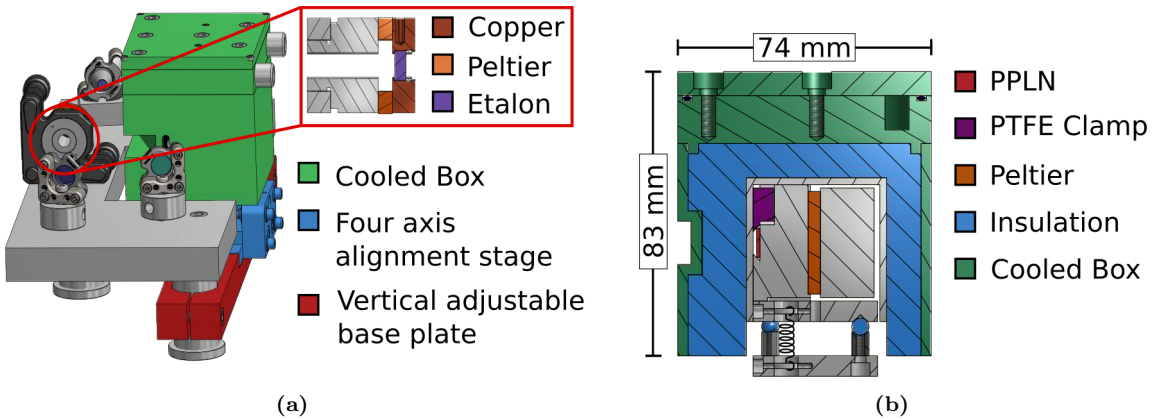

Figure 9.10: (a) Schema of the OPO cavity with highlighted etalon mount (red block). The combination of adjusatble base plate (red) and four axis alignment stage (blue) allows the selection of the poling period and alignment of the PPLN crystal. (b) The outside temperature of the water cooled aluminum box (green) is held near room temperature, while the inside of the box reaches temperatures up to 200 °C.

5mol%) is placed between the two curved mirrors with the poling periods stacked vertically. Therefore, the poling period can be switched by moving the PPLN crystal up or down. A vertically adjustable baseplate enables coarse selection of the poling period. Afterwards,

the baseplate is clamped onto the posts of the breadboard, and the fine adjustment is carried out with a commercial four axis alignment stage (Newport 9071-M). The PPLN sits on an aluminum block and is fixed with a PTFE clamp (Figure 9.10b). To benefit from the full PPLN frequency tuning range, it can be necessary to increase the temperature of the crystal as high as 200 °C. A Peltier element transports the heat between an aluminum reservoir and the mounting block, which are both connected with polyether ether ketone (PEEK) screws. However, the high temperature of the aluminum mounting block relative to the surroundings requires thermal insulation. Thermal insulation in the support structure is provided by three glass spheres, on which the whole PPLN assembly rests. The side and top are insulated by glass wool between the hot mounting block and a larger black anodized and water cooled aluminum box. This insulation and active cooling minimize heat convection inside the cavity, by keeping the outside of the aluminum box at room temperature. The entire OPO assembly is enclosed in a polyvinyl chloride (PVC) box, which thermally insulates the inside of the box from the rest of the table and minimizes air currents in the cavity. By taking these measures, the stability of the OPO is only limited by the temperature fluctuations of the PPLN crystal, the baseplate, and the etalon.

9.5.1 Free Running OPO

In order to keep the OPO idler frequency stable, each individual frequency selective element of the OPO requires temperature stabilization. The main requirement is to keep potential frequency fluctuations within the tuning range permitted by the PZT mirror. However, it is convenient to keep them as small as possible. For example, the temperature of the PPLN crystal determines the center frequency of the gain profile, while a temperature change of the etalon shifts the center of its transmission curve. The last instance of frequency selection is the cavity length, which depends on the thermal expansion of the breadboard. Each single component is carefully temperature stabilized by a self-built proportional-integral-derivative (PID) temperature controller, which is based on a microcontroller (Microchip dsPIC33EP256MU806). The microcontroller generates a pulse-width modulation (PWM) output at 17 kHz with a 13-bit resolution, which is transmitted through a fiber connection (Avago Versatile Link) to the corresponding heater, driving a Peltier element. Additionally, the controller contains a 24-bit analog-digital converter (Texas Instruments ADS1255) that is used to measure the resistance of the resistance temperature detector (RTD). The long term precision of this reading is increased by using relays to switch the direction of the current every 256 samples (10.24 s) to compensate for the thermal electromotive force (EMF). The resistance of the negative temperature coefficient (NTC) RTDs is selected based on the operating temperature of the heated component. For example, it is convenient to use a high resistance NTC RTD (1 MΩ at 25 °C, U.S. Sensor GP105V8J) for the high temperatures of the PPLN, as this brings the resistance at operating temperatures down to the 10-100 kΩ range.

In contrast, the choice of the 10 kΩ RTD (Thorlabs TH10K) for the etalon and 5 kΩ RTD (TE Technology MP-3176) for the cavity breadboard is rather arbitrary but still results in reasonable resistance values when operating near room temperature. Using the temperature controllers, the RMS temperature fluctuations of the individual cavity components were reduced to 170 µK (47 mΩ) for the PPLN, 67 µK (25 mΩ) for the etalon and 26 µK (5 mΩ) for the cavity breadboard.

In the following, the OPO is operated with around 7.5 W pump power, with approximately 1 % intensity fluctuations after the fiber amplifier. The Nd:YAG pump laser is freely running without stabilization to the iodine reference. The PZT inside the OPO cavity is also not controlled. Only the temperatures are stabilized, with the controllers keeping the etalon and the base plate at a fixed temperature around 30 °C and the PPLN crystal temperature around 155 °C. Two percent of the signal wave is coupled out of the cavity, which is subsequently frequency doubled in a single pass through a 10 mm long PPLN at $T = 63.5\,°C$ and $\Lambda = 23\,\mu m$ (Covesion MSHG1650-0.5-10). Afterwards, a wavemeter monitors the frequency of the SHG component (Figure 9.11a) and a power meter samples the intensity of the residual signal wave (Figure 9.11b). These measurements show that

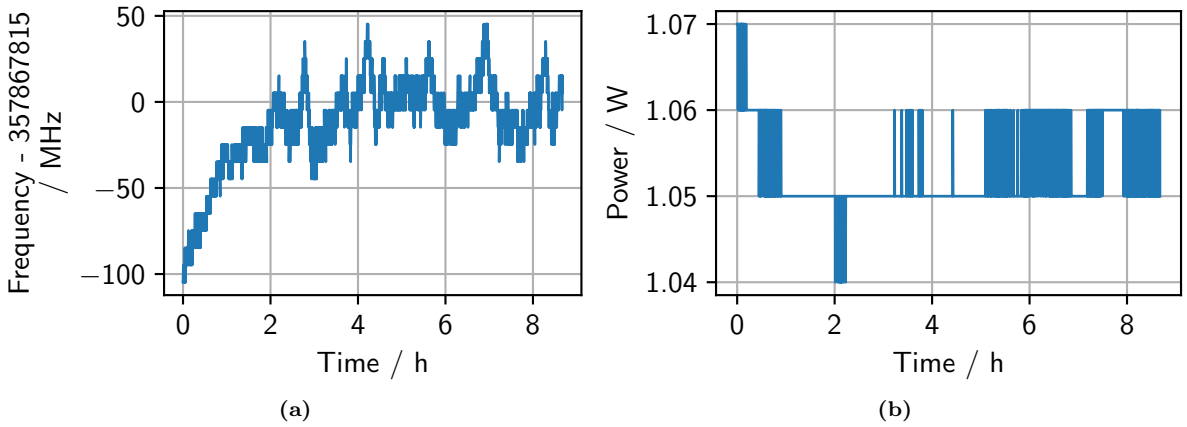

Figure 9.11: (a) Measured frequency of the second harmonic of the signal wave over several hours and (b) the corresponding intensity of the signal output. The steps reflect the resolution of the measurement device.

the temperature equilibrates after two hours, after which the frequency of the second harmonic of the OPO signal remained stable to within ±50 MHz. Similarly, the intensity of the signal wave stabilized within 1 %. These measurements display a promising basis for the further stabilization of the OPO cavity with a PLL which controls the cavity PZT.

9.5.2 OPO Bandwidth

Using an optical beat note between frequency-doubled signal output and the OFC, the frequency of the signal can be measured and stabilized. The quality of the stabilization depends on the frequency bandwidth of the PZT mirror inside the OPO cavity, since only noise contributions within this bandwidth are compensated. Before assembling the cavity, we made measurements of the frequency response of the PZT mirror assembly

using the phase shift measurement setup described in Section 5.3.2. One of the frequency synthesizer (based on the AnlalogDevices AD9854) outputs is amplified up to ±32 V with an offset of 33 V (SVR 150-1), which is afterward connected to the PZT. A modulation of the PZT results in an amplitude modulation in the frequency measurement setup, which is monitored with an oscilloscope through a photodiode. The second frequency synthesizer output supplies the reference signal for the second oscilloscope channel. In the following, the modulation frequency is changed stepwise over the range from 30 kHz to 600 kHz. The demodulation of the signal is performed digitally with an FFT for each frequency step (Section 5.3.2). The frequency dependent phase differences relative to the reference signal are displayed for different mounting blocks of the PZT actuator in Figure 9.12a and 9.12b. The first PZT mounting block follows the basic design of a lead filled copper cone with a

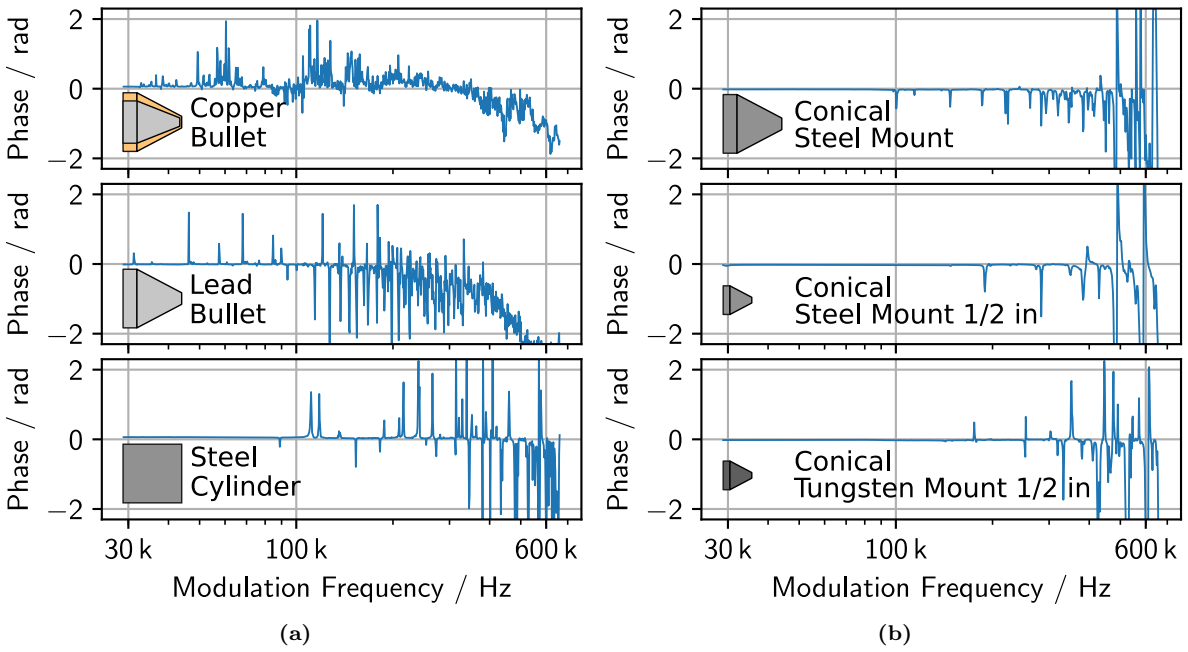

Figure 9.12: (a) Various iterations of the PZT actuator mount, which determines the frequency dependent phase shift between the modulation applied to the PZT and its response. (b) The best design found is a 0.5 inch conical mounting block made of tungsten.

short cylindrical section near the wide end. The length and the diameter of the mounting block are 1 inch, while the diameter of the flat tip is 5 mm. These specifications correspond roughly to a device described in the literature, which promises a resonance-free bandwidth of 180 kHz [204].

However, we were unable to replicate the results presented in that work, despite constructing multiple variants of their device. Our implementations of this design always resulted in numerous resonances, starting from just above 30 kHz. We tried slightly varying shapes of the design of the copper shell, used a mixture of tin and flux on the inside of the copper shell to improve adhesion and even tried absorbing impurities from the molten lead with a slice of potato. Soldering the PZT onto the mounting block instead of gluing it also

had no effect on the measurement result. Replacing the copper lead union with a solid lead block of the same shape improved the resonance structure somewhat by fewer resonance peaks in the important low-frequency range up to 100 kHz. Encouraged by this result, we replaced the lead mount with a cylindrical stainless steel mount of 1 inch diameter and length. Using this block, the first resonance shows up around 90 kHz (Figure 9.12a). Changing the shape of the cylinder into the conical shape used before, shifts the first resonance peak further up to 100 kHz and simultaneously reduces the size of the following resonance. Further, reducing the dimension of the block to 0.5 inch leads to the largest improvement, with the first resonance peak up to 190 kHz. Finally, constructing the block out of tungsten instead of stainless steel reduces the size of the first resonance, although its location shifts again to a lower frequency around 175 kHz (Figure 9.12b).

After these measurements, we selected the tungsten mounting block for the OPO. Thus, the OPO PZT actuator can compensate noise contributions up to a bandwidth of 175 kHz. If the PLL is able to handle the phase shift of the first resonance without inducing oscillations the bandwidth limit could be pushed up to 250 kHz, corresponding to the second resonance peak.

9.6 Molecular Beam

Equally important as the precision laser system is a rotationally and vibrationally cold source of OH or OD molecules. The basics of a molecular beam have been discussed previously (Section 7.1), which allows us to focus now on the technical details. The stainless steel bubbler containing the white fuming nitric acid ($> 95\,\%$ HNO_3) is electropolished from the inside, with a maximum capacity of 160 ml (Wilhelm Schmidt GmbH JEX0.15). It is filled with glass with approximately 10 ml of nitric acid soaked into it, which maximizes the number of exposed molecules to the incoming xenon gas. If the bubbler is left at room temperature, the pulsed solenoid valve (Parker Series 9 General Valve) was found to clog after a few hours. Opening the valve reveals a black substance, which is probably identical to the corrosion products found on the inside of the bubbler. Therefore, the bubbler is cooled to $-15\,°C$, which prevents condensation inside the valve and has little effect on the OH density[205]. The valve is operated at 10 Hz with a pulse width of approximately 100 µs. A 6 mm long quartz capillary is attached to the 1 mm nozzle of the valve. A 8 mJ, 10 ns pulse from an argon fluoride (ArF) excimer laser at 193 nm (GAM EX5/250-180) is weakly focused on to the tip of the capillary and dissociates nitric acid molecules into OH and NO_2 before the supersonic expansion (Figure 9.13). The expansion of the OH molecules results in rotational cooling of the molecules. The translation energy experiences no cooling. The translational degrees of freedom also experience cooling, resulting in a narrow velocity distribution, but the enthalpy of the molecules before the expansion is mostly converted into a large mean forward velocity of the molecules. A time of flight

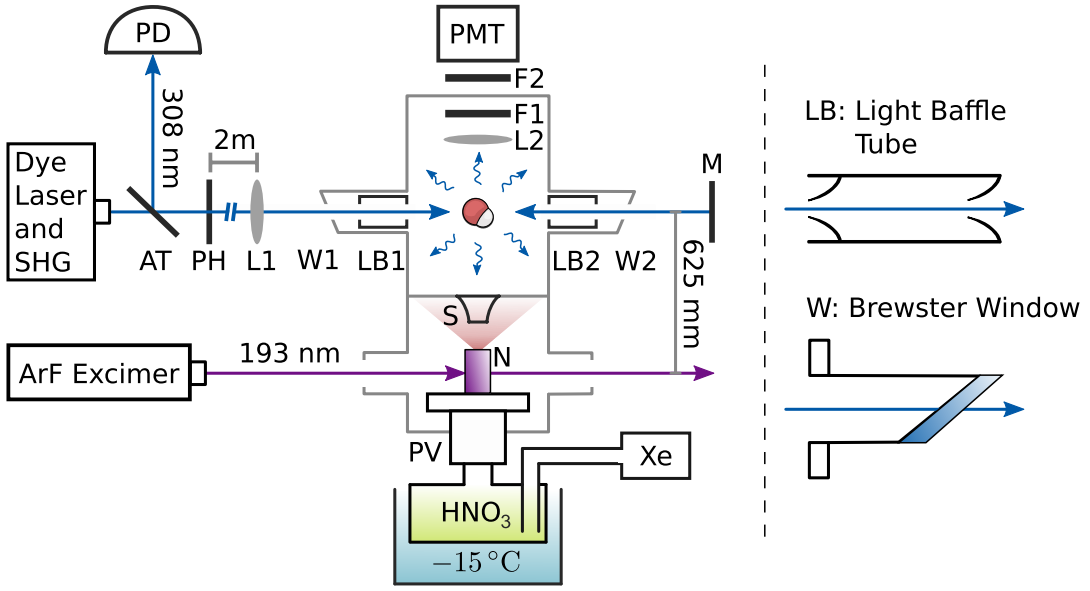

Figure 9.13: Schema of the molecular beam creation and detection setup. Nitric acid (HNO_3) get seeded with xenon (Xe) and propagates through a pulsed valve (PV) into a fused silica nozzle (N). An intense UV pulse of an argon fluoride (ArF) excimer laser dissociates the molecule inside the nozzle, leading to a supersonic expansion of the OH in the first vacuum chamber. Afterwards, a skimmer (S) selects a narrow velocity class of the OH for detection inside a second vacuum chamber. The 308 nm laser beam passes first an attenuator (AT), a pinhole (PH), a lens (L1), a Brewster window and a light baffle (LB1), before exciting the OH. Doppler reduced detection requires excitation of the OH also from the opposite direction. Therefore, a retroreflection mirror (M) sends the beam back. The reflected beam is aligned to maximize the signal on the photodiode (PD). Finally, a photomultiplier (PMT) detects the OH fluorescence light, after it passes a lens (L2) and two color filters (F1, F2).

measurement estimates the molecular velocity to approximately 340 m/s, which is largely determined by the heavier xenon atoms.

A skimmer with an aperture of 4 mm selects a small fraction of the OH molecules before they enter the second differential pumped vacuum chamber. The OH molecules propagate inside the second chamber through a 480 mm long traveling-wave Stark decelerator, with a 4 mm circular profile[206]. For all experiments in this thesis, the decelerator electrodes are grounded, resulting in a negligibly small electric field strength in the spectroscopy region after the decelerator. Additionally, the electrodes act as a geometric aperture and limit the transverse velocity spread to a full width at half maximum (FWHM) of around 2.5 m/s. After the Stark-decelerator the molecules are excited by the 308 nm beam of the UV spectroscopy laser (Section 9.4). Some part of the reemitted fluorescence light is collected with a fused silica lens ($D = 50$ mm) and filtered by two color filters before reaching the on-axis photomultiplier tube (PMT) (ET Enterprises 9829QSB). In detail, a UG5 color filter right behind the lens and a UG11 color filter in front of the PMT both help reduce the intensity of the photodissociation pulse as well the intensity of visible light. The transmission maximum ($> 90\,\%$) of both filters is around 330 nm.

However, the strong dissociation pulse still limits the SNR of the fluorescence signal. This has been improved somewhat by suppressing the gain of the PMT for a 20 µs interval during the time of the dissociation pulse. In detail, electrons emitted from the photo-

cathode inside the PMT are hindered from reaching the first dynode by increasing the potential on the photocathode to a more positive value than the first dynode.

The spectroscopy laser beam at 308 nm passes a neutral density filter and a 0.8 mm circular aperture approximately 27 cm away from the center of the BBO. Afterwards, the beam propagates approximately 2 m in the air from the laser table to the entrance of the vacuum chamber. Here the beam is recollimated with a fused silica lens ($F = 2\,\mathrm{m}$) before it enters the vacuum chamber through an ultrasil fused silica Brewster window. The 5 mm thick window is directly glued on to the flange (Torr Seal). Inside the chamber, it has to pass one light baffle tube, containing two skimmer like circular apertures of 5 mm diameter. The internal surface of the tube is coated with graphite to shield the PMT from potential stray light. Finally, the beam reaches the interaction region of the OH with an estimated elliptical profile of $0.8 \times 1.0\,\mathrm{mm}$ in size. Potential Doppler-shifts can be compensated using a counterpropagating beam along the same axis. Therefore, after the 308 nm beam passes the interaction region and propagates through a second light baffle tube and a window, it is retroreflected on a UV enhanced aluminum coated mirror ($R = 93\,\%$). The beam propagates back along the same path and passes the initial 0.8 mm aperture a second time, but now from the opposite direction. The neutral density filter behind the aperture serves this time as a reflector. The intensity of the reflected light on the photodiode is maximized, which corresponds to an optimal superposition of the two counterpropagating beams. The estimated maximum offset between the two beams at the aperture is around 0.1 mm.

9.7 UV Spectroscopy Measurement

Using the precision laser and the molecular beam system, we can now measure the electronic spectra of OH and OD. The 616 nm CW dye laser frequency is monitored with a wavelength meter (Toptica WS7), and a spectrum analyzer displays the optical beat note relative to the nearest OFC mode. The UV wave at 308 nm follows any frequency changes of the dye laser. Therefore, the coarse frequency selective elements inside the dye laser cavity are aligned based on the wavemeter reading. The two cavity PZT mirrors are controlled externally based on the frequency of the optical beat note. The reference signal for the beat note is provided by a computer controlled frequency synthesizer. A change of the reference frequency results in a change of the optical frequency. The dye laser is tuned in steps of 100 kHz, corresponding to 200 kHz in the UV, over the electronic transitions of OH or OD. A PMT detects the fluorescence light resulting from the excitation. The analog signal of the PMT anode is connected to a digital oscilloscope, with a 100 kΩ load to the ground. The signal on the PMT is recorded starting 1 ms after the excimer pulse for a duration of 2.8 ms with a resolution of 2 µs. The SNR is improved by averaging around 44 shots at a repetition rate of 10 Hz. The measurement is repeated for each frequency

step, so a complete scan over the transition results in a two dimensional (2D) matrix of the PMT signal as a function of time delay and laser frequency (Figure 9.14a). The

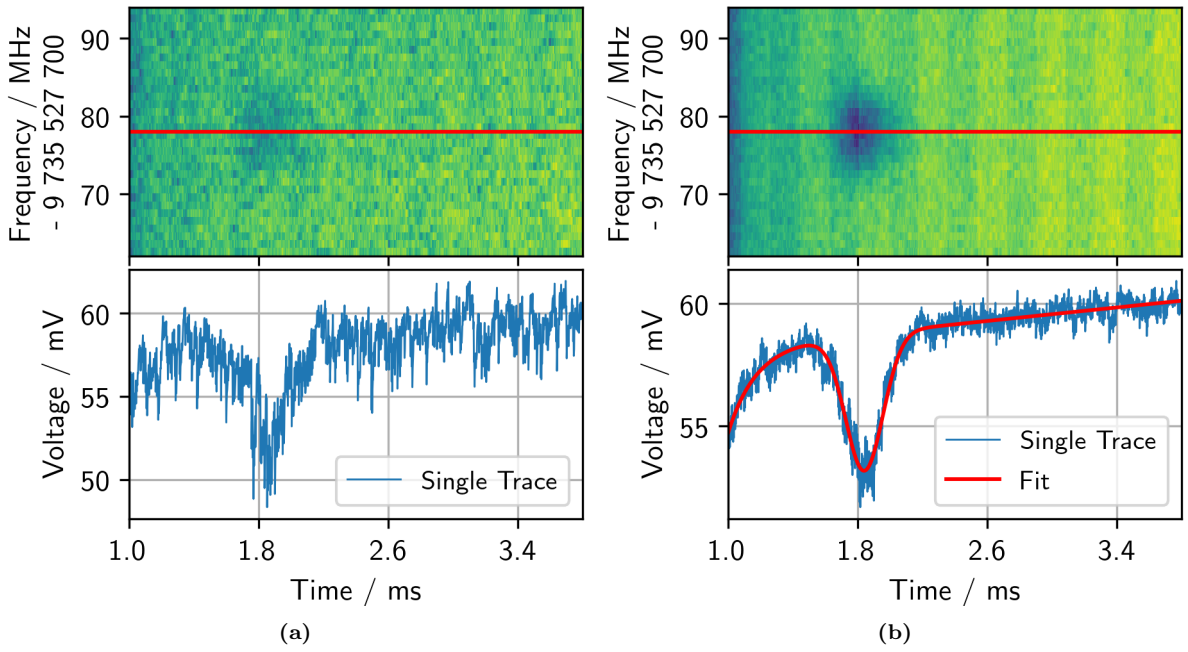

Figure 9.14: (a) Single scan over an electronic transition in the OH. The plot shows the fluorescence intensity as a function of time delay after the excimer pulse and absolute optical frequency, respectively. The cut-though at single laser frequency displays a single, unaveraged oscilloscope trace with poor SNR. (b) Averaging multiple matrices increases the SNR significantly, allowing a fit to extract the signal amplitude at each frequency step.

frequency steps in each scan correspond to fixed beatnote frequencies

Since the repetition rate of the OFC varies slightly over time, the absolute frequency can be slightly different in each measurement. To correct for this, we continuously record the repetition rate of the OFC on a frequency counter. These measurements are time-stamped and can later be correlated with the data from the oscilloscope. The beat note frequencies in each scan are converted to absolute optical frequencies using

$$f_{abs} = 2(n\overline{f}_r + f_{bn}), \tag{9.11}$$

with the averaged repetition rate $\overline{f}_r$ over the time interval of the scan, and n determined using the laser frequency measured by the wavemeter (Figure 9.15a). The prefactor of 2 accounts for SHG of the 616 nm wave into the UV.

Averaging multiple 2D matrices to improve the SNR requires consideration of the changing repetition rate $\overline{f}_r$ between the measurements. The frequency spacing of 200 kHz between each step of the scan is conserved, while the absolute frequency offset in each scan is expressed relative to the first scan (Figure 9.15b). All frequency steps after the first scan are weighted depending on their relative value to the frequencies of the first scan, resulting in a slight frequency shift of all following 2D matrices to match the frequency

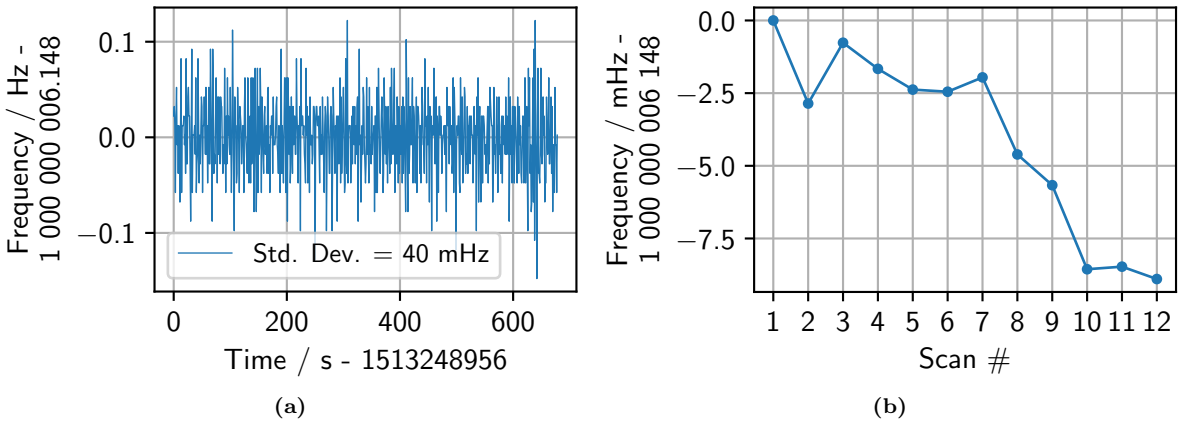

Figure 9.15: (a) Frequency counter measurement of the OFC repetition rate f_r over the time interval of the first scan (#1). The time scale used is unix time, which counts the number of UTC seconds since the 1st January 1970. (b) The averaged OFC repetition rates of each of the following scans (#2-#12), relative to the averaged f_r of the first scan.

axis of the first scan. For instance, Figure 9.14b results from a weighted average of 12 individual matrices, including the one shown in Figure 9.14a.

Extracting the signal amplitude out of the averaged 2D matrix is the next processing step. The scattered light from the spectroscopy laser at the windows and the light baffles contributes to a constant background. Much more severe at early times is the fluorescence light of the quartz capillary induced by the dissociation pulse. The actual fluorescence light of the molecules peaks at around 1.84 ms after the dissociation pulse, but still within the tail of the quartz capillary fluorescence. Therefore, an independent seven parameter fit at each frequency trace is used to separate the contributions of the background and the signal. In detail, the fitted model consists of an exponential and linear function, which address the background, while a Gaussian function approximates the signal

$$f(t) = \underbrace{\exp[-a(t-t_0)] + mt + b}_{\text{background}} + \underbrace{A \exp\left[-(t-t_1)^2/(2\sigma^2)\right]}_{\text{signal}}. \tag{9.12}$$

The fit parameters of the Gaussian function describe the amplitude A of the signal, the arrival time of the molecules t_1 and the standard deviation σ. The total fluorescence intensity of the OH is estimated by subtracting the background contributions and integrating the intensity within a fixed time window $\pm 2\sigma$ around t_1. This total fluorescence intensity is determined independently for each laser frequency in the averaged matrix. Examples of typical spectra of fluorescence intensity versus laser frequency for OH and OD are depicted in Figure 9.16a and Figure 9.16b, respectively. The laser induced fluorescence (LIF) measurements start from the ground state $X^2\Pi_{3/2}$, $J'' = 3/2$ and go to the first electronic excited state $A^2\Sigma^+$. While all hyperfine components are well resolved and separated for OH, which allows a frequency scan over a single transition line. The smaller ground-state

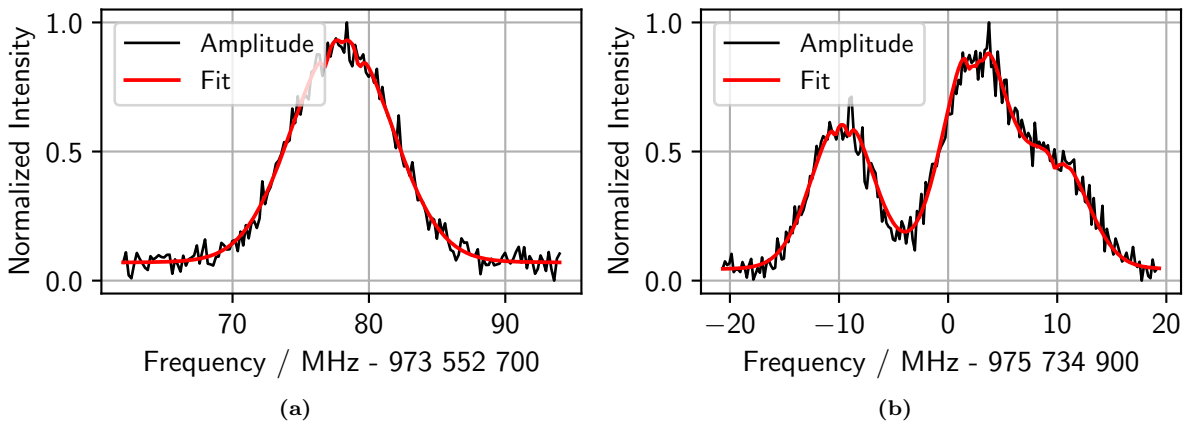

Figure 9.16: (a) Fluorescence intensity of the $N' = 1$, $J' = 1/2$, $F' = 0 \leftarrow f$, $F'' = 1$ transition in OH, with full quantum mechanical fit. (b) Fluorescence intensity of the $N' = 1$, $J' = 3/2$, $F' = 3/2 \leftarrow f$, $F'' = 1/2$, $3/2$ and $5/2$ transition cluster in the OD with fit.

hyperfine splitting in OD results in transition clusters (Section 2.6.1). The spacing of the transitions is similar to the linewidth which results in blending. Therefore, a scan that covers transitions from all of the closely separated hyperfine ground state levels to the excited hyperfine state becomes necessary. The scanning procedure is repeated for the strongest transitions in the OH and the OD at least twice on different days, which ensures reproducibility of the measurements.

9.8 Systematic Effects

9.8.1 Retroreflection Quality

The fundamentals of measuring the geometric retroreflection quality are discussed previously (Section 7.3), as well as in the experimental setup (Section 9.6). The following discussion aims to put a number on the frequency uncertainties originating from imperfect retroreflection. The retroreflection quality is dependent on the angle between the two counterpropagating beams, the amplitude of each beam and the transverse mode structure.

The angle between the counterpropagating beams depends on the precision of the pointing alignment through the 0.8 µm aperture (Figure 9.13). The alignment is carried out based on the light intensity passing through the aperture. The transverse position of the aperture is optimized for the forward propagating beam. Afterwards, the beam passes a distance over 2 m to reach the vacuum chamber and is reflected off the surface of multiple mirrors before propagating back through the same path and the same aperture. The combined sensitivity of the aperture and mirror alignment makes it possible to estimate that the displacement at the aperture between the two beams is within 0.1 mm. The 0.1 mm offset corresponds to an angle of $\alpha = 40\,\mu\text{rad}$ between the two beams, taking the

lens ($F = 2\,\mathrm{m}$) along the propagation path into account. Thus, the resulting maximum frequency shift of the measured transition is around 23 kHz, assuming the offset is along the propagation direction of the molecular beam. Since the laser system on a floating optics table can shift slightly over the course of a few hours, frequent optimization of the pointing is required. Realigning the laser between frequency scans randomizes the sign and the magnitude of the frequency shift. Additionally, the pointing error is not necessarily along the axis of the molecular beam, which represents the worst case. No frequency shift occurs if the pointing error is perpendicular to the propagation direction of the molecular beam. Considering these arguments, the estimated frequency uncertainty of an averaged set of measurements is less than 10 kHz.

The amplitude difference between the counterpropagating wave and the initial wave at the interaction point with the molecules also causes a frequency shift. After the interaction with the OH, the forwards propagating beam passes a fused silica window, is reflected and passes the same window a second time. The measured transmission of the Brewster windows is 98.5 % and the reflectivity of the UV-enhanced aluminum coated mirror is 93 % at 308 nm. Thus, the intensity of the reflected beam is approximately 90 % of the intensity of its forward propagating counterpart. The frequency shift caused by the different intensities is reduced by aligning both beams perpendicular to the molecular beam. This alignment of the retroreflection mirror is carried out with an iterative procedure. First, the laser frequency is scanned through a strong absorption line of the OH with and without retroreflection. Afterwards, all mirrors are optimized, so that the center position of the transition line without retroreflection is the same as the center position with retroreflection. When both measurements show no difference in the line shape, the molecular velocity distribution along the laser propagation direction is interpreted as being maximally symmetric. Therefore, our estimate of the additional error by the amplitude mismatch is less then 5 kHz, so we assign an overall uncorrelated error of 10 kHz for each transition.

The laser beam profile also causes a frequency shifts if it deviates from the Gaussian TEM_{00} mode. The retroreflection quality depends on the intensity measurements behind the aperture. Higher Hermite-Gaussian modes TEM_{0n} shift the center of maximum intensity, corrupting the alignment and decreasing the retroreflection quality. A knife edge measurement predicts around 80 % of the beam intensity inside the TEM_{0n} modes of our UV spectroscopy laser. The remaining 20 % intensity is located in the TEM_{1n} modes. Additionally, around 50 % of the counterpropagating beam passes the 0.8 mm aperture a second time. Combining both observations leads to a potential offset of 0.27 mm between the center of the maximum and the true beam center at the position of the aperture. The 0.27 mm offset corresponds to a 60 kHz frequency shift of the measured transitions. This

frequency offset is the same for all measurements, with the assumption of a constant mode structure and the same alignment procedure of the optical beam path.

9.8.2 Zeeman Shift

The splitting of each hyperfine state inside a magnetic field has been discussed previously (Section 2.2.3.1). All measurements of electronic transitions in OH or OD are carried out in the ambient magnetic field of the laboratory. Thus, estimating the field strength is essential in predicting the corresponding frequency shift. For this purpose, the vacuum chamber was vented, and two Hall-effect probes (Lake Shore Cryotronics HMMT-6J04-VR and HMNA-1904-VR) were placed through an open CF40 flange into the region where the spectroscopy laser and molecules normally interact. To justify this measurement technique, we measured the magnetic field with the turbomolecular pumps on and off. Since we measured no change of the magnetic field strength, we conclude a negligible contribution from the pumps and the associated electronics. The strongest magnetic field strength in the spectroscopy region is along the vertical axis with 75 µT. A much weaker field is along the propagation axis of the spectroscopy laser of 14 µT. A negligible field of 2 µT is along the third axis, perpendicular to the previous two axes. Thus the magnetic field is, in good approximation, vertically oriented. Considering the horizontal polarization of the spectroscopy laser, the transitions expected are those with $\Delta M_F = \pm 1$. For weak magnetic shifts the $\Delta M_F = -1$ and the $\Delta M_F = +1$ transitions are equally shifted, but with opposite signs, resulting in zero net shift. However, with an increasing magnetic field, the corresponding states mix with other hyperfine components. The resulting transitions are shifted by a different amount and have different transition strengths. This effect is rather subtle and is not immediately visible in the blended lines. The previous calculation of a transition cluster in OD highlights the splitting of the hyperfine lines inside an ambient magnetic field of 75 µT (Figure 2.6a-2.6b). Thus, assigning an uncertainty caused solely by the magnetic field has proven to be complicated. Nonetheless, a later theoretical analysis provides an estimate of the contribution of the Zeeman effect on the uncertainty of individual line positions (Section 10.2).

9.8.3 AC Stark Shift

The time-varying electric field of the spectroscopy laser causes an additional shift since transitions between multiple hyperfine components can interact with a single laser frequency. The individual lines experience a laser power dependent shift, called the alternating current (AC) Stark shift (Section 8.2). The individual transitions also experience saturation with increasing laser power. Both effects depend on laser power and are difficult to analyze separately. As with the Zeeman effect, a later theoretical analysis estimate the contribution of these effects to the uncertainty of each line position (Section 10.2).

Chapter 10

Analysis

A full quantum mechanical (QM) fit is used to determine the zero-field line positions for measured electronic transitions in the hydroxyl radical (OH) and the deuterated hydroxyl radical (OD) (Section 9). The analysis is based on an effective Hamiltonian model, computed with the program PGOPHER[56]. Statistical uncertainties are assigned to each transition based on the uncertainties determined in the individual fits and the spread of fitted transition frequencies. Since the uncertainty is at the order of magnitude of the Zeeman effect and the alternating current (AC) Stark shift, it is important to account for these effects when determining the overall line position. To quantify the contributions of these shifts to the extracted line positions a simplified second model was used to determine the line positions ignoring Zeeman and/or AC Stark shifts (Section 10.2).

10.1 Full Quantum Mechanical Fit

A preliminary model is used to make a first estimate of the optical transition frequencies. This model is based on a multi-Gaussian fit to the measured fluorescence spectra and neglects the magnetic field (Figure 10.1). Afterwards, PGOPHER is used to fit an effective Hamiltonian model to the estimated transition frequencies. The Zeeman terms due to the ambient magnetic field of 75 µT, which is perpendicular to the laser polarization, are then added to the effective Hamiltonian. The magnetic g factors used are $g_L = 1$ for the orbital angular momentum in the electronic ground state, $g_s = 2.002$ for the electron spin and $g_r = 0$ for the rotational angular momentum. The preliminary model provided by PGOPHER, including the magnetic field, is used to calculate eigenstates, eigenenergies and electric transition dipole moments, which are used to expand the Hamiltonian with the electric field of the two counter-propagating laser beams. With this, the evolution of the systems density matrix with the Lindblad master equation is used to simulate the fluorescence spectrum. The details on these calculations are elsewhere (Section 8.5).

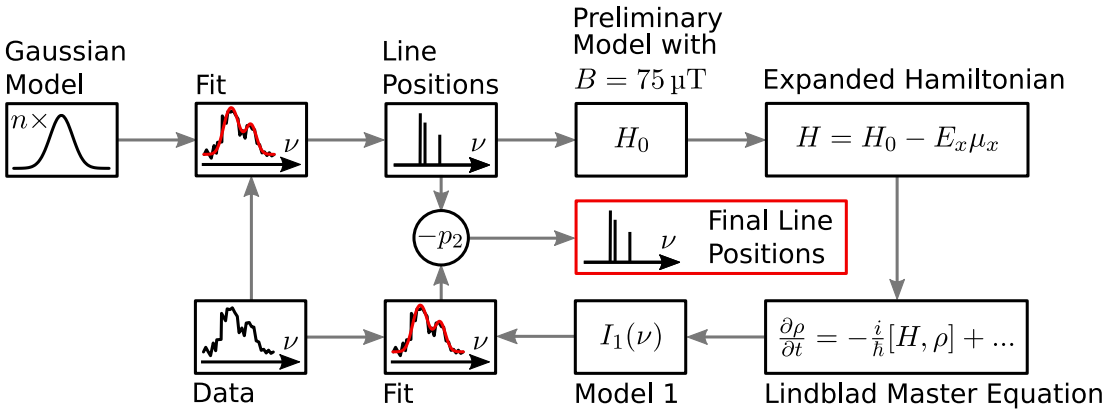

Figure 10.1: Schema of the full QM fitting procedure. A plain multi-Gaussian fit supplies a first estimate of the line positions for the fluorescence data. The line positions are the input parameters for an effective Hamiltonian fit. The model $I_1(\nu)$ includes laser power and linewidth, after expanding the Hamiltonian and simulating the spectrum. Finally, fitting the new model to the measured data supplies a correction parameter p_2. The absolute line positions are determined by subtracting p_2 from the estimated line positions.

The full simulated spectrum is based on approximations that take into account the line positions, the laser power, and the Doppler broadening. A fitting routine aims to minimize the root-mean-squared (RMS) deviation between a measured spectrum and the simulated one. The simulated spectrum is described with the function

$$I_1(\nu) = p_0 + p_1 S(\nu + p_2, p_3, p_4), \tag{10.1}$$

with five free parameters p_0-p_4. The first two parameters p_0 and p_1 are responsible for the scaling and vertical adjustment of the raw simulated spectrum S. The parameters p_3 and p_4 describe the Gaussian linewidth due to Doppler broadening and the laser power, respectively. Finally, the most interesting parameter p_2 accounts the overall frequency offset between the measured data and the preliminary model. Thus, subtracting the p_2 parameter from the line positions of the preliminary model refines the first approximation and supplies absolute zero field line positions (Figure 10.1).

The evaluation of all measured spectra with the full quantum mechanical fitting routine displays some notable characteristics. In general, the order of magnitude of the fitted parameters seems reasonable, but the values of a few parameters deviate slightly between the two isotopes OH and OD. For example, the fitted Gaussian linewidth parameter p_4 clusters around $(3.30 \pm 0.15)\,\mathrm{MHz}$ for OH and $(3.00 \pm 0.15)\,\mathrm{MHz}$ for OD. Despite this, we observed no difference in the time of flight distribution of the molecular beam between the two isotopes. The relative peak intensities inside the spectrum of the OD transitions determine the size of the laser power parameter p_3. In relation to the absolute measured laser power, the parameter p_3 clusters between 0.2 and 0.4 for most spectra. An exception exists for heavily blended lines, which make the assignment of the relative peak heights challenging for the fitting algorithm (Figure 10.2a). The model $I_1(\nu)$ might not capture some effects responsible for this deviation, but the poor signal to noise ratio (SNR) makes

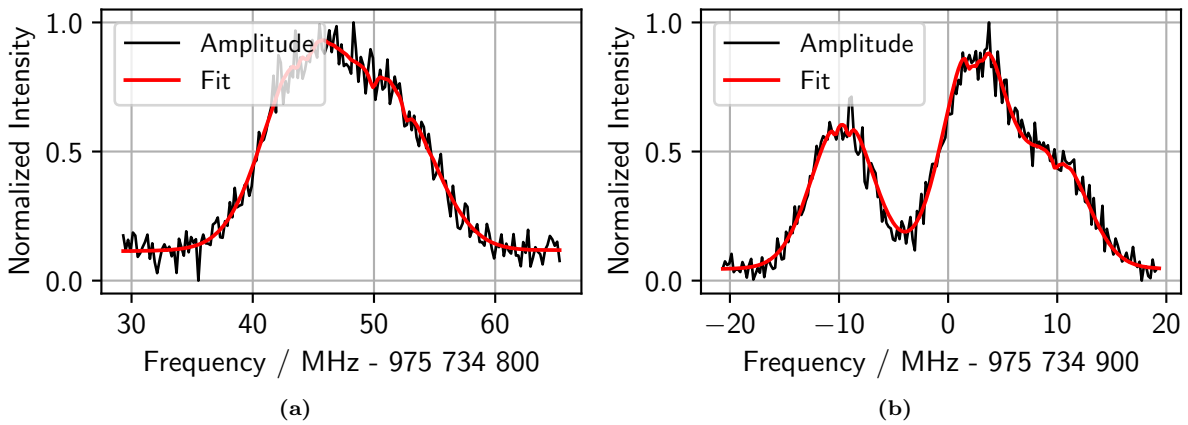

Figure 10.2: (a) Fluorescence spectrum of the $N' = 1$, $J' = 3/2$, $F' = 1/2 \leftarrow f$, $F'' = 1/2, 3/2$ transition cluster in OD, with full quantum mechanical fit. The close spacing between the individual transitions complicates the fit. (b) In contrast, the fluorescence intensity of the $N' = 1$, $J' = 3/2$, $F' = 3/2 \leftarrow f$, $F'' = 1/2, 3/2$ and $5/2$ transition cluster of OD shows higher separation of the individual transitions.

a more detailed analysis impossible. In the OH measurements and measurements of OD transitions with a single hyperfine component, the p_3 parameter is constrained to fall in the 0.2-0.4 range determined in the OD measurements. This is necessary, since these spectra only offer a single peak, and the information needed to determine the laser power is insufficient.

10.2 Uncertainty and Simple Voigt Fit

The fitting procedure of the full QM fit supplies absolute, zero-field positions of the OH and the OD transitions. However, each fitted line position has an associated uncertainty. The task of the simple Voigt model is to assign a line position excluding the AC Stark shift and the Zeeman effect in order to determine the contribution of these effects to the total measurement uncertainty.

The total uncertainty is determined in multiple steps. Each transition measurement is repeated at least twice on different days, sometimes with different laser powers. Fitting a single fluorescence spectrum results in an estimate of a transition frequency ν_i with a statistical uncertainty σ_i. Including the uncorrelated uncertainty of 10 kHz, which comes from the fluctuations of the retroreflected beam (Section 9.8.1), increases the uncertainty to

$$\sigma_i'^2 = \sigma_i^2 + (10\,\mathrm{kHz})^2. \tag{10.2}$$

Now each single transition measurement is associated with an uncertainty of σ_i', which supplies a weighting factor for the calculation of the weighted mean

$$\bar{\nu} = \frac{\sum_{i=1}^{N}(\nu_i \sigma_i'^{-2})}{\sum_{i=1}^{N} \sigma_i'^{-2}} \quad \text{with} \quad \sigma_{\bar{\nu}} = \sqrt{\frac{1}{\sum_{i=1}^{N} \sigma_i'^{-2}}}. \tag{10.3}$$

The uncertainty of the final transition frequency $\bar{\nu}$ is estimated with $\sigma_{\bar{\nu}}$. A particular transition frequency is determined from N individual transition measurements, with the sum computed over all of those. However, a few very small individual uncertainties σ_i' leads to an underestimate of the error $\sigma_{\bar{\nu}}$ relative to the spread of the individual frequencies ν_i. In contrast, calculating the standard deviation of the unweighted mean results in a larger uncertainty of $\bar{\nu}$. In the end, we choose the larger of the two values as the total statistical uncertainty

$$\sigma_{\text{tot}} = \max\left[\sigma_{\bar{\nu}}, \left(\frac{\sum_{i=1}^{N}(\nu_i - \sum_{i=1}^{N}\nu_i/N)^2}{N(N-1)}\right)^{\frac{1}{2}}\right], \tag{10.4}$$

The estimated uncertainties are in general of the same order of magnitude as the Zeeman effect or the AC Stark shift. Frequently, the effects of such shifts are estimated by varying the magnetic field or laser intensity in the measurements, but the large relative uncertainties make extracting their contributions in this manner unfeasible.

The simple Voigt spectrum aims to detect changes of the line positions, by fitting the full QM model (Section 10.1). Since the full QM model supplies the zero-field line positions, the simple model estimates the field dependent line positions. The fitting function is based on a sum of Voigt profiles

$$I_2(\nu) = \tilde{p}_0 + \tilde{p}_1 \sum_i \tilde{p}_2 \left[1 - \exp\left(\frac{-\mu_i^2}{\tilde{p}_2}\right)\right] \times V(\nu - \nu_i + \tilde{p}_3, \tilde{p}_4, \Gamma), \tag{10.5}$$

with the Lorentzian width Γ, Gaussian width $\tilde{p}_4$, transition frequencies ν_i and corresponding transition dipole moments μ_i. The free parameters are $\tilde{p}_0$-$\tilde{p}_4$, where the first two parameters $\tilde{p}_0$ and $\tilde{p}_1$ are a vertical scaling and offset that adjust the simple model relative to the simulated spectrum of the full QM model. Saturation effects that result in peak strengths in the simulated OD spectra that do not match the expected μ_i^2 scaling are accounted with the empirical saturation parameter $\tilde{p}_2$. In spectra with a single peak where there is insufficient information to determine $\tilde{p}_2$, the prefactor $\tilde{p}_2\left[1 - \exp\left(\frac{-\mu_i^2}{\tilde{p}_2}\right)\right]$ is replaced with μ_i^2. In analogy to the full QM model, the parameter $\tilde{p}_3$ accounts for the line positions. Based on $\tilde{p}_3$, the contributions of the Zeeman effect and the AC Stark shift are assigned.

The full QM model $I_1(\nu)$ supplies a parameter set of its own p_0-p_4. After fitting

the model to the measured spectrum, those parameters are well defined. Additionally, the effective Hamiltonian H_0 used in this fit is based on the ambient magnetic field of $B = 75\,\mu\text{T}$. With these two constraints, the model $I_1(\nu)$ describes a fluorescence spectrum separated from noise (Figure 10.3). Changing the magnetic field input of the effective

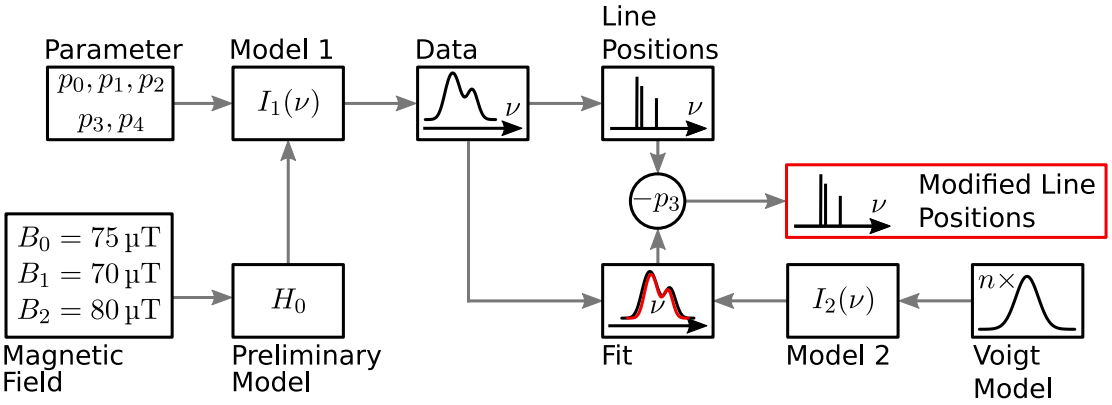

Figure 10.3: Schema of the simple multi-Voigt fit procedure. Based on the previously fit of the full QM model $I_1(\nu)$ the parameters p_0-p_4 are fixed. However, changing the magnetic field strength inside the effective Hamiltonian generates slightly different spectra. The simple multi-Voigt model $I_2(\nu)$ assigns a net shift to these variations after a fit to the simulated spectrum.

Hamiltonian results in slightly different fluorescence spectra $I_1(\nu)$. The fit of the simple multi-Voigt model $I_2(\nu)$ to the simulated spectrum of $I_1(\nu)$ allows an estimate of the transition frequency net shift. The parameter $\tilde{p}_3$ determines the new line positions, by subtracting it from the zero-field transition frequencies computed with $I_1(\nu)$. Based on the magnetic field measurement uncertainty of $\pm 5\,\mu\text{T}$, the magnetic field might well be $70\,\mu\text{T}$ or $80\,\mu\text{T}$. Thus, the fit of the simple model $I_2(\nu)$ to the full QM model $I_1(\nu)$ supplies new line positions at $\nu_{\text{Voigt},80\,\mu\text{T}}$ and $\nu_{\text{Voigt},70\,\mu\text{T}}$, based on the two different magnetic fields. We estimate the uncertainty of the transition frequency due to the Zeeman effect to be

$$\Delta\nu_{\text{Zeeman}} = \frac{\nu_{\text{Voigt},80\,\mu\text{T}} - \nu_{\text{Voigt},70\,\mu\text{T}}}{2}. \tag{10.6}$$

In contrast to the magnetic field dependence of the Zeeman effect, the AC stark shift depends on the laser power. However, the full QM model shows a discrepancy between the measured powers and the fitted values, which are significantly less than half of the measured values. Thus, we estimate the uncertainty due to the AC Stark shift and saturation effects based on the difference

$$\Delta\nu_{\text{Stark}} = \nu_{\text{QM},75\,\mu\text{T}} - \nu_{\text{Voigt},75\,\mu\text{T}}, \tag{10.7}$$

with the fitted transition frequency $\nu_{\text{QM},75\,\mu\text{T}}$ of the full QM model $I_1(\nu)$ and the modified line position $\nu_{\text{Voigt},75\,\mu\text{T}}$ of the simple Voigt model $I_2(\nu)$. In the following, we assume the laser power discrepancy and the ambient magnetic field are constant over the course of all measurements, which means the corresponding uncertainties are correlated. Therefore, the

individual shifts are determined for each measurement (Equation 10.6-10.7), but the overall shift for a particular transition is computed with the weighted mean. This procedure is consistent with the calculation of the transition frequency, with the same weighting factor $\sigma_i'^{-2}$ (Equation 10.3).

10.3 Zero-field Line Positions

The line positions are the result of a full QM fit (Section 10.1), while the frequency uncertainties corresponding to the Zeeman effect Δ_{Zeeman} and the AC Stark shift Δ_{Stark} are estimated with the simple Voigt model (Section 10.2). Those uncertainties are not included inside the statistical uncertainty σ_{tot} of the transitions frequency $\bar{\nu}$. In fact, they are completely left out for the OH measurements, since these effects proved to be negligibly small ($< 2\,\text{kHz}$) for this isotope. Table 10.1 and Table 10.2 summarize the measured OH transitions and OD transitions clusters, respectively. All transitions start from the

Table 10.1: Zero-field transition frequencies for OH, based on the fit of the full QM model. The difference between the observed (O) and the computed (C) frequencies from the effective Hamiltonian model are listed in the last column (O−C).

No.	p''	F''	N'	J'	F'	Frequency $\bar{\nu}$ / MHz	O−C / kHz
1	e	1	0	1/2	0	972 543 544.417(26)	−3
2	e	2	0	1/2	1	972 544 263.293(20)	1
3	f	2	1	1/2	1	973 552 522.962(27)	10
4	f	1	1	1/2	0	973 552 777.917(27)	9
5	f	1	1	3/2	1	973 562 502.848(38)	−15
6	f	2	1	3/2	2	973 562 933.668(41)	−25
7	e	2	2	3/2	2	975 583 190.355(38)	−21
8	e	1	2	3/2	1	975 583 518.439(21)	−13
9	e	1	2	5/2	2	975 600 025.186(28)	17
10	e	2	2	5/2	3	975 600 407.540(27)	16
11	f	2	3	5/2	3	978 623 067.641(37)	−8
12	f	1	3	5/2	2	978 623 423.479(78)	41

rovibronic ground state $X^2\Pi_{3/2}$, $v'' = 0$, $J'' = 3/2$. The parity p'' and the F'' quantum number refer to the ground state, while the N', J' and F' quantum numbers correspond to the first electronic excited state $A^2\Sigma^+$, $v' = 0$. The OD Table 10.2 might suggest that all transitions originate from the state $F'' = 1/2$, but the transitions frequencies are just tabulated this way because the experiment measures an OD transition cluster, with transitions from $F'' = 1/2$, $F'' = 3/2$ and $F'' = 5/2$ blended together. Since the spacing between the ground state levels is well known, the transitions from $F'' = 1/2$ is always given even if that particular transition would be forbidden by angular momentum selection rules. The uncertainty σ_{tot} is in parentheses next to the frequency (Equation 10.4), which is corrected for the recoil shift (Section 7.4). This corresponds to a frequency of 124 kHz for OH and 118 kHz for OD and is subtracted of the observed frequency. Finally, the column

Table 10.2: Zero-field transition frequencies for OD, based on the fit of the full QM model. The contributions of the Zeeman effect Δ_{Zeeman} and the AC Stark shift Δ_{Stark} are based on studies of the full QM model with a simple multi-Voigt profile. The difference between the observed (O) and the computed (C) frequencies from the effective Hamiltonian model are listed in the last column (O−C).

No.	p''	F''	N'	J'	F'	Frequency $\bar{\nu}$ / MHz	Δ_{Zeeman} / kHz	Δ_{Stark} / kHz	O−C / kHz
1	e	1/2	0	1/2	1/2	975 191 151.074(33)	20	−42	−28
2	e	1/2	0	1/2	3/2	975 191 328.844(35)	3	1	44
3	f	1/2	1	1/2	3/2	975 729 510.621(13)	5	0	−5
4	f	1/2	1	1/2	1/2	975 729 554.271(68)	2	−23	63
5	f	1/2	1	3/2	1/2	975 734 850.974(54)	−42	−34	−21
6	f	1/2	1	3/2	3/2	975 734 909.606(45)	5	11	−5
7	f	1/2	1	3/2	5/2	975 735 003.948(17)	3	5	0
8	e	1/2	2	3/2	5/2	976 811 945.177(42)	1	7	−30
9	e	1/2	2	3/2	3/2	976 811 996.579(40)	3	−2	23
10	e	1/2	2	3/2	1/2	976 812 027.711(96)	20	−22	103
11	e	1/2	2	5/2	3/2	976 820 926.936(96)	0	−7	33
12	e	1/2	2	5/2	5/2	976 820 984.166(27)	3	−7	−42
13	e	1/2	2	5/2	7/2	976 821 062.836(26)	2	1	40
14	f	1/2	3	5/2	7/2	978 434 703.880(28)	2	1	11
15	f	1/2	3	5/2	5/2	978 434 756.718(37)	1	−12	−13
16	f	1/2	3	5/2	3/2	978 434 794.681(86)	−28	−34	−1

labeled "O−C" displays the difference between the observed and the calculated transitions frequencies based on a parameter fit of the effective Hamiltonian model (Section 2.7). This column serves as an additional measurement of the quality of the observed transitions. For example, neglecting the magnetic field when determining the zero-field the OD transitions frequencies results in deviations of up to 300 kHz (in the case of transition #5) between the measured line positions and those from the effective Hamiltonian model.

10.4 Effective Hamiltonian

The "O−C" column of Table 10.1 and 10.2 contains the residuals from a minimized root-mean-square (RMS) fit using the A-state effective Hamiltonian parameters. Details on the definition of the Hamiltonian are discussed elsewhere (Section 2.7). This definition is adopted by the program PGOPHER[56] which is the basis for the following parameter fits.

The ground state $X^2\Pi_{3/2}, v'' = 0$ of OH has been well characterized by Drouin[49]. In the reference article, a comprehensive global fit has been carried out, based on microwave, pure rotational and rovibrational spectroscopy for the OH and its various isotopologues. The fit generates out of this large collection of data, a single set of Dunham parameters that can describe multiple vibrational states and multiple isotopes. However, based on the definition

of our effective Hamiltonian model, it is convenient to convert the Dunham parameters into parameters that apply to a single vibrational state and isotope, specifically two sets of parameters for the vibrational state $v'' = 0$ in OH and $v'' = 0$ in OD (Table 10.3a). Inserting the effective Hamiltonian ground state parameters into PGOPHER allows the calculation of the ground state energies for OH and OD, respectively (Table 10.3b-10.3c). These ground-state levels are the origin for all transitions measured in this thesis.

The excited state $A^2\Sigma^+$, $v' = 0$ of OH the OD is less well characterized. Ter Meulen et al. (1986)[207] used microwave double-resonance spectroscopy to measure the OH A-state spin rotational splitting with high precision. German (1976)[208], Carter et al. (2002)[209] and Xin et al. (2003)[210] measured the OD A-state hyperfine splitting.

Stark et al. (2008)[211] and Coxon (1975, 1980)[25,26] supply the best previous values for the A-X transition frequencies in OH and OD. These works contain a rich data set that includes transitions between higher rotational levels.

Since our current measurement setup only allows detection of the lowest rotational states, the previous works can be used to improve our effective Hamiltonian fit. In detail, some fitting parameters of the effective Hamiltonian model are fixed to those previous works. For the OH the parameters H, L, M and γ_H are fixed to the parameters given by Coxon[26]. For OD, the same parameters are constrained to the parameters from Stark et al.[211]. The program PGOPHER performs a fit of the effective Hamiltonian to our 12 measured OH transitions (Table 10.1) and eight additional A-state hyperfine-resolved spin-rotational splittings measured by ter Meulen et al.[207]. A similar fit is performed using the 16 measured OD transitions (Table 10.2) and additional 13 and 8 A-state hyperfine splittings measured by Carten et al.[209] and Xin et al.[210], respectively.

The uncertainties of the fitted parameters depend on the quality of the input data. For example, the residuals between the fit and the measured transitions frequencies are a decent indicator for potential issues in one measurement. If a single frequency measurement shows a deviation larger than 3σ, the reliability of this particular measurement should be called into question. Fortunately, the effective Hamiltonian fit for OH shows no such anomaly for all included measurements. However, the data set used for the OD fit contains two outliers ($> 3\sigma$). In particular, we identify the A-state hyperfine splittings $N = 3$, $J = 7/2$, $F' = 9/2 \leftrightarrow F'' = 7/2$ (Carter[209]) and $N = 1$, $J = 3/2$, $F' = 3/2 \leftrightarrow F'' = 1/2$ (Xin et al.[210]) as outliers. Therefore, these splittings are excluded from the global fit. The resulting effective Hamiltonian parameters for the $A^2\Sigma^+$, $v' = 0$ state are listed in Table 10.4 for OH and Table 10.5 for OD. In general, the uncertainties of the fitted parameters are separated in two categories: a statistical uncertainty and an uncertainty due to systematic effects. PGOPHER computes the one sigma statistical uncertainty for each parameter after fitting the effective Hamiltonian, which is given in the first set of

parentheses behind the parameter value. The contributions of the Zeeman effect Δ_{Zeeman}, the AC Stark shift Δ_{Stark} (Table 10.1-10.2) and the retroreflection quality (Section 9.8.1) are estimated in a second set of parentheses. This second uncertainty is estimated by shifting the transitions frequencies by, for example, Δ_{Zeeman} and repeating the fit of the effective Hamiltonian. The difference between the initial parameters and the parameters originating from shifted frequencies corresponds to the uncertainty due to the Zeeman effect. The uncertainties of the AC Stark shift and retroreflection quality are estimated in the same way using frequency shifts of Δ_{Stark} and a constant 60 kHz, respectively. Finally, all three uncertainties are combined with a Pythagorean sum to the total systematic uncertainty. Since the contribution of the AC Stark shift and the Zeeman effect proved to have a negligible effect on the OH parameters, the systematic uncertainty is only given for the band origin parameter T.

Table 10.3: (a) Effective Hamiltonian parameters of the ground state $X^2\Pi_{3/2}$, $v'' = 0$ in MHz for OH and OD, after a conversion of the Dunham parameters provided by Drouin [49]. (b) Ground state levels of OH, relative to the absolute ground state at −589 594.229 MHz ($p'' = e$, $F'' = 1$). (b) Ground state levels of OD, relative to the absolute ground state at −1 250 744.792 MHz ($p'' = e$, $F'' = 1/2$).

(a)

	^{16}OH	^{16}OD
B	555 661.4693	296 158.6891
D	57.229 288 3	16.143 28
$H \times 10^3$	4.281 065 6	0.6400
$L \times 10^9$	−448.6944	−35
$M \times 10^{12}$	33.315	1.3
$P \times 10^{18}$	−838.20	−6.0
$Q \times 10^{21}$	−796.21	−9.4
A	−4 168 708.0644	−4 167 841.97
A_D	−17.8685	−9.8676
$A_H \times 10^3$	18.631	5.23
γ	−3488.3181	−1858.746
γ_D	0.610 15	0.1714
$\gamma_H \times 10^6$	−73.14	−11
p	7053.354 621	3762.013 17
p_D	−1.551 093 8	−0.436 101
$p_H \times 10^6$	157.746	23.97
$p_L \times 10^9$	−28.57	−2.3
q	−1160.120 299 9	−328.052 845
q_D	0.442 118 25	0.066 052 1
$q_H \times 10^6$	−82.4266	−6.5218
$q_L \times 10^9$	15.1479	0.63
$q_M \times 10^{12}$	−2.525 06	−0.056
$q_P \times 10^{18}$	332.81	3.9
a	86.108 353	13.304 73
b_F	−73.155 434	−11.174 00
c	130.643 272	20.169 23
d	56.683 092	8.772 94
$d_D \times 10^3$	−23.007	−1.872
$c_I \times 10^3$	−98.9043	−8.047
$c_I' \times 10^3$	6.837	0.56
eQq_0		0.285 69
eQq_2		−0.1205

(b)

p''	F''	Frequency / MHz
e	1	0
e	2	53.171
f	1	1 665.402
f	2	1 720.530

(c)

p''	F''	Frequency / MHz
e	1/2	0
e	3/2	7.112
e	5/2	19.229
f	1/2	310.143
f	3/2	317.326
f	5/2	329.591

Table 10.4: ^{16}OH parameters in MHz of the first electronic excited state $A^2\Sigma^+$, $v' = 0$.

	This Thesis	Stark et al. [211]	Coxon [26]
T	971 954 529.223(11)(60)	971 954 376(3)	971 954 664(54)
			971 954 520(60)
B	508 601.5809(53)	508 603.268(66)	508 599(2)
D	61.876 24(52)	61.8903(36)	61.853(15)
$H \times 10^3$	3.69[a]	3.82(11)	3.687(44)
$L \times 10^6$	−0.41[a]	−0.60	−0.412(57)
$M \times 10^9$	−0.11[a]	−0.021	−0.109(27)
γ	6777.832(10)	6775.74(18)	6762(10)
γ_D	−1.435 17(89)	−1.379(11)	−1.430(54)
$\gamma_H \times 10^3$	0.23[a]	0.069	0.228(60)
b_F	772.077(26)		
c	161.732(68)		
c_I	−0.0335(77)		

[a] Parameters are fixed according to values provided by Coxon [26].

Table 10.5: ^{16}OD parameters in MHz of the first electronic excited state $A^2\Sigma^+$, $v' = 0$.

	This Thesis	Stark et al. [211]	Coxon [25]
T	973 940 524.775(21)(62)	973 940 470(3)	973 940 860(60)
B	271 124.841(13)(7)	271 123.980(48)	271 117.4(36)
D	17.3464(14)(7)	17.3428(13)	17.2758(78)
$H \times 10^3$	0.56[a]	0.561(36)	0.4932(84)
$L \times 10^9$	−39[a]	−39	−18.0(42)
$M \times 10^{12}$	−2.1[a]	−2.1	−3.51(87)[c]
γ	3614.148(25)(10)	3616.72(14)	3600.6(63)
γ_D	−0.4093(52)(22)	−0.4011(66)	−0.3580(72)
$\gamma_H \times 10^6$	13[a]	13	
b_F	118.468(20)(18)		
c	24.863(56)(45)		
$c_I \times 10^3$	−2.7[b]		
eQq_0	0.277(26)(4)		

[a] Parameters are fixed according to values provided by Stark et al. [211].
[b] Based on value from OH fit, but scaled with the reduced mass ratio and proton-deuteron g-factor ratio.
[c] Represents difference between M in excited and ground state.

10.5 Comparison to Other Works

It is useful to compare the fitted effective Hamiltonian parameters in this work to those from previous works. Unfortunately, the slightly different definitions of the effective Hamiltonian make it necessary to first transform the parameters (Section 2.7). In some works, the centrifugal distortion parameters of γ are defined in term of $\mathbf{J}^2$ instead of $\mathbf{N}^2$. Equations (2.44)-(2.47) account for the transformation of the A-state parameters affected by this difference of definition. The next complication arises when comparing the band origin of the $A^2\Sigma^+$, $v' = 0$ state because it depends on the definition of the ground state Hamiltonian. In the best previous works of Stark et al.[211] and Coxon[25,26], the Hamiltonian is defined in terms of the rotational quantum number $\mathbf{R}$ instead of $\mathbf{N}$. Additionally, some works rely on a van Vleck transformation of the Hamiltonian, which introduces an additional Λ-doubling parameter o[25,211]. If it is not already absorbed into the band origin T', the transformation rules must account for it (Equation 2.47). Taking these details into account, Tables 10.4 and 10.5 contain the fitted effective Hamiltonian parameters from the previous best works[25,26,211], adapted to our definition of the effective Hamiltonian, next to the fitted parameters determined in this work.

The band origin of the A-state is determined with approximately two orders of magnitude higher precision compared to the previous studies[25,26,211], and the rotational constant B is determined by about one order of magnitude of higher precision. This observation is solely based on the provided uncertainties of the previous works. Considering the difference values of the band origin T and the rotational constant B between those works and ours, the true uncertainty of these parameters is likely much larger than the uncertainty of the constants suggests. Compared to Stark et al.[211], the parameter T deviates by more than $51\,\sigma$ for OH and $18\,\sigma$ for OD, while B differs by $26\,\sigma$ for OH and $18\,\sigma$ for OD. The origin of this deviation is unknown since we can only judge our own measurement setup. However, the previous work of Stark et al.[211] is based on an electrical discharge to produce OH and OD by dissociating H_2O and D_2O, respectively. The iron hollow-cathode discharge source also contains 2.2 Torr of helium, which potentially might cause a pressure shift. Another potential source of the frequency shift is the calibration of the transition lines, which is based on the absolute positions of the FeI lines[212].

The fine/hyperfine parameters of previous studies[207,209,210] generally show a much better agreement with this thesis. For example, the OH parameters b_F, c and γ fitted by ter Meulen et al.[207] agree within $2.2\,\sigma$ with our parameters (Table 10.6a). The exception is the parameter γ_D, which differs by $4\,\sigma$. A potential source of the greater discrepancy is the inclusion of the fixed parameter $\gamma_H = 230\,\mathrm{Hz}$[26] in our model, which is missing in the previous model of ter Meulen et al.[207]. In OD, the deviation between the parameters $b_F = b + c/3$, c and eQq_0 provided by Carter et al.[209] and the parameters in this thesis is

Table 10.6: (a) Comparison of fitted parameter for OH and (b) OD.

(a)

	This Thesis	ter Meulen [207] et al.
b_F	772.077(26)	771.74(22)
c	161.732(68)	161.01(55)
γ	6777.832(10)	6 777.749(36)
γ_D	-1.435 17(89)	-1.426 3(22)

(b)

	This Thesis	Carter [209] et al.	Xin [210] et al.
b_F	118.468(20)(18)	118.422(42)	118.46(7)
c	24.863(56)(45)	24.72(11)	24.85(17)
eQ_{q_0}	0.277(26)(4)	0.238(30)	0.29(5)

less than 2 sigma (Table 10.6b). The comparison with the parameters from Xin et al. [210] shows even better agreement, within one standard deviation. Since the data from these previous works is included in our global fit, the agreement of the fitting parameters is not too surprising.

10.6 Conclusion

In this thesis, OH and OD electronic transition frequencies have been determined using excitation with a narrow-linewidth continuous wave (CW) laser. Although, each measurement is Doppler broadened with a linewidth on the order of 8 MHz, the uncertainty of the fitted line positions is at the 10 kHz level. This is similar to the precision achieved on Doppler broadened molecular transitions in molecular oxygen (O_2) by Bielska et al. [213]. A fit of an effective Hamiltonian model to the measured line positions supplies a set of refined A-state spectroscopic constants and residuals to the applied model. Compared to previous works, the uncertainty of the parameters has been reduced (Section 10.5). In particular, the band origin and the rotational constant are determined with significantly higher precision. The residuals of the effective Hamiltonian fit are an indicator of the accuracy of the individual measured transitions frequencies. The deviations between the observed and the calculated transition frequencies are, in general, within 100 kHz (Section 10.3). This rather small deviation confirms our trust in the measured transition frequencies and the provided spectroscopic constants, even if previous measurements suggest different parameter values.

Chapter 11

Outlook and Summary

This thesis has presented a precision laser system for spectroscopy on small molecules, able to measure and stabilize a narrow linewidth continuous wave (CW) laser in the ultraviolet (UV) as well the infrared (IR). A measurement series of $A^2\Sigma^+$, $v' = 0 \leftarrow X^2\Pi_{3/2}$, $v'' = 0$, $J'' = 3/2$ transitions in the hydroxyl radical (OH) and the deuterated hydroxyl radical (OD) served as a benchmark system of this new apparatus. Potential line shifting effects have been considered, for instance, the Zeeman effect, the saturation, the AC-Stark shift, and the retroreflection quality. By accounting for these effects, we have been able to determine the zero-field transition frequencies with an uncertainty of less than 100 kHz. The zero-field transition frequencies, reported in this thesis, have been combined with previous data[49,207,209,210], and used to refine the effective Hamiltonian parameters of the A, $v' = 0$ state in OH and OD. In particular, the band origin and the rotational constant have been determined with several orders of magnitude higher precision.

11.1 Increasing the Performance of the Setup

The magnetic field and the corresponding Zeeman effect has a significant influence on the measured line positions on the OD measurements. In retrospect, we underestimated the effect the 75 µT ambient magnetic field in the laboratory would have on the measured spectra. This oversight complicated the analysis of the spectra and probably reduced the available precision of the measured transition frequencies. The relatively high laser power needed to overcome the low signal to noise ratio (SNR) and counter-propagating laser beams used to correct for Doppler shifts could have resulted in saturation dips and improved the resolution of the measurements. Thus, the two counterpropagating laser beams in the Doppler reduces measurement setup saturate the transition. Unfortunately, the line splitting inside the magnetic field due to the Zeeman effect leads to multiple saturation dips, which are not at the center of the transition, but instead distort the measured spectrum. Since then, the experimental apparatus has been modified so that future measurements can be performed at zero magnetic field. In particular, two Helmholtz

coils with a diameter of 800 mm along the axis of the laser beam (14 µT) and two additional coils with a diameter of 400 mm along the molecular beam (75 µT) have already been attached to the vacuum chamber. A translatable and rotatable Hall sensor makes it possible to detect magnetic fields along both axes at the molecule interaction region with the laser. Based on the measured field strength, the current inside the Helmholtz coils can be tuned to null-out the ambient magnetic field. The magnetic field along the third axis is neglected since it is at the order of magnitude of the measurement uncertainty (2 µT).

The laser power leads in some measurements to saturation effects, although the precise location of the saturation dips often stays hidden inside the noise floor. An increase of the SNR would open the possibility of Doppler-free saturation spectroscopy. After the measurements, we identified multiple sources of avoidable noise. The major contribution to the background noise is the dissociation pulse of the excimer laser. Although color filters block the laser wavelength in front of the photomultiplier tube (PMT), the fluorescence light generated inside the quartz tube at the nozzle of the molecular beam goes through the filters. This fluorescence also persists for the few milliseconds the molecules require to travel from the source to the laser interaction region. Thus, dissociating the molecules without the quartz tube would get rid of this source of background. Another source of fluorescence light was the fused silica windows of the vacuum chamber for the spectroscopy laser, which have since been replaced by calcium fluoride (CaF_2) windows, which have no detectable fluorescence. The last potential noise source is scattered light from the light baffles around the spectroscopy laser. Although the beam diameter at the center of the interaction region is around 1 mm and the diameter of the light baffles is 5 mm, some minor fraction of the beam scatters into the PMT. Thus, we increased the diameter of light baffles to 10 mm and simultaneously cleaned the mode profile of the laser beam using a single mode fiber. Additionally, the fiber connects the laser setup on the floating laser table with the stationary vacuum chamber, which makes continuous adjustments of the retroreflection obsolete. These changes will increase the SNR significantly.

The data processing is based on an analog signal from the PMT, recorded on a digital oscilloscope. The experiment was performed with a repetition rate of 10 Hz, partly because the oscilloscope could not be read out much faster than this and did not have an appropriate averaging function built in. The pressure inside the vacuum chamber, which increases with the repetition rate of the valve, could have also become a limiting factor, though later tests proved a reliable valve operation up to 50 Hz, with additional cooling to protect the valve from overheating. Higher repetition rates are only possible by producing narrower molecular pulses, which is not feasible with the current valve. However, an in-house developed, corrosive resistant piezoelectric transducer (PZT) based valve has been shown to generate shorter pulses. The corresponding adapter for the vacuum chamber is ready

to use, but the valve itself has not been tested yet with nitric acid (HNO_3). This valve potentially allows experimental repetition rates up to 250 Hz, which is the maximum repetition rate. However, the faster repetition rate produces more data, and the oscilloscope becomes insufficient. The measurement speed, as well as the sensitivity, can be improved by counting the electrical pulses generated by individual photons reaching the PMT. These pulses are small, short in duration, and highly variable but can be converted to transistor-transistor logic (TTL) compatible pulses with constant width using a discriminator. Thus, the data acquisition needs to change. In particular, the oscilloscope has been replaced with a discriminator, which generates a sequence of identical pulses based on the signal from the PMT. Afterwards, the pulse train is using a low-cost logic analyzer which can continuously record a digital signal at 24 mega samples per second (MSPS). It is expected that future measurements will be at least collected five times faster than the data in this thesis. In case of a successful operation of the in-house valve, maybe even 25 times faster.

To conclude the improvements on the measurement setup, we expect an increase of the transition line precision of at least one order of magnitude. But instead of measuring the same transitions again with a higher precision, it is prudent to move on to a different system.

11.2 Beyond the Electronic Excitation of OH

The measured electronic transitions on the OH proved the functionality of our precision spectroscopy laser system and demonstrated the successful detection of the molecules in the vibrational ground state $v'' = 0$. This thesis contains the groundwork for future measurements of vibrational transitions of the OH molecule. The required mid IR optical parametric oscillator (OPO) has been built in this thesis. Improving its tunability and implementing a phase-locked loop (PLL) to stabilize it to the optical frequency comb (OFC) is the next step. Once this is accomplished, we plan to observe vibrational one-photon or two-photon transition in OH at 2.7 µm or 2.9 µm, respectively.

Other molecular systems might also be worth considering. Both the OPO and the dye laser have a wide tuning range, which makes them applicable for a variety of different molecules. In general, the simplest molecules are of greatest interest for testing the standard model of physics. Ab initio calculations are more likely to match experimental precision if the system contains as few electrons as possible. Thus, the H_2 molecule is the perfect candidate for high-resolution spectroscopy of vibrational transitions.

The challenge of measuring vibrational transitions of the symmetric H_2 molecules is the zero dipole moment, since we require a non-zero dipole moment for a one-photon electric dipole transition. One solution might be Raman spectroscopy, which is based on the

difference frequency of two electric fields. This principle also applies for one static field with zero frequency and a second field supplied by the IR OPO. In this case, the constant field induces a dipole moment and allows excitation in the IR. An even more straightforward approach might be a measurement of the HD molecule, which is asymmetric and has a small but non-zero dipole moment without further manipulations. The main change that would need to be made spectroscopy on H_2 or HD is the implementation of a resonance-enhanced multiphoton ionization (REMPI) setup including a mass spectrometer for detection.

References

[1] F. Zwicky, General Relativity and Gravitation **41**, 207 (2009).

[2] M. S. Safronova, D. Budker, D. DeMille et al., Reviews of Modern Physics **90**, 025008 (2018).

[3] S. Perlmutter, Reviews of Modern Physics **84**, 1127 (2012).

[4] A. G. Riess, Reviews of Modern Physics **84**, 1165 (2012).

[5] B. P. Schmidt, Reviews of Modern Physics **84**, 1151 (2012).

[6] R. Adam, P. A. R. Ade, N. Aghanim et al., Astronomy & Astrophysics **594**, 1 (2016).

[7] M. Dine and A. Kusenko, Reviews of Modern Physics **76**, 1 (2004).

[8] J. Engel, M. J. Ramsey-Musolf and U. van Kolck, Progress in Particle and Nuclear Physics **71**, 21 (2013).

[9] J. Lim, J. Almond, M. Trigatzis et al., Physical Review Letters **120**, 123201 (2018).

[10] D. Colladay and V. A. Kostelecký, Physical Review D **58**, 116002 (1998).

[11] J.-P. Uzan, Reviews of Modern Physics **75**, 403 (2003).

[12] J.-P. Uzan, Comptes Rendus Physique **16**, 576 (2015).

[13] T. Nicholson, S. Campbell, R. Hutson et al., Nature Communications **6**, 6896 (2015).

[14] G. C. Dousmanis, T. M. Sanders and C. H. Townes, Physical Review **100**, 1735 (1955).

[15] S. Weinreb, A. H. Barrett, M. L. Meeks et al., Nature **200**, 829 (1963).

[16] M. Rex, I. Wohltmann, T. Ridder et al., Atmospheric Chemistry and Physics **14**, 4827 (2014).

[17] J. A. Miller, R. J. Kee and C. K. Westbrook, Annual Review of Physical Chemistry **41**, 345 (1990).

[18] J. J. Ter Meulen and A. Dymanus, The Astrophysical Journal **172**, L21 (1972).

[19] J. C. Whitehead, Reports on Progress in Physics **59**, 993 (1996).

[20] M. Kirste, X. Wang, H. C. Schewe et al., Science **338**, 1060 (2012).

[21] J. R. Bochinski, E. R. Hudson, H. J. Lewandowski et al., Physical Review Letters **91**, 243001 (2003).

[22] S. Y. T. van de Meerakker, P. H. M. Smeets, N. Vanhaecke et al., Physical Review Letters **94**, 023004 (2005).

[23] B. K. Stuhl, M. T. Hummon, M. Yeo et al., Nature **492**, 396 (2012).

[24] J. M. Beames, F. Liu, M. I. Lester et al., The Journal of Chemical Physics **134**, 241102 (2011).

[25] J. A. Coxon, Journal of Molecular Spectroscopy **58**, 1 (1975).

[26] J. A. Coxon, Canadian Journal of Physics **58**, 933 (1980).

[27] G. Stark, J. W. Brault and M. C. Abrams, J. Opt. Soc. Am. B. **11**, 3 (1994).

[28] P. A. M. Dirac, Nature **139**, 323 (1937).

[29] N. Kolachevsky, A. Matveev, J. Alnis et al., Space Science Reviews **148**, 267 (2009).

[30] R. I. Thompson, Astrophysical Letters **17**, 3 (1975).

[31] S. G. Karshenboim, Canadian Journal of Physics **83**, 767 (2005).

[32] S. A. Levshakov, M. Dessauges-Zavadsky, S. D'Odorico et al., Monthly Notices of the Royal Astronomical Society **333**, 373 (2002).

[33] J. Alnis, A. Matveev, N. Kolachevsky et al., Physical Review A **77**, 053809 (2008).

[34] T. Udem, J. Reichert, R. Holzwarth et al., Optics Letters **24**, 881 (1999).

[35] W. D. Phillips, Reviews of Modern Physics **70**, 721 (1998).

[36] M. Schioppo, R. C. Brown, W. F. McGrew et al., Nature Photonics **11**, 48 (2017).

[37] N. Huntemann, B. Lipphardt, C. Tamm et al., Physical Review Letters **113**, 210802 (2014).

[38] A. Shelkovnikov, R. J. Butcher, C. Chardonnet et al., Physical Review Letters **100**, 150801 (2008).

[39] R. H. Parker, C. Yu, W. Zhong et al., Science **360**, 191 (2018).

[40] M. Born and R. Oppenheimer, Annalen der Physik **20**, 457 (1927).

[41] G. Herzberg, *Molecular Spectra and Molecular Structure: I. Spectra of Diatomic Molecules*, 2nd ed. (Krieger Publishing Company, Malabar, 1989).

[42] J. Brown and A. Carrington, *Rotational Spectroscopy of Diatomic Molecules*, 1st ed. (Cambridge University Press, Cambridge, New York, Port Melbourne, 2003).

[43] J. Brown, J. Hougen, K.-P. Huber et al., Journal of Molecular Spectroscopy **55**, 500 (1975).

[44] F. Hund, N. Mott, H. Bethe et al., *Quantentheorie*, 2nd ed. (Springer-Verlag, Berlin, Heidelberg, 1933).

[45] J. M. Hollas, *Modern Spectroscopy*, 4th ed. (John Wiley & Sons, Chichester, 2004).

[46] R. Zare, *Angular Momentum* (John Wiley & Sons, Chichester, 1987).

[47] E. Hirota, J. M. Brown, J. T. Hougen et al., Pure and Applied Chemistry **66**, 571 (1994).

[48] J. H. Van Vleck, Physical Review **33**, 467 (1929).

[49] B. J. Drouin, Journal of Physical Chemistry A **117**, 10076 (2013).

[50] J. M. Brown, E. A. Colbourn, J. K. G. Watson et al., Journal of Molecular Spectroscopy **74**, 294 (1979).

[51] O. Von Klein, Zeitschrift für Physik **58**, 730 (1929).

[52] J. Van Vleck, Reviews of Modern Physics **23**, 213 (1951).

[53] F. Scheck, *Theoretische Physik 4* (Springer-Verlag, Berlin, Heidelberg, 2007).

[54] J. Brown, M. Kaise, C. Kerr et al., Molecular Physics **36**, 553 (1978).

[55] K. Maeda, M. L. Wall and L. D. Carr, arXiv.org **17**, 1 (2014), arXiv:1410.3849 .

[56] C. M. Western, Journal of Quantitative Spectroscopy and Radiative Transfer **186**, 221 (2017).

[57] K. Maeda, M. L. Wall and L. D. Carr, New Journal of Physics **17**, 045014 (2015).

[58] R. A. Frosch and H. M. Foley, Physical Review **88**, 1337 (1952).

[59] S. V. Berdyugina and S. K. Solanki, Astronomy & Astrophysics **385**, 701 (2002).

[60] G. Herzberg, *The spectra and structure of simple free radicals* (Cornell Universety Press, New York, 1971).

[61] N. Bel and B. Leroy, Astronomy and Astrophysics **335**, 1025 (1998).

[62] L. Veseth, Physica **56**, 286 (1971).

[63] J. M. Brown and J. K. Watson, Journal of Molecular Spectroscopy **65**, 65 (1977).

[64] B. J. Drouin, C. E. Miller, H. S. Müller et al., Journal of Molecular Spectroscopy **205**, 128 (2001).

[65] W. L. Meerts and A. Dymanus, Canadian Journal of Physics **53**, 2123 (1975).

[66] J. K. G. Watson, Journal of Molecular Spectroscopy **80**, 411 (1980).

[67] C. J. H. Schutte, J. E. Bertie, P. R. Bunker et al., Pure and Applied Chemistry **69**, 1633 (1997).

[68] W. Demtröder, *Experimentalphysik 3* (Springer, Berlin, Heidelberg, 1996).

[69] T. J. Kane and R. L. Byer, **10**, 65 (1985).

[70] A. C. Nilsson, E. K. Gustafson and R. L. Byer, IEEE Journal of Quantum Electronics **25**, 767 (1989).

[71] T. J. Kane, A. C. Nilsson and R. L. Byer, Optics Letters **12**, 175 (1987).

[72] B. P. Abbott, R. Abbott, T. D. Abbott et al., Physical Review Letters **116**, 061102 (2016).

[73] P. Kwee, C. Bogan, K. Danzmann et al., Optics Express **20**, 10617 (2012).

[74] T. Schuldt, D. Weise, K. Döringshoff et al., in *International Conference on Space Optics 2012* (SPIE, 2017) pp. 1–5.

[75] D. Spence, P. Kean and W. Sibbett, Optics Letters **16**, 42 (1991).

[76] M. T. Asaki, C.-P. Huang, D. Garvey et al., Optics Letters **18**, 977 (1993).

[77] U. Morgner, F. X. Kartner, S. H. Cho et al., Optics Letters **24**, 411 (1999).

[78] R. Ell, U. Morgner, F. X. Kärtner et al., Optics Letters **26**, 373 (2001).

[79] T. Udem, *Habilitationsschrift* (Munich, 2002) pp. 15–26.

[80] J.-C. Diels, *Ultrashort Laser Pulse Phenomena* (Elsevier Inc., Amsterdam, 2006) pp. 277–291.

[81] J. Stenger and H. R. Telle, Optics Letters **25**, 1553 (2000).

[82] W. J. Wadsworth, A. Ortigosa-Blanch, J. C. Knight et al., Journal of the Optical Society of America B **19**, 2148 (2002).

[83] M. Dieter, *Optics, Light and Lasers*, 2nd ed. (Wiley-VCH Verlag, Weinheim, 2007) pp. 114–116.

[84] J. Reichert, R. Holzwarth, T. Udem et al., Optics Communications **172**, 59 (1999).

[85] J. Ye and S. T. Cundiff, *Femtosecond Optical Frequency Comb: Principle, Operation, and Applications* (Kluwer Academic Publishers, Boston, 2005).

[86] L. Xu, T. W. Hänsch, C. Spielmann et al., Optics Letters **21**, 2008 (1996).

[87] K. W. Holman, R. J. Jones, A. Marian et al., Optics Letters **28**, 851 (2003).

[88] K. W. Holman, R. J. Jones, A. Marian et al., IEEE Journal of Selected Topics in Quantum Electronics **9**, 1018 (2003).

[89] L. Lessing, *Man of High Fidelity: Edwin Howard Armstrong* (Bantam Books, New York, 1969).

[90] K.-P. Pun, J. E. Franca and C. Azeredo-Leme, *Circuit Design for Wireless Communications* (Springer, Boston, 2003).

[91] R. W. Boyd, *Nonlinear Optics*, 3rd ed. (Academic Press, Cambridge, 2008).

[92] L. Corner, J. Gibb, G. Hancock et al., Applied Physics B: Lasers and Optics **74**, 441 (2002).

[93] S. E. Harris, M. K. Oshman and R. L. Byer, Physical Review Letters **18**, 732 (1967).

[94] R. L. Byer and S. E. Harris, Physical Review **168**, 1064 (1968).

[95] J. E. Midwinter and J. Warner, British Journal of Applied Physics **16**, 1135 (1965).

[96] J. A. Armstrong, N. Bloembergen, J. Ducuing et al., Physical Review **127**, 1918 (1962).

[97] M. Yamada, N. Nada, M. Saitoh et al., Applied Physics Letters **62**, 435 (1993).

[98] H. Kogelnik and T. Li, Applied Optics **5**, 1550 (1966).

[99] D. G. Hall, Optics Letters **21**, 9 (1996).

[100] R. W. Boyd, Journal of the Optical Society of America **70**, 877 (1980).

[101] G. D. Boyd and D. A. Kleinman, Journal of Applied Physics **39**, 3597 (1968).

[102] S. Guha, Fei-Jain Wu and J. Falk, IEEE Journal of Quantum Electronics **18**, 907 (1982).

[103] H. E. Major, C. B. E. Gawith and P. G. R. Smith, Optics Communications **281**, 5036 (2008).

[104] N. Lastzka and R. Schnabel, Optics Express **15**, 7211 (2007).

[105] A. E. Siegman, *Lasers* (University Science Books, Mill Valley, 1986).

[106] M. Vainio, J. Peltola, S. Persijn et al., Applied Physics B **94**, 411 (2009).

[107] N. P. Barnes and J. A. Williams-Byrd, Journal of the Optical Society of America B **12**, 124 (1995).

[108] A. Henderson and R. Stafford, Applied Physics B **85**, 181 (2006).

[109] H. Y. Shen, H. Xu, Z. D. Zeng et al., Applied Optics **31**, 6695 (1992).

[110] E. S. Polzik and H. J. Kimble, Optics Letters **16**, 1400 (1991).

[111] O. Gayer, Z. Sacks, E. Galun et al., Applied Physics B **91**, 343 (2008).

[112] J. K. Yamamoto, K. Kitamura, N. Iyi et al., Applied Physics Letters **61**, 2156 (1992).

[113] A. Henderson and R. Stafford, Optics Letters **32**, 1281 (2007).

[114] U. T. Schwarz and M. Maier, Physical Review B **55**, 11041 (1997).

[115] A. Ridah, P. Bourson, M. D. Fontana et al., Journal of Physics: Condensed Matter **9**, 9687 (1997).

[116] J. Kiessling, R. Sowade, I. Breunig et al., Optics Express **17**, 87 (2008).

[117] I. Ricciardi, E. De Tommasi, P. Maddaloni et al., Molecular Physics **110**, 2103 (2012).

[118] H. Abu-Safia, R. Al-Tahtamouni, I. Abu-Aljarayesh et al., Applied Optics **33**, 3805 (1994).

[119] B. J. Frey, D. B. Leviton and T. J. Madison, in *Optomechanical Technologies for Astronomy*, July (SPIE, 2006) p. 62732J.

[120] D. E. Zelmon, D. L. Small and R. Page, Applied Optics **37**, 4933 (1998).

[121] R. Wynne, J. L. Daneu and T. Y. Fan, Applied Optics **38**, 3282 (1999).

[122] Y. Okada and Y. Tokumaru, Journal of Applied Physics **56**, 314 (1984).

[123] F. Riehle, *Frequency Standards*, 1st ed. (WILEY-VCH Verlag, Weinheim, 2004).

[124] J. Rutman, Proceedings of the IEEE **66**, 1048 (1978).

[125] D. Allan, Proceedings of the IEEE **54**, 221 (1966).

[126] E. Rubiola, Review of Scientific Instruments **76**, 054703 (2005).

[127] R. Syndor and D. Allan, *Handbook: Selection and use of precise frequency and time systems* (International Telecomunication Union, Geneva, 1997).

[128] F. Vernotte, M. Lenczner, P.-Y. Bourgeois et al., IEEE Transactions on Ultrasonics, Ferroelectrics, and Frequency Control **63**, 611 (2016).

[129] M. A. Lombardi, T. P. Heavner and S. R. Jefferts, NCSLI Measure **2**, 74 (2007).

[130] W. Markowitz, R. G. Hall, L. Essen et al., Physical Review Letters **1**, 105 (1958).

[131] C. J. Bordé, G. Camy, B. Decomps et al., Journal de Physique **42**, 1393 (1981).

[132] T. Yoon, J. Ye, J. Hall et al., Applied Physics B **72**, 221 (2001).

[133] Jun Ye, L. Robertsson, S. Picard et al., IEEE Transactions on Instrumentation and Measurement **48**, 544 (1999).

[134] R. Felder, Metrologia **42**, 323 (2005).

[135] P. Jungner, M. D. Eickhoff, S. D. Swartz et al., in *Laser Frequency Stabilization and Noise Reduction*, April (SPIE, 1995) pp. 1–14.

[136] K. Doringshoff, K. Mohle, M. Nagel et al., in *2010 European Frequency and Time Forum*, 5 (IEEE, 2010) pp. 1–6.

[137] K. Doringshoff, M. Reggentin, E. V. Kovalchuk et al., in *2012 European Frequency and Time Forum* (IEEE, 2012) pp. 419–421.

[138] M. A. Lombardi, L. M. Nelson, A. N. Novick et al., in *Time and Frequency Measurements Using the Global Positioning System* (Cal. Lab. Int. J. Metrology, 2001) pp. 26–33.

[139] J. Levine, Review of Scientific Instruments **70**, 2567 (1999).

[140] P. Burdack, M. Tröbs, M. Hunnekuhl et al., Optics Express **12**, 644 (2004).

[141] V. Zhang and R. P. Bijunath, *NIST Meridian II precision TimeBase, Test 76120S*, Tech. Rep. (2016).

[142] D. A. Steck, *Quantum and Atom Optics* (available online at http://steck.us/teaching, revision 0.12.0, 16 May, 2017).

[143] P. W. Milonni and M. L. Shih, American Journal of Physics **59**, 684 (1991).

[144] W. Demtröder, *Laserspektroskopie 2* (Springer, Berlin, Heidelberg, 2013).

[145] W. Bennet, Physical Review **126**, 580 (1962).

[146] E. D. Hinkley, Applied Physics Letters **16**, 351 (1970).

[147] J. Reid, J. Shewchun, B. K. Garside et al., Applied Optics **17**, 300 (1978).

[148] P. Maddaloni, M. Bellini and P. De Natale, *Laser-Based Measurements for Time and Frequency Domain Applications*, Series in Optics and Optoelectronics (Taylor & Francis Group, London, New York, 2013).

[149] P. Werle, Spectrochimica Acta Part A: Molecular and Biomolecular Spectroscopy **54**, 197 (1998).

[150] R. N. Hager and R. C. Anderson, Journal of the Optical Society of America **60**, 1444 (1970).

[151] M. Gehrtz, G. C. Bjorklund and E. A. Whittaker, Journal of the Optical Society of America B **2**, 1510 (1985).

[152] G. C. Bjorklund, Optics Letters **5**, 15 (1980).

[153] G. C. Bjorklund, M. D. Levenson, W. Lenth et al., Applied Physics B **32**, 145 (1983).
[154] J. M. Chowing, Journal of the Audio Engineering Society **21**, 526 (1973).
[155] G. C. Bjorklund and M. D. Levenson, Physical Review A **24**, 166 (1981).
[156] J. L. Hall, L. Hollberg, T. Baer et al., Applied Physics Letters **39**, 680 (1981).
[157] R. K. Raj, D. Bloch, J. J. Snyder et al., Physical Review Letters **44**, 1251 (1980).
[158] G. Camy, C. Bordé and M. Ducloy, Optics Communications **41**, 325 (1982).
[159] J. J. Snyder, R. K. Raj, D. Bloch et al., Optics Letters **5**, 163 (1980).
[160] J. H. Shirley, Optics Letters **7**, 537 (1982).
[161] A. Schenzle, R. G. DeVoe and R. G. Brewer, Physical Review A **25**, 2606 (1982).
[162] F. Bertinetto, P. Cordiale, G. Galzerano et al., IEEE Transactions on Instrumentation and Measurement **50**, 490 (2001).
[163] E. Jaatinen, Optics Communications **120**, 91 (1995).
[164] D. J. McCarron, S. A. King and S. L. Cornish, Measurement Science and Technology **19**, 105601 (2008).
[165] W. Demtröder, *Laserspektroskopie 1*, 6th ed. (Springer, Berlin, Heidelberg, 2011).
[166] X. Qin and S. D. Zhang, Journal of the Korean Physical Society **65**, 2017 (2014).
[167] S. Y. T. van de Meerakker, H. L. Bethlem and G. Meijer, Nature Physics **4**, 595 (2008).
[168] D. H. Levy, Science **214**, 263 (1981).
[169] W. Christen and K. Rademann, Physical Review A **77**, 012702 (2008).
[170] G. Scoles, *Atomic and Molecular Beam Methods*, 1st ed. (Osford Univerisy Press, New York, Oxford, 1988).
[171] P. Andresen, N. Aristov, V. Beushausen et al., Journal of Chemical Physics **95**, 5763 (1991).
[172] J. Farthing, I. Fletcher and J. Whitehead, Phys. Chem. **65**, 1663 (1983).
[173] M. C. Van Beek and J. J. Ter Meulen, Chemical Physics Letters **337**, 237 (2001).
[174] L. Ploenes, D. Haas, D. Zhang et al., Review of Scientific Instruments **87**, 053305 (2016).
[175] S. M. Barnett, Journal of Modern Optics **57**, 1445 (2010).
[176] C. Cohen-Tannoudji, J. Dupont-Roc and G. Grynberg, *Atom-Photon Interactions* (Wiley-VCH Verlag, Weinheim, 1998).
[177] J. Dalibard and C. Cohen-Tannoudji, Journal of the Optical Society of America B **2**, 1707 (1985).
[178] B. Mollow, Physical Review **188**, 1969 (1969).
[179] G. Lindblad, Commun. Math. Phys. **48**, 119 (1976).
[180] C. A. Brasil, F. F. Fanchini and R. de Jesus Napolitano, Revista Brasileira de Ensino de Física **35**, 1 (2013).
[181] P. Pearle, European Journal of Physics **33**, 805 (2012).
[182] J. Johansson, P. Nation and F. Nori, Computer Physics Communications **183**, 1760 (2012).
[183] J. Johansson, P. Nation and F. Nori, Computer Physics Communications **184**, 1234 (2013).
[184] K. R. German, The Journal of Chemical Physics **62**, 2584 (1975).
[185] A. L. Stancik and E. B. Brauns, Vibrational Spectroscopy **47**, 66 (2008).
[186] A. Kolchencko, S. Rautian and R. Sokolovskii, Soviet Physics JETP **28**, 986 (1969).
[187] R. G. Brewer and A. Mooradian, *Laser Spectroscopy* (Springer, Boston, 1974).
[188] J. L. Hall, C. J. Bordé and K. Uehara, Physical Review Letters **37**, 1339 (1976).
[189] C. J. Bordé, G. Camy and B. Decomps, Physical Review A **20**, 254 (1979).
[190] R. C. Hilborn, American Journal of Physics **50**, 982 (1982).
[191] T. Schuldt, K. Döringshoff, A. Milke et al., Journal of Physics: Conference Series **723**, 012047 (2016).
[192] A. Nevsky, R. Holzwarth, J. Reichert et al., Optics Communications **192**, 263 (2001).
[193] J. Hrabina, O. Acef, F. Burck et al., Measurement Science Review **14**, 213 (2014).
[194] E. Jaatinen, D. J. Hopper and J. Back, Measurement Science and Technology **20**, 025302 (2009).
[195] P. C. D. Hobbs, Applied Optics **36**, 903 (1997).

[196] R. W. P. Drever, J. L. Hall, F. V. Kowalski et al., Applied Physics B **31**, 97 (1983).

[197] H. R. Barry, B. Bakowski, L. Corner et al., Chemical Physics Letters **319**, 125 (2000).

[198] C. E. Wieman and L. Hollberg, Review of Scientific Instruments **62**, 1 (1991).

[199] L. Ricci, M. Weidemüller, T. Esslinger et al., Optics Communications **117**, 541 (1995).

[200] C. J. Hawthorn, K. P. Weber and R. E. Scholten, Review of Scientific Instruments **72**, 4477 (2001).

[201] B. Mroziewicz, Opto-Electronics Review **16**, 347 (2008).

[202] T. Führer, D. Stang and T. Walther, Optics Express **17**, 4991 (2009).

[203] T. Führer, S. Euler and T. Walther, Journal of the Optical Society of America B **28**, 508 (2011).

[204] T. C. Briles, D. C. Yost, A. Cingöz et al., Optics Express **18**, 9739 (2010).

[205] L. Scharfenberg, *Crossed beam scattering with a Stark-decelerated molecular beam*, Ph.D. thesis, Technische Universität Berlin (2012).

[206] S. A. Meek, M. F. Parsons, G. Heyne et al., Review of Scientific Instruments **82**, 093108 (2011).

[207] J. J. Ter Meulen, W. Ubachs and A. Dymanus, Chemical Physics Letters **129**, 533 (1986).

[208] K. R. German, The Journal of Chemical Physics **64**, 4192 (1976).

[209] R. T. Carter, I. M. Povey, H. Bitto et al., The Journal of Chemical Physics **104**, 5365 (1996).

[210] J. Xin, I. Ionescu, D. Kuffel et al., Chemical Physics **291**, 61 (2003).

[211] G. Stark, J. W. Brault and M. C. Abrams, Journal of the Optical Society of America B **11**, 3 (1994).

[212] R. C. M. Learner and A. P. Thorne, Journal of the Optical Society of America B **5**, 2045 (1988).

[213] K. Bielska, S. Wójtewicz, P. Morzyński et al., Journal of Quantitative Spectroscopy and Radiative Transfer **201**, 156 (2017).

Abbreviations

AC	alternating current
AlGaInP	aluminium gallium indium phosphide
AOM	acoustic-optical modulator
AR	anti-reflective
AVAR	Allan variance
BBO	beta barium borate
BIPM	bureau of weights and measures
CIPM	international committee for weights and measures
CORDIC	coordinate rotation digital computer
CW	continuous wave
DC	direct current
DFB	distributed feedback
DFG	difference frequency generation
ECDL	external cavity diode laser
EDM	electric dipole moment
EMF	electromotive force
EOM	electro-optic modulator
ERF	error function
FEM	finite element method
FFT	fast Fourier transform
FM	frequency modulation
FPGA	field-programmable gate array
FPI	Fabry-Perot interferometer
FSR	free spectral range
FT	Fourier transform
FWHM	full width at half maximum
GMT	greenwich mean time
GNSS	global navigation satellite system
GPS	global positioning system
HR	high-reflective
HV	high voltage

IR	infrared
IUPAC	international union of pure and applied chemistry
LHC	large hadron collider
LIF	laser induced fluorescence
LISA	laser interferometer space antenna
MBD	maxwell-boltzmann distribution
MDEV	modified Allan deviation
MPI	multiphoton ionization
MTS	modulation transfer spectroscopy
MVAR	modified Allan variance
Nd:YAG	neodymium-doped yttrium aluminum garnet
NIST	national institute of standards and technology
NPRO	non-planar ring oscillator
NTC	negative temperature coefficient
OD	deuterated hydroxyl radical
OFC	optical frequency comb
OH	hydroxyl radical
OPA	optical parametric amplification
OPO	optical parametric oscillator
PBS	polarizing beam splitter
PCF	photonic crystal fiber
PD	photodiode
PDH	Pound-Drever-Hall
PEEK	polyether ether ketone
PI	proportional-integral
PID	proportional-integral-derivative
PLL	phase-locked loop
PMM	phase mismatching
PMT	photomultiplier tube
PPLN	periodically-poled lithium niobate
PPM	perfectly phase matched
PPS	pulse per second
PTFE	polytetrafluoroethylene
PVAR	parabolic variance
PVC	polyvinyl chloride
PWM	pulse-width modulation
PZT	piezoelectric transducer
QM	quantum mechanical
QPM	quais phase matching

RAM	residual amplitude modulation
REMPI	resonance-enhanced multiphoton ionization
RFT	rotating-frame transformation
RMS	root-mean-square
RTD	resistance temperature detector
RWA	rotating-wave approximation
SAW	surface acoustic wave
SFG	sum frequency generation
SHG	second-harmonic generation
SM	standard model
SNR	signal to noise ratio
SSE	sum of square errors
TAI	international atomic time
TB	thermal background
TDLAS	tunable diode laser absorption spectroscopy
TEC	temperature controller
TEM	transverse electromagnetic mode
TOF	time-of-flight
TTL	transistor-transistor logic
UHV	ultra-high vacuum
ULE	ultra-low expansion
USNO	united states naval observatory
UTC	coordinated universal time
UV	ultraviolet
VCXO	voltage-controlled crystal oscillator
WM	wavelength modulation
YAG	yttrium aluminum garnet

Acknowledgments

During the last couple of years, I worked side by side with great people. Foremost, I would like to especially thank Dr. Samuel Meek for inviting me into his group and providing excellent conditions for our work. I am grateful for his continuous support, mentoring, brilliant ideas in advancing the project and great motivational speeches.

Furthermore, I would also like to thank Prof. Dr. John Furneaux as a constant source of knowledge during my first year. Without his contributions, I probably would not have come this far.

A big thank-you goes out to Prof. Dr. Alec Wodtke for hosting our group and providing the best working environment possible. The laboratory I was allowed to work in was great, but the real treasures are the people, the group members at the university, as well the ones sitting at the MPI who I could ask anytime for advice, and it was provided.

I am also thankful to Tim Diedrich and Reinhard Bürsing for technical suggestions to my drawings, moving them from good to excellent. As well I am thanking the mechanical workshop for transferring my drawings into precise physical objects.

I am especially thankful to Prof. Dr. Ansgar Reiners, who joined my thesis advisory committee and allowed me to enroll in the GAUSS program. Furthermore, I would like to thank Prof. Dr. Claus Ropers, Prof. Dr. Stefan Mathias, Prof. Dr. Dirk Schwarzer and Dr. Holger Nobach for being members of my examination board.

Sincere thanks are also given to all my colleagues, who helped me to clear my mind during a good game of table soccer, namely Marvin Kammler, Sven Kaufmann, Nils Hertl, Jascha Lau and Tim Diedrich. The order in this list does not reflect the skill level. You are all awesome!

Special gratitude goes to my parents, for their faith in me and providing the old sunflower Toyota, so I could swiftly move up the Fassberg. And last but not least Nora, you have my gratitude for your love, encouragement, and support. I'm grateful for the quality time together, and even more for your patience when I spent to little time with you.

Thank you all so very much.